INSTITUT POLYTECHNIQUE DE PARIS

NNT : 2021IPPAX041

Thèse de doctorat

CPHT Centre de Physique Théorique

ÉCOLE POLYTECHNIQUE

IP PARIS

Out-of-equilibrium dynamics and quench spectroscopy of ultracold many-body quantum systems

Thèse de doctorat de l'Institut Polytechnique de Paris
préparée à l'École Polytechnique

École doctorale n°626 de l'Institut Polytechnique de Paris (EDIPP)
Spécialité de doctorat : Physique

Thèse présentée et soutenue à Palaiseau, le 09/07/2021, par

LOUIS VILLA

Composition du Jury :

Patrizia Vignolo Professeure, Université de Nice-Sophia Antipolis (Institut Non-Linéaire de Nice)	Présidente
David Clément Maître de Conférences, Institut d'Optique Graduate School (Laboratoire Charles Fabry)	Rapporteur
Nicolas Pavloff Professeur, Université Paris-Saclay (Laboratoire de Physique Théorique et Modèles Statistiques)	Rapporteur
Gabriele De Chiara Reader, Queen's University of Belfast (Centre for Theoretical Atomic, Molecular and Optical Physics)	Examinateur
Luca Tagliacozzo Ramon y Cajal Fellow, Universitat de Barcelona (Departamento de Fisica Cuantica i Astrofisica)	Examinateur
Laurent Sanchez-Palencia Directeur de recherche, École Polytechnique (Centre de Physique Théorique)	Directeur de thèse

Contents

1 Out-of-equilibrium dynamics and quantum simulation of strongly correlated systems 7
1.1 Strongly correlated quantum systems 8
1.1.1 Lineland 8
1.1.2 Confining bosons on a chain 10
1.1.3 Spin chains 13
1.2 Out-of-equilibrium dynamics 17
1.2.1 Quantum quenches 17
1.2.2 Equilibration towards a long-time steady state 18
1.2.3 Correlation and information spreading 20
1.2.4 Numerical simulations 22
1.3 Ultracold atom quantum simulators 24
1.3.1 Creating the system 24
1.3.1.1 Trapping and cooling using light 24
1.3.1.2 Tuning the interactions 26
1.3.1.3 Versatile experimental platforms 28
1.3.2 Measuring the system properties 29
1.3.2.1 Time-of-flight 29
1.3.2.2 Quantum microscopes 30
1.3.2.3 Pump-probe spectroscopies 32
Appendix 1.A Exact solution of the Lieb-Liniger model from the Bethe ansatz 37
Appendix 1.B Quantum ergodicity and thermalisation of the long-time steady state . . 49
Appendix 1.C Details about the quench action 53
Appendix 1.D Excitations in the strongly interacting Mott insulator 55
Appendix 1.E Density-phase representation of the field operator 57

2 Correlation spreading 59
2.1 A short review of correlation spreading in short-ranged lattice models 59
2.1.1 Early studies of the out-of-equilibrium dynamics 59
2.1.2 Generalisation of the quasiparticle picture 62
2.2 Observation of a generic twofold structure 66
2.2.1 The superfluid mean-field regime 67
2.2.2 Strongly correlated phases at unit filling 68
2.2.3 Loss of the double structure 71
2.2.4 Strongly interacting superfluid regime at low filling 72
2.2.5 Extension to long-range systems 73
Appendix 2.A Phase and group velocities and the wake-pattern in classical physics . . 77
Appendix 2.B Convergence of the MPS results 80
Appendix 2.C Mapping the Bose-Hubbard model to a Luttinger liquid 81

3 Quench spectroscopy 85
3.1 Review of standard pump-probe spectroscopies 86
3.1.1 Response function in the linear regime 86
3.1.2 Spectral functions, dynamics and excitations 87
3.2 Global quench spectroscopy 89
3.2.1 The quench spectral function (QSF) 90
3.2.2 Probing excitation spectra from global quench dynamics 94

3.2.2.1 Benchmarks on the Bose-Hubbard chain . . . 94
3.2.2.2 The strongly interacting superfluid regime . . . 96
3.2.2.3 Spin chains . . . 99
3.2.3 Link with the generic form of two-point correlators after a global quench . 102
3.3 Local quench spectroscopy . . . 103
3.3.1 The need for a new definition of the QSF for local quenches . . . 104
3.3.2 Choosing the initial state and the observable . . . 105
3.3.2.1 General strategy . . . 105
3.3.2.2 Examples of local quench protocols . . . 106
3.3.3 Extracting excitation spectra . . . 107
3.3.4 Probing transition energies . . . 113
3.3.5 Extracting additional information from the QSF . . . 117
3.3.5.1 Probing non-local excitations of the transverse-field Ising chain . 118
3.3.5.2 Two-excitation continuum in the Bose-Hubbard chain . . . 120
Appendix 3.A Approximate Bethe ansatz for the Bose-Hubbard model . . . 124
Appendix 3.B Comparison between the dynamical structure factor and the QSF . . . 133
4 Quench spectroscopy for disordered systems . . . 135
4.1 Why are disordered systems interesting? . . . 135
4.1.1 Anderson localisation . . . 136
4.1.2 Quantum glasses and many-body localisation . . . 137
4.2 The disordered Bose-Hubbard model . . . 138
4.2.1 The Bose glass . . . 138
4.2.2 Detecting the Bose glass and probing the phase diagram . . . 141
4.3 Disordered quench spectroscopy of the Bose-Hubbard chain . . . 145
4.3.1 Quench protocol and QSF for disordered systems . . . 145
4.3.2 A benchmark: the phase-diagram from standard probes . . . 148
4.3.3 Spectral properties of the excitations within each phase . . . 149
4.3.4 Reconstructing the phase diagram from the excitations dynamics . . . 156
5 Conclusions and perspectives . . . 161

Remerciements

Je tiens tout d'abord à remercier vivement les rapporteurs d'avoir accepté de lire attentivement le manuscrit, et l'ensemble du jury pour leurs remarques et les échanges constructifs qui ont suivi la soutenance de ces travaux de thèse. Ces travaux ont été financés par une bourse de l'École Normale Supérieure de Lyon (contrat ASN) et par la bourse d'excellence Gaspard Monge de l'École Polytechnique. Je remercie vivement les deux institutions pour ce précieux soutien financier.

L'ensemble des recherches présentées ci-dessous ne sont pas le fruit de mon seul travail. Je dois tout d'abord un immense merci à Laurent Sanchez-Palencia pour m'avoir offert l'opportunité de travailler dans son groupe au sein du Centre de Physique Théorique de l'École Polytechnique. J'ai beaucoup appris avec toi Laurent, scientifiquement mais aussi sur le fonctionnement de la recherche et j'ai en particulier beaucoup gagné sur le plan de l'écriture scientifique. Tu m'as toujours laissé la liberté d'explorer librement de nouvelles pistes, et tu as toujours su m'éclairer ou me rediriger lorsque je commençais à m'égarer. Je dois également beaucoup aux deux co-auteurs et collaborateurs des publications: Julien Despres et Steven Thomson. Merci Julien pour m'avoir aiguillé au début de la thèse et m'avoir enseigné ce que tu savais de la propagation des corrélations et plus généralement de la physique des atomes froids. De même Steven, merci d'abord pour ton enthousiasme sur le projet de spectroscopie par quench et tes enseignements précieux sur la physique des systèmes désordonnés, mais surtout pour ta présence et ton investissement sans faille au fil des confinements successifs et jusqu'à ce jour. Je remercie également l'ensemble de notre groupe, et plus spécialement Hepeng Yao et Jan Schneider pour nos nombreuses discussions qui, si elles n'ont pas abouti à des collaborations directes, ont enrichi ma vision de la physique et égaillé les journées au bureau. Merci enfin à tous les collègues du CPHT qui rendent cet endroit si spécial, stimulant et agréable. J'ai aussi eu la chance au cours du doctorat d'enseigner le modal de physique de matière molle pour le deuxième cycle polytechnicien avec Mathilde Reyssat en 2018-2019 puis avec Anaïs Gauthier en 2019-2020, et je tiens à les remercier chaleureusement pour la confiance qu'elles m'ont témoigné. Merci aussi à Ambre Bouillant pour nous avoir tant aidé dans 'son' laboratoire, ainsi qu'à tout le LadHyX pour son accueil.

Au delà des chercheurs et collègues, je tiens à remercier tout particulièrement l'encadrement du CPHT, en premier lieu son directeur, Jean-René Chazottes, extrêmement investi tout en restant toujours disponible et à l'écoute des doctorants. Je remercie également tout le secrétariat pour son efficacité et sa gentillesse, et en particulier Malika Lang, Florence Auger et Fadila Debbou. Merci de m'avoir permis de me concentrer sur la recherche le plus possible, en me simplifiant autant qu'il était possible de le faire la 'vie administrative'. Je tiens aussi à remercier le service informatique pour une rapidité et une efficacité sans commune mesure, et en particulier Danh Pham-Kim, Jean-Luc Bellon (bonne retraite!) et Yannick Fitamant.

Le cheminement jusqu'au doctorat est long, et je voudrais remercier certaines personnes qui ont joué un rôle majeur pour attiser puis entretenir ma flamme de physicien. Tout d'abord Robert Bédoret et Jean-Yves Degorce, pour leur soutien et leur amitié sans faille mais surtout leur passion communicative de la physique. Merci également à l'ensemble des professeurs de l'ENS de Lyon, qu'il serait déraisonnable de lister ici. Je dois également chaleureusement remercier Gabriele De Chiara pour un stage de 3 mois en 2017, qui a initié cette passion pour la physique atomique et les atomes froids. Mentor idéal, c'était un immense honneur de t'avoir dans le jury de thèse!

Un grand merci aux personnes plus éloignées de Polytechnique, tous mes amis et plus spécialement les membres du groupe Jolidon pour cette aventure incroyable et de longue haleine jusqu'à la publication du livre, ainsi qu'à Camille pour son aide si précieuse avec LaTeX. Enfin un immense merci à ma famille, en particulier mes parents et mon frère, pour leur soutien sans faille, leur inspiration et leur motivation quotidienne. Pour terminer, un merci tout particulier à Claire, pour la sérénité et l'apaisement que tu m'apportes depuis si longtemps déjà.

Introduction

Strongly correlated quantum systems have emerged as a burgeoning field of modern research. First at equilibrium, where they give rise to exotic phases of matter with fascinating properties, then when driven out-of and far-from equilibrium, where understanding their dynamics quickly became a pressing question. Besides the fundamental interest in understanding quantum matter, progress in this area promises fascinating applications in particular for quantum technologies. Compared to the equilibrium situation, the physics out-of and far-from equilibrium, which constitutes the central topic of this thesis, is only in its early stages. When a many-body quantum system is isolated from its environment, by which mechanism does it dynamically reaches thermal equilibrium (if it does), and how can we characterise the behaviour of correlations and the propagation of quantum information? Hints about such questions concerning transport are usually given by a precise understanding of the system elementary excitations, and are experimentally probed by spectroscopic techniques which commonly rely on linear response theory. Historically, transport properties have been investigated within the realm of linear response theory, and have provided a crucial understanding of transport coefficients such as the conductivity of materials. In classical systems, out-of-equilibrium phenomena such as ageing effects in glasses or hydrodynamical instabilities are examples where non-linear effects become relevant. In quantum systems, especially in the strongly correlated regime, out-of-equilibrium dynamics beyond the linear regime constitutes a great challenge.

Thanks to the dramatic experimental progress within the past two decades in cooling, trapping and engineering of quantum systems, it became possible to transpose these questions from solid-state physics to ultracold atoms. The latter can investigate dynamical properties with an unprecedented accuracy, down to the single-atom and single-site precision. The increased level of control gave birth to many experimental platforms but also many tools at our disposal, arguably the most powerful of which to bring a system out-of-equilibrium is the one of a quantum quench. Two important examples are global and local quenches. In a global quench, the quantum system is initially prepared in the ground state of a Hamiltonian with some initial parameters, and then one abruptly changes one of its parameters to induce dynamics. In a local quench, the Hamiltonian is not changed, but a local perturbation such as a defect is introduced in the initial state so as to induce dynamics.

We will also focus on non-relativistic theories of quantum physics, which do not set a fundamental limit to the speed at which information can propagate. However, such systems do admit under certain conditions a bound for the spreading of quantum correlations and information. One dimensional quantum systems offer a privileged playground to investigate such questions. Some of them are amenable to powerful analytical methods such as bosonisation or the Bethe ansatz for integrable systems, and provide invaluable exact solutions in the strongly interacting regime. Another prowess of one dimensional models is that they are often amenable to efficient numerical simulations, that can be solved up to an arbitrary precision under a reasonable time. An example of such numerical method which we will use below is the density matrix renormalisation group (DMRG) algorithm, together with the time-dependent variational principle (TDVP) approach which simulates the evolution of the out-of-equilibrium system following a quantum quench. We also emphasise that one dimensional quantum systems, besides being convenient for benchmarking, also possess intrinsic properties which cannot be directly transposed to their higher dimensional counterpart. Lastly, in the presence of disorder, particles tend to localise in real-space. This emergent phenomena gives rise to new dynamical phases of matter with intriguing properties, for instance admitting gapless excitations while being globally insulating.

Framework of our study

So far, the propagation of correlations has been studied mainly using Lieb-Robinson bounds. However, it has recently been realised that the space-time structure of correlation functions contains richer information [Cevolani et al., 2018]. In this thesis, we have studied the information that can be extracted from these space-time patterns. Our main result is the proposal of a new spectroscopy based on the analysis of these structures. We show that one can indeed determine spectral properties about the excitations and in particular reconstruct the full excitation spectrum in a momentum-resolved manner by a variety of patterns after a local or a global quench. We also show that quench spectroscopy can be used to determine the phase diagram of disordered systems. More precisely, the manuscript is organised as follows.

Chapter 1 serves as a general introduction to out-of-equilibrium dynamics and the physics of ultracold atoms. We present the one dimensional models used in the rest of the thesis (interacting bosons and spin chains) and we discuss their ground state properties as well as the elementary excitations they admit. We also discuss the main tools to investigate their dynamics after quantum quenches, analytically (Lieb-Robinson bounds, quasiparticle picture, exact results on integrable models) as well as numerically (mainly the density-matrix renormalisation group within the framework of matrix product states). We finally discuss the experimental implementation of such models, and the tools at disposal to measure their physical properties with a particular emphasis on spectroscopic methods.

In Chapter 2 we begin by introducing a generalised quasiparticle picture which was proposed on analytical grounds recently and provides a physical mechanism to explain the propagation of correlations in lattice quantum systems. We verify this picture based on exact numerical results and highlight that in general, correlation spreading in lattice quantum systems is twofold. Two characteristic velocities can be extracted from the dynamics, one of which determines precisely the value at which information, carried by the excitations of the system, is propagating. These two velocities are solely determined by the elementary excitations of the model, and they differ when the energy-momentum relation (dispersion relation) of the quasiparticles is non linear (dispersive).

Chapter 3 builds on the link mentioned in the previous chapter between the after-quench dynamics and the properties of the elementary excitations of the model. We propose a novel spectroscopic method named *quench spectroscopy* which is capable of reconstructing spectral properties such as the excitation spectrum from a series of snapshots of the out-of-equilibrium dynamics. We compare this method to existing ones such as pump-probe spectroscopies, and we argue about some advantages that quench spectroscopy provides. In particular, it allows to access spectral properties in a momentum-resolved manner, without requiring a specific calibration for each momentum value. We address quench spectroscopy in two main scenarios for clean systems, which are the ones of a global quench and of a local quench. We emphasise the role played by the observable on spectral properties throughout various examples.

In Chapter 4, we extend quench spectroscopy to disordered systems. We begin this chapter with a brief introduction to the physics of disordered systems. Using the disordered Bose-Hubbard chain as an example, we show how quench spectroscopy detects specific spectral signatures within each phase and allows to detect the emerging phase in the presence of disorder called the Bose glass. We discuss the Bose glass properties using quench spectroscopy, and the properties of the elementary excitations in all phases in the presence of disorder. We then define a local spectral probe and show that it is capable of distinguishing the real-space local structure of each phase. Such probe based on single-site measurements, can be used to reconstruct the full phase diagram of the model, as we demonstrate numerically.

Finally we conclude our study in Chapter 5 by providing a summary of the main results and several possible extensions.

Technical details and notes for further reading have been moved to Appendices. I have taken the liberty of adapting the notations of some figures (labels, units, etc) from the literature to fit more naturally with the discussion and notations used in this thesis. Wherever this is the case, it is indicated by "Adapted from [X]" in the caption. All rights remain to the authors of the original publications. Throughout the manuscript we often use natural units such that $\hbar = 1$ and set the lattice spacing in lattice models to $a = 1$.

List of publications

Despres, J., Villa, L., & Sanchez-Palencia, L. (2019). Twofold correlation spreading in a strongly correlated lattice Bose gas. *Scientific Reports*, *9*(1), 4135. https://doi.org/10.1038/s41598-019-40679-3

Villa, L., Despres, J., & Sanchez-Palencia, L. (2019). Unraveling the excitation spectrum of many-body systems from quantum quenches. *Physical Review A*, *100*(6), 063632. https://doi.org/10.1103/PhysRevA.100.063632

Villa, L., Despres, J., Thomson, S. J., & Sanchez-Palencia, L. (2020). Local quench spectroscopy of many-body quantum systems. *Physical Review A*, *102*(3), 033337. https://doi.org/10.1103/PhysRevA.102.033337

Villa, L., Thomson, S. J., & Sanchez-Palencia, L. (2021a). Finding the phase diagram of strongly-correlated disordered bosons using quantum quenches. https://arxiv.org/pdf/2105.06396.pdf

Villa, L., Thomson, S. J., & Sanchez-Palencia, L. (2021b). Quench spectroscopy of a disordered quantum system. https://arxiv.org/pdf/2105.05774.pdf

Résumé en français

Les systèmes quantiques fortement corrélés sont devenus un domaine de recherche moderne en plein essor. D'abord à l'équilibre, où ils donnent naissance à des phases exotiques de la matière aux propriétés fascinantes, puis lorsqu'ils sont entraînés hors de l'équilibre et loin de celui-ci, où la compréhension de leur dynamique est rapidement devenue une question cruciale. Outre l'intérêt fondamental que présente la compréhension de la matière quantique, les progrès réalisés dans ce domaine promettent des applications fascinantes, notamment pour les technologies quantiques. Par rapport à la situation d'équilibre, la physique hors et loin de l'équilibre, qui constitue le sujet central de cette thèse, n'en est qu'à ses débuts. Lorsqu'un système quantique à plusieurs corps est isolé de son environnement, par quel mécanisme atteint-il dynamiquement l'équilibre thermique (s'il y parvient), et comment pouvons-nous caractériser le comportement des corrélations et la propagation de l'information quantique ? Les indices sur ces questions concernant le transport sont généralement donnés par une compréhension précise des excitations élémentaires du système, et sont sondés expérimentalement par des techniques spectroscopiques qui reposent généralement sur la théorie de la réponse linéaire. Historiquement, les propriétés de transport ont été étudiées dans le cadre de cette théorie, et ont permis de comprendre les coefficients de transport tels que la conductivité des matériaux. Dans les systèmes classiques, les phénomènes hors équilibre tels que les effets du vieillissement dans les verres ou les instabilités hydrodynamiques sont des exemples où les effets non linéaires deviennent pertinents. Dans les systèmes quantiques, en particulier dans le régime fortement corrélé, la dynamique hors équilibre au-delà du régime linéaire constitue un grand défi. Grâce aux progrès expérimentaux spectaculaires réalisés au cours des deux dernières décennies en matière de refroidissement, de piégeage et d'ingénierie des systèmes quantiques, il est devenu possible de transposer ces questions de la physique de l'état solide aux atomes ultrafroids. Ces derniers peuvent étudier les propriétés dynamiques avec une précision sans précédent, jusqu'à une résolution d'un atome et/ou d'un site unique. Le niveau de contrôle accru a donné naissance à de nombreuses plateformes expérimentales mais aussi à de nombreux outils à notre disposition, dont le plus puissant pour amener un système hors d'équilibre est sans doute celui d'un quench (trempe) quantique.

Jusqu'à présent, la propagation des corrélations a été étudiée principalement à l'aide des bornes de Lieb-Robinson. Cependant, il a été récemment réalisé que la structure spatio-temporelle des fonctions de corrélation contient des informations plus riches [Cevolani et al., 2018]. Dans cette thèse, nous avons étudié l'information qui peut être extraite de ces structures spatio-temporelles. Notre principal résultat est la proposition d'une nouvelle spectroscopie basée sur l'analyse de ces structures. Nous montrons qu'il est possible de déterminer les propriétés spectrales des excitations et en particulier de reconstruire le spectre complet d'excitation d'une manière résolue en vecteur d'onde, et ce par une étude de la dynamique hors équilibre faisant suite à un quench quantique local ou global. Nous montrons également que la spectroscopie par quench peut être utilisée pour déterminer le diagramme de phase de systèmes désordonnés. Plus précisément, le manuscrit est organisé comme suit.

Le chapitre 1 sert d'introduction générale à la dynamique hors équilibre et à la physique des atomes ultra-froids. Nous présentons les modèles unidimensionnels utilisés dans le reste de la thèse (bosons en interaction et chaînes de spin) et nous discutons leurs propriétés à l'état fondamental ainsi que les excitations élémentaires qu'ils admettent. Nous discutons également des principaux outils permettant d'étudier leur dynamique après un quench quantique, aussi bien analytiquement (bornes de Lieb-Robinson, représentation en terme de quasiparticules, résultats exacts sur les modèles intégrables) que numériquement (principalement le groupe de renormalisation de la matrice de densité dans le cadre des états de produits matriciels). Nous discutons enfin de la mise en œuvre expérimentale de ces modèles et des outils à disposition pour mesurer leurs propriétés physiques, en mettant l'accent sur les méthodes spectroscopiques.

Dans le chapitre 2, nous commençons par présenter une image généralisée des quasiparticules qui a été proposée récemment sur des bases analytiques et qui fournit un mécanisme physique pour expliquer la propagation des corrélations dans les systèmes quantiques sur réseau. Nous vérifions cette image sur la base de résultats numériques exacts et mettons en évidence qu'en général, la propagation des corrélations dans les systèmes quantiques possède une double structure. Deux vitesses caractéristiques peuvent être extraites de la dynamique, dont l'une détermine précisément la valeur à laquelle l'information, portée par les excitations du système, se propage. Ces deux vitesses sont uniquement déterminées par les excitations élémentaires du modèle, et elles diffèrent lorsque la relation entre l'énergie et le vecteur d'onde (relation de dispersion) des quasi-particules est non linéaire (dispersive).

Le chapitre 3 s'appuie sur le lien mentionné dans le chapitre précédent entre la dynamique hors d'équilibre et les propriétés des excitations élémentaires du modèle. Nous proposons une nouvelle méthode spectroscopique appelée *spectroscopie par quench* qui est capable de reconstruire les propriétés spectrales telles que le spectre d'excitation à partir d'une série d'instantanés de la dynamique hors équilibre. Nous comparons cette méthode aux méthodes existantes, telles que les spectroscopies pompe-sonde, et nous discutons de certains avantages de la spectroscopie par quench. En particulier, elle permet d'accéder aux propriétés spectrales d'une manière résolue en vecteur d'onde, sans nécessiter une calibration spécifique pour chaque valeur. Nous abordons la spectroscopie par quench dans deux scénarios principaux pour les systèmes en l'absence de désordre, à savoir ceux d'un quench global et d'un quench local. Nous soulignons le rôle joué par l'observable sur les propriétés spectrales à travers divers exemples.

Dans le chapitre 4, nous étendons la spectroscopie par quench aux systèmes désordonnés. Nous commençons ce chapitre par une brève introduction à la physique des systèmes désordonnés. En utilisant la chaîne de Bose-Hubbard désordonnée comme exemple, nous montrons comment la spectroscopie par quench détecte des signatures spectrales spécifiques dans chaque phase et permet de détecter la phase émergente en présence de désordre, appelée le verre de Bose. Nous discutons des propriétés du verre de Bose en utilisant la spectroscopie par quench, et des propriétés des excitations élémentaires dans toutes les phases du modèle en présence de désordre. Nous définissons ensuite une sonde spectrale locale et montrons qu'elle est capable de distinguer la structure locale de chaque phase dans l'espace réel. Une telle sonde, basée sur des mesures en site unique, peut être utilisée pour reconstruire le diagramme de phase complet du modèle, comme nous le démontrons numériquement.

Enfin, nous concluons notre étude dans le chapitre 5 en fournissant un résumé des principaux résultats et plusieurs extensions possibles.

1 Out-of-equilibrium dynamics and quantum simulation of strongly correlated systems

Quantum mechanics primarily focused on weakly interacting systems, for which most properties can be described essentially by perturbation theory or mean-field approaches. Two of the most prominent examples, both from a theoretical and an experimental perspective, are given by the discovery of new states of matter with intriguing properties such as superconductivity (discovered on mercury by Onnes in 1911; explained by Bardeen-Cooper-Schrieffer theory) and superfluidity (discovered on helium 4 by Kapitsa in 1937; explained by Bogoliubov-Landau theory). In solid state physics, electronic properties of metals in three dimensions were successfully described within Landau's Fermi liquid theory formalism postulating the existence of long-lived quasiparticles, adiabatically connecting the interacting system to a non-interacting one.

As soon as strongly interacting systems lurked around the corner, unanswered questions began to pile up. Some pressing ones are still unanswered to this day, arguably the most important being the explanation for high temperature superconductivity which would probably guide us towards ambient temperature and pressure real-world material examples. We will discuss many other examples in the following. In order to answer them, minimal models have been built, but even these are extremely difficult to solve. Apart from the hydrogen atom and the harmonic oscillator, extremely invaluable exact solutions were scarce in the early days of quantum mechanics, and the more involved many-body problem long remained untouched. The biggest exception is Bethe's work, who in 1931 solved the Heisenberg model in one dimension by using an ansatz for the wave function to compute all eigenstates and eigenfunctions exactly. His work long remained as a little-known curiosity, before many other exact solutions were found using a similar technique on one-dimensional systems in the 1960s [Lieb and Liniger, 1963; Lieb et al., 1961; Lieb and Wu, 1968]. All these exactly solvable models are one dimensional ones, and are now referred to as *integrable*. Integrability immensely developed in the branch of mathematical physics in the past 50 years, and initially paved the way for our understanding of strongly correlated quantum systems by providing exact solutions of quantum models for arbitrary interactions. The behaviour of electrons in the one dimensional world cannot be described by Fermi liquid theory and is superseded by the Luttinger liquid theory, proposed by Haldane [F. D. M. Haldane, 1981a, 1981b]. This *bosonisation*[1] procedure became a pivotal tool since it captures the low-energy physics of one dimensional gapless systems (for reviews, see [Cazalilla et al., 2011; Giamarchi, 2004; Schulz, 1995]).

One dimensional systems are the prime examples of strongly interacting systems: they admit a few exact solutions, they can be simulated numerically in an efficient way and they can be easily realised in current state-of-the-art experiments. Considerable experimental progress in ultracold atomic physics led to the creation, control and study of interacting many-body quantum systems with considerable accuracy. Such systems can be decoupled from the environment (isolated) to a very good approximation and therefore evolve under unitary dynamics. Less sensitive to decoherence [Zurek, 2003] than their open counterpart, the closed systems realised experimentally are good candidates for (universal) quantum simulators, which has become a growing field of quantum

[1] By linearising the energy-momentum relation close to the Fermi level, collective excitations can be cast into the bosonic modes of a quantum harmonic oscillator, hence the name.

engineering [Blatt and Roos, 2012; Bloch et al., 2012; Cirac and Zoller, 2012; Georgescu et al., 2014]. Therefore besides the fundamental interest in strongly interacting quantum systems, the growing field of quantum engineering and quantum computing developed quickly thanks to back-to-back experimental breakthroughs in the last two-decades. This gives hope towards the realisation of Feynman's vision of a universal quantum computer in the distant future, and of reliable large scale quantum simulators in the near future. The high degree of experimental precision and control showed that many surprises still hold even at equilibrium, in particular concerning the equilibration and possible thermalisation of the system at long times. We commonly rely on a statistical (thermal) ensemble governed by a few variables to predict using statistical physics (or thermodynamics) the behaviour of a system. The underlying assumption at the foundation of statistical mechanics, the ergodic hypothesis, remains a subject of ongoing investigations. The related topic of quantum thermalisation will be briefly introduced below.

In a nutshell, the following introductory chapter attempts to encapsulate the following topics: why are strongly interacting systems interesting, how can we build them, and finally what are the tools at our disposal to study and measure them.

1.1 Strongly correlated quantum systems

In this Sec. 1.1, we discuss the various quantum phases and their fascinating properties (ground state and elementary excitations) for typical quantum models amenable to the strongly correlated regime and which we will use throughout the manuscript.

1.1.1 Lineland

One dimensional systems constitute the most suitable category of strongly correlated systems. The first illustration stems from the fact that dimensionality plays an important role in reaching the strongly interacting regime: on a line, particles cannot pass through each other without colliding. This topological effect has dramatic consequences, for instance forcing excitations to become collective ones or separating the spin and the charge of electrons [Giamarchi, 2004]. In one dimension, our main focus will be bosons. This choice is not very restrictive, since here into "bosons" we include spins-1/2 and spinless fermions. As we will detail below, indeed in one dimension hard core bosons can be mapped into spins-1/2 using the Holstein-Primakoff transformation, and to spinless fermions using the Jordan-Wigner transformation. Commonly in one dimension, the bosonic or fermionic behaviour of the system depends on the interaction regime[2]. We will also mostly discuss the zero temperature physics, where any existing phase transition will be driven by quantum fluctuations rather than thermal ones. Such quantum phase transitions are indicated by non-analytic singularities in the ground state energy. The reason for this choice is that a D dimensional $T = 0$ quantum system can be mapped to a $D+1$ dimensional classical one at $T > 0$, from which point one can use a theorem named after Mermin, Wagner and Hohenberg, which states that classical short-ranged systems in $D \leq 2$ dimensions at finite temperature [thus also quantum systems at $T = 0$ in $D \leq 1$ dimensions] cannot break a continuous symmetry. This amounts to the absence of long-range order and restricts the number of possible phase transitions[3].

[2]For instance, the wave function of hard core bosons is similar (up to an absolute value to preserve the symmetry) to the one of free fermions given by a Slater determinant. Some of the bosonic correlation functions (involving an even number of field operators) may be computed from free fermionic ones. This behaviour is referred to as *fermionisation*. The funny thing in one dimension is that fermions can be bosonised and bosons fermionised.

[3]In 3D, bosons undergo Bose-Einstein condensation by spontaneously breaking the continuous $U(1)$ symmetry, however in 1D the quantum phase fluctuations are always sufficiently strong to prevent the formation of the condensate, in agreement with the above mentioned theorem. One dimension admits quasi-condensates, characterised by small density fluctuations but large phase fluctuations. Of course, not all phase transitions are associated to a spontaneous symmetry breaking, for instance Berezinskii-Kosterlitz-Thouless (BKT) ones can happen without contradicting the MWH theorem. The latter also does not apply to discrete symmetries.

Solving a strongly correlated quantum system in an exact way is often impossible, at the exception of a few one dimensional examples referred to as *integrable*. Such noticeable exceptions include both lattice models (Heisenberg and XY spin chains, or the fermionic Hubbard chain) and continuum models (the relativistic sine-Gordon model, or the non-relativistic Lieb-Liniger model discussed below) and can be solved using the machinery of the Bethe ansatz. Other models can be mapped into free theories (in most cases a free fermionic one using a Jordan-Wigner transformation, for instance the transverse-field Ising chain). Note however that, excluding the latter, the computation of correlation functions often requires tremendous work [Korepin et al., 1997]. Exact numerical methods have been developed in one dimension, noticeably the density matrix renormalisation group (DMRG), which we will make use of and introduce in Sec. 1.2.4. This analytical/numerical particular behaviour is the second illustration of the special role played by one dimensional models.

The third illustration is given by the development of experimental techniques which led to an unprecedented accuracy in the simulation and control of such systems in condensed matter, contributing to grow our understanding of strongly correlated quantum matter. Below we begin by discussing the paradigmatic integrable Lieb-Liniger chain on which we shall illustrate a few other characteristic properties of the 1D world.

The Lieb-Liniger model The Lieb-Liniger model arises very generally by considering a system of N ultracold bosons whose interactions can be restricted to two-body processes, of the form $V(x_i, x_j)$. Provided that the de Broglie wavelength is much larger than the range of the interatomic van der Waals potential (therefore at sufficiently low temperature), the latter can be substituted by an effective contact interaction[4] $V(x_i, x_j) = g\,\delta(x_i - x_j)$ so that one obtains [Lieb, 1963; Lieb and Liniger, 1963]

$$H_{\rm LL} = -\frac{\hbar^2}{2m}\sum_{i=1}^{N}\frac{\partial^2}{\partial x_i^2} + g\sum_{i<j}\,\delta(x_i - x_j), \tag{1.1}$$

where $\delta(.)$ is the delta distribution, m the boson mass, and x_i the position of the $i^{\rm th}$ particle in real space. The constant g is sometimes also written as $\hbar^2 c/m$. The first term of the Hamiltonian is the kinetic energy of the particles and the second the interaction energy. In the following, $n = N/L$ stands for the gas density and L the size of the system.

This model captures the rather counter-intuitive fact that in one dimension it is for small densities that the interactions are the strongest. From Eq. (1.1), if the particles are localised, the total energy per particle reduces to the kinetic component[5] which can be estimated by $E_{\rm kin} \sim \hbar^2 n^{2/D}/2m$. On the contrary, if the particles are completely delocalised over the system size, the total energy per particle reduces to the interaction energy $E_{\rm int} \sim gn$. The ratio $\gamma = E_{\rm int}/E_{\rm kin}$ dictates the transition between the weakly interacting and the strongly interacting regime

$$\gamma = \frac{mg}{\hbar^2 n^{(2/D)-1}}, \tag{1.2}$$

and highlights the role played by the dimension to realise strongly interacting systems

$$\begin{aligned} \gamma_{\rm 1D} \gg 1 \quad &\Leftrightarrow \quad n_{\rm 1D} \ll \tfrac{mg}{\hbar^2} \\ \gamma_{\rm 3D} \gg 1 \quad &\Leftrightarrow \quad n_{\rm 3D} \gg \left(\tfrac{\hbar^2}{mg}\right)^3 . \end{aligned} \tag{1.3}$$

In 3D, strongly interacting systems require high density while in 1D, diluted systems are suited to investigate strongly correlated physics.

[4] For a detailed exposition of scattering theory, see for instance [Schwabl, 2002], Chap.18.

[5] At first, this may sound a bit strange. The particles are localised because they strongly repel each other, but since they are not in contact with one another (their wave function do not overlap), the total interaction energy of the system is indeed zero.

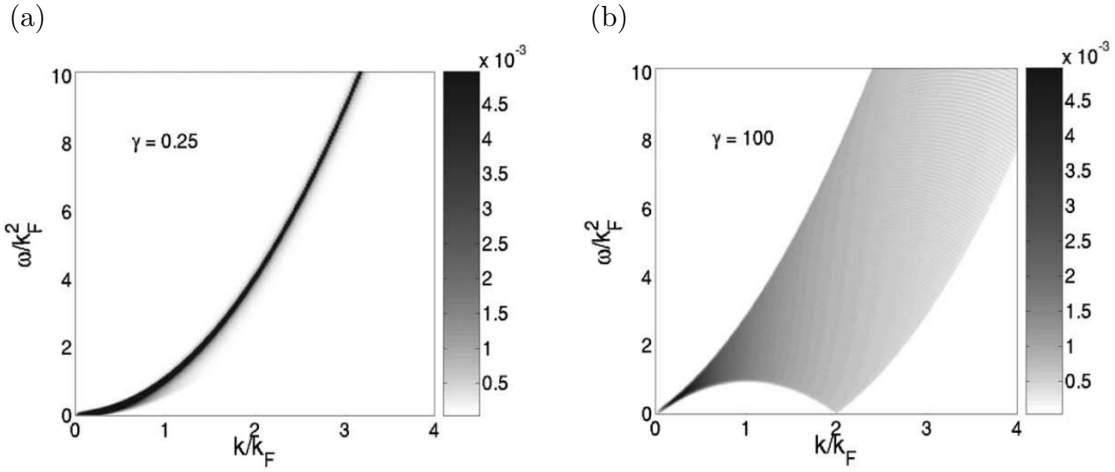

Fig. 1.1 Exact excitation spectrum of the Lieb-Liniger model computed using the Bethe ansatz. (a) In the weakly interacting regime, a single type of excitations matters, and they coincide with the particle-like excitations of the Bogoliubov regime. (b) When the interactions increase, hole-like excitations are necessary to describe the excitation spectrum which blurs from a single branch into a continuum. From [Caux and Calabrese, 2006].

As mentioned above, the Lieb-Liniger model is integrable and thus exactly solvable in the sense that its eigenenergies and eigenfunctions can be computed exactly. Full details about this procedure within the coordinate Bethe ansatz formalism are given in Appendix 1.A. This approach is well suited to a numerical study of the model thermodynamics (ground state and excitations properties) and of the excitation spectrum, which is represented in Fig. 1.1. In the weakly interacting regime, only the particle-like excitations matter, while in the strongly interacting regime, the hole-like excitations need to be taken into account (see Appendix 1.A for details on the explicit construction of the excitations).

Exact analytical results can also be obtained from the Bethe ansatz by computing the Tan contact [Olshanii and Dunjko, 2003; Tan, 2008a, 2008b, 2008c], which is a scalar quantity appearing in contact interacting models that relates thermodynamical properties to the decay of some correlation functions. The contact is proportional to the total interaction energy of the system, and can be measured experimentally from the long tail of the momentum distribution in momentum space. Besides, the scaling of the contact with the interactions and the temperature offers a way to detect the fermionised regime [H. Yao et al., 2018].

Let us finally mention that the low-energy physics of the Lieb-Liniger model can be accurately described by bosonisation. This approach is well suited for investigating the behaviour of correlation functions, while avoiding the cumbersome algebraic Bethe ansatz formalism of the quantum inverse scattering method.

1.1.2 Confining bosons on a chain

While the Lieb-Liniger model was a continuum one, we will now discuss its discrete generalisation. Slightly anticipating what follows, the motivation for this generalisation is that to reach strong interactions, one can dilute a one-dimensional system as described above, but a preferable method is to confine the atoms by trapping them on a lattice.

In second quantisation, using the field operator $\hat{\psi}(x)$ at the position x, a generic two-body Hamiltonian reads as

$$\hat{H} = \int \mathrm{d}x\, \hat{\psi}^\dagger(x) \frac{-\hbar^2\nabla^2}{2m} \hat{\psi}(x) + \frac{1}{2}\int \mathrm{d}x\, \mathrm{d}y\, \hat{\psi}^\dagger(x)\hat{\psi}^\dagger(y) V(x,y) \hat{\psi}(x)\hat{\psi}(y). \tag{1.4}$$

On the continuum, it is advantageous to decompose the field operator onto delocalised Bloch functions. But on a discrete chain, the atoms are more localised on the lattice sites and the basis

of Wannier functions (linear combinations of the Bloch ones) is more convenient to work with. As we restrict to low temperatures (alternatively deep lattices), we only retain the lowest-band, and because the Wannier functions w are very localised around each lattice site, we restrict to nearest-neighbour interactions so as to write $\hat{\psi}(x) = \sum_R w(x-R)\,\hat{a}_R(x)$. The only remaining parameters are the hopping amplitude $J > 0$ and the on-site interaction energy $U > 0$ defined as

$$\begin{aligned} J &= \int \mathrm{d}x\, w^\star(x-R)\left(-\frac{\hbar^2}{2m}\nabla^2 + V_{\mathrm{cl}}(x)\right) w(x-R\pm 1), \\ U &= \frac{4\pi\hbar^2 a_{\mathrm{s}}}{m}\int \mathrm{d}x\, |w(x)|^4, \end{aligned} \tag{1.5}$$

with $V_{\mathrm{cl}}(x)$ a possible external potential (used to confine the system). One then obtains the Bose-Hubbard model, first introduced by [Fisher et al., 1989], whose Hamiltonian takes the form

$$\hat{H}_{\mathrm{BH}} = -J\sum_R \left(\hat{a}_R^\dagger \hat{a}_{R+1} + \mathrm{h.c.}\right) + \frac{U}{2}\sum_R \hat{n}_R(\hat{n}_R - 1), \tag{1.6}$$

with $\hat{a}_R^{(\dagger)}$ the annihilation (creation) operator of a boson at the lattice site R, and $\hat{n}_R = \hat{a}_R^\dagger \hat{a}_R$ the corresponding on-site occupation number. Physically, each atom can tunnel from one site to its neighbour, and if a site hosts more than one boson then they interact. The first term of Eq. (1.6) represents the kinetic energy, proportional to the tunnelling probability $J > 0$. The negative sign in Eq. (1.6) always favours a uniform phase, which for $U = 0$ delocalises the particles over the entire lattice. The second term is an on-site interaction term which penalises energetically the system for high on-site occupation numbers. The operator $\hat{n}_R(\hat{n}_R - 1)/2$ counts the number of pairs of bosons on the site R occupied by n_R bosons, as we restricted to two-body interactions.

Depending on the value of the interactions J/U and the filling $\bar{n} = N/La$ (average particle density), with a the lattice spacing, there are two important distinct regimes. For integer filling and J/U sufficiently small, the system enters the Mott-insulator[6] (MI) phase. At $\bar{n} = 1$ in 1D, the critical value below which we enter the MI phase is $(J/U)_{\mathrm{c}} = 0.305(2)$ [Ejima et al., 2011; Ejima et al., 2012; Kashurnikov and Svistunov, 1996]. In the MI, the ground state has a fixed number of particles with negligible density fluctuations. Translation invariance imposes that the on-site occupation number n_R are unchanged and do not depend on the chemical potential μ, so the reduced compressibility $\kappa = \partial n/\partial\mu$ identically vanishes. For non-integer filling or if J/U is large enough, the system reaches a compressible superfluid phase (SF). A transition between these two regimes can happen when the interactions are varied or when the number of particles is changed. For fixed particle number, the critical behaviour of the Bose-Hubbard chain at $T = 0$ is in the same universality class as the classical bidimensional XY model (an example of the quantum to classical mapping) which exhibits a Berezinskii-Kosterlitz-Thouless (BKT) phase transition (in agreement with the Mermin-Wagner-Hohenberg theorem). The transition can also be crossed at fixed interactions and by varying the particle number (commensurate-incommensurate transition), and is mean-field like [Fisher et al., 1989] (sometimes also called of the Pokrovsky-Talapov type [Pokrovsky and Talapov, 1979]). In the grand canonical ensemble, the phase diagram displays a series of asymmetric Mott lobes that decrease in size as the filling increases. The first Mott lobe at $\bar{n} = 1$ is shown in Fig. 1.2(a). Experimentally, the MI-SF transition was observed in 3D by [Greiner et al., 2002] and will be discussed in Sec. 1.3.

The excitation spectrum of the model is also very different in both phases: while the SF excitation branch is gapless and linear at the origin, the MI one is gapped (adding a particle into the system cannot be done below a certain value set by the gap). However, the precise excitation

[6] The name comes from the fermionic Hubbard model at half-filling (one electron per site). While band theory would predict the system to be metallic, interactions are making the system insulating. To distinguish from conventional insulators, the phase was named a Mott insulator as a tribute to Mott (NP 1977).

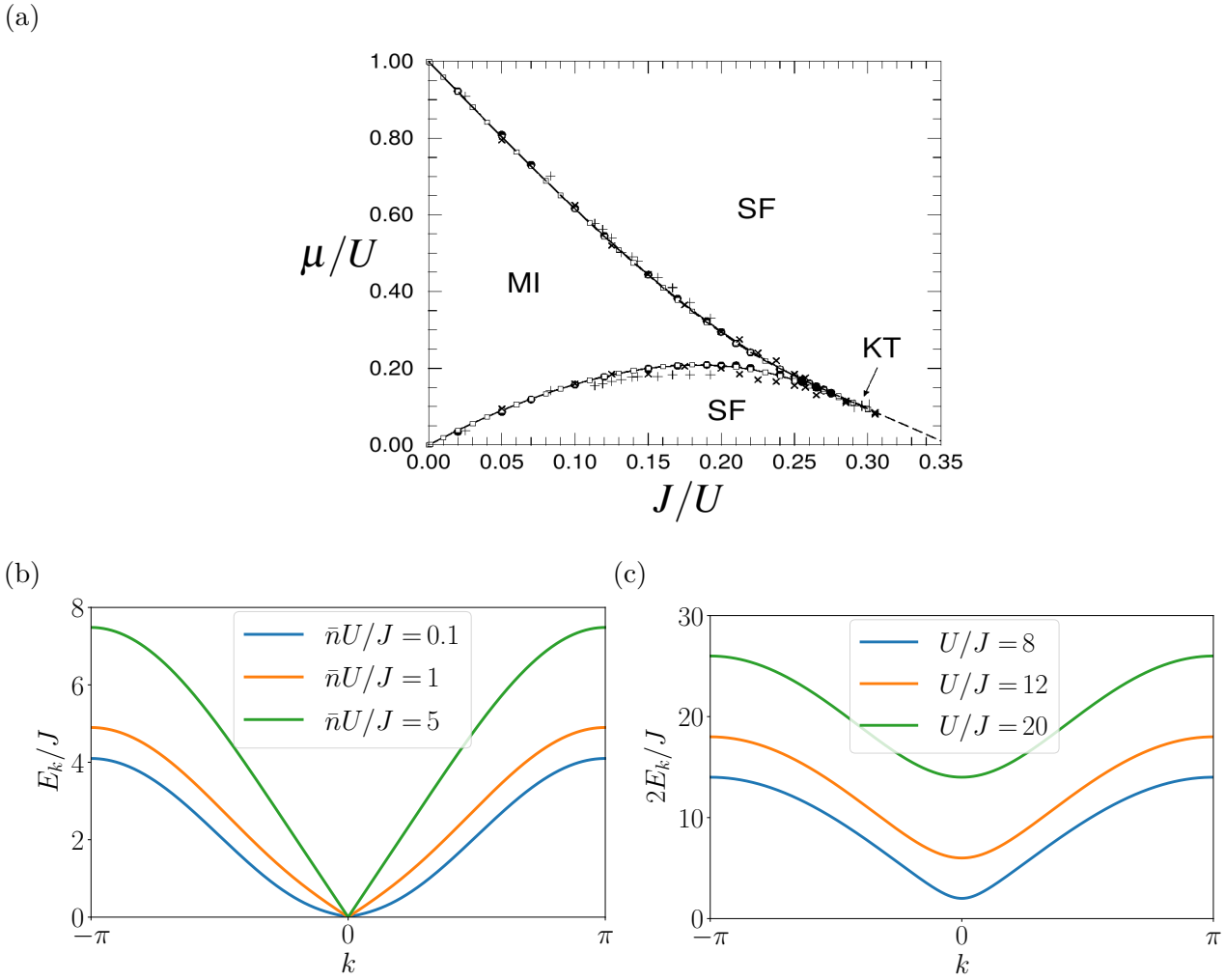

Fig. 1.2 (a) Portion of the phase diagram of the Bose-Hubbard chain in the grand canonical ensemble showing the first Mott lobe at $\bar{n} = 1$, from [Kühner et al., 2000]. The solid line is a strong coupling expansion, the "+" and "×" symbols are QMC data, filled circles and empty squares are DMRG data. The tip of the Mott lobe is closing exponentially as the transition is approached, making it challenging to resolve precisely numerically. Dispersion relation of the elementary excitations (b) in the mean-field SF regime [Eq. (1.7)] and (c) in the strongly interacting MI [Eq. (1.8)].

spectrum is only known in limiting cases. In the weakly interacting SF regime characterised by $U/(2J\bar{n}) \ll 1$, the excitations are Bogoliubov quasiparticles (see also Appendix 1.E) with the excitation spectrum

$$E_k = 2J\sqrt{2\sin^2\left(\tfrac{k}{2}\right)\left[2\sin^2\left(\tfrac{k}{2}\right) + \bar{n}\tfrac{U}{J}\right]}. \tag{1.7}$$

We plot the dispersion relation of the Bogoliubov quasiparticles in Fig. 1.2(b) for different values of $\bar{n}U/J$. The branch is always linear for $k \to 0$, and the linear regime increases with $\bar{n}U/J$. Deep in the MI for $U > 4(\bar{n}+1)J$, the Bose-Hubbard chain can be mapped to a fermionic model which admits two types of excitations [Barmettler et al., 2012]. The full derivation is detailed in Appendix 1.D, and will be extensively used throughout the manuscript. Here we only quote the result, which is that in the strongly interacting regime, the elementary excitations are approximately characterised by doublon-holon pairs and admit the following dispersion relation for $\bar{n} = 1$

$$2E_k = J\sqrt{\left(\tfrac{U}{J} - 6\cos k\right)^2 + 32\sin^2 k}, \tag{1.8}$$

plotted in Fig. 1.2(c) for different values of U/J.

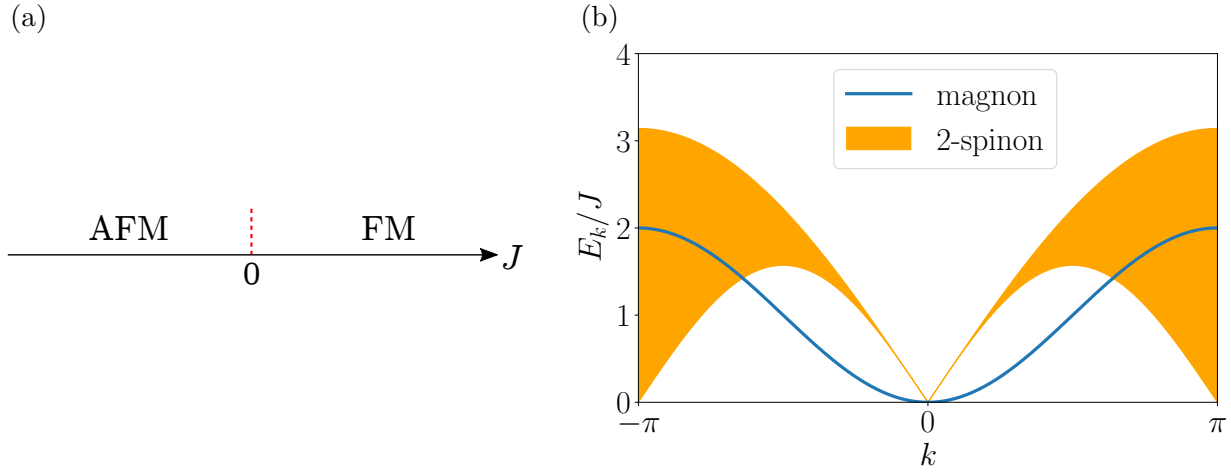

Fig. 1.3 (a) Phase diagram of the Heisenberg chain at zero temperature separating the ferromagnetic from the antiferromagnetic ground state. (b) Low-energy excitation spectrum in both cases, either the magnon (FM) or the 2-spinon continuum (AFM).

1.1.3 Spin chains

In some regimes, bosonic models can be mapped to spin chain models, as we will detail in Sec. 1.3.1.3. Below we discuss two spin chain models which we will make use of throughout the manuscript: the Heisenberg chain and the transverse-field Ising chain.

Heisenberg chain The Heisenberg spin-1/2 chain was the first exactly solved interacting quantum model: its ground state and elementary excitations were expressed without resorting to any approximation[7]. It provides a minimal model of a quantum magnet, and is governed in one dimension by the Hamiltonian

$$\hat{H}_{\mathrm{H}} = -J \sum_{R} \left(\hat{S}^x_R \hat{S}^x_{R+1} + \hat{S}^y_R \hat{S}^y_{R+1} + \hat{S}^z_R \hat{S}^z_{R+1} \right), \tag{1.9}$$

where J is the isotropic spin exchange coupling between nearest neighbours, and $\hat{S}^\alpha_R$ the spin operator along the axis α on the lattice site R. The ground state and the low-energy excitations only depend on the sign of J (its strength $|J|$ sets the energy scale). The Heisenberg chain is a non-trivial interacting model with a highly degenerate ground state in which all spins are aligned in the same but arbitrary direction for $J > 0$ (ferromagnetic order), and in opposite but still arbitrary direction for $J < 0$ (antiferromagnetic order) [Fig. 1.3(a)]. Despite its apparent simplicity, finding the eigenstates and eigenvalues of the model is a difficult task which was performed by Bethe back in 1931, using an ansatz for the form of the wave function that now bears his name [Bethe, 1931]. The Bethe ansatz solution of this model shares similarities with the Lieb-Liniger model discussed in Appendix 1.A, with slight modifications due to the additional internal degree of freedom due to the spin (see for instance [Franchini, 2017] for the derivation).

What about the excitation spectrum of the model? Since spin operators obey the $SU(2)$ algebra (angular momentum) commutation rules, the spin commutator for two different directions is an operator (not proportional to the identity). This makes it cumbersome to analytically work with spin degrees of freedom. Interestingly, spin operators can be mapped to bosonic ones obeying bosonic commutation relations by the Holstein-Primakoff transformation which for an arbitrary spin S reads as [Holstein and Primakoff, 1940]

$$\hat{S}^+_R = \sqrt{2S - \hat{n}_R}\, \hat{a}_R\,, \qquad \hat{S}^-_R = \hat{a}^\dagger_R \sqrt{2S - \hat{n}_R}\,, \qquad \hat{S}^z_R = S - \hat{n}_R\,, \tag{1.10}$$

[7] There cannot be any "small" parameter here anyway, since the only parameter J sets the energy scale.

where $\hat{S}^{\pm}_R = \hat{S}^x_R \pm i\hat{S}^y_R$. This transformation greatly simplifies the interpretation for the excitations of the model in some regimes. It is most useful if the ground state is sufficiently polarised along z (thus FM) such that the spin deviation around this axis can be considered small, $\langle \hat{n}_R \rangle \ll 2S$, meaning that the number of excitations remains small. The Holstein-Primakoff transformation can then be linearised into

$$\hat{S}^+_R = \hat{a}_R\,, \qquad \hat{S}^-_R = \hat{a}^\dagger_R\,, \qquad \hat{S}^z_R = S - \hat{n}_R\,. \tag{1.11}$$

This semi-classical linear spin-wave theory lets us interpret the low-energy excitations for $J > 0$ as magnons, with the dispersion relation[8]

$$E_k = J(1 - \cos k), \tag{1.12}$$

shown in Fig. 1.3(b). Magnons are quantised spin waves and can be interpreted as single spin flips, *i.e.* a single $\hat{b}$ operator [Fig. 1.4(a)]. Importantly, this dispersion relation can be shown to be exact directly from the Bethe ansatz (without involving the Holstein-Primakoff transformation and its linear approximation), see for instance [Karbach and Müller, 1997]. Here, the semi-classical picture from linear spin-wave theory adequately accounts for the quantum reality.

The situation is very much different in the antiferromagnetic case. First, the alternating state $|\uparrow\downarrow\uparrow\downarrow\cdots\rangle_z$ is not the ground state (in fact not even an eigenstate), which suggests already the breaking of the semi-classical picture. In the true ground state, quantum fluctuations play an important role: the antiferromagnetic order is only preserved locally (the spin-spin correlation function decays algebraically with the distance and not exponentially, signalling quasi-long range order) [Fig. 1.4(b)].

The semi-classical picture given by spin-wave theory fails to describe quantitatively the ground state in the antiferromagnetic case, as well as the excitations. The low-lying excitations are instead given by a two-spinon continuum[9] defined by [des Cloizeaux and Pearson, 1962]

$$\tfrac{\pi}{2} J\,|\sin k| \leq \omega \leq \pi J \left|\sin\left(\tfrac{k}{2}\right)\right|. \tag{1.13}$$

Detailed explanations about the Bethe ansatz procedure to derive this continuum in the antiferromagnetic Heisenberg model can be found in [Karbach et al., 1998]. Even though spinons have no classical interpretation, one may *qualitatively* think about them as non-local domain walls in the Néel state [Fig. 1.4(b)]. A spinon is a spin 1/2 particle, and spinons can only be created in pairs on a chain with an even number of spins. Since a pair is equivalent to a single spin flip of the chain, the elementary excitations (pairs of spinons) have a spin 1 [Faddeev and Takhtajan, 1981].

Such continuum can be probed by the dynamical structure factor, which can be measured in a scattering experiment. We will come back to this point later in Sec. 1.3.2.3, but in short, the picture above is validated.

The transverse-field Ising chain The last model we will discuss is the short-range transverse-field Ising (TFI) spin-1/2 chain, described by the Hamiltonian

$$\hat{H}_{\mathrm{TFI}} = -J \sum_{R=1}^{N-1} \hat{\sigma}^x_R \hat{\sigma}^x_{R+1} - h \sum_{R=1}^{N} \hat{\sigma}^z_R, \tag{1.14}$$

[8] The Hamiltonian can be rewritten as a quadratic form $\hat{H} = -|J|N/4 - |J|/2 \sum_R \left(\hat{a}^\dagger_{R+1}\hat{a}_R - \hat{a}^\dagger_R \hat{a}_R + \mathrm{h.c.}\right)$ for $S = 1/2$, which can be immediately diagonalised by moving to Fourier space. The modes of the obtained bosonic harmonic oscillator $E_k = J(1 - \cos k)$ are the magnons.

[9] In principle, the 4-spinon contribution should be taken into account as it is not negligible and its region in not all concluded within the 2-spinon one. However, its major contributions are included in the region defined by the 2-spinon continuum [Mourigal et al., 2013] (Supplemental Material).

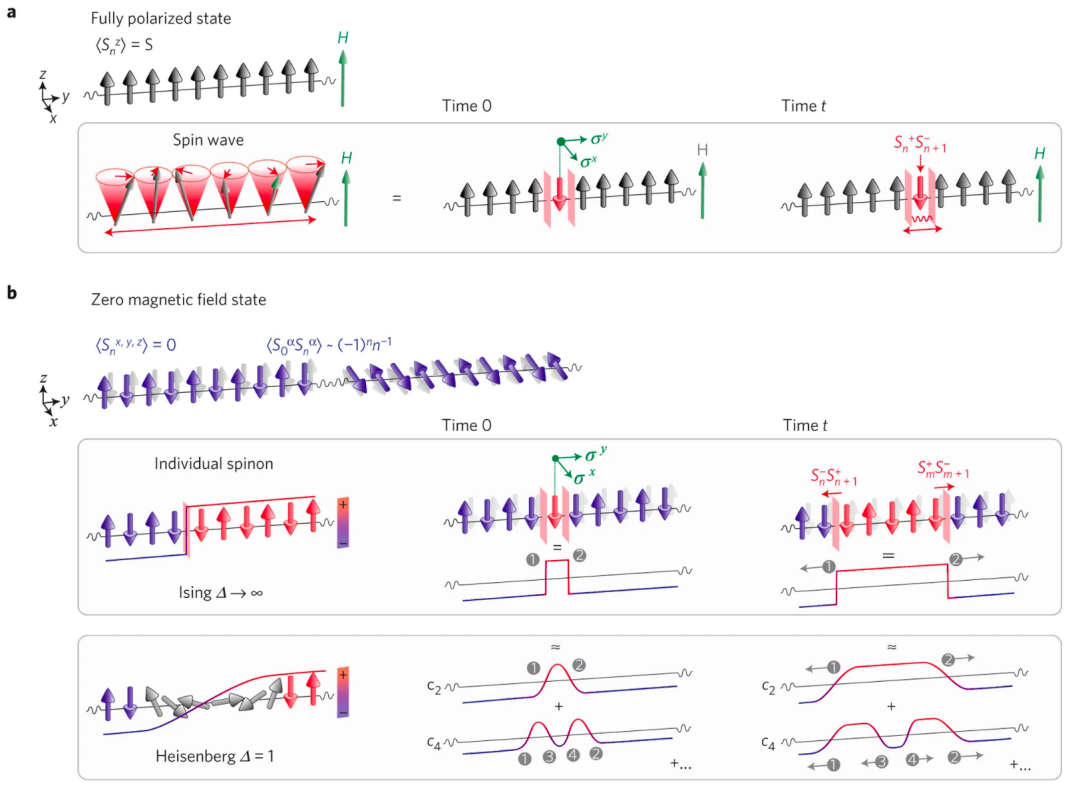

Fig. 1.4 Representation of the excitations for the Hamiltonian $\hat{H} = -J\sum_n \left(\hat{S}_n^x \hat{S}_{n+1}^x + \hat{S}_n^y \hat{S}_{n+1}^y + \Delta \hat{S}_n^z \hat{S}_{n+1}^z\right) - g\mu_B H \hat{S}_n^z$, with $J < 0$ (antiferromagnetic). (a) Representation of a magnon excitation in the presence of the external field. The excitation is the same as in the ferromagnetic isotropic Heisenberg chain (zero field), but it is harder to picture since all spins except one can be aligned in an arbitrary direction. (b) Top: representation of the highly degenerate ground state, where only two possible states with the spins aligned along z are represented. Middle: In the Ising limit, the spin flip excitation in the antiferromagnetic ground state can be pictured as a pair of counter-propagating non-local domain walls (spinons). Bottom: the first excited state is approximately represented by a combination of two and four spinons (higher order contributions are negligible). The excitation spectrum broadens into a continuum given by the Bethe ansatz [Eq. (1.13)]. From [Mourigal et al., 2013].

where h is the transverse field, $J > 0$ the ferromagnetic exchange coupling. The phase diagram displays a quantum phase transition at $h = J$ which separates a z-polarised paramagnetic phase (for $h > J$) from a doubly-degenerate $\pm x$-polarised ferromagnetic phase (for $h < J$) [Fig. 1.5(a)]. The biggest advantage of this model is that its exact excitation spectrum can be obtained simply by a mapping to non-interacting spinless fermions using the Jordan-Wigner transformation, followed by a Bogoliubov transformation [Franchini, 2017]. This yields

$$E_k = 2\sqrt{h^2 + J^2 - 2hJ\cos k}, \tag{1.15}$$

which we represent in Fig. 1.5(b) for various values of h/J. In the z-polarised phase, the elementary excitations are local spin flips [Sachdev, 2011]. In contrast, the x-polarized phase is characterized by topologically non-local domain walls (reminiscent of the ones described in the antiferromagnetic Heisenberg model). Interestingly, the excitation spectrum in the x-polarized phase can be obtained from that of the z-polarised phase using the self-dual symmetry of the model.

Duality mapping – The TFI chain admits non-local excitations for $h < J$, which can be understood using a self-duality mapping between its two phases (for a review, see [Kogut, 1979], IV.B.). Our aim is to rewrite the Hamiltonian (1.14). We introduce new variables associated

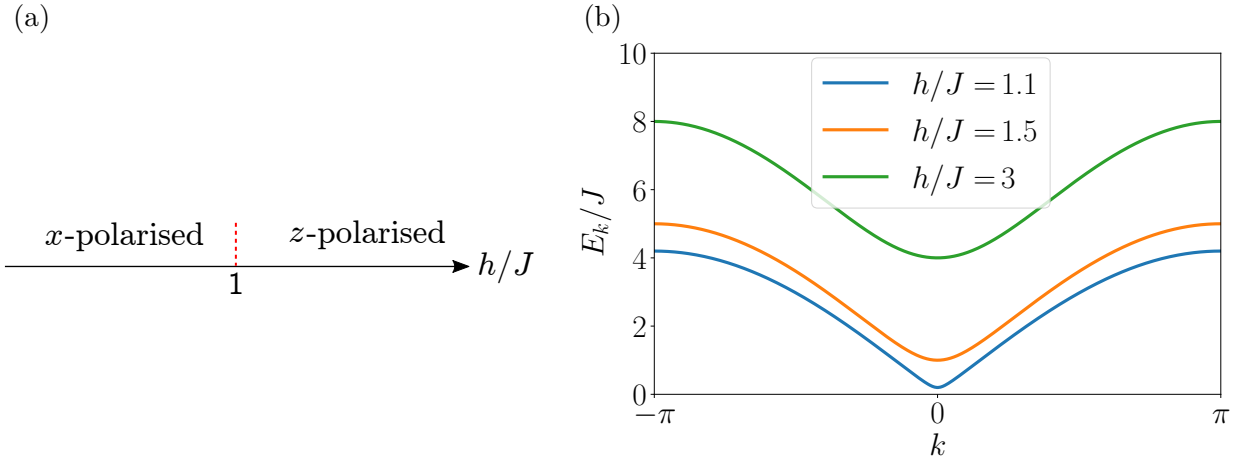

Fig. 1.5 (a) Phase diagram of the transverse-field (along z) Ising chain at zero temperature separating a z-polarised phase for $h/J > 1$ from a $\pm x$-polarised phase for $h/J < 1$. (b) Exact excitation spectrum for $h/J > 1$. The spectrum for $h/J < 1$ can be obtained from self-duality $E_k(\frac{h}{J}) = \frac{h}{J} E_k(\frac{J}{h})$.

to the bonds between spins, labelled by Greek indices $\alpha = 1, \cdots, N-1$. On each bond, a spin operator alongside x is introduced with a $+1/2$ value if the bond is ferromagnetic along z ($\uparrow\uparrow$ or $\downarrow\downarrow$) and $-1/2$ for an antiferromagnetic one ($\uparrow\downarrow$ or $\downarrow\uparrow$). An example for a given configuration with $N = 6$ is shown in Fig. 1.6(a). It corresponds to the introduction of the new set of Pauli matrices

$$\hat{\mu}^x_\alpha = \prod_{j=1}^{\alpha} \hat{\sigma}^z_j \qquad \text{and} \qquad \hat{\mu}^z_\alpha = \hat{\sigma}^x_{i+1}\hat{\sigma}^x_i, \tag{1.16}$$

which obey the $SU(2)$ algebra. We may then rewrite the initial Hamiltonian as

$$\hat{H} = -h \sum_{\alpha=1}^{N-2} \hat{\mu}^x_\alpha \hat{\mu}^x_{\alpha+1} - J \sum_{\alpha=1}^{N-1} \hat{\mu}^z_\alpha - h\,(\hat{\sigma}^z_1 + \sigma^z_N)\,. \tag{1.17}$$

The last term becomes irrelevant in the thermodynamic limit, and the energy spectrum satisfies $E_k(\frac{h}{J}) = \frac{h}{J} E_k(\frac{J}{h})$. Up to a global rescaling factor, the effect of the mapping is to swap J and h. To overcome the difficulty caused by the doubly-degenerate ground state, a gauge may be picked so that the mapping becomes uniquely defined. Here we choose the first spin to be always up.

For $h > J$, excitations are spin flips in the original lattice. From the duality mapping, for $h < J$, the excitations are also spin flips, but in the *reciprocal* lattice, which are equivalent to non-local domain walls in the original one [Fig. 1.6(b)].

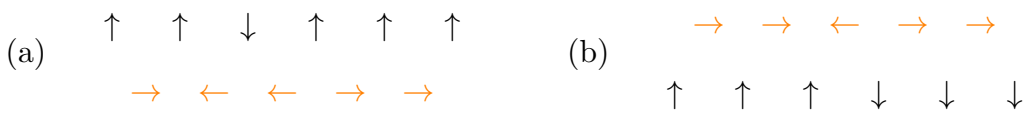

Fig. 1.6 (a) Self-duality of the TFI chain, with an original lattice configuration (black) and the reciprocal lattice configuration (orange). With given boundary conditions, the mapping is bijective if the value of the first (or last) spin is fixed in real space (gauge choice). (b) A spin flip in the reciprocal lattice is equivalent to a domain wall in the original one. From [Villa et al., 2020].

1.2 Out-of-equilibrium dynamics

We now focus on the out-of-equilibrium evolution, which can be induced by the so-called quantum quenches (Sec. 1.2.1). At long times after the quench, the system eventually relaxes towards a long-time steady state. The relaxation process is described in Sec. 1.2.2 and the difficulty of analytically evaluating the evolution at arbitrary times after the quench is highlighted. Elementary excitations, or quasiparticles, play a role in the microscopic relaxation process by transporting information and quantum correlations, as discussed in Sec. 1.2.3. We also briefly introduce Lieb-Robinson bounds, which give an upper bound to such transport processes. This discussion will be complemented by the next chapter of the thesis were we discuss our results on correlation spreading. Finally, in Sec. 1.2.4, we briefly discuss some exact numerical methods used throughout the manuscript to compute the out-of-equilibrium dynamics.

1.2.1 Quantum quenches

To move a system out-of-equilibrium one can modify one of its parameters: this is called a quantum quench. We will restrict to sudden quenches where the modification is made instantaneously. We focus on two different quench protocols, depending whether the Hamiltonian or the quantum state is modified.

A **global quench** defines a protocol where a parameter of the Hamiltonian is changed at the time $t = 0$ such that $\hat{H}_\mathrm{i} \to \hat{H}$. The quantum state immediately before the quench (the pre-quench state) is identical to the one immediately after (the post-quench state). Because the Hamiltonian is modified, this initial state $|\psi_\mathrm{i}\rangle = |\psi(t = 0^+)\rangle = |\psi(t = 0^-)\rangle$ evolves as

$$|\psi(t > 0)\rangle = \mathrm{e}^{-i\hat{H}t}\,|\psi_\mathrm{i}\rangle\,. \tag{1.18}$$

We will explain in Sec. 1.3.1 how the system parameters can be controlled in time experimentally in order to perform global quenches. We will take the initial state to be the ground state of the pre-quench Hamiltonian, namely $|\psi_\mathrm{i}\rangle = |\psi_0\rangle$. We stress already that the ground state of the pre-quench Hamiltonian $|\psi_0\rangle$ should not be confused with the ground state of the post-quench Hamiltonian governing the time-evolution, which will be denoted by $|0\rangle$.

A **local quench** is a protocol where on the contrary the Hamiltonian is not modified (thus simply denoted by $\hat{H}$), but a local action is performed on the state at $t = 0$ (for instance adding a defect). Denoting by $\hat{L}$ the associated local operator, the initial state is given by $|\psi_\mathrm{i}\rangle = |\psi(t = 0^+)\rangle = \hat{L}\,|\psi(t = 0^-)\rangle$. If the action of the operator $\hat{L}$ on $|\psi(t = 0^-)\rangle$ does not create an exact eigenstate of the Hamiltonian $\hat{H}$, the initial state also evolves according to Eq. (1.18). The difference with the previous case is that the Hamiltonian is unchanged but the initial state is not prepared in the same manner. In the following, we consider the case $|\psi(t = 0^-)\rangle = |0\rangle$ (the ground state of the Hamiltonian). Again, the initial state denotes the post-quench state which is the one relevant for the time-evolution. Both quench protocols are sketched in Fig. 1.7.

Quantum quenches are widely used due to their simplicity and common experimental implementation, which will be discussed in Sec. 1.3. They also captured a lot of theoretical interest, as many analytical results have been obtained on exactly solvable models. For instance, the Luttinger model has been investigated by [Cazalilla, 2006; Iucci and Cazalilla, 2009], and provided that a representation of the eigenstates is known exactly, the time-evolution of local observables can be computed exactly in the thermodynamic limit for arbitrary times after the quench. Other exactly solvable models are integrable (Bethe ansatz solvable) ones, on which many results following quenches have been obtained already. General analytical results have mostly been obtained using the quench action [Caux, 2016] (see Sec. 1.2.2) or hydrodynamical approaches [Bertini et al., 2016; Castro-Alvaredo et al., 2016] which apply for weakly inhomogeneous states and make use of a quasiparticle picture which we will begin to discuss in Sec. 1.2.3. Most analytical approaches require an exact representation of eigenstates, which is rather rarely the case. For this reason,

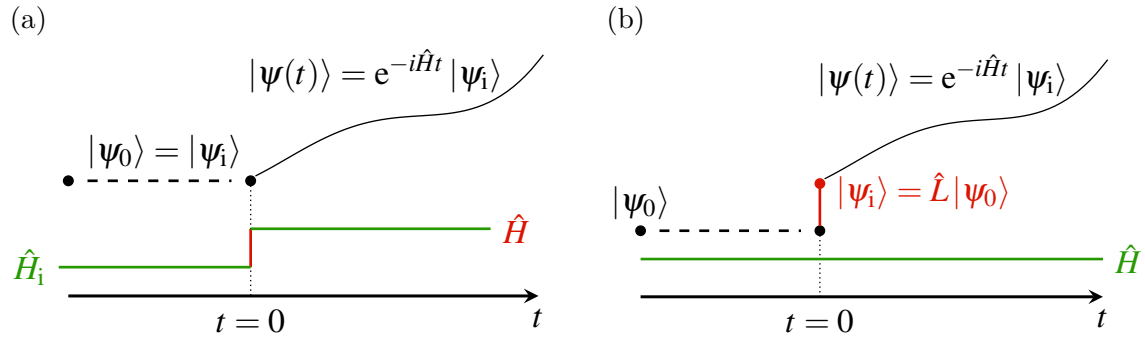

Fig. 1.7 The system is prepared in an state $|\psi_0\rangle$, usually taken as the ground state of a local Hamiltonian $\hat{H}_i$. (a) At $t = 0$, a **global quench** is performed: the Hamiltonian is instantaneously changed by modifying one of its parameters, but the quantum state for $t = 0^-$ and $t = 0^+$ are identical. (b) At $t = 0$, a **local quench** is performed: the quantum state is instantaneously changed by the action of a local operator $\hat{L}$, but the Hamiltonian stays the same. In both cases, unitary dynamics is induced for $t > 0$ (the system is isolated immediately after the quench, so its energy is conserved for $t > 0$). The initial state refers to the quantum state immediately after the quench such that $|\psi_i\rangle = |\psi(t = 0^+)\rangle$.

most quenches investigated analytically start from or end up to free systems. Some approaches combining analytics and numerics based on the Bethe ansatz have also been used [Caux, 2009].

1.2.2 Equilibration towards a long-time steady state

After a system has been perturbed from equilibrium, we expect it to eventually reach a steady-state at sufficiently long times. How can we describe such a state? Two main definitions for relaxation towards equilibrium (equilibration) are used in the literature [Essler and Fagotti, 2016; Polkovnikov et al., 2011]. The first one focuses on the local relaxation of the system subparts, and is formalised by the use of reduced density matrices. By tracing out the degrees of freedom that belong to the complementary subspace $\bar{A}$ of the subsystem A considered, local relaxation is satisfied if the following limit exists $\forall \bar{A}$

$$\lim_{t\to\infty}\lim_{L\to\infty}\hat{\rho}_A(t) = \lim_{t\to\infty}\lim_{L\to\infty}\mathrm{Tr}_{\bar{A}}\,\hat{\rho}(t) = \hat{\rho}_A(\infty). \tag{1.19}$$

Then, if the system has relaxed locally, one may ask if the full system has reached a stationary state. This is the case if a time-independent density matrix $\hat{\rho}^{\mathrm{st}}$ (which describes the full system) can be found such that

$$\lim_{L\to\infty}\mathrm{Tr}_{\bar{A}}(\hat{\rho}^{\mathrm{st}}) = \hat{\rho}_A(\infty). \tag{1.20}$$

The dynamics brings the initial state towards a state (often mixed) and remains arbitrarily close to it for almost all[10] times. In this definition of local relaxation, the thermodynamic limit has been taken first, and then the infinite time limit was considered. The second definition of relaxation focuses on the long-time average of observables for finite systems, such that the order of the limits is reversed. In this case, equilibration is defined by the fact that the expectation values of the physical observables are, again for most times during the evolution, close to their time averaged value defined by

$$\langle\hat{O}\rangle_{\mathrm{eq}} := \lim_{T\to\infty}\frac{1}{T}\int_0^T \mathrm{d}t\,\langle\hat{O}\rangle_t. \tag{1.21}$$

Namely, the system equilibrates if

$$\frac{1}{T}\int_0^T \mathrm{d}t\left[\mathrm{Tr}\big(\hat{\rho}(t)\hat{O}\big) - \langle\hat{O}\rangle_{\mathrm{eq}}\right]^2 \ll \langle\hat{O}\rangle_{\mathrm{eq}}^2, \tag{1.22}$$

[10] This ensures the compatibility with rare fluctuations and quantum recurrences or revivals [Gogolin and Eisert, 2016].

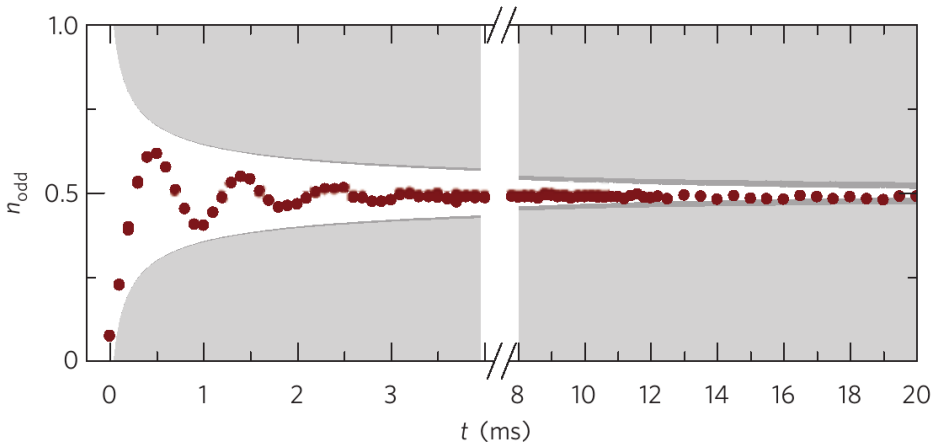

Fig. 1.8 In the Bose-Hubbard model, the density observable on odd sites quickly relaxes towards its equilibrium value after a time of a few milliseconds (of the order of h/J) after the initial state was prepared as a density wave $|1010\cdots\rangle$. From [Trotzky et al., 2012].

which then justifies to name the long-time time-averaged limit of Eq. (1.21) the equilibrium value. For our purposes (local operators), both definitions should be equivalent. We refer to the above mentioned references for subtleties. The relaxation towards equilibrium has been observed experimentally on the Bose-Hubbard model (Fig. 1.8). To understand the physical mechanism by which the system relaxes and about how long it takes, we have to wait until Sec. 1.2.3 where we will discuss Lieb-Robinson bounds and the associated quasiparticle picture.

After equilibration, naturally follow questions about ergodicity (to what extent can we assimilate a time-average to an ensemble average?) and thermalisation (if the system has relaxed, can it be described by a Gibbs ensemble?). These topics, not essential for the rest of the thesis, are addressed in Appendix 1.B.

Describing the steady state analytically Computing the evolution of local observables in the thermodynamic limit at an arbitrary time after the system was driven out of equilibrium is a notoriously difficult problem: even when the eigenstates $\hat{H}\,|n\rangle = E_n\,|n\rangle$ are exactly known, the Hilbert space is too large to attempt a brute force calculation. Since $\{|n\rangle\}$ forms a complete basis we can decompose the initial state as

$$|\psi_0\rangle = \sum_n |n\rangle\,\langle n|\psi_0\rangle = \sum_n \mathrm{e}^{\ln\langle n|\psi_0\rangle}\,|n\rangle := \sum_n \mathrm{e}^{-S(n,\psi_0)}\,|n\rangle \tag{1.23}$$

where $S(n,\psi_0) = -\ln\langle n|\psi_0\rangle$ is a complex number. The time-evolution of the state is simply

$$|\psi(t)\rangle = \sum_\Phi \mathrm{e}^{-S(n,\psi_0)-iE_nt}\,|n\rangle\,, \tag{1.24}$$

and (so far without approximation) the time-average of observables reads as

$$\langle\hat{O}(x,t)\rangle_{\psi_0} = \sum_{n,n'} \mathrm{e}^{-[S^\star(n,\psi_0)+S(n',\psi_0)]}\,\mathrm{e}^{i(E_n-E_{n'})t}\,\langle n|\,\hat{O}(x)\,|n'\rangle\,. \tag{1.25}$$

This form is exact but the bottleneck here is the computational cost required by the double sum. However, most of the terms are vanishingly small, so one can hope to approximate Eq. (1.25) by a simpler formula. This approach was taken by [Caux and Essler, 2013] and named the "quench action". It applies when an exact representation of the eigenstates in terms of a continuum distribution can be used, typically for Bethe ansatz solvable models. The quench action defines a measure on the Hilbert space which quantifies the contribution of each eigenstate to the time evolution. Under a few assumptions discussed in Appendix 1.C, the double sum over all eigenstates of

the quench Hamiltonian [Eq. (1.25)] is reduced to a single one using a saddle point approximation. In the infinite time limit describing the stationary state, only a single representative eigenstate is needed to compute the stationary value: the saddle point of the quench action.

1.2.3 Correlation and information spreading

Lieb-Robinson bounds. Immediately after the quench, out-of-equilibrium dynamics is induced. If the system eventually reaches a steady-state, as we have discussed, it is because interactions between its subparts redistribute extensive variables (energy, particle number, etc.). Thanks to the propagation of information carried by elementary excitations, the subparts of the system eventually reach equilibrium. In this part I mostly follow the discussion and adopt notations of the review by [Essler and Fagotti, 2016].

In 1972, Lieb and Robinson showed that the speed at which information can propagate through local[11] correlators in short-range Hamiltonian models is bounded in one dimension, such that the operator norm of the commutator of two operators at different times is given by [Lieb and Robinson, 1972]

$$\left\|\left[\hat{O}_A(t),\hat{O}_B(0)\right]\right\| \leq c\min\left(|A|,|B|\right)\left\|\hat{O}_A\right\|\left\|\hat{O}_B\right\|\mathrm{e}^{-(L-v|t|)/\xi}. \tag{1.26}$$

The operators $\hat{O}_A$ and $\hat{O}_B$ are supported on two regions of size $|A|$ and $|B|$ respectively, distant of L, and c, v, ξ are just constants. Equation (1.26) tells us how an observable acting on a finite region can affect another region distant of L after a time t. It shows that information propagation is exponentially suppressed outside a causal-cone. The Hamiltonian being local (finite-ranged), a modification of a finite region of the lattice takes a finite time to affect a distant one. The time it takes, called the activation time $t^\star$, is proportional to the distance R between the two regions. The proportionality constant, homogeneous to a velocity, is called the Lieb-Robinson velocity v. By representing the value of the correlator on a space-time phase diagram, one obtains a causal-cone[12], representing a ballistic propagation of information through the lattice. From Eq. (1.26), the information leaking out of the cone is negligible if $L \gg v|t|$, or equivalently if $|t| \ll t^\star$. Note that it is usually very difficult to express the value of v from first principles on a given model. More importantly, as it is only a bound, the velocity v does not tell us the effective speed at which information propagates.

Later on, Lieb-Robinson bounds have been used to demonstrate that the build-up of correlations and entanglement also obey similar bounds [Bravyi et al., 2006]. This extension showed that in non-relativistic quantum mechanics if the evolution is governed by a local Hamiltonian, information, correlations and entanglement are effectively limited concerning their spreading to an effective causal-cone. Assuming a state with a finite correlation length χ in which all connected correlation functions[13] decay exponentially $\left|\langle\hat{O}_A\hat{O}_B\rangle_\mathrm{c}\right| \leq \tilde{c}\,\mathrm{e}^{-L/\chi}$ with normalised operators $\left\|\hat{O}_A\right\|, \left\|\hat{O}_B\right\| \leq 1$, [Bravyi et al., 2006] showed that a generic equal-time connected two-point correlator was bounded by

$$\left|\langle\hat{O}_A(t)\hat{O}_B(t)\rangle_\mathrm{c}\right| < c'\left(|A|+|B|\right)\mathrm{e}^{-(L-2v|t|)/(\chi+2\xi)}. \tag{1.27}$$

We stress again that these bounds do not tell us at which velocity physical information or correlations really propagate, as the bounds are generally not saturated.

Interpretation using the Calabrese-Cardy picture. The latter issues about the exact speed of propagation as well as the underlying physical mechanism by which information or correlations are built and then propagate through the lattice were solved by [Calabrese and Cardy, 2006]. They

[11] An operator is called local if its support remains constant and finite independently of the system size.
[12] Sometimes referred to as "light-cone", by analogy with special relativity.
[13] Defined by $\langle\hat{O}_A\hat{O}_B\rangle_\mathrm{c} = \langle\hat{O}_A\hat{O}_B\rangle - \langle\hat{O}_A\rangle\langle\hat{O}_B\rangle$.

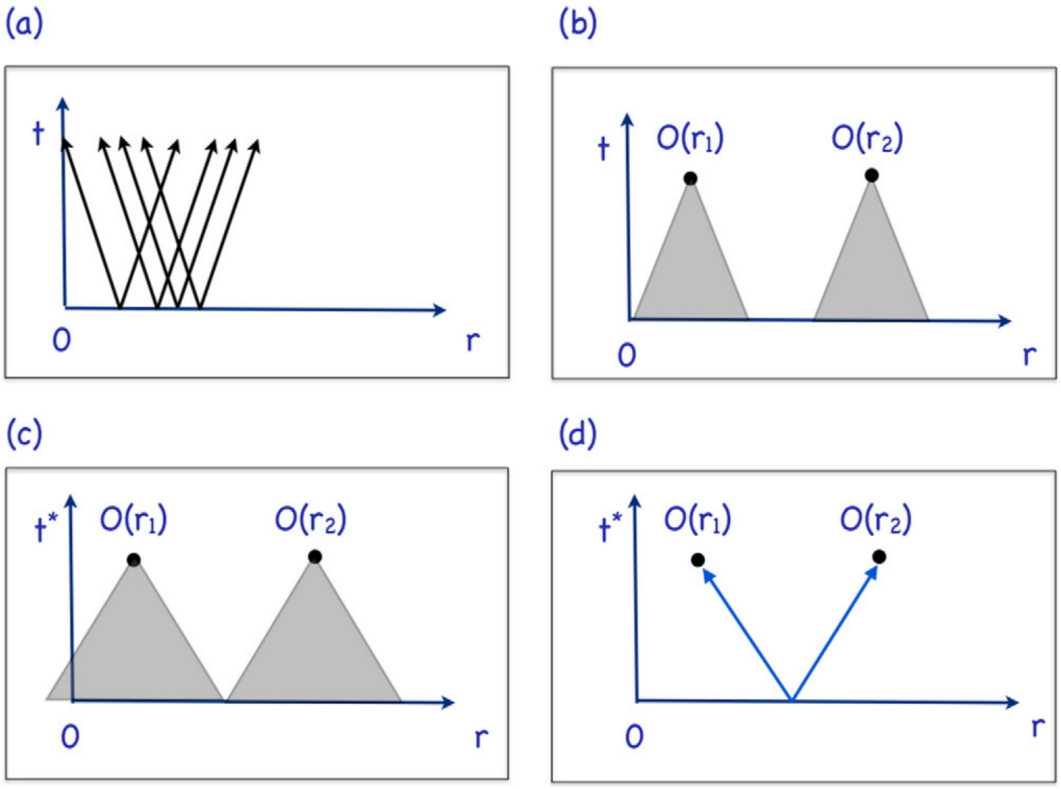

Fig. 1.9 (a) At $t = 0$, the system acts as a source of quasiparticles which start to propagate at a given velocity v (linear excitation spectrum) in both directions. (b) Information only propagates within each causal-cone and is negligible outside, for $|t| \ll t^\star$. (c) The causal-cone between the two regions touch, and the measurements between both regions become correlated at $v = L/2t^\star$. This can be reinterpreted as a correlation emerging from a quasiparticle pair emitted back to back and traveling at the group velocity v, as schematised in (d). From [Essler and Fagotti, 2016].

provided a physical interpretation for the emergence of this causal-cone using a quasiparticle picture (and incidentally also explained the factor of two between information and correlation bounds) that can be summarised by the following. Immediately after the quench, the initial state possesses extra energy compared to the ground state of the initial Hamiltonian, and is therefore highly excited. It acts as a source of quasiparticle excitations, which are emitted from $t = 0^+$ and then propagate throughout the system. While being initially quantum entangled, the quasiparticles then propagate semi-classically. Assuming that all excitations propagate with the same velocity v (which means that the excitation spectrum is linear $E_k = vk$), the connected correlation function after a given time t of two regions distant of R is significantly modified only after the two entangled quasiparticles emitted at $t = 0$ from the same region have travelled in opposite directions the distance $R/2$ in time $R/2v$. On the contrary, if we were comparing the values of the operators at $t = 0^+$ and t, the information would be built from a single quasiparticle having travelled the distance R in time R/v. Incoherent quasiparticles (in the sense that they were emitted from different points originally) will indeed cause relaxation of local observables (except if they are conserved quantities) through their interference (dephasing). This picture is summarised in Fig. 1.9. Note that the quasiparticle picture can be adapted to a non-linear excitation spectrum, in which case v should be replaced by the fastest group velocity of the signal, $V_g^\star = \max_k \partial_k E_k$. Despite being justified by conformal field theory arguments, the quasiparticle picture was argued to be generally valid in higher dimensions. We will discuss throughout the thesis how to extract physical information from inside the causal-cone of the Calabrese-Cardy picture, the latter of which will be extended in Sec. 2.1.2.

1.2.4 Numerical simulations

The Hilbert space is notoriously large, and its size is truly beyond imagination. Say we wish to represent the state of the arguably simplest interacting quantum system, a chain of N-spins 1/2 without internal degrees of freedom. Storing this quantum state on a classical computer requires 2^N numbers encoded on 8 bits and represents for $N = 40$ already more than 1 Tb of data. Multiply the number of spins by two and you need more than 10^{12} Tb [Georgescu et al., 2014]. And the previous statement did not even mention the dynamics, which in its simplest form requires the exponentiation (and diagonalisation) of a $2^{80} \times 2^{80}$ square matrix.

The simplest workaround this problem is simply to avoid facing it, by restricting to small sizes such that exact diagonalisation (ED) of the Hamiltonian can be performed. This technique suffers the drawback of being limited to small system sizes, but has the advantage of being exact, straightforward to implement for the dynamics, and valid for arbitrary models. Smart ED implementations, for instance by exploiting the symmetries of the Hamiltonian, by computing it in a specific basis as a sparce matrix (Lanczos algorithm) and then (tri)diagonalise it using efficient routines to reduce data and memory overload, enable to reach system sizes for spin chains with a magnetic field of about 40 sites [Lüscher and Läuchli, 2009]. For a bosonic model like the Bose-Hubbard chain, the Hilbert space dimension is $\dim(\mathcal{H}) = \binom{N+L-1}{N}$ where N is the total number of bosons and L the system size, which quickly restricts the size and atom number available. The 1 Tb value required to store the quantum state is already reached for $N = L = 21$.

After the quantum state has been obtained at a given time, generating the time evolution using ED can be performed efficiently by noticing that the unitary evolution during a small time step $\mathrm{d}t$ can be expanded as a power series

$$|\psi(t + \mathrm{d}t)\rangle = \mathrm{e}^{-i\hat{H}\mathrm{d}t} |\psi(t)\rangle = \sum_{n=0}^{\infty} \frac{(-i\mathrm{d}t)^n}{n!} \hat{H}^n |\psi(t)\rangle \,. \tag{1.28}$$

For a given precision, the upper bound in the sum can be replaced by a finite value N_{steps}, such that the time evolved state is obtained by applying successively the Hamiltonian to the initial quantum state. In practice, the convergence is generally not too bad, and the dynamics is usually not the limiting factor (the diagonalisation is).

In one dimension, reaching larger system size has been possible thanks to the density matrix renormalisation group (DMRG) approach, initially developed by [White, 1992, 1993] (see [Schollwöck, 2005] for a review), and nowadays understood in the framework of matrix product states and tensor networks (see [Schollwöck, 2011] for a review). In the following I mostly follow the pedagogical introduction presented by [Orús, 2014].

Not all the states in the Hilbert space are equally relevant, and their relevance can be quantified by their entanglement, or more precisely how their entanglement entropy scales with the system volume. For gapped Hamiltonians with local interactions, it was proven that the low-energy states have an entanglement entropy which scales like the area of the cut, and not like its volume. In one dimension, this means that the entanglement entropy of such states obeying the area law is constant with respect to the system size. Since these states constitute a tiny fraction of the Hilbert space, but such fraction contains the portion of states relevant for the dynamics (in the sense that it constitutes the only portion of states explored by the system in a reasonable evolution time), it becomes important to find a way to target them directly. This is what tensor networks do, in striking contrast with the wave function language. Given a many-body wave function with all its coefficients in a given basis, one cannot have any intuition about the entanglement between its subpartitions. On the contrary, tensor networks represent quantum states (and operators) from elementary blocks, which are then glued together (contracted) in a way that represents the structure of the entanglement. Matrix product states (MPS) are a particular tensor network representation of states as a one dimensional array. The contraction indices between the blocks, called bond indices, can take different values and the total number of such values is referred to

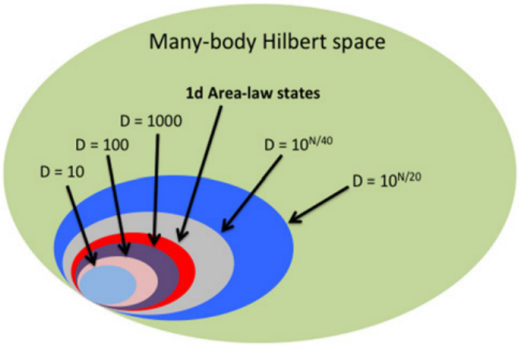

Fig. 1.10 From [Orús, 2014]. Structure of the many-body Hilbert space. The portion of relevant states obeying the area law is represented in red and represent a tiny fraction of it. When the bond dimension (noted D instead of χ) grows, the explored portion of the area-law states increases.

as the bond dimension noted χ. The higher the bond dimension, the higher the entanglement allowed[14], but the longer the computational time for a given accuracy. Expectation values of MPS can also be computed exactly in a polynomial time $O(Np\chi^3)$ where N is the particle number and p the number of accessible states (degrees of freedom). Importantly, MPS are dense in the Hilbert space, which means that, given a sufficient bond dimension, MPS can represent any quantum state. Note that this is no longer true in higher dimensions [Ge and Eisert, 2016].

Despite their immense advantages, MPS do have one strong limitation. They can only simulate efficiently gapped systems far from criticality in the sense that the correlation functions of an MPS always decay exponentially. Gapless phases can be simulated, but the above mentioned theorems (in particular exactness of the result and its polynomial bound in time) no longer hold, and the accuracy of the result needs to be checked individually. For instance, the entanglement entropy of gapless phases often diverges logarithmically with the size of the region (breaking the area law, but not too strongly such that a simulation is still possible).

In all our numerical simulation for quench dynamics, DMRG is used as a first step to obtain the ground state of a Hamiltonian which we use to initialise our models in their pre-quench equilibrium ground state. A time-dependent variational principle (TDVP) algorithm is then used in a second step, in which we compute the time-evolution following the quench. TDVP is a dynamical variational procedure strongly related to the DMRG algorithm [Haegeman et al., 2011; Haegeman et al., 2016], which can efficiently simulate the non-equilibrium dynamics of the systems we consider. I have been very fortunate to collaborate with J. Despres on the global quench spectroscopy project [Villa et al., 2019] and then with S.J. Thomson on the extension to local quenches and disordered systems [Villa et al., 2020; Villa et al., 2021a, 2021b], and I acknowledge them for the numerical simulations performed using DMRG and TDVP presented in this work. We acknowledge the package TenPy [Hauschild and Pollmann, 2018] used in part of our TDVP simulations and the package QuSpin [Weinberg and Bukov, 2017, 2019] used in preliminary ED simulations.

[14] In 1D, the entanglement entropy scales as $S(L) = -\operatorname{Tr}(\rho \log \rho) = O(\log \chi)$.

1.3 Ultracold atom quantum simulators

Quantum simulators may be defined as "experimental systems that mimic simple models of some relevance for applications and/or fundamental understanding, which are computationally very hard for classical computers to be simulated under reasonable time and memory restrictions, and allow for a broad control of the parameters and preparation, manipulation and detection of states of the system" (summarised from [Lewenstein et al., 2012]). They offer various platforms where theoretical ideas can be tested which as a result motivates additional theoretical studies to investigate the system specificities or exploit them in an original manner (for instance through a quench spectroscopy as we will discuss in Chap. 3 and 4). In this Sec. 1.3, we discuss the experimental implementation and measurement of the previously discussed models. This quantum simulation is paramount to understanding their properties, especially out-of-equilibrium where exact results are scarce. The basic engineering tools to create and control the system are discussed in Sec. 1.3.1. The measurement procedures and different probes are discussed separately in Sec. 1.3.2. The discussion below has been mainly inspired by [Bloch and Greiner, 2005; Lewenstein et al., 2012; Schäfer et al., 2020] and the series of lectures by [Dalibard, 2012, 2015] (in French).

1.3.1 Creating the system

We begin our discussion by the control over the system in terms of trapping and cooling allowed by the use of lasers (Sec. 1.3.1.1), and then explain how the interactions can be tuned in particular using Feshbach resonances or optical lattices (Sec. 1.3.1.2). We finally show the versatility of the experimental platforms used in quantum simulation (Sec. 1.3.1.3).

1.3.1.1 Trapping and cooling using light

When light interacts with matter, it gives rises to two forces. The first one is conservative (the dipole force), and can trap the atoms. The sign of its associated potential can be controlled by the detuning of the laser with respect to the atomic transition to create attractive or repulsive forces. Microscopically, the ground state experiences a shift of its energy (ac-Stark effect), proportional to the intensity of the electromagnetic field. When the electric field varies in space, so does the energy shift, creating a position dependent potential for the atoms used to trap them in so called optical lattices.

To understand in a simple manner how the trapping works, we neglect the Gaussian profile of the beam and assimilate it to a classical monochromatic plane wave. The electric field resulting from the sum of the two counterpropagating incident beams $E_0 \cos(kx \pm \omega t)$ is thus a standing wave $E(x) = 2E_0 \cos(kx)\cos(\omega t)$. If the amplitude of the field is weak, the induced dipolar moment can be written as $\boldsymbol{d}(\omega) = \alpha(\omega)\boldsymbol{E}(\omega)$ where $\alpha(\omega)$ is the polarisability of the gas. By averaging over an integer number of periods in time, one can rewrite the interaction potential felt by the particles as

$$V(x) = -\frac{1}{2}\langle \boldsymbol{d}(\omega)\boldsymbol{E}(\omega)\rangle = -V_{\text{lat}}\cos^2(kx) \qquad \text{with} \quad V_{\text{lat}} = \text{Re}\left[\alpha(\omega)\right] E_0^2 \tag{1.29}$$

where V_{lat} represents the depth of the optical lattice, controlled by the laser intensity $I = 2\epsilon_0 c E_0^2$. By generalising to an arbitrary optical potential $V(\boldsymbol{r})$, and introducing the spontaneous emission rate of the excited level Γ, the potential created by the lattice can be rewritten as

$$V(\boldsymbol{r}) = \frac{3\pi c^2 \Gamma}{2\omega_0^3 \Delta} I(\boldsymbol{r}), \tag{1.30}$$

where $\Delta = \omega - \omega_0$ is the detuning between the laser and the (dipolar) atomic two-level transition. Its associated conservative force is simply $\boldsymbol{F}_{\text{dip}}(\boldsymbol{r}) = -\boldsymbol{\nabla} V$. A red detuned laser ($\Delta < 0$) attracts the atoms towards the high intensity region where the potential is minimum. Conversely, a blue

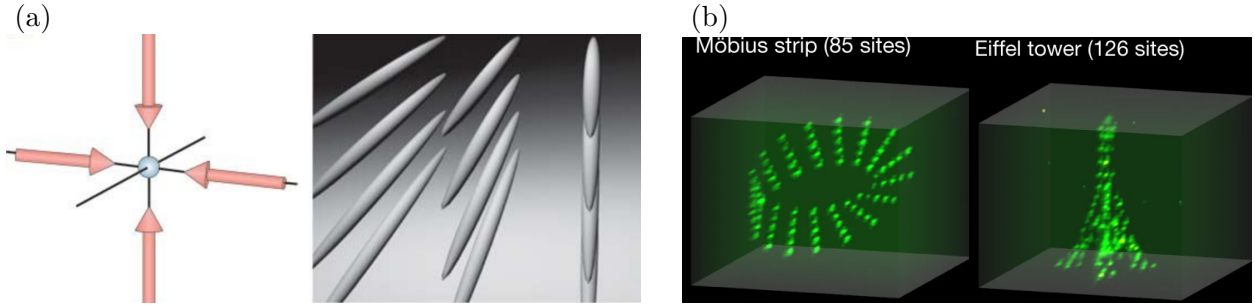

Fig. 1.11 Trapping of atoms using light. (a) 1D tubes are created in the orthogonal direction to the counterpropagating pairs of lasers, which form a 2D optical lattice. From [Bloch, 2005]. (b) Almost arbitrary potentials can nowadays be engineered. From [Barredo et al., 2018].

detuned one ($\Delta > 0$) repels the atoms from such regions since in this case the potential minima are in the low intensity regions. In practice, to reach deep lattices required for the strongly interacting regime, it is better to increase the laser power rather than reduce the detuning, since heating caused by inelastic scattering scales as $I(r)/\Delta^2$. Overlapping two pairs of lasers with the same intensity and orthogonal polarisations yields an optical potential of the form

$$V(x, y) = -V_{\text{lat}} \left(\cos^2(kx) + \cos^2(ky) \right). \tag{1.31}$$

This form of potential can be used to generate one dimensional tubes along the z direction [Fig. 1.11(a)]. State dependent optical potentials can be engineered (they depend on the hyperfine level F, its magnetic state m_F and the polarisation of the light from the laser), as well as arbitrary forms due to the unprecedented controlability achievable in current experiments [Fig. 1.11(b)]. We also note that disordered potentials can be created by adding to the periodic lattice an optical speckle pattern, and quasiperiodic potentials can be created from a bichromatic potential by superimposing two optical lattices with incommensurate wavelengths [Sanchez-Palencia and Lewenstein, 2010]. This can be used to investigate disordered systems (Chap. 4).

Taking into account the finite width of the Gaussian beam shows that (by a first order Taylor expansion around the center of the beam) harmonic potentials are globally imposed on the system, and ensure the stability of the tubes. This harmonic potential is defined by its oscillation frequencies in the transverse $\omega_\perp$ and the longitudinal direction of the tubes ω_z. Typically, $\omega_z \in [10; 100]$ Hz whereas $\omega_\perp \in [10; 100]$ kHz. This additional trapping effect helps to isolate the system but leads to an inhomogeneous density distribution both within each tube, and between the tubes during the loading procedure. This inhomogeneity can be accounted for by a local density approximation which considers a space dependent chemical potential.

The second force arising from the interaction of light on matter is dissipative, and can be used to cool the atoms using the Doppler effect. Reaching cold enough temperatures (in the sense that the thermal de Broglie wavelength becomes of the order of the interparticle distance) is necessary to observe quantum properties. We note that in general, Doppler or subrecoil laser cooling are not sufficient to enter the quantum regime. They constitute pre-cooling steps and need to be supplemented by other methods such as evaporative cooling. To this end, alkali atoms such as ^{7}Li, ^{23}Na, ^{39}K or ^{87}Rb are commonly used in experiments for various reasons. Their closed optical transitions are in a convenient frequency range to enable both simple laser cooling and trapping [Grimm et al., 1999]. More importantly, elastic collisions dominate the inelastic two and three-body collisions, making evaporative cooling efficient [Ketterle et al., 1999]. When sufficiently low temperatures are reached[15], the only relevant scattering process becomes the uniform s-wave scattering and the interatomic potential can be replaced by an effective contact interaction

$$V(x_i, x_j) = \frac{4\pi\hbar^2 a_{\text{s}}}{m} \delta(x_i - x_j), \tag{1.32}$$

[15] We give orders of magnitude at the end of Sec. 1.3.1.2.

which only depends on the 3D s-wave scattering length a_s. Neglecting the external potential confining the atoms, this can simulate the Lieb-Liniger model, where the strength of interaction is often rewritten as $g \simeq -2\hbar^2/(ma_{1D})$ with a_{1D} the 1D s-wave scattering length. This model has been extensively studied in the last two decades in the cold atom community [Boéris et al., 2016; Haller et al., 2009; Kinoshita et al., 2004; Meinert et al., 2015]. The Bose-Hubbard model can also be simulated, by adding to the previous lattices an additional one in the direction of the 1D tube [Paredes et al., 2004].

1.3.1.2 Tuning the interactions

Interactions can be tuned in many different ways. We focus on three methods in the following and we discuss their respective advantages and drawbacks. On the Lieb-Liniger model for instance, the interaction parameter is $\gamma = g/n$ (Sec. 1.1.1). A first idea is to use ultra-diluted systems in order to lower n. This approach was demonstrated by [Kinoshita et al., 2004], who reached $\gamma \sim 5$ on the Lieb-Liniger model and observed the fermionisation of the bosonic gas. Another idea is to change directly g, which in the case $|a_s| \ll l_\perp = \sqrt{\hbar/(m\omega_\perp)}$[16] may be expressed as [Bergeman et al., 2003; Olshanii, 1998]

$$g \simeq 2\hbar\omega_\perp a_s. \tag{1.33}$$

We avoid modifying $\omega_\perp$, which would change the system geometry and in particular the arrangement of the tubes. The interactions are thus modified by changing the scattering length a_s using an external magnetic field, making use of Feshbach resonances [Chin et al., 2010]. Generally speaking, a Feshbach resonance reflects the modification of the scattering cross section of an incident particle on a target if it has the energy to create a quasi-bound state. In the field of ultracold atoms where collisions happen at almost zero energy, alkalis possess a fine and hyperfine structure sensitive to the Zeeman coupling (the energy levels are magnetic-field dependent). Therefore it becomes possible by tuning the magnetic field to couple two internal states with almost the same energy such that the energy of one level (open channel) coincides with the bound state energy of the other (closed channel), and when the two levels cross, a resonance appears [Fig. 1.12(a)]. In short, Feshbach resonances modify the interactions between the atoms of the gas by tuning the scattering length a_s.

Most of the time, the values for the resonance B_0 determine whether or not it is possible to use experimentally a Feshbach resonance to change the interactions. This technique is of little practical use in situations where the value of B_0 is too high or if the resonance width Δ is too narrow (which is not the case for alkali atoms). In practice though, Feshbach resonances suffer from an important disadvantage, at least for bosons. When the scattering length diverges close to the Feshbach resonance, the condensate lifetime also sharply decreases because of larger two and three body losses, which rapidly leads to the loss of all atoms [Bloch et al., 2008]. In contrast, for fermionic atoms, close to a Feshbach resonance the condensate lifetime increases. They have been used to investigate the BEC-BCS crossover of fermionic ^{6}Li atoms [Bartenstein et al., 2004].

Finally, the third technique to vary the interactions is to confine the atoms on an optical lattice. Historically, the strongly interacting regime necessary to detect the SF-MI phase transition was entered using this method by [Greiner et al., 2002] following the proposal of [Jaksch et al., 1998]. Using an optical lattice reduces the issues of the condensate lifetime for bosons mentioned in the Feshbach resonance method. By comparing the expression of the on-site interaction U for the Bose-Hubbard model with the strength of the contact interaction g in the Lieb-Liniger situation [Eq. (1.5)], one sees that the localisation imposed by the optical lattice confinement effectively increases the interaction contribution by a factor $\int \mathrm{d}x\, |w(x)|^4$ (it also increases the effective mass $m = \hbar^2/(2Ja^2)$ which diminishes the contribution of the kinetic energy, so that the ratio U/J

[16] For rubidium, even with $\omega_\perp = 100\,\mathrm{kHz}$ one has $l_\perp \simeq 85\,\mathrm{nm}$ compared to $|a_s| \simeq 5\,\mathrm{nm}$. For the full expression, see the references mentioned.

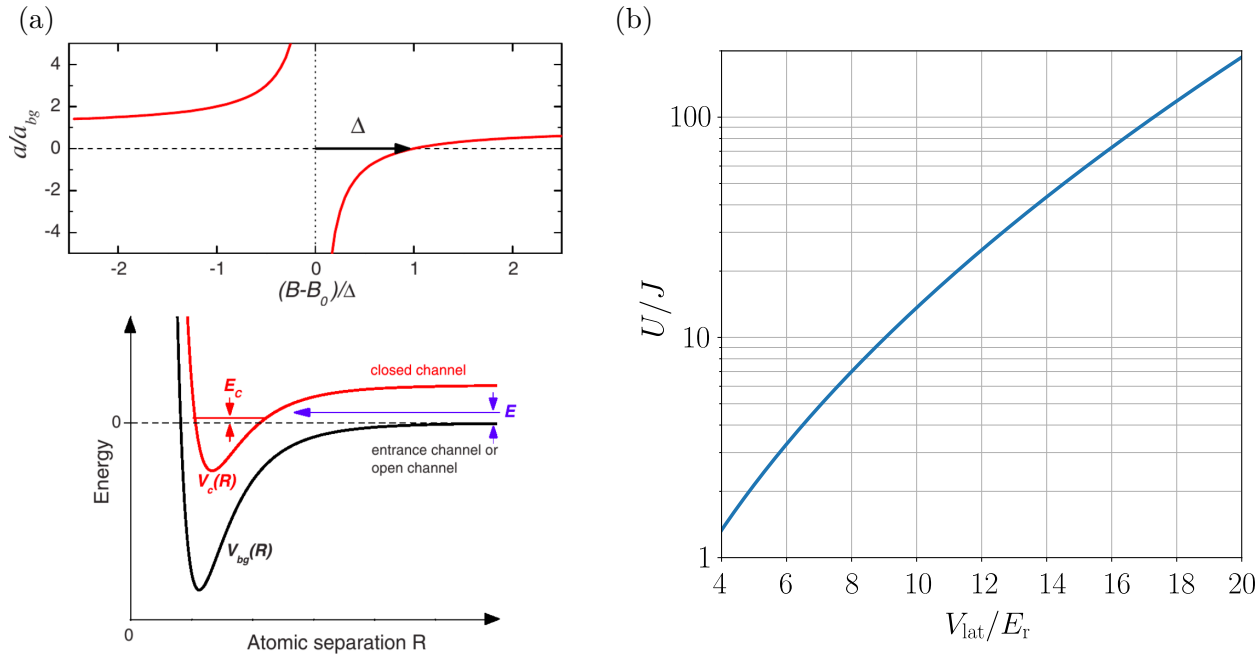

Fig. 1.12 Two methods to tune the interactions. (a) Using a Feshbach resonance to couple two states with nearly equal energy, using for instance a magnetic field (Zeeman effect). A resonance appears when the energy difference E between the open channel and the bound state of the closed channel vanishes, creating a divergence of the scattering length $a_{\rm s}$. The resonance, centred around B_0, is of the form $a_{\rm s} = a_{\rm bg}\left(1 - \frac{\Delta}{B-B_0}\right)$ with Δ the resonance width. From [Chin et al., 2010]. (b) By varying the lattice depth from the laser power. The curve represents Eq. (1.34) with $\lambda = 1\,\mu$m and the properties of ^{87}Rb given in the text.

indeed globally increases [Dalibard, 2012]).

In the deep lattice limit ($V_{\rm lat} \gg E_{\rm r}$), the tunnelling can be expressed in terms of experimental parameters by solving exactly the Mathieu equation and the on-site interaction can be estimated by approximating the Wannier functions by Gaussian functions [Zwerger, 2003]

$$\begin{cases} \dfrac{J}{E_{\rm r}} \simeq \dfrac{4}{\sqrt{\pi}} \left(\dfrac{V_{\rm lat}}{E_{\rm r}}\right)^{3/4} \mathrm{e}^{-2\sqrt{V_{\rm lat}/E_{\rm r}}} \\ \dfrac{U}{E_{\rm r}} \simeq 4\sqrt{2\pi}\, \dfrac{a_{\rm s}}{\lambda} \left(\dfrac{V_{\rm lat}}{E_{\rm r}}\right)^{3/4} \end{cases} \quad \Rightarrow \quad \frac{U}{J} = \sqrt{2\pi^2}\, \frac{a_{\rm s}}{\lambda}\, \mathrm{e}^{2\sqrt{V_{\rm lat}/E_{\rm r}}}, \tag{1.34}$$

where $E_{\rm r} = \hbar^2 k^2/2m = h^2/2m\lambda^2$ is the recoil energy with λ the wavelength of the laser and m the mass of the trapped atoms. The scattering length for the two states $|F=1, m_F=-1\rangle$ and $|F=2, m_F=2\rangle$ of ^{87}Rb is about 5 nm [Julienne et al., 1997]. The ratio U/J for ^{87}Rb is plotted as a function of the lattice depth in units of the recoil energy $E_{\rm r}$ in Fig. 1.12(b). The obvious advantage of this method is that interactions can be varied by tuning the laser power, which controls the lattice potential depth [see Eq. (1.29)].

Orders of magnitude. Using all the above expressions (for rubidium), we get $E_{\rm r}/k_{\rm B} \simeq 100\,$nK, and assuming typically $V_{\rm lat}/E_{\rm r} \sim 10$ such that $U/J \sim 10$, we have $J/E_{\rm r} \sim 2\times10^{-2}$ and $U/E_{\rm r} \sim 2\times10^{-1}$. The dynamics is controlled by the tunnelling, and the typical time given by $\hbar/J$ is on the millisecond scale ($E_{\rm r} \sim 10^{-30}\,$J so $\hbar/E_{\rm r} \sim 10^{-4}\,$s). This time scale must be compared to the one during which the system can be considered isolated, about a few hundreds of milliseconds. The system thus always evolves unitarily in excellent approximation during that time scale, and particle-loss through heating processes can safely be neglected and the particle number considered almost constant [Langen et al., 2016]. Finally, the order of magnitude of the temperature required to enter the strongly interacting regime can be estimated from $k_{\rm B}T \sim J^2/U$ [Lewenstein et al.,

2012]. Assuming this regime is entered for $U/J \sim 1$, we get $T \sim \frac{J}{U}\frac{J}{E_\mathrm{r}}\frac{E_\mathrm{r}}{k_\mathrm{B}} \sim 10\,\mathrm{nK}$, which is the order of magnitude observed experimentally[17].

1.3.1.3 Versatile experimental platforms

All the models introduced in Sec. 1.1 and used throughout the manuscript can be simulated using lattice ultracold bosons. We have already discussed how to simulate the Lieb-Liniger and the Bose-Hubbard model. The simulation of spin chain models is very similar due to the mappings between bosons and spins (Holstein-Primakoff transformation). We start our discussion on this well-developed experimental platform.

A truncated lattice bosonic model where the local occupation numbers are restricted to $2S+1$ values can be mapped to a spin model with pseudo-spin S. In the low-filling and hard core regime ($J, \mu \ll U$), the occupation numbers are restricted to 0 or 1, which may be mapped to a spin value $|\downarrow\rangle$ and $|\uparrow\rangle$ for the hole and the particle respectively, such that the model becomes equivalent to the XY model with Hamiltonian

$$\hat{H}_{XY} = -J\sum_R \left(\hat{\sigma}^x_R\hat{\sigma}^x_{R+1} + \hat{\sigma}^y_R\hat{\sigma}^y_{R+1}\right) - \mu\sum_R \hat{\sigma}^z_R. \tag{1.35}$$

The latter is exactly solvable using a Jordan-Wigner transformation [Lieb et al., 1961]. Note that a similar strategy may be applied for any non-integer filling factor between $\mathrm{int}(\bar{n})$ and $\mathrm{int}(\bar{n}+1)$.

Many other spin Hamiltonians can be modelled by using a single-band Bose-Hubbard model with two bosonic species called a and b (Bose-Bose mixtures), whose Hamiltonian reads as [Altman et al., 2003; Duan et al., 2003; Garcia-Ripoll and Cirac, 2003]

$$\hat{H}_{\mathrm{BH},2} = \sum_{R,\sigma=a,b} -J_\sigma\left(\hat{a}^\dagger_{R,\sigma}\hat{a}_{R+1,\sigma} + \mathrm{H.c.}\right) + \frac{U_\sigma}{2}\hat{n}_{R,\sigma}(\hat{n}_{R,\sigma}-1) + U_{ab}\,\hat{n}_{R,a}\hat{n}_{R,b}. \tag{1.36}$$

Starting from the Mott insulator with integer filling ($\langle\hat{n}_{R,a}\rangle + \langle\hat{n}_{R,b}\rangle = 1$) in the strongly interacting limit ($J_\sigma \ll U_\sigma, U_{ab}$), this Hamiltonian maps to

$$\hat{H}_\mathrm{eff} = \sum_R -J_\perp(\hat{\sigma}^x_R\hat{\sigma}^x_{R+1} + \hat{\sigma}^y_R\hat{\sigma}^y_{R+1}) + J_z\,\hat{\sigma}^z_R\hat{\sigma}^z_{R+1} - h\,\hat{\sigma}^z_R, \tag{1.37}$$

by introducing $\hat{\sigma}^z_R = \hat{n}_{R,a} - \hat{n}_{R,b}$, $\hat{\sigma}^x_R = \hat{a}^\dagger_{R,a}\hat{a}_{R,b} + \hat{a}^\dagger_{R,b}\hat{a}_{R,a}$, $\hat{\sigma}^y_R = -i(\hat{a}^\dagger_{R,a}\hat{a}_{R,b} - \hat{a}^\dagger_{R,b}\hat{a}_{R,a})$, and the constants

$$J_\perp = \frac{J_aJ_b}{U_{ab}}, \qquad J_z = -\frac{J_a^2}{U_a} - \frac{J_b^2}{U_b} + \frac{(J_a^2+J_b^2)}{2U_{ab}}, \qquad h = \frac{J_a^2}{U_a} - \frac{J_b^2}{U_b}. \tag{1.38}$$

In the particular case where $J_a \simeq J_b \simeq J$ and $U_a \simeq U_b \simeq U_{ab} \simeq U$, one simulates the isotropic Heisenberg chain, controlled by the super-exchange coupling coefficient J^2/U, as can be explained from a simple second order perturbation theory argument. Note that everything remains identical if one uses fermionic mixtures instead of bosonic ones, except that the sign of $J_\perp$ is reversed and the expression for J_z simplifies to $(J_a^2+J_b^2)/(2U_{ab})$. It is also possible to use a single species but with two degenerate internal states (for instance two hyperfine levels). Using ^{87}Rb, most experiments now chose the two long-lived hyperfine levels $|F=1, m_F=-1\rangle$ and $|F=2, m_F=-2\rangle$ (mapped to $|0\rangle = |\downarrow\rangle$ and $|1\rangle = |\uparrow\rangle$). This scheme led to the experimental investigation of correlation functions with single-site resolution including dynamical properties and defect propagation in Heisenberg and XXZ spin chains [Fukuhara, Kantian, et al., 2013; Fukuhara, Schauß, et al., 2013; Hild et al., 2014; Weitenberg et al., 2011].

Quantum simulation is not restricted to ultracold atoms, and versatile platforms have emerged over the past decades, expanding the scope of the systems that can be studied. Among them,

[17] Strictly speaking, Eq. (1.34) only applies for $V_\mathrm{lat} \gg E_\mathrm{r}$, but we use it here since we are only looking for an order of magnitude.

trapped cold ions are particularly fruitful ([Blatt and Roos, 2012] for a review), as they are able to reach the required low temperatures and offer a high degree of control, including the single-site/atom addressability which we will discuss in Sec. 1.3.2.2.

Quantum magnet models (for instance the transverse-field Ising model) can be realised experimentally using cold ions[18] [Blatt and Roos, 2012; Buluta and Nori, 2009; Porras and Cirac, 2004]. After the ions are trapped and cooled by laser beams (magnetic trapping is also possible), the basic idea is that in each ion, two internal levels play the role of an effective spin. The spin-spin interactions are usually engineered by state-dependent optical dipole forces (polarisation of the laser field for instance), similar to the one discussed for ultracold atoms. Alcaline-earth ions ($^{9}Be^{+}$,$^{25}Mg^{+}$,$^{40}Ca^{+}$ ...) are commonly used in experiments, because the valence-electron spin state naturally serves as a spin-1/2 (or qubit). Each qubit can be read by a fluorescence measurement which couples only one of the two internal states to an external short-lived excited level. This platform is very promising for building a quantum computer since the seminal proposal of [Cirac and Zoller, 1995], due to its nearly perfect qubit readout (more than 99.99% for 10^6 trials [Myerson et al., 2008]). Common quantum magnets models have been successfully realised over the past few years [Friedenauer et al., 2008; Jurcevic et al., 2015; Lanyon et al., 2011]. Interestingly, this platform has been used by [Richerme et al., 2014] to simulate the long-range XY model, where the tunnelling term J is replaced by an algebraically decaying coupling $J/|R|^{\alpha}$, with α a constant that can be tuned experimentally. In this experiment, a lanthanide element ($^{171}Yb^{+}$) was used to encode the spin value into two hyperfine states. Nowadays, lanthanides elements are also used for their large dipole magnetic moment, which gave birth to another related platform: dipolar gases. Supersolid signatures (coexistence of both crystalline and superfluid order) have recently been reported in experiments on dipolar gases, and the phase diagram mapped out [Chomaz et al., 2019].

This emphasises how all these new platforms are contributing to our understanding of strongly interacting quantum matter. The latter observations make use of a Feshbach resonance to access the supersolid phase by changing the interactions through the scattering length, and time-of-flight measurements were used to probe the density and the phase coherence properties. We discuss some measurement techniques in the following.

1.3.2 Measuring the system properties

How can we characterise the system that has been created experimentally? Averaged correlation functions may be accessible using a widely used method, where the atoms expand freely after switching of the trap (time-of-flight). One then images the density distribution and relates it to the momentum distribution of the atoms inside the trap (Sec. 1.3.2.1). Local correlations requiring single-site addressing and single-atom resolution are also discussed (Sec. 1.3.2.2). Another method to characterise the system is through its excitations. This can be done by perturbing the system and studying its response using pump-probe spectroscopic techniques (Sec. 1.3.2.3).

1.3.2.1 Time-of-flight

One of the simplest measurements to describe is the one of the momentum distribution, as it is proportional to the density of the atomic gas after expansion. The gas is initially prepared in an equilibrium state, and at $t = 0$, the trap is suddenly switched off and the atoms start to fall due to gravity. After a large enough time of flight t, they are imaged by light absorption on a CCD camera. If the atoms can be considered as non-interacting after the release of the trap, the initial momentum of the atoms in the trap $\boldsymbol{k}$ is related to the time of flight t and the distance travelled by the atoms $\boldsymbol{r}$ according to $\boldsymbol{k} = m\boldsymbol{r}/(\hbar t)$. The momentum distribution in the initial trapped

[18] Nowadays, Rydberg atoms also provide a way to simulate spin models directly [Labuhn et al., 2016]. Although also very interesting (and promising from the point of view of quantum computation [Bernien et al., 2017]), we will not discuss this platform here and refer to the review [Browaeys and Lahaye, 2020].

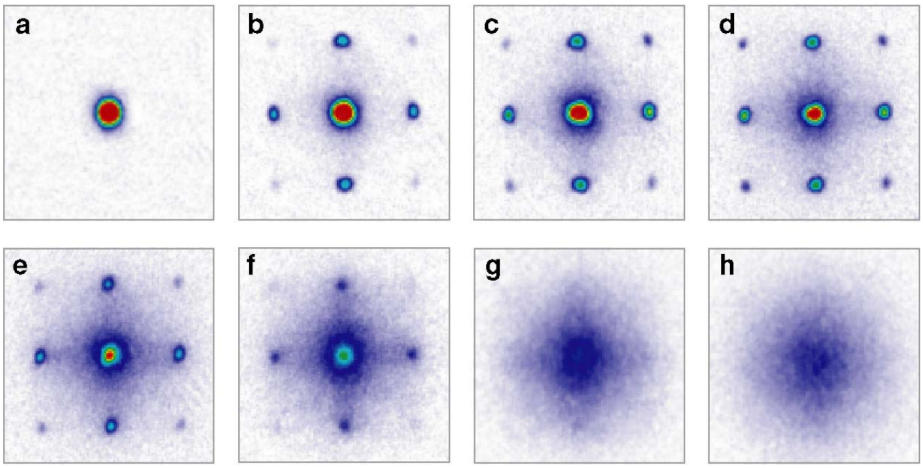

Fig. 1.13 Absorption images of interference patterns for the 3D Bose-Hubbard model, after release of the trap, for $V_{\rm lat}/E_{\rm r} = 0, 3, 7, 10, 13, 14, 16, 20$ (from a to h). Initially superfluid, the gas progressively enters the Mott insulating phase where its coherence properties completely disappear. From [Greiner et al., 2002].

state is therefore proportional to the density distribution [Altman et al., 2004]

$$\langle n(\boldsymbol{k} = \tfrac{m\boldsymbol{r}}{\hbar t})\rangle_{\rm trap} \propto \langle n(\boldsymbol{r})\rangle_{\rm tof}. \tag{1.39}$$

Even if it looks simple, there are two main difficulties with this method. The first one is that the atoms from the gas are assumed not to interact during the ballistic expansion such that an unbiased image of the pre-quench atomic distribution is observed. Thus the lattice depth has to be almost instantaneously set to zero, any parasite external field cancelled, and the free-atom collision cross section as small as possible (far from Feshbach resonances). The second one is that during the imaging process, the density measured is averaged over the height of the expanding cloud so one accesses a column-integrated momentum distribution rather than the momentum distribution itself.

As an interferometric technique, time-of-flight can be used to measure correlation functions such as $G_1(\boldsymbol{r}, \boldsymbol{r'}) = \langle \boldsymbol{r'}| \hat{\rho}_1 |\boldsymbol{r}\rangle$, called the one-body correlator, which is sensitive to the existence of (quasi)-long range order in the system. Absorption images can therefore be used to reveal phase correlations and distinguish different phases of matter, in particular the superfluid from the Mott insulator, for instance in the (3D) Bose-Hubbard model as shown in Fig. 1.13.

Two-particle correlation functions, in particular density-density correlations can also be measured from time-of-flight images [Duan, 2006]. The idea is similar, one uses noise correlations

$$\langle n(\boldsymbol{k})n(\boldsymbol{k'})\rangle_{\rm trap} \propto \langle n(\boldsymbol{r})n(\boldsymbol{r'})\rangle_{\rm tof}, \tag{1.40}$$

in order to access the (averaged) connected density-density correlation function[19]

$$G_2(\boldsymbol{r}) = \int \mathrm{d}\boldsymbol{r'}\langle \hat{n}(\boldsymbol{r}+\boldsymbol{r'})n(\boldsymbol{r'})\rangle - \int \mathrm{d}\boldsymbol{r'}\langle \hat{n}(\boldsymbol{r}+\boldsymbol{r'})\rangle\langle \hat{n}(\boldsymbol{r'})\rangle. \tag{1.41}$$

1.3.2.2 Quantum microscopes

Obtaining single-site resolution is essential to extract local correlations and in particular particle-particle correlation functions characteristic of the strongly correlated regime. On an optical lattice, the lattice spacing is set by the laser wavelength according to $a = \lambda_{\rm lat}/2$, while the minimum size

[19] Sometimes another definition is used in the literature, with $(1+)G_2(\boldsymbol{r}) = \dfrac{\int \mathrm{d}\boldsymbol{r'}\langle \hat{n}(\boldsymbol{r}+\boldsymbol{r'})\hat{n}(\boldsymbol{r'})\rangle}{\int \mathrm{d}\boldsymbol{r'}\langle \hat{n}(\boldsymbol{r}+\boldsymbol{r'})\rangle\langle \hat{n}(\boldsymbol{r'})\rangle}$.

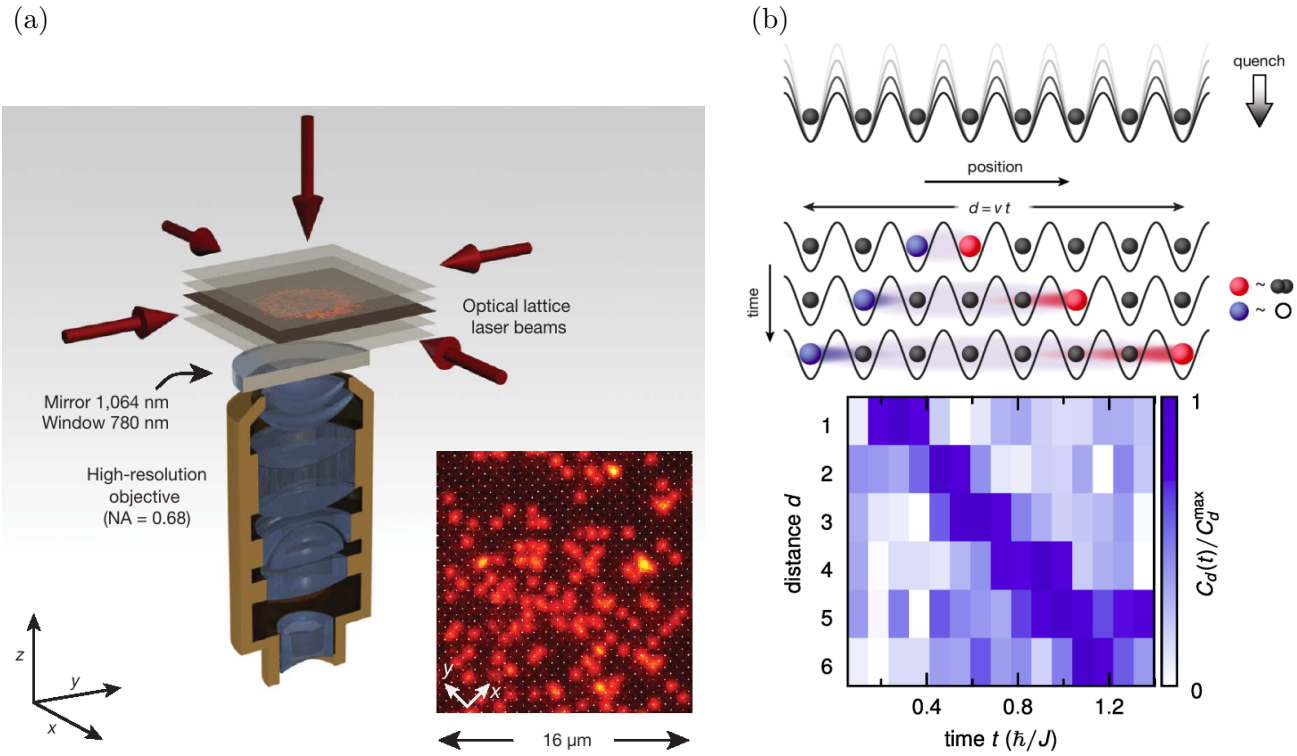

Fig. 1.14 (a) Example of a (bosonic) quantum gas microscope with single-site adressability. From [Sherson et al., 2010]. (b) After a quench lowering the lattice depth, excitations build correlations and the quantum microscope enables the observation of the causal-cone in real space. Doubly occupied and empty site are indistinguishable due to light-induced collisions. From [Cheneau et al., 2012].

that can be distinguished by an optical system is set by $\lambda/(2\,\mathrm{NA})$ where NA is the numerical aperture which defines the angular region over which the system accepts light. The first idea was to avoid counterpropagating lasers to create the lattice, and make the beams intersect with an angle θ such that the lattice period is increased to $\lambda/(2\sin(\theta/2))$ for small angles. This method was succesfully used to reach single-site resolution for a lattice spacing of about 5 µm [Nelson et al., 2007]. However to reach the strongly interacting regime tunneling and on-site interaction have to be of the same order of magnitude, and larger than the temperature of the system which requires to decrease the lattice spacing to about 500 nm. The numerical aperture must then be high, and the trapped atoms placed as close as possible to the imaging surface of the microscope. By lithographically producing the lattice using a holographic mask, [Bakr et al., 2009] realised the first high fidelity site-resolved single-atom detection using bosons. Such microscopes were then improved on bosonic systems [Endres et al., 2011; Sherson et al., 2010] and extended to spins [Weitenberg et al., 2011] (adding state selectivity[20]) and fermions [Haller et al., 2015]. The latter added "true" single-atom selectivity, since due to light-induced collisions which emit pairs of atoms, the bosonic detection is only sensitive to the parity (particle number modulo 2) [Bloch et al., 2012]. Just like the TOF, the imaging scheme of the microscope is often based on a light absorption imaging onto a CCD camera with pixel size smaller than a [Fig. 1.14(a)].

This single-site addressability led to the direct observation of correlation spreading after a global quench in the Bose-Hubbard model [Cheneau et al., 2012]. The causal-cone structure discussed in Sec. 1.2.3 was observed [Fig. 1.14(b)], and interpreted from the quasiparticle picture in the strongly interacting regime where excitations reduce to doublons and holons (Appendix 1.D).

Very recently, single-atom resolution in momentum space has been demonstrated in two groups

[20] The microscope can be made spin selective by applying a selective removal procedure of one species (for instance using Zeeman effect to separate them).

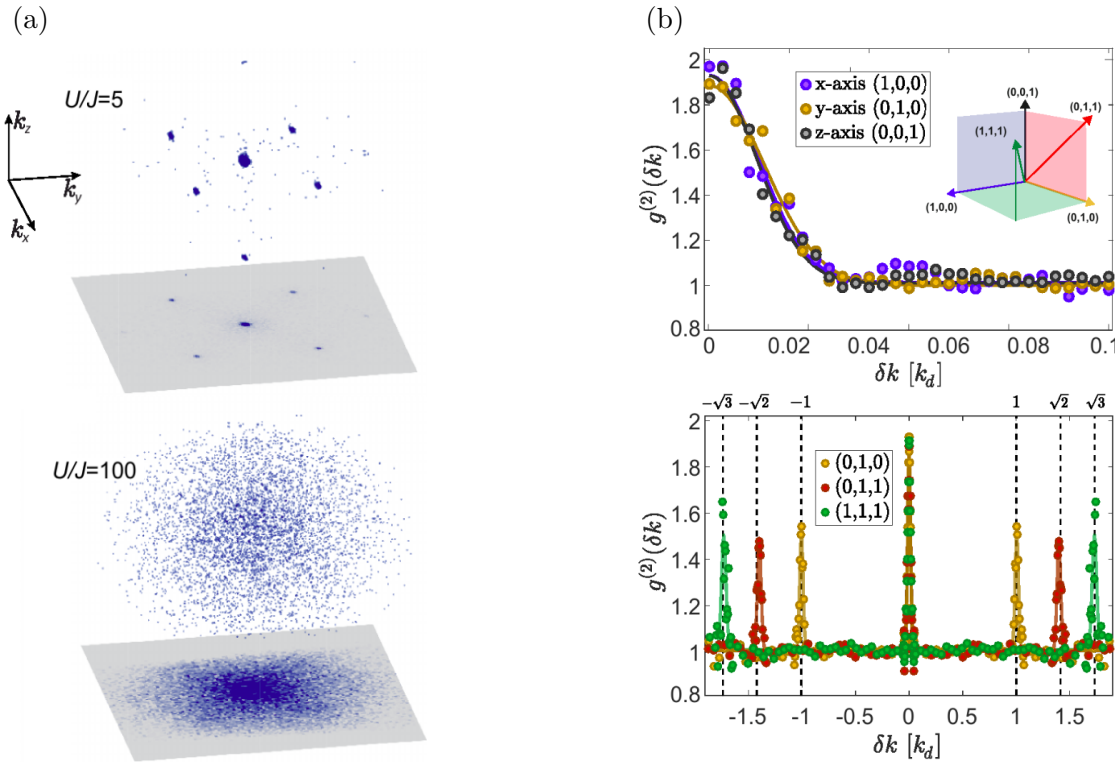

Fig. 1.15 Momentum microscope using ^{4}He* atoms. (a) Full momentum distribution reconstructed using a 3D detector. As in Fig. 1.13, the coherence of the SF phase ($U/J = 5$) is destroyed when the lattice depth is increased to reach the MI phase ($U/J = 100$). (b) The density-density correlation function can be measured with an unprecedented resolution in momentum space (top). Bunching, characteristic of bosonic atoms in the MI can be observed (bottom). Adapted from [Carcy et al., 2019].

using excited helium atoms ^{4}He* [Carcy et al., 2019; Cayla et al., 2018; Hodgman et al., 2017]. This technique opens a new path to probe correlations directly in momentum-space (one-point and two-point functions but also higher order ones) at the single-atom level with an unprecedented accuracy [Fig. 1.15].

1.3.2.3 Pump-probe spectroscopies

Spectroscopy initially began as the study of the interaction between matter and an external field excitation (usually electromagnetic). Today, it is more generally understood as a method to probe the spectrum of matter in order to understand its (band) structure and the properties of its excitations. Albeit important from a theoretical point of view, spectroscopy is also absolutely tantamount to the development and implementation of quantum technologies. Formally, one usually distinguishes two types of excitations in many-body systems. Collective excitations are responsible for the macroscopic response of the system, and are commonly probed by weakly perturbating the system around equilibrium. At low momentum transfer, the Kubo formula derived from linear response theory shows that one can probe the response of the system to the fluctuations induced by an operator (the pump). The other type of excitations are elementary or single particle-like excitations, which in contrast are generally probed at high momentum transfer through inelastic scattering of individual atoms [Lewenstein et al., 2012]. This is the essence of pump-probe spectroscopies discussed below: the spectral function (first order correlator) probes individual excitations for the addition or removal of single particles, while the dynamical structure factor (second order correlator) probes the collective excitations. We will come back to all these technical details in Sec. 3.1, while here we focus on the experimental point of view for a few

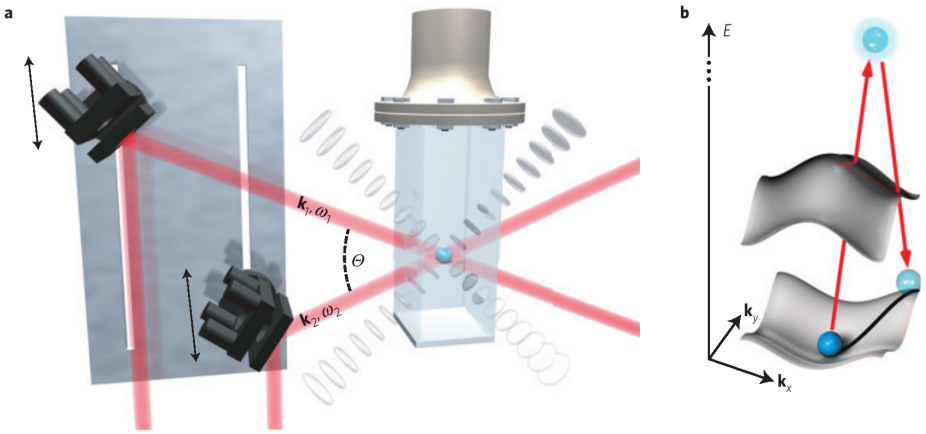

Fig. 1.16 (a) Experimental scheme of the two-photon Bragg spectroscopy. The laser beams are shifted by the angle Θ which controls the momentum transfer $\hbar(k_1 - k_2)$ and the detuning $\hbar(\omega_1 - \omega_2)$ controls the energy transferred to the atoms. The process in energy-momentum space is represented in (b). Note that the atom internal state is not changed during the process. From [Ernst et al., 2010].

spectroscopic techniques[21]. Throughout the thesis, we will expose a new spectroscopic technique, called quench spectroscopy, which differs from usual pump-probe spectroscopies. To highlight the differences, we review the pump-probe spectroscopies below.

Two-photon Bragg spectroscopy This is the most frequently used technique in ultracold atoms: two lasers illuminate an ensemble of atoms so as to induce a two-photon transition where a photon is absorbed from one beam and emitted into the other. Importantly, the frequency detuning $\omega_1 - \omega_2$ between the lasers is chosen to be off-resonant with any atomic transition so as to avoid changing the internal state of the atom[22]. This frequency shift $\omega_1 - \omega_2$, usually of a few kHz is detuned by a few GHz from the closest atomic transition, and it controls the energy absorbed by the atom. Bragg spectroscopy was initially used on Bose-Einstein condensates to measure properties of the momentum distribution [Stenger et al., 1999] and was soon extended to measure the Bogoliubov excitation spectrum and associated dynamical struture factor at fixed momentum transfer [Stamper-Kurn et al., 1999; Steinhauer et al., 2003; Steinhauer et al., 2002].

Importantly, Bragg spectroscopy can be made momentum-resolved. During the scattering processes where photons are exchanged between the two lasers, the associated momentum difference $k_1 - k_2$ is transferred to the atom. It can be tuned by the angle Θ between the laser fields of wavelength λ such that $k_1 - k_2 = 4\pi \sin(\Theta/2)/\lambda$ (Fig. 1.16). Details about the procedure to calibrate the angle Θ can be found in [Clément et al., 2009], here we simply mention that a non-trivial calibration has to be performed for each value of Θ and is thus rather time-consuming. Nonetheless, this method is required to access the excitation spectrum over the full Brillouin zone [Clément et al., 2010; Ernst et al., 2010; Fabbri et al., 2012] [Fig. 1.17(b)].

Lattice modulation spectroscopy This technique, also known as lattice shaking, can be seen as an application of two-photon Bragg spectroscopy. Rather than induced by a pair of lasers, the excitation is generated by a modulation of the amplitude of the lattice of the form (in 1D)

$$V(x,t) = A_{\mathrm{mod}} \cos(\omega_{\mathrm{mod}} t) \cos^2(kx). \tag{1.42}$$

[21] The major missing one is probably angle-resolved photoemission spectroscopy [Damascelli, 2004]. The reason we skip it is that it is limited to electronic systems and thus more useful in solid-state physics than ultracold bosons.

[22] Bragg spectroscopy is thus different from Raman spectroscopy [Dao et al., 2009], in which the *internal* state of the atom is modified by the absorption of a photon.

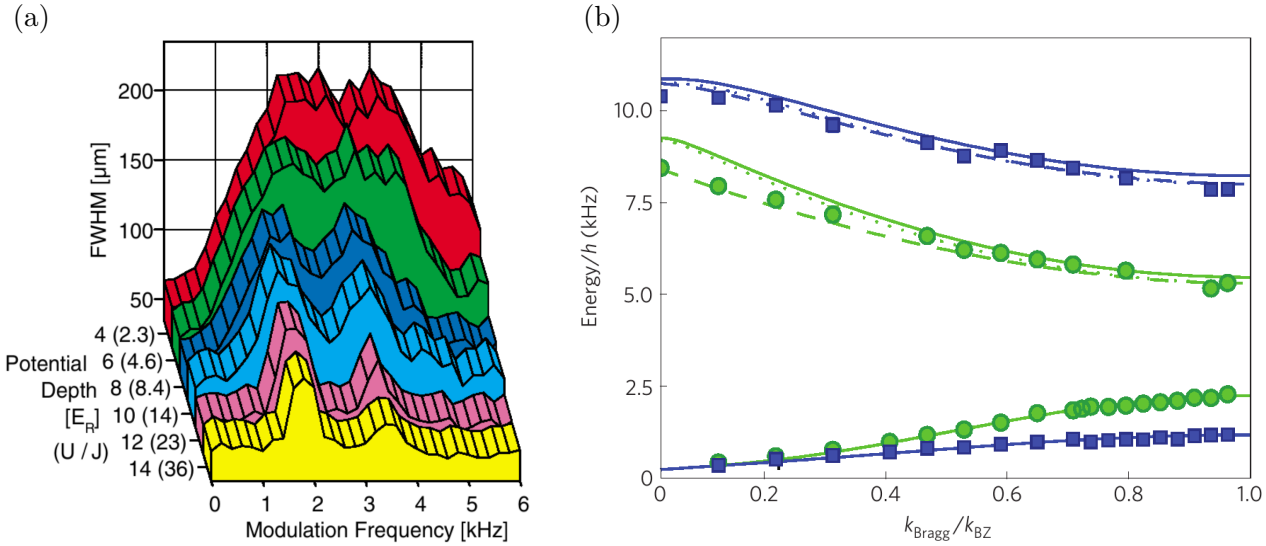

Fig. 1.17 (a) Excitation spectrum at $k = 0$ of the 1D Bose-Hubbard model measured using lattice modulation spectroscopy, from [Stöferle et al., 2004]. The SF (red, green) displays a broad spectrum while the MI displays a double-peak structure centred at U and $2U$. (b) Momentum-space resolution of the excitation spectrum of the 2D Bose-Hubbard model measured by Bragg spectroscopy along the [1,1] direction, from [Ernst et al., 2010]. The SF (gapless) and MI (gapped) bands can be accurately reconstructed by individually controlling the momentum through a mechanical modification of the mirrors positions.

This modulation introduces two sidebands, shifted by the energy $\hbar\omega_{\text{mod}}$ compared to the laser, which defines the excitation energy. Advantageously, the excitation energy is thus precisely determined and does not need to be calibrated. One disadvantage of the method is that it does not give access to momentum space resolution of the excitations (only the $k = 0$ component of the spectrum can be obtained). Lattice modulation spectroscopy can investigate the SF-MI phase transition in the Bose-Hubbard model, and was used by [Stöferle et al., 2004] to measure the excitation spectrum (for $k = 0$, distinguishing the existence or the absence of a gap) [Fig. 1.17(a)]. A

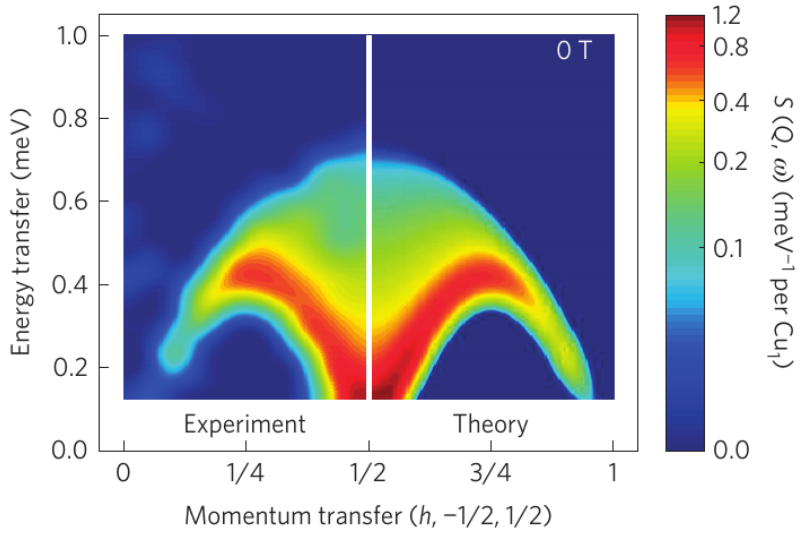

Fig. 1.18 Excitation spectrum of the cuprate Sr_2CuO_3 measured through a scattering experiment, and compared to the exact Bethe ansatz result for the AFM Heisenberg model (the signal amplitude comes from the evaluation of the dynamical structure factor). The fractional spinon excitations continuum given by Eq. (1.13) describes well the collective excitations probed experimentally. From [Mourigal et al., 2013].

brief general theoretical description of pump-probe spectroscopies is postponed to Sec. 3.1.

Neutron scattering Historically, the inelastic scattering of neutrons was used to measure the excitation spectrum of liquid helium [Pitaevskii and Stringari, 2016]. The interaction with the neutrons can be described by a potential of the form $V(r) \propto a_{\mathrm{s,n}}\hat{n}(r)$ which linearly couples to the density operator $\hat{n}$ ($a_{\mathrm{s,n}}$ is the neutron-atom s-wave scattering length). Using the Born-approximation, it is possible to show that the differential (per unit of energy or frequency ω and solid angle Ω) inelastic neutron cross section is proportional to the dynamical structure factor, which is the Fourier transform of the density-density correlation function

$$\frac{\mathrm{d}^2\sigma}{\mathrm{d}\Omega\mathrm{d}\omega} \propto S(q,\omega) = \int \mathrm{d}r\,\mathrm{d}t\,\mathrm{e}^{i(qr-\omega t)}\langle\hat{n}(r,t)\hat{n}(0,0\rangle. \tag{1.43}$$

The latter quantity is sensitive to the collective excitations of the system, such that neutron scattering experiments give access to the excitation spectrum. This can be efficiently used for instance on materials which can be modelled by unidimensional integrable spin chains where exact results are known [Lake et al., 2013; Mourigal et al., 2013] (Fig. 1.18).

In the following, we will introduce a new spectroscopic technique named quench spectroscopy, which probes spectral properties from the out-of-equilibrium dynamics induced after a quench.

Appendices

1.A Exact solution of the Lieb-Liniger model from the Bethe ansatz

In this part we study the exact analytical resolution of the integrable Lieb-Liniger model at zero temperature[23] by making use of the Bethe ansatz. We start by recalling the procedure to obtain the Bethe equations, following [Franchini, 2017; Sutherland, 1985]. We then focus on results provided by the numerical solution of the equations.

1.A.1 The coordinate Bethe ansatz

Interacting many-body systems are difficult to solve because of many-body scattering processes. Integrable systems are exactly solvable partially because all many-body collisions can be exactly decomposed as pairs of two-body collisions in a self-consistent manner. At equilibrium, all the necessary thermodynamic information is therefore contained in the two-body scattering matrix, which is the key quantity to evaluate.

1.A.1.1 Two particles

We begin with only two bosons, where the Lieb-Liniger Hamiltonian reads as

$$H_{\mathrm{LL}} = -\frac{\partial^2}{\partial x_1^2} - \frac{\partial^2}{\partial x_2^2} + c\left[\delta(x_1 - x_2) + \delta(x_2 - x_1)\right], \tag{1.44}$$

with $c = mg/\hbar^2$ and we set $\hbar = 1 = 2m$. We look for the spectrum of the Hamiltonian (eigenfunctions and eigenvalues). We shall split the wave function in two sectors, each associated to a specific ordering of the particles, $\mathcal{Q} = \{x_1 \leq x_2\}$ and $\mathcal{Q}' = \{x_2 \leq x_1\}$. The two particles interact for $x_1 = x_2$ where the two sectors intersect and are equivalent. We introduce the reduced wave function $f_{\mathcal{Q},\mathcal{Q}'}$, defined on either $\mathcal{Q}$ or $\mathcal{Q}'$, as the restriction of the global wave function ψ to a specific sector. While f is not a physical quantity (because contrary to ψ, it is not symmetric under the exchange of the two particles), it is related to the physical wave function by

$$\psi = f_{\mathcal{Q}}\,\Theta(x_2 - x_1) + f_{\mathcal{Q}'}\,\Theta(x_1 - x_2), \tag{1.45}$$

where $\Theta(x)$ is the Heaviside distribution.

The Bethe ansatz can be thought of as an educated guess for the form of the reduced wave function in each sector, consisting of a sum of plane waves with unknown amplitudes

$$\begin{aligned} f_{\mathcal{Q}} &= A_{\mathcal{Q}}(k_1, k_2)\,\mathrm{e}^{i(k_1 x_1 + k_2 x_2)} + A_{\mathcal{Q}}(k_2, k_1)\,\mathrm{e}^{i(k_2 x_1 + k_1 x_2)}, \\ f_{\mathcal{Q}'} &= A_{\mathcal{Q}'}(k_1, k_2)\,\mathrm{e}^{i(k_1 x_2 + k_2 x_1)} + A_{\mathcal{Q}'}(k_2, k_1)\,\mathrm{e}^{i(k_2 x_2 + k_1 x_1)}. \end{aligned} \tag{1.46}$$

For an integrable model, this guess turns out to provide the exact solution – in the sense that it exhausts the Hilbert space such that all physical solutions are non-diffractive (plane-waves) wave functions. The amplitudes A and the momenta k_j are unknown at this point. By injecting this ansatz into the Schrödinger equation, we will see how the interactions come into play. We choose $x_1 = x_2 := \bar{x}$ (otherwise the interaction term is always zero and we simply have a free system), and by discarding the irrelevant global phase prefactor $\mathrm{e}^{i(k_1+k_2)\bar{x}}$ we get

$$\begin{aligned} \frac{\partial^2\psi}{\partial x_1^2} + \frac{\partial^2\psi}{\partial x_2^2} = &\left(\frac{\partial^2 f_{\mathcal{Q}}}{\partial x_1^2} + \frac{\partial^2 f_{\mathcal{Q}}}{\partial x_2^2}\right)\Theta(x_2 - x_1) + \left(\frac{\partial^2 f_{\mathcal{Q}'}}{\partial x_1^2} + \frac{\partial^2 f_{\mathcal{Q}'}}{\partial x_2^2}\right)\Theta(x_1 - x_2) \\ &- 2\left(\frac{\partial f_{\mathcal{Q}}}{\partial x_1} - \frac{\partial f_{\mathcal{Q}}}{\partial x_2}\right)\delta(x_2 - x_1) + 2\left(\frac{\partial f_{\mathcal{Q}'}}{\partial x_1} - \frac{\partial f_{\mathcal{Q}'}}{\partial x_2}\right)\delta(x_1 - x_2) \\ &+ 2 f_{\mathcal{Q}}\,\delta'(x_2 - x_1) + 2 f_{\mathcal{Q}'}\,\delta'(x_1 - x_2). \end{aligned} \tag{1.47}$$

[23] The modifications introduced by finite temperature were discussed by [Yang and Yang, 1969].

When applied to the reduced wave function, we have $\delta(x_1 - x_2) = \delta(x_2 - x_1)$ and $\delta'(x_2 - x_1) = -\delta(x_1 - x_2)$, so the last term vanishes. Physically, this reflects the continuity of the wave function at the boundary $x_1 = x_2$ where the two sectors are equivalent $f_{\mathcal{Q}} = f_{\mathcal{Q}'}$. However, their derivatives differ due to the discontinuity imposed by the contact interaction. On the boundary, Eq. (1.47) can be rewritten as

$$\begin{aligned}\frac{\partial^2\psi}{\partial x_1^2} + \frac{\partial^2\psi}{\partial x_2^2} = &-\left(k_1^2 + k_2^2\right)\psi - 2i(k_1 - k_2)\,\delta(x_1 - x_2) \\ &\times \left[\left(A_{\mathcal{Q}}(k_1, k_2) - A_{\mathcal{Q}}(k_2, k_1)\right) + \left(A_{\mathcal{Q}'}(k_1, k_2) - A_{\mathcal{Q}'}(k_2, k_1)\right)\right].\end{aligned} \tag{1.48}$$

The amplitudes coincide on the boundary, so we may eliminate everything related to $\mathcal{Q}'$ such that

$$\begin{aligned}\hat{H}_{\mathrm{LL}}\psi = &\left(k_1^2 + k_2^2\right)\psi \\ &+ 2\,\delta(x_1 - x_2)\left\{c\left(A_{\mathcal{Q}}(k_1, k_2) + A_{\mathcal{Q}}(k_2, k_1)\right) + i(k_1 - k_2)\left[A_{\mathcal{Q}}(k_1, k_2) - A_{\mathcal{Q}}(k_2, k_1)\right]\right\}.\end{aligned} \tag{1.49}$$

Something interesting appears: the first term on the first line of Eq. (1.49) is the result we would expect for a free system of bosons. Because the two bosons are interacting, it is no surprise that the energy gets modified by the term on the second line. The amplitudes are arbitrary up to now, but it proves convenient to choose them so as to cancel the term in the second line because the energies then have the same *form* as the free system. The interactions are incorporated directly into the wave function amplitudes, or alternatively in the distribution of quasimomenta $\{k_j\}$, provided that

$$A_{\mathcal{Q}}(k_1, k_2) + A_{\mathcal{Q}}(k_2, k_1) = \frac{i(k_1 - k_2)}{c}\left[A_{\mathcal{Q}}(k_1, k_2) - A_{\mathcal{Q}}(k_2, k_1)\right], \tag{1.50}$$

which can be rewritten by using $\mathrm{e}^{-2i\arctan(u)} = \frac{1-iu}{1+iu}$ (for $u > 0$) as

$$\frac{A_{\mathcal{Q}}(k_1, k_2)}{A_{\mathcal{Q}}(k_2, k_1)} = \frac{k_1 - k_2 + ic}{k_1 - k_2 - ic} = -\frac{1 - i(k_1 - k_2)/c}{1 + i(k_1 - k_2)/c} = -\mathrm{e}^{-2i\arctan\left(\frac{k_1 - k_2}{c}\right)}. \tag{1.51}$$

Necessarily, $k_1 \neq k_2$. By *reductio ad absurdum*, the second line of Eq. (1.49) would only be zero if and only if either $c = 0$ (trivial non interacting case) or if $A_{\mathcal{Q}}(k_1, k_2) = -A_{\mathcal{Q}}(k_2, k_1)$. The latter is non physical for $k_1 = k_2$ because the global wavefunction ψ identically vanishes. It can further be proven that $\forall c > 0$, all k's are real (absence of bound states in the system) [Lieb and Liniger, 1963].

It is convenient to define a function θ such that

$$\frac{A_{\mathcal{Q}}(k_1, k_2)}{A_{\mathcal{Q}}(k_2, k_1)} := -\mathrm{e}^{i\theta(k_1 - k_2)}, \tag{1.52}$$

which by identification with Eq. (1.51) gives

$$\theta(k) = -2\arctan\left(\frac{k}{c}\right). \tag{1.53}$$

The dispersion relation has the same form as the one of a non-interacting system provided that the previous constraint on the amplitudes of the reduced wave functions Eq. (1.53) is satisfied. The interactions are included into the distribution of the quasimomenta rather than directly reflected by the form of the dispersion relation. The global wavefunction of the system ψ (up to a normalisation factor) has been obtained using the Bethe ansatz, as well as the associated eigenenergies. For this integrable model, it can be shown explicitly that all wavefunctions which are solutions of the Schrödinger equation are of the form given by the Bethe ansatz, proving the completeness of the exact solution [Dorlas, 1993].

1.A.1.2 Many particles

Since the Lieb-Liniger model is integrable, the N-body interaction problem can be factorised exactly in pairs of 2-body interactions. A necessary condition for a system to be integrable is that the Yang-Baxter equation holds. Simply put, this equation means that a many-body scattering can be decomposed as a series of two-body ones, independently of the ordering, so that the two-particle constraints previously derived can all be satisfied simultaneously and in a consistent manner. The previous method can then be extended in the following way: a given configuration of particles specifies their coordinates $\{x_j\}$, and their quasimomenta $\{k_j\}$ before and after they rearrange upon scattering, which can be modelled by a given permutation $\mathcal{P}$ of N elements. The Bethe ansatz takes the reduced wave function to be of the form

$$f(x_1, x_2, \cdots, x_N) = \sum_{\mathcal{P}} A_{\mathcal{P}}\, \mathrm{e}^{\,i \sum_{j=1}^{N} k_{\mathcal{P}j} x_j}. \tag{1.54}$$

For bosons, the global wave function is fully symmetric under the exchange of any pair of particles so that the solution obtained in a particular sector is the same in any of the $N!$ sectors.

Consider for simplicity two transpositions $\mathcal{T}$ and $\mathcal{T}'$ which exchange only the two quasimomenta k_i and k_j of two particles i and j. From the previous analysis, the two amplitudes $A_{\mathcal{T}}$ and $A_{\mathcal{T}'}$ are related by

$$A_{\mathcal{T}} = \frac{k_i - k_j + ic}{k_i - k_j - ic} A_{\mathcal{T}'} = -\mathrm{e}^{i\theta(k_i - k_j)} A_{\mathcal{T}'}, \tag{1.55}$$

as the terms unchanged by the permutations factorise on both sides of the equation. Decomposing an arbitrary permutation $\mathcal{P}$ as successive transpositions, the general case can be decomposed as products of two-particle exchanges so that by induction

$$A_{\mathcal{P}} = A_0\, (-1)^{\varepsilon(\mathcal{P})} \prod_{j<l} \left(k_{\mathcal{P}_j} - k_{\mathcal{P}_l} + ic \right), \tag{1.56}$$

where A_0 is the amplitude of the plane wave in the initial sector (without any permutation), and $\varepsilon(\mathcal{P})$ stands for the signature of the permutation $\mathcal{P}$ (the minimal number of transpositions to do to go from the initial sector to the final one). Now that we know the expression for $A_{\mathcal{P}}$ – the constant prefactor A_0 is set by the normalisation –, the reduced wave function in Eq. (1.54) can be expanded, and by symmetry the global wave function ψ can be reconstructed. By construction, it is an eigenfunction of the Hamiltonian with eigenvalue $E = \sum_{j=1}^{N} k_j^2$. The energy only depends indirectly on the interaction, through the distribution of quasimomenta $\{k_j\}$. It is thus crucial to understand how they are distributed.

1.A.1.3 Distribution of the quasimomenta k_j

Universal properties of the model are determined by looking at the thermodynamic limit, in which the precise choice of boundary conditions becomes irrelevant. For convenience, we choose a system of size L with periodic boundary conditions (PBC) so that $\forall j = 1 \cdots N$,

$$\psi(x_1, \cdots, x_j + L, \cdots, x_N) = \psi(x_1, \cdots, x_j, \cdots, x_N). \tag{1.57}$$

Decomposing again an arbitrary permutation $\mathcal{P}$ into transpositions, we get

$$\mathrm{e}^{ik_j L} = \prod_{l \neq j} \left(\frac{k_j - k_l + ic}{k_j - k_l - ic} \right) = (-1)^{N-1} \prod_{l=1}^{N} \mathrm{e}^{i\theta(k_j - k_l)}, \tag{1.58}$$

and by taking the logarithm we find

$$k_j L = 2\pi \left(\tilde{I}_j - \frac{N-1}{2} \right) + \sum_{l=1}^{N} \theta(k_j - k_l), \tag{1.59}$$

where $\tilde{I}_j$ are integers from 1 to N. We choose for convenience $I_j = \tilde{I}_j - (N-1)/2$, which are integers if N is odd, and half-integers if N is even. This gives the so-called Bethe equations of the system

$$k_j L = 2\pi I_j + \sum_{l=1}^{N} \theta(k_j - k_l), \tag{1.60}$$

where the two-particle phase shift θ has been defined in Eq. (1.53). Through the choice of the ensemble $\{I_j\}$, we can describe all physical states in a unique way. If $\{I_j\}$ spans all integers from 1 to N, it describes the ground state of the system. From now on we focus on this case. The excitations will be described in Sec. 1.A.3.

> All k_j are distinct in the Bethe equations (the proof is similar to the $N = 2$ case mentioned in Sec. 1.A.1.1). In quasimomentum space, the particles cannot have the same quasimomentum, and this property is often referred to as a Pauli's exclusion principle (in quasimomentum space). These quasimomenta are a practical bookkeeping tool, but are not related in a simple manner to the physical momenta of the bosonic particles.

1.A.1.4 The thermodynamic limit

We focus on the repulsive ($c > 0$) bosonic Lieb-Liniger model, for which the quasimomenta are all real[24] and distinct [Yang and Yang, 1969]. They can therefore be unambiguously ordered. It is convenient to define a counting function

$$y(k_j) := k_j - \frac{1}{L} \sum_{l=1}^{N} \theta\left(k_j - k_l\right), \tag{1.61}$$

and a quasimomentum density

$$\rho(k_j) := \lim_{N,L\to\infty} \frac{1}{L\left(k_{j+1} - k_j\right)}. \tag{1.62}$$

The advantage of these definitions is transparent in the thermodynamic limit where

$$\sum_j = \sum_j \frac{k_{j+1} - k_j}{k_{j+1} - k_j} = L \sum_j \rho(k_j)\left(k_{j+1} - k_j\right) \longrightarrow L \int \rho(k)\,\mathrm{d}k. \tag{1.63}$$

By taking the derivative of the counting function with respect to k_j and using the Bethe equations (1.60), we obtain in the thermodynamic limit

$$\frac{\mathrm{d}y}{\mathrm{d}k} = 2\pi\rho(k), \tag{1.64}$$

where the quasimomenta are now described by the continuous variable k. It is crucial to be able to organise the k_j so that in the thermodynamic limit the counting function $y(k)$ is well defined (only under this assumption $y(k_{j+1}) - y(k_j) = 2\pi/L$ for the ground state).

Taking the thermodynamic limit of Eq. (1.61), computing its derivative and substituting in Eq. (1.64) yields

$$2\pi\rho(k) = 1 - \int_{k_{\min}}^{k_{\max}} K(k - k')\rho(k')\,\mathrm{d}k', \tag{1.65}$$

where we defined $K(k) := \frac{\mathrm{d}\theta(k)}{\mathrm{d}k}$. Equation (1.65) is called the Lieb-Liniger equation [Lieb and Liniger, 1963]. It is a closed equation for $\rho(k)$, the only unknown parameter of the problem since $\theta(k) = -2\arctan\left(k/c\right)$ and thus

$$K(k - k') = \frac{-2c}{c^2 + (k - k')^2}. \tag{1.66}$$

[24] The fermionic counterpart admits complex valued k_j, which describe bound states. The solutions of the Bethe equations organise into so-called Bethe strings. Such strings are characterised by a root, which is a real number. Roots can thus be ordered, and a similar procedure applies. All solutions are then reconstructed from the roots.

With the closed equation (1.65), $\rho(k)$ can be obtained for any value of the interaction, with the normalisation constraint for the density

$$n = \frac{N}{L} = \int_{-k_\mathrm{F}}^{k_\mathrm{F}} \rho(k)\,\mathrm{d}k. \tag{1.67}$$

All thermodynamic quantities are then expressed as functions of the quasimomentum density $\rho(k)$, for instance the ground state energy is given by $E_0 = L\int_{-k_\mathrm{F}}^{k_\mathrm{F}} k^2\rho(k)\,\mathrm{d}k$. In practice, rather than expressing all thermodynamic quantities – such as the chemical potential μ, the compressibility κ or the thermodynamic speed of sound $v_{\mathrm{s,th}}$ – as functions of $\rho(k)$, it appears more convenient to express them through the function

$$e(\gamma) := \frac{E_0}{Ln^3} = \frac{1}{n^3}\int_{-k_\mathrm{F}}^{k_\mathrm{F}} k^2\rho(k)\,\mathrm{d}k. \tag{1.68}$$

> The reasoning behind this choice is the following [Lieb and Liniger, 1963]. The ground state energy should be proportional to N to be extensive. With $m = 1/2$ and $\hbar = 1$, an energy is homogeneous to a (length)$^{-2}$. The only choice is thus the form $E_0 = Nn^2 \times e$, where e is a function of dimensionless and intensive variables. The only variable satisfying both constraints is γ, leading to the definition of $e(\gamma)$ given above.

In terms of $e(\gamma)$ and its derivatives with respect to γ, we get

$$\mu = \left.\frac{\partial(E_0/L)}{\partial n}\right|_{c,L} = \left.\frac{\partial(n^3 e(\gamma))}{\partial n}\right|_{c,L} = n^2\left[3e(\gamma) - \gamma e'(\gamma)\right] \tag{1.69a}$$

$$\kappa_{\mathrm{red}}^{-1} = \frac{1}{n^2}\kappa_{\mathrm{phys}}^{-1} = \left.\frac{\partial\mu}{\partial n}\right|_{c,L} = 6ne(\gamma) - 4n\gamma e'(\gamma) + n\gamma^2 e''(\gamma) \tag{1.69b}$$

$$v_{\mathrm{s,th}} = \left[\frac{L}{nm}\frac{\partial^2 E_0}{\partial L^2}\right]^{1/2} = \left(\frac{\kappa_{\mathrm{phys}}^{-1}}{mn}\right)^{1/2} = \frac{n}{\sqrt{m}}\left(6e(\gamma) - 4\gamma e'(\gamma) + \gamma^2 e''(\gamma)\right)^{1/2}. \tag{1.69c}$$

κ_{red} stands for the reduced compressibility, often just called compressibility in the literature.

1.A.2 Numerical solution and dimensionless equations

Equation (1.65) with the constraint (1.67) cannot be solved analytically, except in the weakly interacting regime (where a Bogoliubov expansion can be used) or the strongly interacting one (where a strong coupling expansion using fermionisation can be used) [Ristivojevic, 2014]. For arbitrary interactions, a numerical solution is necessary. As we focus on the ground state, the integration bounds on the quasimomentum are symmetric and the cutoff is set by the Fermi momentum[25] k_F such that $k_{\max} = k_\mathrm{F} = -k_{\min}$. It is convenient to work with dimensionless parameters so we define the following variables

$$x = k/k_\mathrm{F}, \qquad \alpha = c/k_\mathrm{F}, \qquad \gamma = c/n, \tag{1.70}$$

and we call $g(x)$ the rescaled quasimomentum density. In dimensionless form the main equations are

$$\frac{n}{k_\mathrm{F}} = \frac{\alpha}{\gamma} = \int_{-1}^{1} g(x)\,\mathrm{d}x \tag{1.71a}$$

$$2\pi g(x) = 1 + \int_{-1}^{1} \frac{2\alpha g(y)\,\mathrm{d}y}{\alpha^2 + (x-y)^2} \tag{1.71b}$$

$$e(\gamma) = \frac{\gamma^3}{\alpha^3}\int_{-1}^{1} x^2 g(x)\,\mathrm{d}x. \tag{1.71c}$$

[25] We work with bosons, but there is a Fermi sea in quasimomentum space as mentioned in Sec. 1.A.1.3.

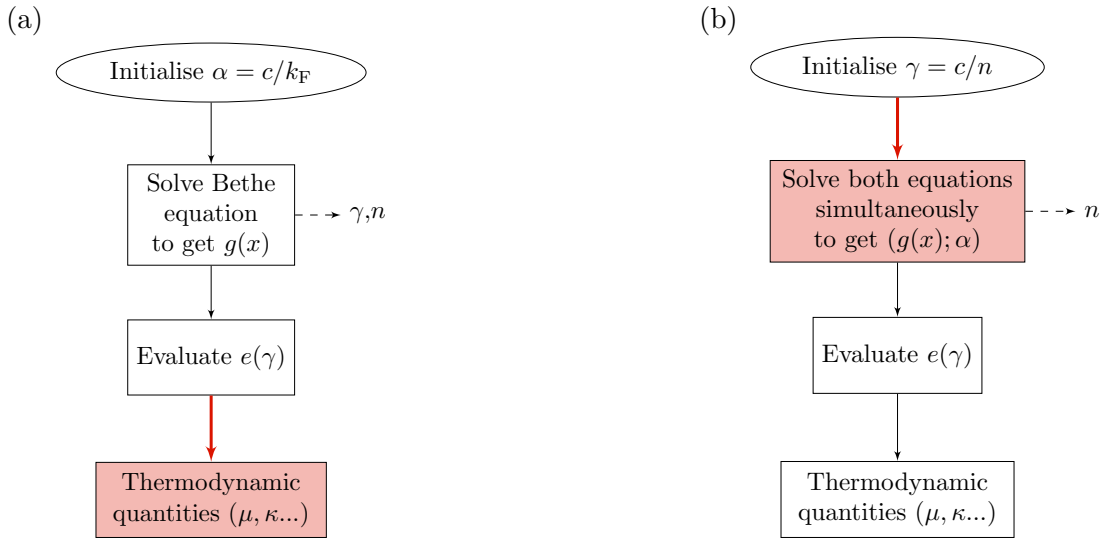

Fig. 1.19 Flowchart of (a) the naive algorithm and (b) the one we use to compute thermodynamic quantities in the Lieb-Liniger model. The difficult part of each algorithm is represented in red.

The system of equations (1.71) depends only on 3 parameters: α, γ and $g(x)$. From the equations, it seems that fixing α is the simplest choice: one can then solve Eq. (1.71b) alone to get $g(x)$, and finally use Eq. (1.71a) to get γ. This procedure is summarised in Fig. 1.19(a). However, fixing γ is most convenient numerically, since all thermodynamic quantities depend on the single interaction parameter γ and it is crucial to have a controlled range for γ to compute $e'(\gamma)$ and $e''(\gamma)$ accurately. Therefore, we set γ, and then solve simultaneously Eq. (1.71a) and (1.71b) to get α and $g(x)$. The density is then obtained from Eq. (1.71a).

> The function $e(\gamma)$ does not depend on α, contrary to what could be deduced from a quick look at Eq. (1.71c). Equation (1.71a) can be used to rewrite Eq. (1.71c) as
>
> $$e(\gamma) = \frac{\int_{-1}^{1} x^2 g(x)\,\mathrm{d}x}{\left[\int_{-1}^{1} g(x)\,\mathrm{d}x\right]^3}. \tag{1.72}$$
>
> Since $g(x)$ only depends on α from Eq. (1.71b), using Eq. (1.71a) again, we can express γ as a unique function of α. Importantly, this function is analytic and bijective on the region $[0; \infty[$ as discussed by [Lieb and Liniger, 1963]. Choosing γ over α is also physically more satisfactory, since the density n is easier to interpret (and more meaningful experimentally) than the Fermi quasimomentum k_F.

The principle of the algorithm we used to solve the equations numerically is illustrated on the flowchart in Fig. 1.19(b). The numerical results obtained for the equation of state by solving the Bethe equations are given in Fig. 1.20. It is fruitful to compare the exact result given by the Bethe ansatz to the two limit cases where the interactions are infinitely weak (Bogoliubov) or infinitely strong (Tonks-Girardeau). In both cases, one can show that $\mu_{BG} = 2\gamma n^2$ and $\mu_{TG} = (\pi n)^2$ with the convention $\hbar = 1 = 2m$ (see [Lieb and Liniger, 1963] for a derivation of these expressions). The Bethe ansatz exactly interpolates between these two regimes.

1.A.3 The spectrum of elementary excitations

Now that we know how to describe thermodynamic properties of the ground state, what about excited states? The elementary excitations of the model conserve the number of particles, and can be of two types, easier to interpret in the fully fermionised regime [Lieb, 1963]. The first type of excitation in quasimomentum space amounts to remove a particle at k_F, and place it at $k_p > k_F$. The energy of this elementary excitation is $\epsilon_1 = k_p^2 - k_F^2$ and its quasimomentum $p = k_p - k_F$. The excitation spectrum of this branch is then given by $\epsilon_1(p) = p^2 + 2k_F|p|$ where $p \in]-\infty; +\infty[$.

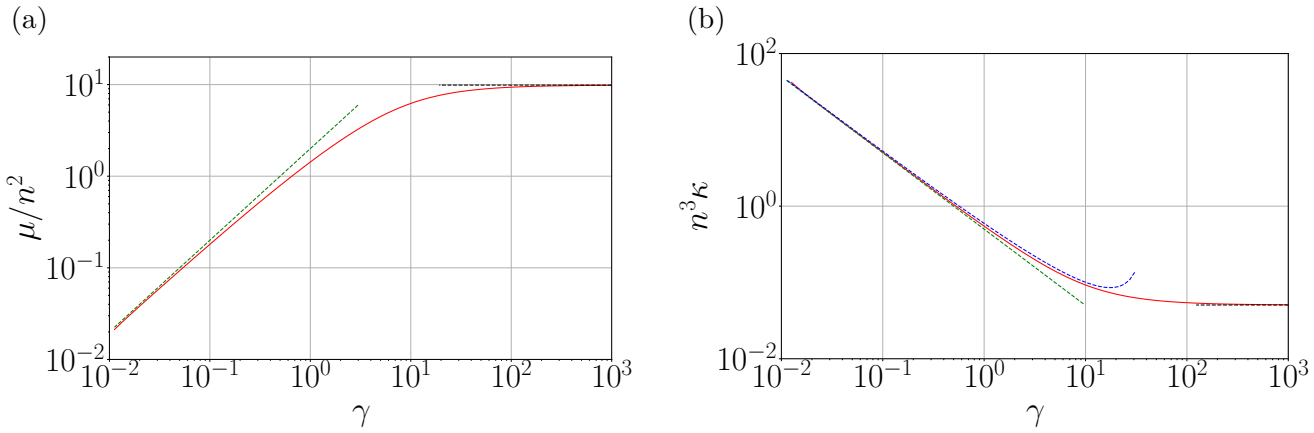

Fig. 1.20 Results for thermodynamic quantities (log scale) using the Bethe ansatz approach for the Lieb-Liniger model (a) for the chemical potential and (b) the compressibility. For hard core bosons $\mu/n^2 = \pi^2$ and $n^3\kappa = 1/(2\pi^2)$: the gas is fermionised (black). Recall that $E_\mathrm{F} = (\pi n)^2$ (Fermi energy) and $v_\mathrm{F} = \pi n$ (Fermi momentum), in the strongly interacting regime with $\hbar = 1 = 2m$. In the weakly interacting regime, the Bogoliubov prediction $\mu/n^2 = 2\gamma$ (green), or the weakly interacting expansion (blue) are recovered.

The second type is obtained by taking a particle from $0 < k_\mathrm{h} < k_\mathrm{F}$ to k_F[26]. The energy of this elementary excitation is $\epsilon_\mathrm{h} = k_\mathrm{F}^2 - k_\mathrm{h}^2$ and its momentum $p = k_\mathrm{F} - k_\mathrm{h}$ so that $\epsilon_2(p) = -p^2 + 2k_\mathrm{F}|p|$ where $p \in [-k_\mathrm{F}; k_\mathrm{F}]$. Below we discuss how these elementary excitations are modified for finite interactions.

> The calculation below can be performed in two conceptually different ways. Lieb's method [Lieb, 1963] considers that the quasimomenta k_j initially belong to the $N-1$ particle ground state; whereas in Yang and Yang's method [Yang and Yang, 1969], they belong to the N particle ground state. The values of Δk_j are different in the two cases, and the backflow definitions differ. Lieb does not include the chemical potential in the energy contrary to Yang and Yang. Ultimately both methods are equivalent.

1.A.3.1 Lieb's representation of the elementary excitation

One method to parametrise the excitations is the one of [Lieb, 1963]. To describe the excited state containing a type-I excitation, we note $k_N^\star$ the quasimomentum of the excited particle. In the presence of the excitation, the Bethe equations for N particles are modified: the remaining quasimomenta redistribute in the presence of interactions, and we denote this new distribution using the superscript "$\star$". The Bethe equations give for $j \in [1; N-1]$

$$k_j^\star L = \sum_{l=1}^{N} \theta(k_j^\star - k_l^\star) + 2\pi I_j^\star = \sum_{l=1}^{N-1} \theta(k_j^\star - k_l^\star) + \theta(k_j^\star - k_N^\star) + 2\pi I_j^\star, \tag{1.73a}$$

$$k_N^\star L = \sum_{l=1}^{N} \theta(k_N^\star - k_l^\star) + 2\pi I_N^\star, \tag{1.73b}$$

where we isolated the contribution of the excited particle $j = N$. This appears convenient because $I_N^\star$ is arbitrary, but for $j \in [1; N-1]$, $I_j^\star \in [-(N-1)/2; ((N-1)/2) - 1]$ (Fig. 1.21). The ground state of a system with $N-1$ particles obeys the following Bethe equations $\forall j \in 1 \cdots N-1$

$$k_j L = \sum_{l=1}^{N-1} \theta(k_j - k_l) + 2\pi I_j, \tag{1.74}$$

where in this case $I_j \in [-(N-2)/2; (N-2)/2]$. To compare how the quasimomenta redistribute

[26] Rigorously $k_\mathrm{F} + 2\pi/L$, but we disregard finite size corrections in the thermodynamic limit.

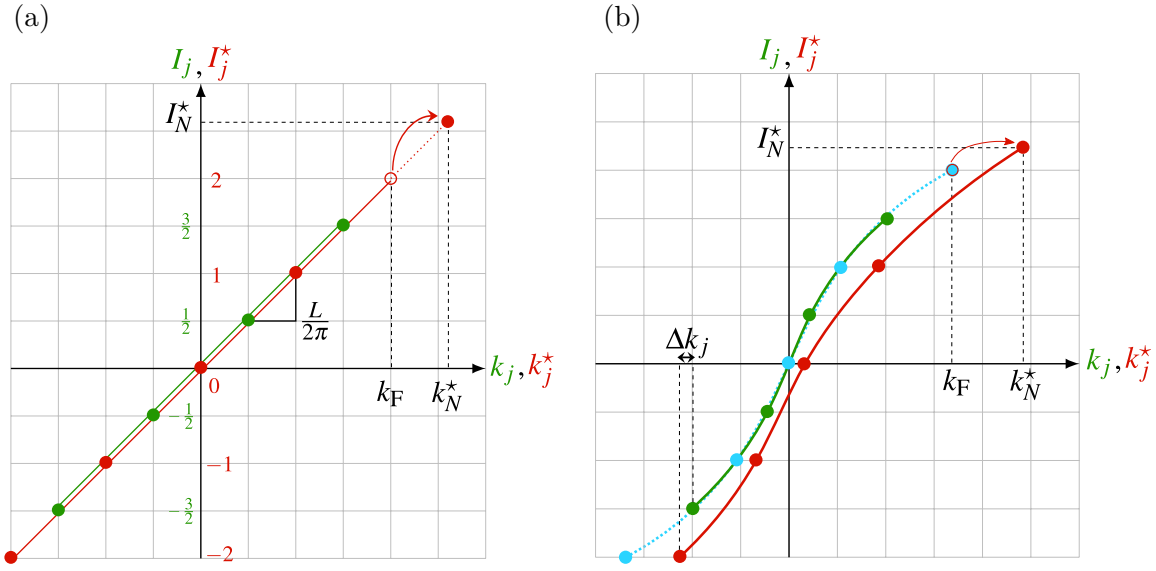

Fig. 1.21 Lieb's representation of the excitations with $N = 5$. (a) Represents a $N-1$ particle ground state (green) and a N-particle excited state (red) for infinite interactions (red and green line were slightly shifted for visibility). Since $\theta = 0$, $I_j \propto k_j$. Except for the added particle $j = N$, the quasimomenta and the associated quantum numbers between the two states are simply shifted by a constant factor ($I_j^\star - I_j = -1/2$). The ground state with $N-1$ particles has a total momentum $P = \sum_j k_j = 0$ while for the N-particle excited state containing a single type-I excitation $P = k_N^\star - k_F$. (b) Same for finite interactions ($\theta \neq 0$), where we also indicated the N-particle ground state (blue). The quasimomenta are now related in a non-trivial way, $k_j^\star = k_j + \Delta k_j$ where $\Delta k_j \ll k_j$ can be evaluated from the backflow function. As finite interactions modify the quasimomentum distribution, $P > k_N^\star - k_F$.

due to the interactions after the excited particle is introduced, we take the difference between Eq. (1.73a) and (1.74). We define the change in quasimomentum $\Delta k_j = k_j^\star - k_j$, such that

$$\begin{aligned}\Delta k_j L &= \sum_{l=1}^{N-1} \left[\theta(k_j^\star - k_l^\star) - \theta(k_j - k_l)\right] + \theta(k_j^\star - k_N^\star) + 2\pi(I_j^\star - I_j) \\ &= \sum_{l=1}^{N-1} (\Delta k_j - \Delta k_l)\, K(k_j - k_l) + \theta(k_j^\star - k_N^\star) - \pi,\end{aligned} \tag{1.75}$$

where in the second equality we used that for $j \in [1; N-1]$, $I_j^\star - I_j = -1/2$ (Fig. 1.21), and a first order Taylor expansion $\theta(k_j^\star - k_l^\star) = \theta(k_j - k_l) + (\Delta k_j - \Delta k_l)\, K(k_j - k_l)$ where $K(k_j - k_l) = -2c/(c^2 + [k_j - k_l]^2)$. Putting everything together

$$\Delta k_j L \left\{1 - \frac{1}{L}\sum_{l=1}^{N-1} K(k_j - k_l)\right\} = -\sum_{l=1}^{N-1} \Delta k_l\; K(k_j - k_l) + \theta(k_j^\star - k_N^\star) - \pi. \tag{1.76}$$

Using the derivative of Eq. (1.61) to simplify the left-hand side and limiting to first order such that $\theta(k_j^\star - k_N^\star) \simeq \theta(k_j - k_N^\star)$ we get

$$2\pi\rho(k_j)\Delta k_j L = -\pi + \theta(k_j - k_N^\star) - \sum_{l=1}^{N-1} \Delta k_l\; K(k_j - k_l). \tag{1.77}$$

To account for the redistribution of quasimomenta between the excited state and the ground state, it proves convenient to define the backflow function

$$J(k_j) := \frac{k_j^\star - k_j}{k_{j+1} - k_j} = \Delta k_j L \rho(k_j). \tag{1.78}$$

In the thermodynamic limit, Eq. (1.77) can be rewritten as

$$2\pi J(k) = -\pi + \theta(k - k^\star) - \int_{-k_\mathrm{F}}^{k_\mathrm{F}} J(k')K(k - k')\,\mathrm{d}k'. \tag{1.79}$$

In dimensionless form, and by writing explicitly the kernel we finally get

$$J(x) = -\frac{1}{2} - \frac{1}{\pi}\arctan\left(\frac{x - x^\star}{\alpha}\right) + \frac{\alpha}{\pi}\int_{-1}^{1} \frac{J(y)\,\mathrm{d}y}{\alpha^2 + (x-y)^2}. \tag{1.80}$$

This last equation is crucial: solving it gives us the energy-momentum picture of the excitations. Indeed, the total momentum of the excited state is given by

$$P = \sum_{j=1}^{N-1} k_j^\star + k_N^\star = \sum_{j=1}^{N-1} \Delta k_j + k_N^\star \xrightarrow{\mathrm{TL}} k^\star + \int_{-k_\mathrm{F}}^{k_\mathrm{F}} J(k)\,\mathrm{d}k, \tag{1.81}$$

where we used that $\sum_{j=1}^{N-1} k_j = 0$ (ground state with $N-1$ particles).

> In the limit $c \to \infty$, both $\theta(k)$ and $K(k)$ are zero. Eq. (1.79) gives a constant backflow $J(k) = -1/2$. The momentum of the excited state is then $P = k^\star - k_\mathrm{F}$ as expected.

In dimensionless form it reads as

$$\frac{P}{n} = \frac{\gamma}{\alpha}\left(x^\star + \int_{-1}^{1} J(x)\,\mathrm{d}x\right), \tag{1.82}$$

where we rescaled the momentum by the inverse of a length (the density) since $\hbar = 1$. The energy difference between the excited state and the ground state can also be computed from the backflow

$$\Delta E = \sum_{j=1}^{N-1} k_j^{\star\,2} + k_N^{\star\,2} - E_0(N) = -\mu + 2\sum_{j=1}^{N-1} k_j \Delta k_j + k_N^{\star\,2} \xrightarrow{\mathrm{TL}} -\mu + k^{\star\,2} + 2\int_{-k_\mathrm{F}}^{k_\mathrm{F}} kJ(k)\,\mathrm{d}k, \tag{1.83}$$

where in the second equality we used that $\mu = E_0(N) - E_0(N-1)$ and neglected a second order term in $(\Delta k_j)^2$.

> In the limit $c \to \infty$ where $J(k) = -1/2$, we have $\Delta E = k_N^{\star\,2} - \mu$. In the fully fermionised regime, $\mu = k_\mathrm{F}^2$ ($\hbar = 1 = 2m$), such that $\Delta E = k_N^{\star\,2} - k_\mathrm{F}^2$ as expected.

In dimensionless form we get

$$\frac{\Delta E}{n^2} = -\frac{\mu}{n^2} + \left(\frac{\gamma}{\alpha}\right)^2\left(x^{\star\,2} + 2\int_{-1}^{1} xJ(x)\,\mathrm{d}x\right), \tag{1.84}$$

where we rescaled the energy by a momentum squared (since $m = 1/2$), hence by the inverse of a density squared. The curve $\Delta E/n^2 = f(P/n)$ defines the dispersion relation of the excitations. For a given value of the interactions γ (α in rescaled units), the backflow equation given by Eq. (1.80) is solved numerically, and then using Eq. (1.82) and Eq. (1.84) the dispersion relation can be constructed. Such elementary excitations are sometimes referred to as particle-like, but it should be explicit from their construction that they conserve particle number by adding both a particle above the Fermi surface and a hole at the Fermi surface. We will thus prefer to call them type-I excitation, as in [Lieb, 1963]. After numerically solving the linear integral equation Eq. (1.80) to get the backflow, it is possible to compute the dispersion relation using Eq. (1.82) and (1.84) for different values of γ. The result is shown in Fig. 1.22. There also exists a branch for type-II excitations: a hole in created inside the Fermi sea and a particle is added at the Fermi level

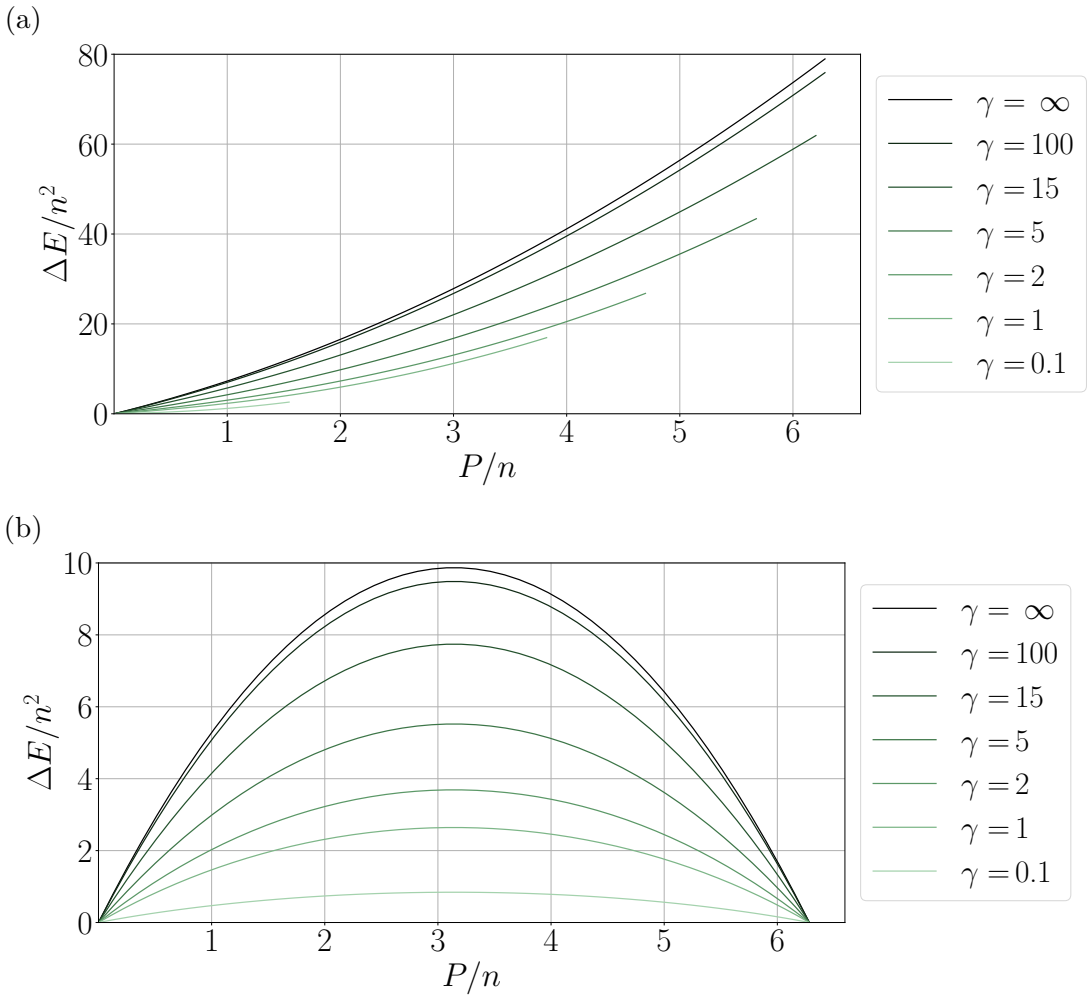

Fig. 1.22 Exact dispersion relation of the (a) type-I excitation and (b) type-II excitation in the Lieb-Liniger model obtained by Bethe ansatz, for different values of the interaction parameter. The data agrees with results found by [Lieb, 1963].

to conserve the number of particles. We will not give further details about this branch, further details can be found for instance in [Lieb, 1963]. We simply point out that they can be found by solving a similar (up to some signs) integral equation

$$J(x) = \frac{1}{2} + \frac{1}{\pi}\arctan\left(\frac{x - x^\star}{\alpha}\right) + \frac{\alpha}{\pi}\int_{-1}^{1} \frac{J(y)\,\mathrm{d}y}{\alpha^2 + (x-y)^2}, \tag{1.85}$$

with the definitions

$$\begin{cases} \dfrac{P}{n} = \dfrac{\gamma}{\alpha}\left(-x^\star + \displaystyle\int_{-1}^{1} J(x)\,\mathrm{d}x\right) \\ \dfrac{\Delta E}{n^2} = \dfrac{\mu}{n^2} + \left(\dfrac{\gamma}{\alpha}\right)^2\left(-x^{\star\,2} + 2\displaystyle\int_{-1}^{1} xJ(x)\,\mathrm{d}x\right). \end{cases} \tag{1.86}$$

We may also calculate the speed of sound from the excitation spectrum using $v_{\mathrm{s,ex}} = \lim_{p\to 0} \frac{\partial \varepsilon}{\partial p}$. The result is equivalent to the one obtained by the thermodynamic relation [Eq. (1.69c)], namely $v_{\mathrm{s,th}} = v_{\mathrm{s,ex}}$. This result is not general but specific to the Lieb-Liniger model and the structure of its Bethe equations (see [Korepin et al., 1997], Appendix I.3.). In Fig. 1.23 we show the speed of sound obtained from the Bethe ansatz, and compare with two known limits in the Bogoliubov weakly interacting regime. For stronger interactions, the speed of sound reaches a constant value, equal to the Fermi velocity, and we recover the fermionisation of the bosonic gas.

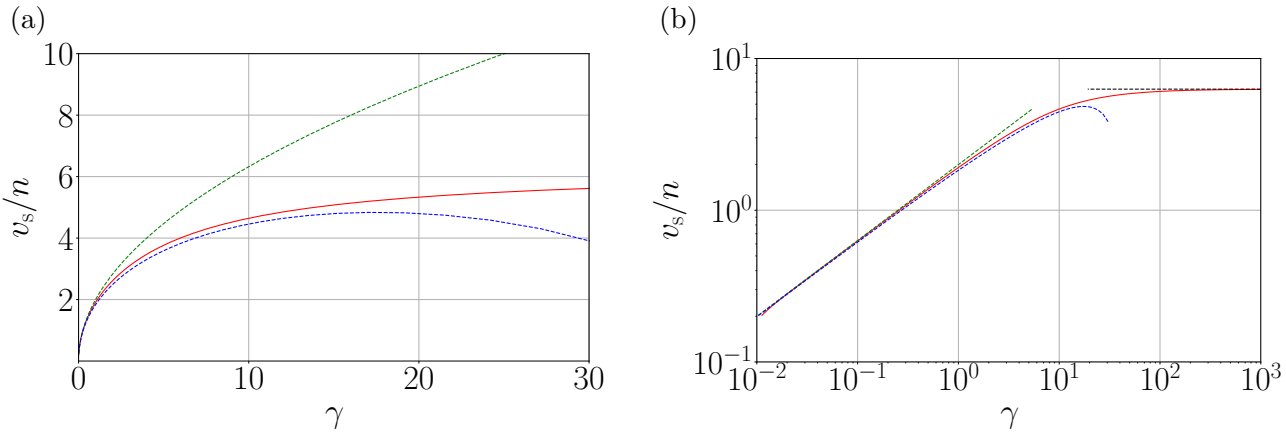

Fig. 1.23 Speed of sound obtained numerically from the exact Bethe ansatz method for the Lieb-Liniger model (a) in linear scale, (b) in log-log scale. The Bogoliubov result $v_s = 2n\gamma^{1/2}$ (green curve) and the weak coupling expansion $v_s = 2n[\gamma - (\frac{1}{2\pi})\gamma^{3/2}]^{1/2}$ (blue curve, see [Ristivojevic, 2014]) are recovered for small interactions. For strong interactions, the fermionisation can be observed as the speed of sound is equal to the Fermi velocity $v_F/n = 2\pi$ (independent of γ, black line), with $\hbar = 1 = 2m$.

1.A.3.2 Yang-Yang's alternative representation of the elementary excitations

In this final section, we show an alternative parametrisation of the elementary excitations given by [Yang and Yang, 1969]. Physically, we may consider an excitation to be the move of a particle (labelled by an index α) with quasimomentum k_α, initially somewhere inside the Fermi sea (not necessarily at the Fermi level) to an arbitrary value above the Fermi level, written $k^\star_\alpha$. Formally, the Bethe equations will be obtained by taking directly the difference with the N particle ground state (instead of $N-1$ as in Lieb's representation). The equations for the momentum and energy of the excited state will be modified, so as the backflow, because the excitations are parametrised in a different way. Of course, in the end, all physical observables are identical within both representations.

The Bethe equations for N particles in the ground state and in the excited state read as

$$\begin{cases} k_j L &= \sum_l \theta(k_j - k_l) + 2\pi I_j, \\ k^\star_j L &= \sum_l \theta(k^\star_j - k^\star_l) + 2\pi I^\star_j. \end{cases} \tag{1.87}$$

Since we create a single excitation, $I^\star_j = I_j$ except for $j \neq \alpha$. Therefore, $\forall j \neq \alpha$ we have

$$\Delta k_j L = \sum_l (\Delta k_j - \Delta k_l) K(k_j - k_l) = \sum_{l\neq\alpha} (\Delta k_j - \Delta k_l) K(k_j - k_l) + \theta(k^\star_j - k^\star_\alpha) - \theta(k_j - k_\alpha). \tag{1.88}$$

To first order, $\theta(k^\star_j - k^\star_\alpha) = \theta(k_j - k^\star_\alpha) + \Delta k_j K(k_j - k^\star_\alpha) \simeq \theta(k_j - k^\star_\alpha) + \Delta k_j K(k_j - k_\alpha)$, such that

$$\begin{aligned} \Delta k_j L \left(1 - \frac{1}{L}\sum_l K(k_j - k_l)\right) &= 2\pi\rho(k_j)\Delta k_j L \\ &= -\sum_{l\neq\alpha} \Delta k_l\, K(k_j - k_l) + \theta(k_j - k^\star_\alpha) - \theta(k_j - k_\alpha). \end{aligned} \tag{1.89}$$

Defining the backflow using Eq. (1.78) (for $j \neq \alpha$), we get in the thermodynamic limit

$$2\pi J(k) = \theta(k - k^\star_\alpha) - \theta(k - k_\alpha) - \int_{-k_F}^{k_F} J(k')K(k - k')\,\mathrm{d}k'. \tag{1.90}$$

The momentum of the excited state is defined as

$$P = \sum_j k^\star_j = k^\star_\alpha + \sum_{j\neq\alpha}(k_j + \Delta k_j) = k^\star_\alpha - k_\alpha + \sum_{j\neq\alpha} \Delta k_j, \tag{1.91}$$

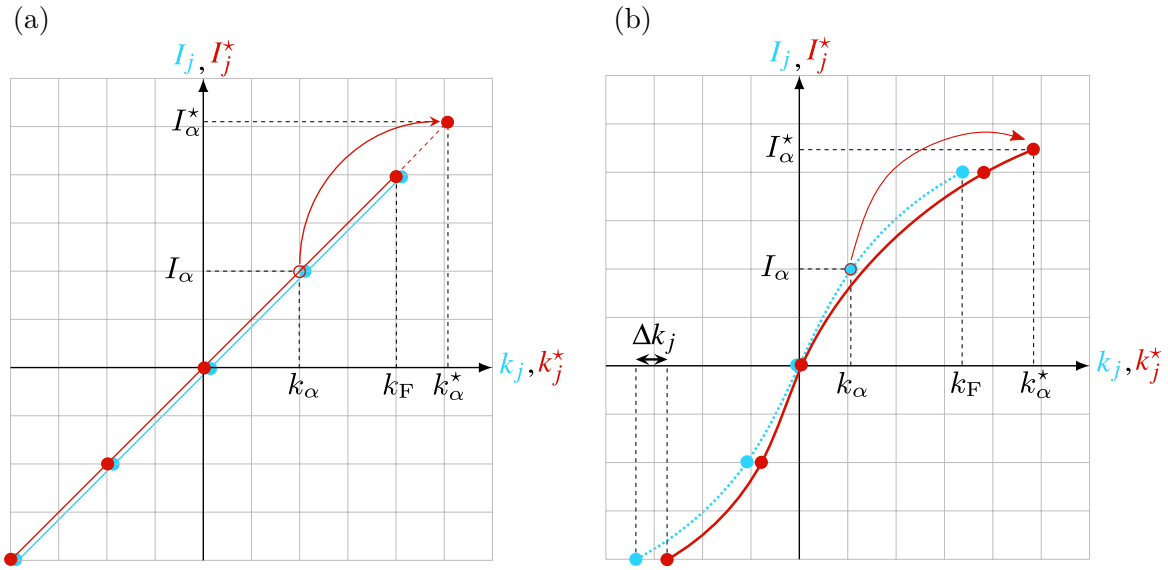

Fig. 1.24 Yang-Yang's representation of the excitations for $N = 5$. (a) Ground state (blue) and excited state (red) with N particles for infinite interactions. Both distributions coincide except for the moved particle α but we slightly shifted the blue one to improve visibility. The quasimomenta cannot redistribute ($\theta = 0$) and $k_j = k_j^\star$ and $I_j = I_j^\star$ except for $j = \alpha$. The k_j are linearly related to the I_j. In the ground state $P = 0$, and for the excited state $P = k_\alpha^\star - k_\alpha$. (b) For finite interactions, the quasimomenta $k_j^\star$ for $j \neq \alpha$ redistribute and are non-trivially related to the ground state distribution by $k_j^\star = k_j + \Delta k_j$ where $\Delta k_j \ll k_j$. As finite interactions modify the quasimomentum distribution, $P > k_\alpha^\star - k_\alpha$.

where we used that for the ground state $\sum_j k_j = 0$. Similarly, the energy difference between the excited state and the ground state reads as

$$\Delta E = \sum_j k_j^{\star\,2} - \sum_j k_j^2 = k_\alpha^{\star\,2} - k_\alpha^2 + 2\sum_{j\neq\alpha} k_j\,\Delta k_j \tag{1.92}$$

where we neglected a second order term in Δk_j^2. Therefore in the thermodynamic limit and using the definition of the backflow we get

$$\begin{aligned} P &= k_\alpha^\star - k_\alpha + \int_{-k_\mathrm{F}}^{k_\mathrm{F}} J(k)\,\mathrm{d}k, \\ \Delta E &= k_\alpha^{\star 2} - k_\alpha^2 + 2\int_{-k_\mathrm{F}}^{k_\mathrm{F}} kJ(k)\,\mathrm{d}k. \end{aligned} \tag{1.93}$$

In this representation, in the limit where $c \to \infty$, Eq. (1.90) yields $J(k) = 0$ since $\theta(k)$ and $K(k)$ both vanish. Equation (1.93) then reduces to $P = k_\alpha^\star - k_\alpha$ and $\Delta E = k_\alpha^{\star 2} - k_\alpha^2$.

The advantage of this representation is transparent from the previous remark in the strongly interacting regime. The removed particle with quasimomentum k_α can be interpreted as a hole, and the added one with quasimomentum $k_\alpha^\star$ as a particle. This allows to construct the full excitation spectrum of the Lieb-Liniger model in an efficient way. The elementary excitations considered by Lieb correspond to one choice of either $k_\alpha = k_\mathrm{F}$ (type-I excitation, particle-like) or $k_\alpha^\star = k_\mathrm{F}$ (type-II excitation, hole-like).

1.B Quantum ergodicity and thermalisation of the long-time steady state

Questions about the definition of quantum ergodicity and thermalisation date back to the foundations of quantum statistical mechanics and were first asked by Schrödinger and von Neumann [Goldstein et al., 2010]. We will only scratch the surface of this fundamental subject here. The following discussion is built upon [D'Alessio et al., 2016; Essler and Fagotti, 2016; Gogolin and Eisert, 2016; Linden et al., 2009; Polkovnikov et al., 2011] to which we refer for more details.

By which mechanism does an isolated[27] system equilibrate and thermalise? As the Schrödinger equation is linear and deterministic, a system initially in a pure state remains pure at all times and its global entropy vanishes. Is it still possible to build thermal ensembles following Jaynes' principle of maximum entropy? It turns out that such issues are resolved by considering a partition of the global system, and requiring equilibration and/or thermalisation on a *local* subsystem, the remaining part acting as an effective environment. While it is true that an isolated quantum system initially in a pure state cannot relax towards equilibrium globally, its subsystems can individually reach it. In stark contrast with classical statistical mechanics, individual states can be described by statistical properties. For instance, even when a system is described by a pure state, its subparts can be described by mixed states. The complete knowledge of the behaviour of the full quantum system is not equivalent to the complete knowledge of all its subparts, due to the presence of entanglement. Concerning the role played by ergodicity, once again quantum statistical mechanics differs from its classical counterpart. The ergodic hypothesis lies at the foundation of classical statistical mechanics, and follows as a consequence of the stronger mixing condition, referring to the dense exploration of the phase space and the notion of chaos. But the quantum analogue of the mixing condition is never satisfied [Lebowitz and Penrose, 1973; Penrose, 1979]. Finding a quantum analogue to classical chaos is still a work in progress, although recent experiments suggested connections between regions admitting classical chaotic dynamics and high bipartite entanglement entropy (Fig. 1.25). We elaborate on such points in the following.

Ergodicity – We denote by $\hat{\rho}$ the density matrix of the system, which acts on a complex-valued configurational space (the Hilbert space) and represents quantum states. By definition, the expectation value of an observable $\hat{O}$ in the ensemble of states described by $\hat{\rho}$ at time t is $\langle\hat{O}\rangle_t = \mathrm{Tr}\left[\hat{\rho}_t\hat{O}\right]$. For isolated systems, we know that the density matrix evolves through the Schrödinger-Von Neumann equation $i\partial_t\hat{\rho}_t = [\hat{H},\hat{\rho}_t]$, which implies that if $\hat{H}$ is not explicitly time-dependent, the evolution is unitary $\hat{\rho}_t = \mathrm{e}^{-i\hat{H}t}\hat{\rho}_0\mathrm{e}^{i\hat{H}t}$, and then by decomposing on the eigenstates

$$\langle\hat{O}\rangle_t = \mathrm{Tr}\left[\hat{O}\,\mathrm{e}^{-i\hat{H}t}\hat{\rho}_0\,\mathrm{e}^{i\hat{H}t}\right] = \sum_{n,m}\rho_0^{nm}\,\langle m|\,\hat{O}\,|n\rangle\,\mathrm{e}^{i(E_m-E_n)t}. \tag{1.94}$$

We can now insert this into Eq. (1.21) to obtain

$$\langle\hat{O}\rangle_{\mathrm{eq}} = \sum_{n,m}\rho_0^{nm}\,\langle m|\,\hat{O}\,|n\rangle\left[\lim_{T\to\infty}\frac{1}{T}\int_0^T \mathrm{d}t\,\mathrm{e}^{i(E_m-E_n)t}\right]. \tag{1.95}$$

The term within brackets is non-zero only when $E_m = E_n$, such that

$$\langle\hat{O}\rangle_{\mathrm{eq}} = \mathrm{Tr}\left[\hat{\rho}_{\mathrm{diag}}\hat{O}\right], \tag{1.96}$$

where $\hat{\rho}_{\mathrm{diag}}$ is called the diagonal ensemble and in the absence of degeneracies it has zero off-diagonal elements. At its core, ergodicity is used to make an ensemble average match with a long-time average, and we might be at first satisfied with Eq. (1.96). But this definition of

[27] Isolated systems allow to investigate the fundamental principles of thermalisation. Otherwise, if the system is in contact with a thermal reservoir, how did the reservoir reached thermal equilibrium in the first place?

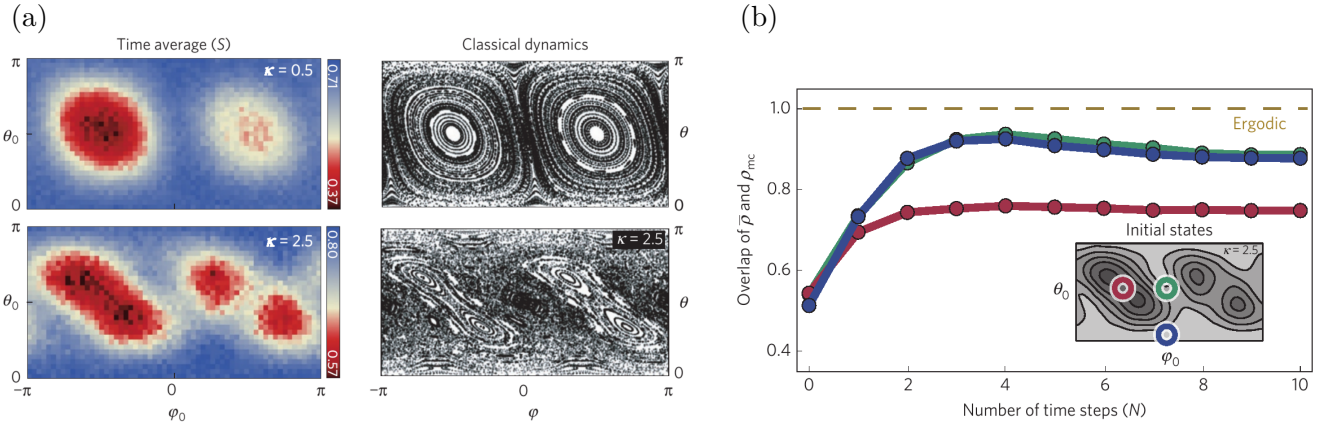

Fig. 1.25 (a) Connection between classical chaotic dynamics and states with high bipartite entanglement entropy, in a three-qubit system with interaction strength κ. (b) When the system starts in a high entanglement entropy state, its dynamics is almost perfectly ergodic, in contrast with an initial low entanglement state. From [Neill et al., 2016].

ergodicity is too naive, as all quantum systems (with non-degenerate energy levels) would be ergodic. The proper definition is the following: a system is ergodic if its equilibrium value can be computed in the microcanonical ensemble. A quantum system having discrete energy levels, the quantum definition of the microcanonical ensemble has to be coarse-grained on an intermediate energy scale (we take a shell of energy $\mathrm{d}E$ between E and $E+\mathrm{d}E$, and we denote as $\Gamma(E)$ the subset of states of the Hilbert space belonging to this shell) which contains $\mathcal{N}$ microstates, namely $\hat{\rho}_{\mathrm{mc}}(E) = \sum_{\alpha\in\Gamma(E)} \frac{1}{\mathcal{N}} |\psi_\alpha\rangle \langle\psi_\alpha|$. Interestingly, the equivalence $\hat{\rho}_{\mathrm{diag}} \sim \hat{\rho}_{\mathrm{mc}}$ does not hold at the level of microstates (as in the classical case) but only at the level of observables. Indeed, assume that for any initial condition in $\Gamma(E)$ written as $|\psi_0\rangle = \sum_{\alpha\in\Gamma(E)} c_\alpha |\psi_\alpha\rangle$, the long time average is given by $\hat{\rho}_{\mathrm{mc}}(E)$. Then, for non-degenerate states, requiring $\hat{\rho}_{\mathrm{mc}} = \hat{\rho}_{\mathrm{diag}}$ at the level of states would imply

$$\forall \alpha \in \Gamma(E), \quad \frac{1}{\mathcal{N}} = |c_\alpha|^2. \tag{1.97}$$

Unfortunately now, this condition is too restrictive to define ergodicity. Instead, the equivalence has to hold at the level of observables, such that

$$\mathrm{Tr}\left[\hat{\rho}_{\mathrm{diag}}\hat{O}\right] = \mathrm{Tr}\left[\hat{\rho}_{\mathrm{mc}}\hat{O}\right]. \tag{1.98}$$

Proving that a system is not ergodic is doable by finding one observable which violates the ensemble equivalence (Fig. 1.25). Proving the equivalence of Eq. (1.98) is not possible for *all* observables. In practical cases, the "relevant" observables can be restricted to local ones to simplify the proof.

Thermalisation– Standard statistical mechanics addresses the behaviour of many-body systems at thermal equilibrium, where an ensemble description can be used to describe the system only in terms of a few variables. One thus forgets about the microscopic details of the systems and only focuses on some relevant macroscopic parameters (for instance, the global magnetisation of a chain instead of the individual spin projection along a given axis). In a thermal ensemble, it is the external world (environment) which acts as a reservoir and fixes the average energy (and possibly the average number of particles) of the system through a Lagrange multiplier $\beta = 1/T$ (and possibly μ/T where μ is the chemical potential). Such Gibbsian ensembles maximise the entropy under the constraints fixed by the environment, and are commonly constructed as such [Jaynes, 1957]. A system is therefore called thermal if its equilibrium expectation values can be described by a Gibbs ensemble. The macroscopic system is then described by mixed states, which consist of statistical ensembles of pure states. In the thermodynamic limit and for short-ranged systems, all Gibbs ensembles are equivalent. Therefore in the quantum regime, ergodicity and thermalisation

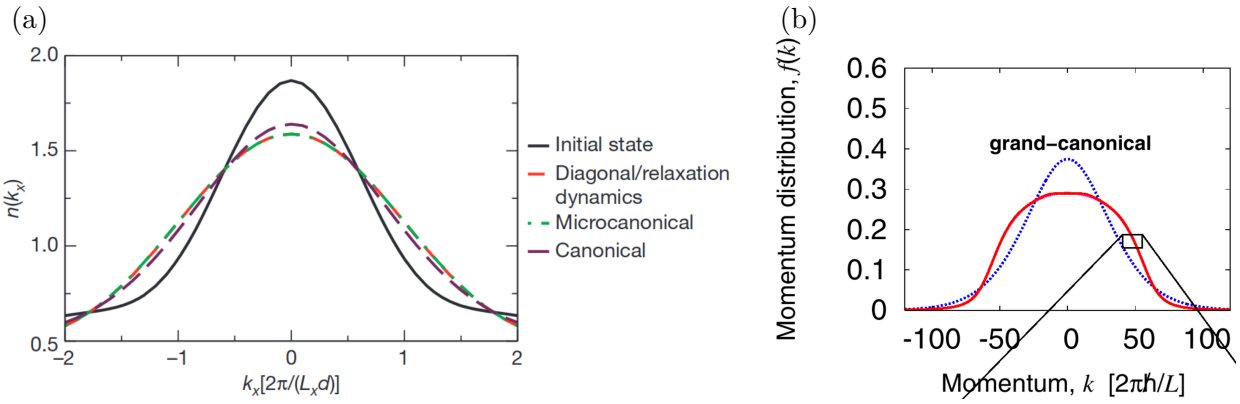

Fig. 1.26 (a) For a generic (non-integrable) system, the initial state (black) eventually relaxes to stationary state described by any usual Gibbs ensemble. The discrepancy between microcanonical and canonical is a finite size effect. (b) The quenched state of the integrable Tonks-Girardeau gas does not relax to a thermal stationary state. Its properties can be described by the GGE, whereas usual Gibbs ensembles (grand canonical) fail. From [Rigol et al., 2008; Rigol et al., 2007].

are often used indistinguishably [Abanin et al., 2019] (for the subtleties, see the introduction of [D'Alessio et al., 2016]).

When a system is driven out of equilibrium and eventually relaxes to a steady state, is it possible to predict whether such state will be thermal or not? The answer turns out to depend whether or not the system is integrable. Integrability in the quantum regime is loosely defined [Caux and Mossel, 2011; Gogolin et al., 2011], here we will focus on the definition implying the existence of an extensive number of conserved and mutually commuting algebraically independent operators. Generic (non integrable) systems, for instance an isolated one which has only its average energy as a conserved quantity, will locally relax to a stationary state described by a Gibbs ensemble [Fig. 1.26(a)]. The fact that independently of the microscopic details, generic systems thermalise was interpreted from the eigenstate thermalisation hypothesis (ETH). Its idea dates back to [Jensen and Shankar, 1985] and was further developed in [Deutsch, 1991] and [Srednicki, 1994]. It can be summarised in the following way: in a sufficiently small energy window and for few body observables, $\langle n|\,\hat{O}\,|n\rangle$ does not vary significantly with the chosen eigenstate $|n\rangle$. Furthermore, the off-diagonal elements $\langle n|\,\hat{O}\,|n'\rangle$ are exponentially small (with the number of degrees of freedom). Mathematically, for a given initial state $|\psi(t)\rangle = \sum_n C_n \mathrm{e}^{-iE_n t}\,|n\rangle$, the expectation value of an observable $\hat{O}$ at time t reads as

$$\langle\hat{O}\rangle_t = \langle\psi(t)|\,\hat{O}\,|\psi(t)\rangle = \sum_n |C_n|^2\,\langle n|\,\hat{O}\,|n\rangle + \sum_{n\neq m} C_n^\star C_m\,\mathrm{e}^{i(E_n-E_m)t}\,\langle n|\,\hat{O}\,|m\rangle \tag{1.99}$$

and after dephasing at long time in the absence of degeneracies the last term vanishes. The ETH assumes that $\langle n|\,\hat{O}\,|n\rangle$ is independent of the eigenstate n within the energy window covered by the initial state, and since $\sum_n |C_n|^2 = 1$, the equilibrium value is given by the thermal averaged independently of the initial state. A comparison with the classical thermalisation is shown in Fig. 1.27. In both situations, the initial state is essentially irrelevant at long times, either because of chaos in a classical system or because all eigenstates are essentially equivalent in the quantum case according to the ETH. Essentially, thermalisation hides the information about the initial state. The unitary evolution cannot erase information, but entanglement simply transports it to subparts of the system such that it cannot be recovered from local measurements [Nandkishore and Huse, 2015].

Not all systems thermalise, and for instance the ETH does not apply to integrable systems. This was verified by the quantum Newton cradle experiment [Kinoshita et al., 2006]: a one dimensional ultracold gas was split using a Bragg pulse sequence is two opposite directions from the center of the trap, then they oscillate, recombine and interact twice for each period. Even

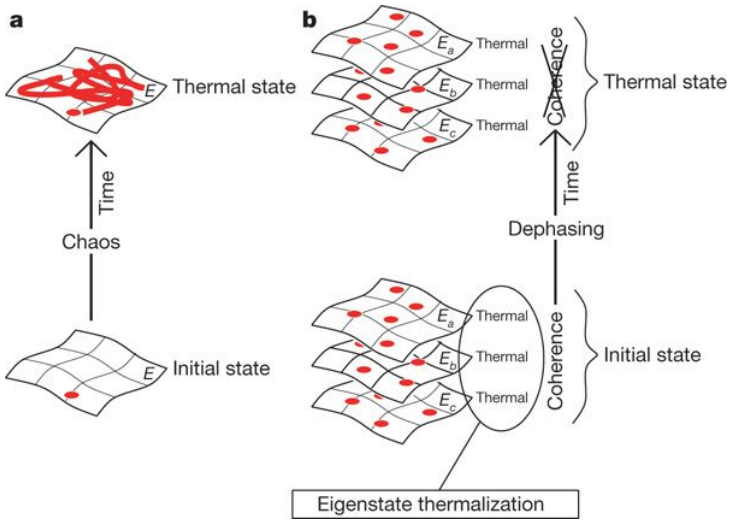

Fig. 1.27 Thermalisation in (a) classical and (b) quantum mechanics. Due to chaos, in classical physics, the system evolves to a completely different state, and looses memory of its initial state. In quantum physics, every eigenstate of the Hamiltonian holds information about the thermal state it relaxes to. This eigenstate thermalisation hypothesis (ETH) holds for generic systems, but not integrable ones. From [Rigol et al., 2008].

after a large number of oscillations, the two clouds did not thermalise. The fact that integrable systems are very peculiar is due to the presence of additional conservation laws and associated local or quasi-local conserved quantities which prevent the system from thermalising by strongly constraining its dynamics. Even though the out-of-equilibrium system eventually relaxes locally towards a steady state, it is generally non-thermal. This can be observed in numerical simulations where Gibbs ensembles and the diagonal ensemble do not yield the same prediction [Fig. 1.26(b)].

To describe the quasi-stationnary state reached at long times by integrable systems, a generalised Gibbs ensemble (GGE)[28] [Rigol et al., 2008; Rigol et al., 2007] can be constructed in the same spirit as Jaynes, by using all local (and quasi-local) conserved quantities as constraints and maximising the entropy with respect to them. The GGE has proven helpful to understand the properties the non-thermal steady state reached at long times in integrable systems that were put out of equilibrium. In practice though, constructing the GGE is difficult, and initial explicit examples focused on free cases or systems that can be mapped to free ones (Tonks-Girardeau gas, quadratic Hamiltonians) where the conservation laws are linearly related to the occupation number. More involved situations have been considered recently ([Vidmar and Rigol, 2016] and references therein).

[28]The literature sometimes refers to generalised thermalisation to indicate thermalisation to a generalised Gibbs ensemble. I will rather call the system non thermal.

1.C Details about the quench action

In this Appendix, we detail the procedure behind the quench action, following [Bucciantini, 2016; Caux, 2016; Caux and Essler, 2013]. The goal is to approximate Eq. (1.25) which is our starting point.

Assumption 1: Weak operators. Local operators generally do not change too much the state they are acting on, so that the matrix elements $\langle n|\,\hat{O}(x)\,|n'\rangle$ are rapidly decaying functions of the difference between the two states $|n\rangle$ and $|n'\rangle$. The only non-zero matrix elements are such that $|n'\rangle \sim |n+e\rangle$, meaning that theses states only differ by a small number of excitations. When this assumption holds, the operator $\hat{O}$ is said weak[29]. Eq. (1.25) then reduces to

$$\langle \hat{O}(x,t)\rangle_{\psi_0} = \sum_n \sum_e \mathrm{e}^{-[S^\star(n,\psi_0)+S(n+e,\psi_0)]}\,\mathrm{e}^{i(E_n-E_{n+e})t}\,\langle n|\,\hat{O}(x)\,|n+e\rangle\,. \tag{1.100}$$

Assumption 2: Averaging procedure. Universal properties hold in the thermodynamic limit, where the expectation values of observables depend on macroscopic variables, but are not sensitive to the microscopic details of the system. For example, microscopic states are specified by the value of each quantum number (say the quasimomentum of each particle); which in the thermodynamic limit, becomes a quasimomentum distribution. During this averaging procedure, some information is lost and to account for the degeneracy at the macroscopic level an entropy has to be defined. The Yang-Yang entropy[30] measures how many microscopic states are represented by the same macroscopic quasimomentum density. We may then recast one sum in Eq. (1.25) as a functional integral over the quasimomentum density $|n\rangle \to |\rho\rangle\,,\quad \sum_n \to \int \mathcal{D}\rho\ \mathrm{e}^{S^{\mathrm{YY}}_\rho}$. Formally, we introduce δE_e and δS_e, the microscopic differences (sub-extensive) in energy and overlap logarithm between the macroscopic states $|\rho\rangle$ and $|\rho+e\rangle$ such that

$$\begin{aligned} &E_\rho - E_{\rho+e} = \delta E_e \\ &S^\star(\rho,\psi_0) + S(\rho+e,\psi_0) = 2\,\mathrm{Re}\,[S(\rho,\psi_0)] + \delta S_e(\rho,\psi_0) \end{aligned} \tag{1.101}$$

and Eq. (1.100) becomes

$$\frac{\langle \hat{O}(x,t)\rangle_{\psi_0}}{\langle\psi_0|\psi_0\rangle} = \frac{\int \mathcal{D}\rho\ \mathrm{e}^{-\left(2\mathrm{Re}[S(\rho,\psi_0)]-S^{\mathrm{YY}}_\rho\right)} \sum_e \mathrm{e}^{-\delta S_e(\rho,\psi_0)-i\delta E_e t}\,\langle\rho|\,\hat{O}(x)\,|\rho+e\rangle}{\int \mathcal{D}\rho\ \mathrm{e}^{-\left(2\,\mathrm{Re}[S(\rho,\psi_0)]-S^{\mathrm{YY}}_\rho\right)}}. \tag{1.102}$$

The important quantity is $S^{\mathrm{QA}}(\rho,\psi_0) = 2\,\mathrm{Re}\,[S(\rho,\psi_0)] - S^{\mathrm{YY}}_\rho$ named the quench action. It is extensive, real-valued and bounded from below (due to state normalisation). It can be interpreted as an equivalent of the free energy for out-of-equilibrium dynamics.

Assumption 3: Saddle point approximation. Eq. (1.102) can be further simplified since the states $|\rho\rangle$ and $|\rho+e\rangle$ differ only by a small shift in quantum numbers. Explicitly, $\delta S_e(\rho,\psi_0)$ and δE_e being sub-extensive (contrary to $\mathrm{Re}\,[S(\rho,\psi_0)]$ and E_ρ), they do not shift the saddle point of the numerator with respect to the one in the denominator. Because the operator $\hat{O}$ is also local, the matrix elements $\langle\rho|\,\hat{O}(x)\,|\rho+e\rangle$ are not exponential in system size, so the saddle point is not shifted either (when this approximation holds, $\hat{O}$ is refered to as a "thermodynamically finite operator" [Caux, 2016]). The term containing the sum over excitations can then be pulled out of the integral, and since the normalization factor cancels with the numerator, one gets

$$\langle \hat{O}(t)\rangle = \frac{1}{2}\sum_e \left(\mathrm{e}^{-i\delta E_e t-\delta S_e}\,\langle\rho_{\mathrm{S}}|\,\hat{O}\,|\rho_{\mathrm{S}}+e\rangle + \mathrm{e}^{i\delta E_e t-\delta S_e^\star}\,\langle\rho_{\mathrm{S}}+e|\,\hat{O}\,|\rho_{\mathrm{S}}\rangle\right), \tag{1.103}$$

[29] $\hat{O}$ is weak if it produces finite Shannon entropy modifications on the state it acts on, and thus has a subextensive operator entropy [Caux, 2016].

[30] In the Lieb-Liniger model, it is defined by $S^{\mathrm{YY}}_\rho = L\int \mathrm{d}k(\rho+\rho_{\mathrm{h}})\ln(\rho+\rho_{\mathrm{h}}) - \rho\ln\rho - \rho_{\mathrm{h}}\ln\rho_{\mathrm{h}}$ where we introduced the quasimomentum density for the holes ρ_{h} and dropped the k-dependency to simplify the notations.

where the saddle point distribution ρ_{S} is determined by

$$\frac{\delta S^{\mathrm{QA}}\left[\rho,\psi_0\right]}{\delta\rho}(\rho_{\mathrm{S}})=0. \tag{1.104}$$

This equation states that in the thermodynamic limit, the expectation value of local operators is determined in a good approximation by the quasimomentum distributions close to the saddle point one (they differ by a small amount of particle-hole excitations). The stationary state reached at $t\to\infty$ can be computed using the stationary phase approximation which reads $\frac{\delta(\delta E_e)}{\delta\rho}=0$ hence

$$\lim_{t\to\infty}\langle\hat{O}(x,t)\rangle=\langle\rho_{\mathrm{S}}|\,\hat{O}(x)\,|\rho_{\mathrm{S}}\rangle\,. \tag{1.105}$$

Only a single state, the fixed point of the quench action, eventually matters to describe the stationary value of local observables. This quench action approach has been used to describe quench dynamics of integrable models such as the transverse-field Ising model [Caux and Essler, 2013] or the Lieb-Liniger model [De Nardis et al., 2014], starting for specific initial states where the overlaps could be evaluated in a simple way. Other examples are discussed in the review [Caux, 2016].

1.D Excitations in the strongly interacting Mott insulator

We will discuss extensively the excitations in the strongly interacting Mott insulator throughout the thesis, here we recall the steps of the derivation presented by [Barmettler et al., 2012]. Deep in the Mott phase, density fluctuations are strongly suppressed, and the local Hilbert space can be truncated to 3 states, noted $|\bar{n}+m\rangle_R$ where $m=-1,0,1$ refers to the particle number modification from the background. Particle and holes from the homogeneous $\bar{n}$ Mott insulator can be written in terms of 2 auxiliary bosonic operators $\hat{b}_{R,\sigma}$ which are linked to the original bosonic operators $\hat{a}_R$ according to

$$\hat{a}_R^\dagger = \sqrt{\bar{n}+1}\,\hat{b}_{R,+}^\dagger + \sqrt{\bar{n}}\,\hat{b}_{R,-}. \tag{1.106}$$

These auxiliary operators locally act on $|\bar{n}\rangle_R$ as

$$\begin{aligned} \hat{b}_{R,\pm}^\dagger |\bar{n}\rangle_R &= |\bar{n}\pm 1\rangle_R\,, \\ \hat{b}_{R,\pm} |\bar{n}\rangle_R &= 0, \end{aligned} \tag{1.107}$$

and they obey bosonic commutation relations. From Eq. (1.106) and (1.107), adding a physical particle can be interpreted by the superposition (with different weights due to the Bose enhancement factor) of a particle and the removal a hole. To preserve the restriction to the local Hilbert space, for instance $\hat{a}_R^\dagger |\bar{n}+1\rangle_R = 0$, the hard core constraint $\left(\hat{b}_{R,\sigma}^\dagger\right)^2 = \left(\hat{b}_{R,\sigma}\right)^2 = 0$ must be enforced and double occupancies eliminated $\hat{n}_{R,+}\hat{n}_{R,-}=0$.

We now make use of a mapping between strongly interacting bosons and spinless fermions due to Jordan and Wigner [Jordan and Wigner, 1928]. It consists in fermionising the auxiliary bosons, to automatically account for the hard core constraint. Up to a phase only relevant for commutation relations, $\hat{b}_{R,\sigma} \sim \hat{c}_{R,\sigma}$. The operator $\hat{c}_+^\dagger$ creates a doublon whereas $\hat{c}_-^\dagger$ creates as a holon. Pauli's exclusion principle ensures that $\left(\hat{c}_{R,\sigma}^\dagger\right)^2 = 0$, while the second constraint $\hat{n}_{R,+}\hat{n}_{R,-}=0$ is *assumed* to hold in order to work with the effective quadratic Hamiltonian in momentum space

$$\hat{H}_{\mathrm{UF}} = \sum_{k,\sigma=\pm} e_\sigma(k)\hat{c}_{k,\sigma}^\dagger\hat{c}_{k,\sigma} + \sum_k Q(k)\left(\hat{c}_{k,+}^\dagger\hat{c}_{-k,-}^\dagger - \hat{c}_{-k,-}\hat{c}_{k,+}\right), \tag{1.108}$$

with

$$\begin{aligned} e_+(k) &= -2J(\bar{n}+1)\cos k + \tfrac{U}{2}, \\ e_-(k) &= -2J\bar{n}\cos k + \tfrac{U}{2}, \\ Q(k) &= 2iJ\sqrt{\bar{n}(\bar{n}+1)}\sin k. \end{aligned} \tag{1.109}$$

Being quadratic, the effective Hamiltonian can be diagonalised by a Bogoliubov transformation. The elementary excitations of the effective model are Bogoliubov quasiparticles which are linear combinations of the doublons and holons

$$\hat{\gamma}_{k,\pm}^\dagger = u(k)\hat{c}_{k,\pm}^\dagger \pm v(k)\hat{c}_{-k,\mp} \tag{1.110}$$

with

$$\begin{aligned} u(k) &= u(-k) = u^\star(-k) = 1 + O\left(\tfrac{J^2}{U^2}\right) \\ v(k) &= -v(-k) = -v^\star(k) = 2i\tfrac{J}{U}\sqrt{\bar{n}(\bar{n}+1)}\sin k + O\left(\tfrac{J^3}{U^3}\right). \end{aligned} \tag{1.111}$$

Because in the hard core limit we have $\hat{\gamma}_{k,\pm}^\dagger = \hat{c}_{k,\pm}^\dagger$ (pure doublons and holons), we will refer to the quasiparticle created by the operator $\hat{\gamma}_{k,+}^\dagger$ as a d-Bogoliubon and the one created by the operator

$\hat{\gamma}^\dagger_{k,-}$ as a h-Bogoliubon. In terms of these Bogoliubons, the Hamiltonian becomes a simple sum of quantum harmonic oscillators

$$\hat{H}_{\mathrm{UF}} = \sum_{k,\sigma=\pm} E_\sigma(k)\hat{\gamma}^\dagger_{k,\sigma}\hat{\gamma}_{k,\sigma} \qquad \text{with} \quad E_\pm(k) = \mp J\cos k + \omega(k). \tag{1.112}$$

The quantity $2\omega(k) = U - 2J(2\bar{n}+1)\cos k + O\left(\frac{J^2}{U^2}\right)$ represents the energy of a *pair* of two distinct quasiparticles with opposite momenta. Specifically for $\bar{n} = 1$, the excitation spectrum is parametrised by

$$E_\pm(k) = \mp J\cos k + \frac{1}{2}\sqrt{(U - 6J\cos k)^2 + 32J^2\sin^2 k}. \tag{1.113}$$

There are thus two branches (modes), in the strongly interacting regime and both of them are gapped. We emphasise that strictly speaking only in the hard core regime (such that $u(k) = 1$ and $v(k) = 0$) these elementary excitations coincide with the doublons and holons. In general, the elementary excitations are to be understood as superpositions of doublons and holons with different weights.

1.E Density-phase representation of the field operator

We briefly recall how the field operator should be expanded in one dimension in comparison to the three dimensional case, following [Natu and Mueller, 2013a; Ristivojevic and Matveev, 2016]. Generally speaking, a two-body contact Hamiltonian can be cast into the following form

$$\hat{H} = \frac{\hbar^2}{2m}\int \mathrm{d}\boldsymbol{x}\,(\boldsymbol{\nabla}\hat{\Psi}^\dagger)(\boldsymbol{\nabla}\hat{\Psi}) + \frac{g}{2}\int \mathrm{d}\boldsymbol{x}\,(\hat{\Psi}^\dagger\hat{\Psi})^2, \tag{1.114}$$

and is expected to give an approximation to describe bosonic systems at low temperatures. To recover the Lieb-Liniger model[31] one should expand the field operator onto Bloch functions (plane waves). Here we want to discuss the weakly interacting regime, called the Bogoliubov regime, where $g \ll \hbar^2 n/m$ with n the mean density[32]. To approximate the Hamiltonian (1.114) in the weakly interacting regime, in 3D one expands $\hat{\Psi}(\boldsymbol{x}) = \sum_{\boldsymbol{k}} \mathrm{e}^{-i\boldsymbol{k}\boldsymbol{x}}\hat{a}_{\boldsymbol{k}}$ and separates the density of bosons into a condensed component $n_0 = \langle a_{k=0}\rangle^2$ and a non-condensed part characterised by

$$\hat{a}_{k\neq 0} = u_k\hat{b}_k + v_k^\star\hat{b}_{-k}^\dagger, \tag{1.115}$$

where $\hat{b}_k^{(\dagger)}$ are the annihilation (creation) operator of a Bogoliubon and u_k and v_k obey the Bogoliubov-de Gennes equations. Their expression can be found by expanding up to quadratic order the Hamiltonian in terms of Bogoliubons and then diagonalising it by cancelling the cross-terms involving $\hat{b}^{(\dagger)\,2}$. The problem in one dimension is that the assumption underlying this development, namely that the number of Bogoliubons is small compared to the condensed number of atoms, breaks down. Indeed a quasi-condensate in 1D is characterised by small density fluctuations but a divergence of phase fluctuations which prevent long-range order.

The solution is to formally write the field operator in terms of a density and a phase $\hat{\Psi} = \mathrm{e}^{i\hat{\phi}}\sqrt{\hat{\rho}}$ with $\left[\hat{\rho}(x), \hat{\phi}(y)\right] = -i\delta(x-y)$ (such that the field operator obeys bosonic commutation relation). If we only care about the low energy physics, where the phase gradient $\boldsymbol{\nabla}\hat{\phi}$ and the density variation from the mean value $\delta\hat{\rho} = \hat{\rho} - \rho_0$ remain small, then an expansion to lowest order in the operators allows to rewrite the Hamiltonian (1.114) as

$$\hat{H} = \frac{\hbar^2}{2m}\int \mathrm{d}\boldsymbol{x}\left(\rho_0(\boldsymbol{\nabla}\hat{\phi})^2 + \frac{(\boldsymbol{\nabla}\hat{\rho})^2}{4\rho_0}\right) + \frac{g}{2}\int \mathrm{d}\boldsymbol{x}\,\hat{\rho}^2. \tag{1.116}$$

We recognise in the first term (kinetic energy) a quantum harmonic oscillator, and in fact what we just discussed is nothing but a hydrodynamic Luttinger liquid representation (bosonisation) of the Hamiltonian. If the last term representing the interaction energy is negligible (Bogoliubov approximation), the excitations can be understood as Bogoliubons (which are the modes of the previously discussed harmonic oscillator, emerging from phase and density fluctuations of the field operator). These modes can be formally represented as

$$\frac{\delta\hat{\rho}_k}{2\sqrt{\rho_0}} + i\sqrt{\rho_0}\,\hat{\phi}_k = u_k\hat{b}_k + v_k^\star\hat{b}_{-k}^\dagger, \tag{1.117}$$

and from there we can recover the common expression (1.115) in 3D.

Substituting Eq. (1.117) into the Hamiltonian (1.116) and retaining only the quadratic terms in $\hat{b}^{(\dagger)}$, the usual 3D Bogoliubov Hamiltonian is recovered (up to the substitution $\rho_0 \to n$). Therefore the dispersion relation is of the form $E_k = \sqrt{\varepsilon_k(\varepsilon_k + 2gn)}$ with $\varepsilon = (\hbar k)^2/2m$ on the continuum and $\varepsilon_k = 4J\sin(k/2)^2$ together with $gn = U\bar{n}$ on a lattice.

[31] For Bose-Hubbard, one expands the field operator onto the Wannier functions and restrict to the lowest-band.
[32] On a lattice, this condition reads as $U/(2J\bar{n}) \ll 1$ (see Sec. 2.2.2 for details).

2 Correlation spreading

Before possibly reaching an equilibrium steady state, a system brought out of equilibrium undergoes some relaxation dynamics. Such dynamics can be understood from a quasiparticle picture introduced by [Calabrese and Cardy, 2006] which explains how information and correlations are transferred throughout the system. This picture allows to interpret the bounds for the speed at which information [Lieb and Robinson, 1972] or correlations [Bravyi et al., 2006] propagate in short-ranged one dimensional lattice models. But more importantly, this picture gives a value to the correlation spreading governed by the maximum velocity of the elementary excitations (quasiparticles) of the microscopic underlying model.

We begin this chapter by discussing early investigations and following questions that emerged from them soon after the numerical and experimental verifications of the quasiparticle picture. These studies first demonstrated the ballistic propagation of correlations, as well as the oscillatory behaviour of the correlation functions inside the causality cone. Some questions emerged about the quantitative value for the correlation spreading velocity, and led [Cevolani et al., 2018] to propose an extended quasiparticle picture which resolved observed inconsistencies and provided a complete physical picture for the correlation spreading (Sec. 2.1). We then discuss the first observation of a generic twofold structure in numerically exact t-MPS simulations for various phases and models and for different observables (Sec. 2.2). The latter section closely follows our publication [Despres et al., 2019], which validates the extended quasiparticle picture also beyond the mean-field regime. We finally discuss related works and perspectives, particularly with regard to long-range models which have received increased attention recently.

2.1 A short review of correlation spreading in short-ranged lattice models

In the early years when quantum simulators became accessible, measurements of the correlation spreading were conducted, both experimentally and numerically.

2.1.1 Early studies of the out-of-equilibrium dynamics

A detailed preliminary study of correlation spreading was performed by [Läuchli and Kollath, 2008] on the Bose-Hubbard chain using both exact diagonalisation (ED) with $L = 14$ sites and the density-matrix renormalisation group (DMRG) with $L = 32$ sites. The dynamics of the density-density correlation function was studied, often after rather *strong* quenches (in the sense that a quantum phase transition is crossed during the quench) for instance from $(U/J)_\mathrm{i} = 2$ (SF) to $(U/J)_\mathrm{f} = 40$ (MI) as shown in Fig. 2.1(a). The expected light-cone like structure is clearly visible, and its speed may be extracted from a fit and compared to known analytical results. Interestingly, the extracted velocities appear consistent with microscopic well-established results, depending on the regime [Fig. 2.1(b)]. In the weakly interacting regime $\gamma = U/(2J\bar{n}) \lesssim 2$, a comparison with the sound velocity was made with (i) a mapping to the continuum limit of the Lieb-Liniger model [Lieb, 1963]; in the strongly interacting MI a comparison was used with (ii) the dispersion relation of a particle-hole excitation computed using a slave-particle approach from [Huber et al., 2007]; and finally in the strongly interacting SF at low filling the velocity can be compared to (iii) the sound velocity of an effective fermionic model with attractive correlated hopping [Cazalilla, 2003,

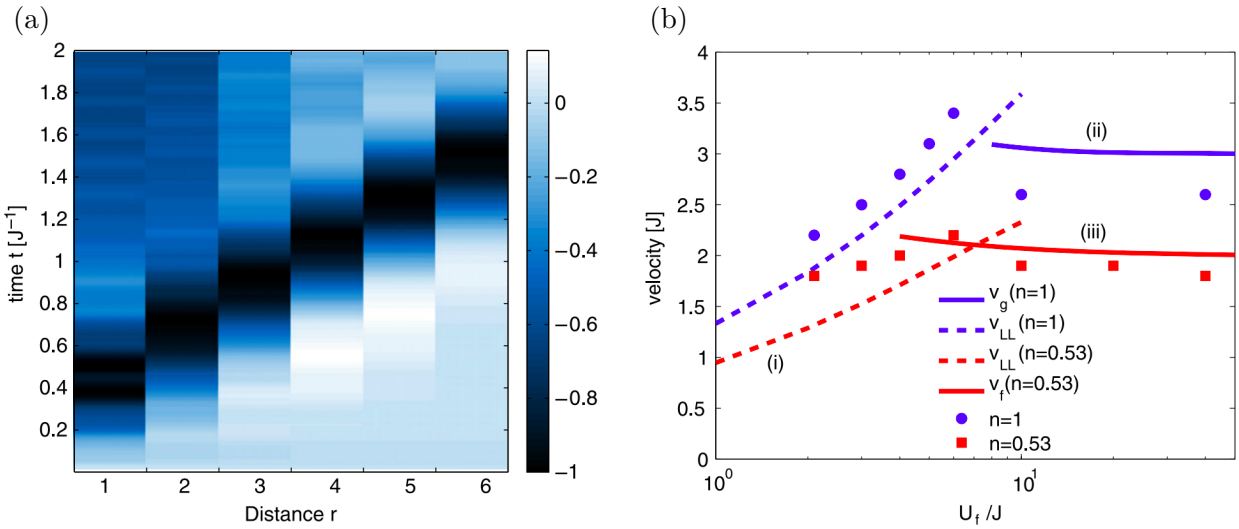

Fig. 2.1 (a) Dynamics of the density-density correlation function, after a quench from $(U/J)_\mathrm{i} = 2$ (SF) to $(U/J)_\mathrm{f} = 40$ (MI) at fixed $\bar{n} = 1$, computed using ED with $L = 14$. (b) The velocities extracted from the numerical data by a linear fit of the causal-cone front (points for unit filling, squares close to half filling) are compared to different theoretical predictions given in Eq. (2.1). The velocities given here correspond to *half* of the signal propagation, in order to facilitate the comparison with $v_\mathrm{g}^\star = \max_k \partial_k E_k$ from the quasiparticle picture. The initial state is always $(U/J)_\mathrm{i} = 2$. From [Läuchli and Kollath, 2008].

2004]. All respective expressions are summarised below

$$\begin{aligned} &\text{(i)} \quad v_\mathrm{s} = 2J\bar{n}\sqrt{\gamma}\sqrt{1-\sqrt{\gamma}/2\pi} \quad \text{with} \quad \gamma = U/(2J\bar{n}), \\ &\text{(ii)} \quad v_\mathrm{g} = \partial_k \left[\tfrac{1}{2}\sqrt{U^2 - 4J(2\bar{n}+1)U\cos k + 4J^2\cos^2 k}\right], \\ &\text{(iii)} \quad v_\mathrm{f} = 2J\sin(\pi\bar{n})\left[1 - 8\bar{n}J\cos(\pi\bar{n})/U\right]. \end{aligned} \tag{2.1}$$

This comparison suggested that the quasiparticle interpretation was correct also beyond the critical region described by the conformal field theory. We will use again the models described above and comment further on the microscopic velocities present in Eq. (2.1) in Sec. 2.2.

[Manmana et al., 2009] investigated the correlation spreading using the DMRG algorithm on a chain of spinless fermions at half-filling on larger systems (up to $L = 50$ sites) with Hamiltonian

$$\hat{H} = -J\sum_R \left(\hat{c}_{R+1}^\dagger \hat{c}_R + \text{h.c.}\right) + V\hat{n}_R\hat{n}_{R+1}. \tag{2.2}$$

A phase transition at $(V/J)_\mathrm{c} = 2$ separates a Luttinger liquid (LL) regime for $V/J < 2$ from a charge density-wave (CDW) insulating one for $V/J > 2$. In the Luttinger phase, the model can be mapped to the XXZ chain using a Jordan-Wigner transformation. The latter model is integrable and exactly solvable using the Bethe ansatz, and enables a quantitative comparison with the velocity of the correlation spreading. The time-evolution of the density-density correlation function after a quench starting from $(V/J)_\mathrm{i} = 10$ displays a light-cone pattern represented in Fig. 2.2(a). By extracting the light-cone velocity from the local maxima of the equal-time density correlation function [Fig. 2.2(b)], the propagation is found to be consistently smaller than the maximal possible velocity predicted by the quasiparticle picture. Although the Calabrese-Cardy picture qualitatively agrees with the observations, the authors note that "the propagation does not take place with the maximal possible velocity [..., and] there appear to be small corrections to a horizon velocity obtained from the exactly known velocity of charge excitations". This reduced apparent velocity was attributed to the contribution of lower-velocity excitations created by the strong quench which excites high-energy modes.

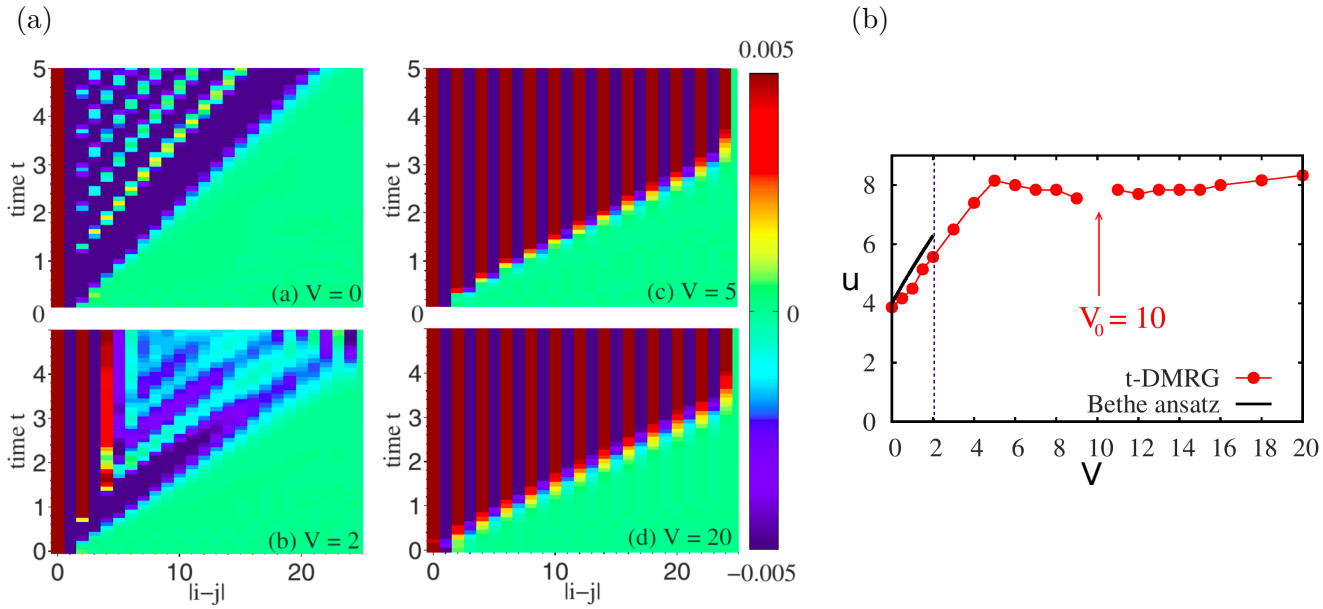

Fig. 2.2 (a) Dynamics of the density-density correlation function, after a quench from $(V/J)_\mathrm{i} = 10$ (CDW) to $(V/J)_\mathrm{f} = 0$ (free fermions), 2 (critical) or 5 and 20 (CDW), computed using DMRG with $L = 50$ sites. (b) Extracted velocity u according to the final interaction value V and comparison with the Bethe ansatz exact result in the LL regime. Adapted from [Manmana et al., 2009].

Let us now come back to the Bose-Hubbard model. [Läuchli and Kollath, 2008] suggested that "the value of the observed signal velocity might depend on the initial state", in contrast to the Calabrese-Cardy prediction. To close the debate, it was necessary to perform weak quenches and estimate the uncertainties on the fitted causal-cone velocity, in particular due to finite size effects. This was undertaken by [Carleo et al., 2014], who investigated in particular the superfluid phase at unit filling using a time-dependent variational Monte Carlo (t-VMC) algorithm. They concluded that after weak quenches which do not abruptly cross a phase transition, the propagation velocity was independent of the initial state. They also noted that the correlation propagating is always clearly supersonic throughout the SF phase [Fig. 2.3(b)], even for weak quenches for instance from $(U/J)_\mathrm{i} = 1$ to $(U/J)_\mathrm{f} = 1.1$. The elementary excitations at low-energy which propagate the correlations do not seem to be phononic modes (or at least not with the velocity expected from Luttinger liquid theory). However, by extracting the propagation speed from the local maxima of the space-time correlation pattern $v_\mathrm{inst}(R) = \frac{2}{t^\star(R+1)-t^\star(R-1)}$ [reaching a constant value after a few time steps, see inset in Fig. 2.3(a)], the authors conclude that the maximum velocity of the excitations $v_\mathrm{g}^\star$ is not reached. This suggested that the conformal field theory results used to demonstrate the quasiparticle picture may apply only close to the critical point, where all the characteristic velocities match [Fig. 2.3(b)]. This apparent mismatch between the extracted velocity and the maximum group velocity expected from the Lieb-Robinson bound is explained below in Sec. 2.1.2.

The first experimental verification of light-cone like spreading was performed by [Cheneau et al., 2012] on the Bose-Hubbard chain mentioned previously [Fig. 1.14(b)]. They explored the MI regime, with quenches from $(U/J)_\mathrm{i} = 40$ to $(U/J)_\mathrm{f} = 9, 7$ and 5 at $\bar{n} = 1$. The velocities were extracted from the local maxima close to the correlation edge [Fig. 2.4(a)]. In this case, the fitted velocities (Fig. 2.4(b), blue points) are in fair agreement with the Calabrese-Cardy prediction within experimental uncertainties (green area). Note, however, that the data were taken in the MI regime for values of $(U/J)_\mathrm{f}$ such that the characteristic velocities (of the local maxima close to the edge and of the edge itself) are almost indistinguishable within experimental accuracy. This last point will be important in the following. As a final point on this introductory part, we also mention

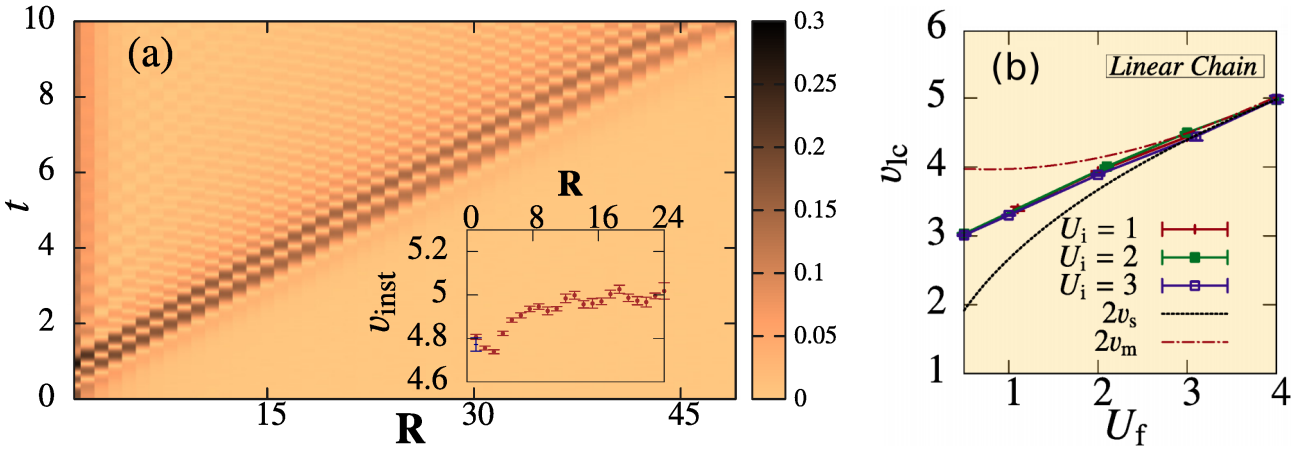

Fig. 2.3 (a) Light-cone like dynamics of the density-density correlation $\langle \hat{n}(R,t)\hat{n}(0,t)\rangle - \langle \hat{n}(R,0)\hat{n}(0,0)\rangle$ in the Bose-Hubbard chain after a quench at unit filling from $(U/J)_{\mathrm{i}} = 2$ to $(U/J)_{\mathrm{i}} = 4$. (b) Extracted velocity for different final interaction values $(U/J)_{\mathrm{f}}$, compared with twice the sound velocity $2v_{\mathrm{s}}$ and twice the maximum excitation velocity (group velocity), here noted $2v_{\mathrm{m}}$. Adapted from [Carleo et al., 2014].

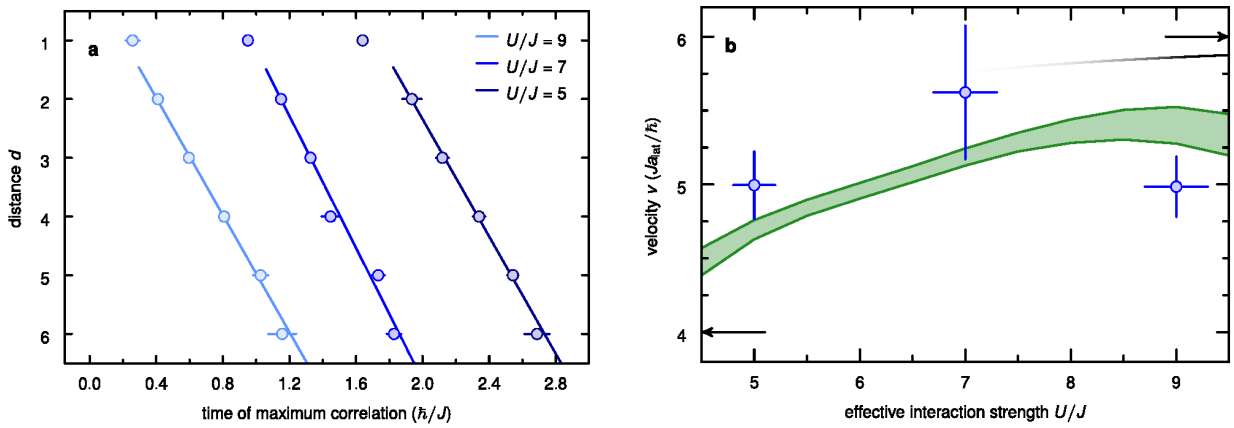

Fig. 2.4 Experimental observation of light-cone-like spreading of correlations on the Bose-Hubbard chain. (a) Velocities extracted from the local maxima. (b) Comparison between the experimental values and the numerical simulation prediction (shaded green). From [Cheneau et al., 2012].

that light-cone spreading of correlation has also been studied experimentally on spin chain models (simulated using ultracold bosons) by [Fukuhara, Schauß, et al., 2013]. Specifically, the isotropic Heisenberg chain was modelled. They validated the Calabrese-Cardy picture by observing free magnons propagating at the maximal speed $J_{\mathrm{ex}}a/\hbar$ consistent with the prediction $v_{\mathrm{g}}^{\star} = \max_k \partial_k E_k$ from the exact Bethe ansatz dispersion relation of the excitations $E_k = J_{\mathrm{ex}}(1-\cos k)$ with J_{ex} the super-exchange coupling.

2.1.2 Generalisation of the quasiparticle picture

A generic form for the correlation spreading. The propagation velocities for the correlation spreading were addressed in a systematic way by [Cevolani et al., 2018], who pointed out that the propagation velocity of the local maxima close to the edge differs in general from the propagation velocity of the edge of the causal-cone itself. Building on a series of closely related works using mean-field arguments [Cevolani et al., 2015, 2016], they proposed that correlators after a global quantum quench in a translation invariant system can be cast into the following generic

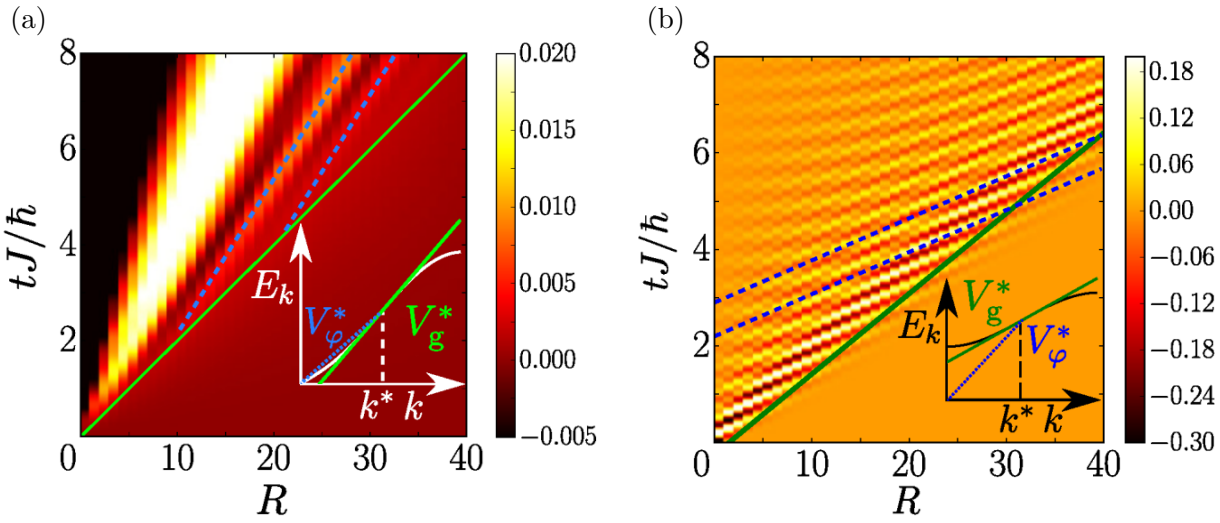

Fig. 2.5 Computation of the analytical expression (2.3) using the expression for $\mathcal{F}(k)$ derived for (a) a quench in the mean-field SF from $(U\bar{n}/J)_\mathrm{i} = 1$ to $(U\bar{n}/J)_\mathrm{f} = 0.5$ and (b) a quench in the strongly interacting MI from $(U/J)_\mathrm{i} = \infty$ to $(U/J)_\mathrm{f} = 18$ at $\bar{n} = 1$ where the observable is the one-body correlator. The insets illustrate how the phase velocity E_k/k and the group velocity $\partial_k E_k$ are determined from the excitation spectrum E_k, at $k^\star$ where $V_\mathrm{g}(k)$. From [Cevolani et al., 2018].

form (in arbitrary dimensions D)

$$G(\boldsymbol{R}, t) = g(\boldsymbol{R}) - \int_{\mathrm{BZ}} \frac{\mathrm{d}\boldsymbol{k}}{(2\pi)^D} \mathcal{F}(\boldsymbol{k}) \frac{\mathrm{e}^{i(\boldsymbol{k}\cdot\boldsymbol{R} + 2E^\mathrm{f}_{\boldsymbol{k}} t)} + \mathrm{e}^{i(\boldsymbol{k}\cdot\boldsymbol{R} - 2E^\mathrm{f}_{\boldsymbol{k}} t)}}{2}. \tag{2.3}$$

Equation (2.3) represents the propagation of two waves with energy $E^\mathrm{f}_{\boldsymbol{k}}$ (which only depend on the final state reached by the quench) propagating in opposite directions with a given momentum dependent weight $\mathcal{F}(\boldsymbol{k})$. This function $\mathcal{F}(\boldsymbol{k})$ also depends on the specific observable under consideration and on the initial pre-quench state, and thus hides the complexity of the non-generic behaviour of the dynamics. In specific regimes and for some observables, the function $\mathcal{F}(\boldsymbol{k})$ can be expressed analytically and gives access to the out-of-equilibrium dynamics by computing Eq. (2.3). On the Bose-Hubbard chain, for a quench in the SF phase from $(U\bar{n}/J)_\mathrm{i} = 1$ to $(U\bar{n}/J)_\mathrm{f} = 0.5$ and choosing the one-body correlator as an observable, they obtained the space-time pattern showed in Fig. 2.5(a). For a quench in the MI phase at unit filling from $(U/J)_\mathrm{i} = \infty$ to $(U/J)_\mathrm{f} = 18$ they obtained the one displayed in Fig. 2.5(b) with the same observable (we refer to the publication for the expressions of $\mathcal{F}(k)$ in both cases). We stress that these results rely on the evaluation of Eq. (2.3), where both $\mathcal{F}(k)$ and E^f_k are determined analytically from approximate methods (mean-field theory or a strong coupling expansion). We observe in Fig. 2.5 a complex spike-like pattern, which can be decomposed into two main parts. A ballistic causal cone (solid green line) is visible, outside which correlations decay exponentially, as expected from the Calabrese-Cardy picture. More interestingly, a second feature appears where local maxima start to propagate ballistically from the cone edge (dashed blue lines). For each feature, a velocity can be extracted from a linear fit, and its value is given by the inverse of the slope in units of $Ja/\hbar$. Clearly, two distinct velocities emerge, one for the local maxima V_m and one for the correlation edge V_CE. [Cevolani et al., 2018] showed that the velocity of the local maxima can be related to the phase velocity of the quasiparticles $V_\varphi(k) = E_k/k$, which is a sole property of the dispersion relation of the elementary excitations E_k. In general, if the dispersion relation E_k is not linear (that is if it is dispersive), $V_\varphi(k)$ differs from the group velocity $V_\mathrm{g}(k) = \partial_k E_k$ which characterises the physical propagation of information in a given medium (see Appendix 2.A for a brief reminder about the notion of group and phase velocities in a general context). We will show below that only a single quasimomentum, noted $k^\star$, is relevant to understand this twofold pattern, and it corresponds to the maximum of the

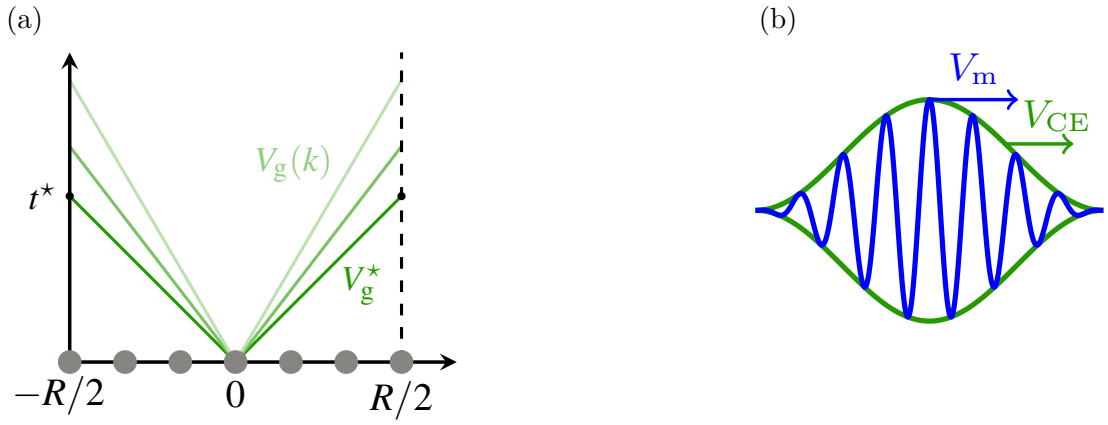

Fig. 2.6 Quasiparticle interpretation for the correlation spreading. The correlation edge propagates at the velocity V_{CE}, related to the group velocity of the fastest excitations by $V_{CE} = 2V_g^\star$. Local maxima around the edge propagate at V_m related to the phase velocity of the fastest quasiparticles $V_m = 2V_\varphi^\star$. See also the insets in Fig. 2.5. Adapted from [Despres et al., 2019].

group velocity accessible to the system, namely $k^\star = \max_k V_g(k)$. The fact that $V_g(k^\star) \neq V_m(k^\star)$ is responsible for the twofold structure. In the mean-field SF regime [Fig. 2.5(a)], the phase velocity is smaller than the group velocity (see the slopes in the inset). On the contrary, in the strongly interacting MI phase [Fig. 2.5(b)], the phase velocity is larger than the group velocity (see again the slopes in the inset). We stress that the latter case does not contradict the Calabrese-Cardy interpretation of the Lieb-Robinson bound since physical information is not transported by the phase velocity.

To understand the patterns of Fig. 2.5, it is fruitful to approximate Eq. (2.3) in the infinite time and space limit at fixed ratio R/t by making use of the saddle point approximation. In one dimension, the stationary phase is given by the solution of $\partial_k(kR \mp 2E_k t) = R \mp 2\partial_k E_k t = 0$. It defines the group velocity as $V_g(k) = \partial_k E_k|_k = \pm R/2t$. Assuming $V_g(k)$ is bounded by $V_g^\star = V_g(k^\star)$, and defining $t^\star = R/(2V_g^\star)$ we see that for $t < t^\star$ there is no stationary phase such that $G(R,t)$ vanishes. The time $t^\star$, referred to as the activation time, corresponds to the minimal time required for the correlations to spread between two points distant of R. We will show below that it can be interpreted from the generalised quasiparticle picture as the arrival time at the points $\pm R/2$ of a wave packet carrying correlations which originated from the middle point 0. On the contrary, for $t > t^\star$ there is a solution to the stationary phase and the correlation function in Eq. (2.3) may be simplified in 1D as

$$G(R,t) \propto \frac{\mathcal{F}(k^\star)}{(|\,\partial_k^2 E_k|_{k=k^\star}|t)^{1/2}} \cos\left(k^\star R - 2E_{k^\star} t + \frac{\pi}{4}\right), \tag{2.4}$$

(see Appendix 2.A for the detailed derivation).

Physical picture. The following intuitive physical representation can be built from Eq. (2.4). Immediately after the global quench, a bunch of quasiparticle excitations are emitted from all points in the system in pairs, where the pairs have different velocities but the two particles forming a pair have opposite velocity [Fig. 2.6(a), where for clarity we only represent a single emission from the point 0 but it should be understood that the same applies to all points]. All pairs are emitted with different velocities (different green colors), but only the fastest ones build a correlation over a distance R at a time $t^\star$ (dark green). It corresponds to the first pair which induces a correlation between two points R and R', was emitted from the central point $(R+R')/2$ and travelled with the fastest group velocity. The other quasiparticles propagate slower and did not yet build any correlation. Taking into account all pairs emitted from all points, the signal close to the edge results

from the propagation of a wave packet [Fig. 2.6(b)]. Since all quasiparticle pairs were initially emitted from spatially distinct points, their interferences lead through dephasing to a blurring of the inside of the cone (far from the edge). Close to the correlation edge, local maxima propagate at a speed $V_{\mathrm{m}} = 2V_{\varphi}^{\star} = 2E_{k^\star}/k^\star$ [Eq. (2.4)] related to the phase velocity of the fastest quasiparticles and the edge of the cone itself propagates at a velocity $V_{\mathrm{CE}} = 2V_{\mathrm{g}}^{\star} = 2\,\partial_k E_k|_{k=k^\star}$ [Eq. (2.4)] related to the group velocity of the fastest quasiparticles. The correlation at a distance R and a time t is thus built from a coherent superposition of the contributions of the various quasiparticles. In the vicinity of the CE, only the fastest quasiparticles, *i.e.* those with a quasimomentum k close to $k^\star$ contribute. It creates a sine-like signal at the driving spatial frequency $k^\star$, whose extrema move at twice the phase velocity. The dispersion around $k^\star$ then modulates the sine-like signal by an envelope moving at the CE velocity. This behaviour is reminiscent of the propagation of a coherent wave packet in a dispersive medium, among which the propagation of water waves in deep water mentioned in Appendix 2.A.

This generalised quasiparticle picture shed new light on the early results discussed in Sec. 2.1.1. In general, the local maxima are more visible than the edge, and the former are the ones measured. However, when the underlying excitations of the many-body system have a non-linear dispersion relation, the phase velocity and the group velocity differ, and so do the velocities of the local maxima and of the edge. The study of [Carleo et al., 2014] where large system sizes have been investigated allows for a quantitative comparison, and it turns out that the fitted velocities are in excellent agreement with $2V_{\varphi}(k^\star)$ but differ significantly from $2V_{\mathrm{g}}(k^\star)$. Far from the transition, the two velocities are sufficiently different to make the distinction clear [Fig. 2.3(b)]. In the other early numerical investigations, the quantitative comparison is not possible because of small system sizes leading to finite size effects and consequently important uncertainties, especially considering that the investigated regimes often correspond to the ones where both velocities are approximately equal. The strongly correlated MI was investigated by [Läuchli and Kollath, 2008], but the combination of strong quenches and/or small system sizes probably explains why the twofold structure was not observed. This is also the case for the experimental work of [Cheneau et al., 2012] on the Bose-Hubbard chain, since the values of $(U/J)_{\mathrm{f}}$ are close to the transition where the velocities are almost identical.

In conclusion, a complex dynamics, characterised by two characteristic velocities can be observed for the correlation spreading in lattice models. The velocity of the edge and of the local maxima are related to properties of the elementary excitations through the group and phase velocity. This effect was not present in the original picture of Calabrese and Cardy since they restricted to a linear excitation spectrum where dispersion is absent and thus both velocities are identical.

Range of applicability. Is the generic form discussed previously and its associated physical picture general, or are there cases where they do not apply?

The scope and wide range of applicability of the generic form (2.3) was unveiled throughout a series of works [Cevolani et al., 2015, 2016; Cevolani et al., 2018], but had been demonstrated explicitly on specific models and phases before. This includes the short-ranged Bose-Hubbard model both in the mean-field SF where $\gamma = U/(2J\bar{n}) \ll 1$ [Natu and Mueller, 2013b] and in the strongly interacting MI where $U > 4J(\bar{n}+1)$ [Barmettler et al., 2012]. It can also be extended to long-range models such as a fermionic hopping model [Buyskikh et al., 2016], various spin models such as the XY and the XXZ models also in 2D [Frérot et al., 2017, 2018] and the transverse field Ising chain [Buyskikh et al., 2016; Hauke and Tagliacozzo, 2013] (at least in the strongly polarised phases where linear spin-wave results hold). This extension requires a little care, because the group velocity may be unbounded, however the generic form Eq. (2.3) can still be used (except in the instantaneous regime where E_k^{f} is unbounded). The previous results also apply to short-ranged spin chains, which can be considered as the limit of their long-range equivalent when the range of interactions $1/|R|^\alpha$ decays to zero with $\alpha > D+1$. Similar results have also been obtained on spin

lattices of various geometries in their strongly polarised phases [Menu and Roscilde, 2018]. Last but not least, the generic form also applies to the exactly solvable model of a chain of coupled quantum harmonic oscillators, where the exact equal-time two-point correlation function can be cast in the form [Calabrese and Cardy, 2006]

$$\langle\phi(R,t)\phi(0,t)\rangle - \langle\phi(R,0)\phi(0,0)\rangle = \int_{\mathrm{BZ}} \mathrm{d}^d k\, \mathcal{F}(k)\, \mathrm{e}^{ikR} \left[1 - \cos\left(2E_k^{\mathrm{f}} t\right)\right], \tag{2.5}$$

with explicitly $\mathcal{F}(k) = (E_k^{\mathrm{i}\,2} - E_k^{\mathrm{f}\,2})/(E_k^{\mathrm{i}} E_k^{\mathrm{f}\,2})$ and $E_k^{\mathrm{i,f}}$ the initial or final single-particle dispersion relation respectively.

Even if the range of applicability of the generic form is very large, it is not completely general. First, the form applies only for translation invariant initial states and systems, therefore for global quenches in clean systems. We will explain this from a more fundamental point of view when we will discuss quench spectroscopy in Chap. 3. Second, we will also show in Sec. 2.2.3 that the generic form does not apply to the density-density correlation function $G_2(R,t)$ in the strongly interacting MI phase of the Bose-Hubbard chain. This is a very peculiar situation where the twofold structure reduces to a single one. Third, the excitation spectrum of the elementary excitations should have a well-defined excitation branch, namely at a given value of k should correspond a single value of E_k. We will explicitly show a counterexample in the strongly interacting SF phase of the Bose-Hubbard chain where the excitation spectrum rather takes the form of a continuum, and therefore the generic form cannot be used to understand the dynamical properties (Sec. 2.2.4). We will also come back to this specific example in Sec. 3.2.2.2.

2.2 Observation of a generic twofold structure

One of the aims of the following section is to validate the previously discussed generalised quasiparticle picture which explains the coexistence of several signals related to the non-linearity of the quasiparticle excitation spectrum and which are governed by different scaling laws. In particular, we will quantitatively check the predictions $V_{\mathrm{m}} = 2V_\varphi^\star = 2E_{k^\star}/k^\star$ and $V_{\mathrm{CE}} = 2V_{\mathrm{g}}^\star = 2\,\partial_k E_k|_{k=k^\star}$ using numerically exact t-MPS simulations, without requiring the use of the generic form (2.3) and the analytical input of the dispersion relation E_k^{f}. We closely follow[1] the presentation of our publication [Despres, 2019] in the following. Our results are particularly important as the generalised quasiparticle picture was established in specific regimes (for instance within a mean-field approximation) and as such ignores potentially important dynamical effects among which quasiparticle collisions and finite lifetime.

In the following, we induce out-of-equilibrium dynamics by performing a global quench: we initialise our system in its ground state for some parameters $(U/J)_{\mathrm{i}}$ for a fixed filling $\bar{n}$, and at $t = 0$ the Hamiltonian is modified instantaneously by changing the interaction ratio to $(U/J)_{\mathrm{f}} \neq (U/J)_{\mathrm{i}}$. We consider a variety of quenches in order to span the phase diagram, sketched in Fig. 2.7. We investigate correlation spreading through two observables: the one-body correlation function

$$G_1(R,t) = \langle\hat{a}^\dagger(R,t)\hat{a}(0,t)\rangle - \langle\hat{a}^\dagger(R,0)\hat{a}^\dagger(0,0)\rangle, \tag{2.6}$$

representing phase fluctuations, and the two-body connected correlation function

$$G_2(R,t) = \langle\hat{n}(R,t)\hat{n}(0,t)\rangle - \langle\hat{n}(R,0)\hat{n}(0,0)\rangle - \left[\langle\hat{n}(R,t)\rangle\langle\hat{n}(0,t)\rangle - \langle\hat{n}(R,0)\rangle\langle\hat{n}(0,0)\rangle\right], \tag{2.7}$$

representing density fluctuations.

Such observables are commonly measured in experiments using time-of-flight and light absorption imaging as mentioned in Sec. 1.3.2. Some of the results below simulate properties of gapless phases where, as discussed in Sec. 1.2.4, the convergence of the MPS is not guaranteed. A careful

[1] Like with all papers I authored, I have not hesitated to paraphrase sentences whenever appropriate.

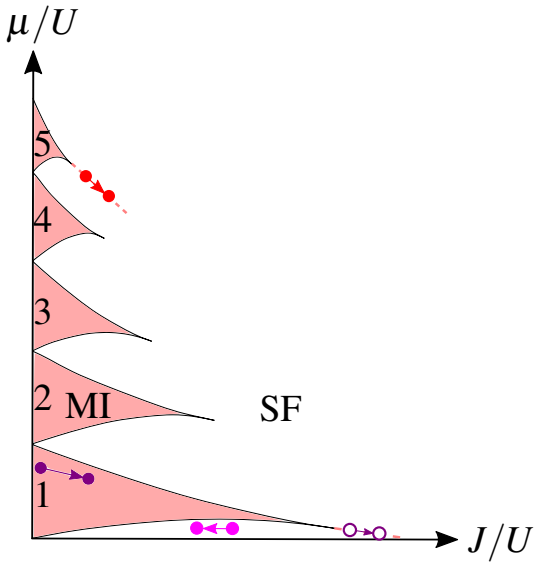

Fig. 2.7 Schematic phase diagram and quenches considered (arrows) including one in the mean-field SF regime (red), one in the strongly interacting MI (full purple), one in the strongly interacting superfluid at low filling (pink) and one in the SF phase close to the transition at fixed unit filling (empty purple). Adapted from [Despres et al., 2019].

analysis of the numerical cutoff (local Hilbert space dimension and bond dimension) has been systematically performed to certify the convergence of the results in all phases considered, and is summarised in Appendix 2.B.

2.2.1 The superfluid mean-field regime

We begin our investigation on the superfluid mean-field regime, where the generalised quasiparticle picture and the generic form of Eq. (2.3) are expected to hold. In this regime characterised by a small interaction parameter $\gamma = U/(2J\bar{n}) \ll 1$, we observe the space-time correlation pattern of $G_2(R,t)$ for a quench (red arrow in Fig. 2.7) with fixed $\bar{n} = 5$ from $(U/J)_\mathrm{i} = 0.2$ to $(U/J)_\mathrm{f} = 0.1$ (thus $\gamma_\mathrm{i} = 0.02$ to $\gamma_\mathrm{f} = 0.01$). We display the result in Fig. 2.8(a). It clearly shows a spike-like structure, characterised by two different velocities. Firstly, a series of parallel extrema move along straight lines corresponding to a constant propagation velocity V_m (the dashed blue lines show fits for two of these minima). Secondly, the various local extrema start at different activation times $t^\star(R)$, aligned along a straight line with a different slope (solid green line), corresponding to a constant velocity V_CE. The latter defines the correlation edge (CE) beyond which the correlations are suppressed.

The same analysis holds for the G_1 function, as shown in Fig. 2.8(b) for the same quench. The values of the correlation edge ($\hbar V_\mathrm{CE}/J = 4.4(3)$) and maxima ($\hbar V_\mathrm{m}/J = 3.3(2)$) velocities obtained using linear fits agree with those found for the G_2 function within less than 10%. This agreement between the spreading velocities for different correlation functions was found in all regimes, and is consistent with the prediction that these velocities are characteristic of the microscopic excitation spectrum and not of the details of the macroscopic observable. However, the full space-time pattern depends on the correlation function. In this phase, the signal for G_1 is less sharp than the one for G_2. This may be attributed to the long-range phase correlations present in the initial state, which blur the space-time signal observed from the correlation function.

By conducting a systematic analysis for various quenches within this SF mean-field regime and tracking the local extrema and the activation time, we extracted the velocities V_m and V_CE from the t-MPS simulations. In Fig. 2.9(b), we report the results of the analysis following the G_2 observable which has the clearest space-time pattern and thus reduces fitting uncertainties. We can quantitatively compare the extracted velocities to the predicted values, as in this regime the

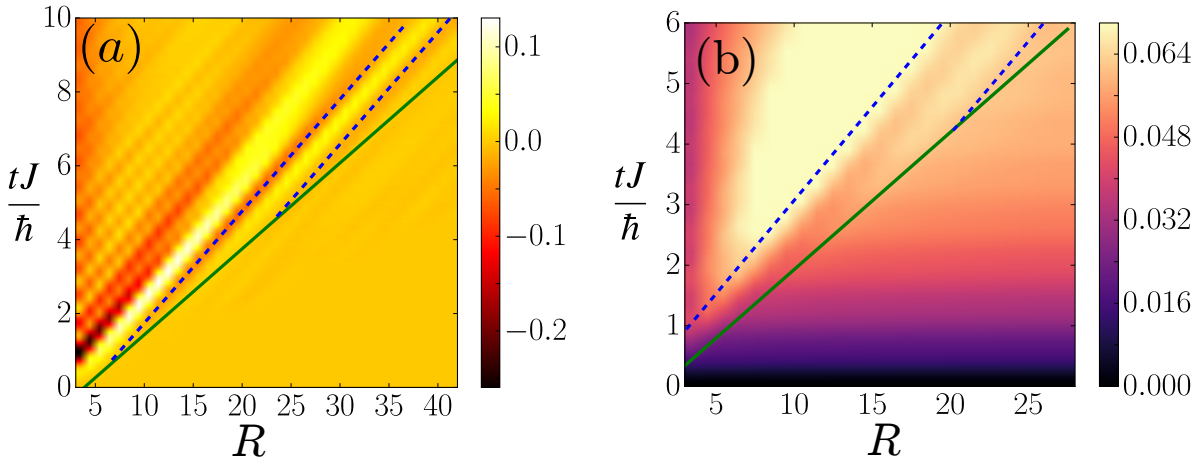

Fig. 2.8 Twofold structure in the space-time pattern for a quench within the mean-field SF phase ($\bar{n} = 5$, from $(U/J)_\mathrm{i} = 0.2$ to $(U/J)_\mathrm{f} = 0.1$) for the observable (a) G_2 and (b) G_1. The best fits for the correlation edge velocity (solid green) and the local maxima (dashed blue) are represented. Adapted from [Despres et al., 2019].

excitation spectrum E_k is known, therefore $V_\mathrm{g}^\star$ and $V_\varphi^\star$ can be computed. In the mean-field regime, we have already mentioned that the elementary excitations of the system are Bogoliubov quasi-particles with the dispersion relation $E_k = \sqrt{\varepsilon_k(\varepsilon_k + 2\bar{n}U)}$ with $\varepsilon_k = 4J\sin^2(k/2)$ the dispersion relation of the free-particle tight-binding model[2]. The relevant velocities are

$$V_\varphi(k) = \frac{\sqrt{\varepsilon_k(\varepsilon_k + 2\bar{n}U)}}{k}, \quad V_\mathrm{g}(k) = \frac{2J\sin k\,(\varepsilon_k + \bar{n}U)}{\sqrt{\varepsilon_k(\varepsilon_k + 2\bar{n}U)}}, \quad V_\mathrm{s} = \lim_{k\to 0} V_\mathrm{g}(k) = \sqrt{2J\bar{n}U}. \tag{2.8}$$

The next step is to find $k^\star$ defined as the value for which $V_\mathrm{g}(k)$ is maximum. The analytical expression for $k^\star$ is not very informative, and we do not reproduce it here. It is simpler to collect it numerically for a given parameter $(U\bar{n}/J)$ and plot $V_\varphi(k^\star)$, $V_\mathrm{g}(k^\star)$ and V_s (in units of $J/\hbar$) as a function of this parameter [Fig. 2.9(a)]. The fact that our results are in excellent agreement (within the fitting errorbars) with the above theory yielding $V_\mathrm{CE} = 2V_\mathrm{g}^\star$ and $V_\mathrm{m} = 2V_\varphi^\star$ validates this physical picture [Fig. 2.9(b)]. Neither of the two velocities coincide with a soundlike mode. Essentially, the after quench out-of-equilibrium dynamics in this regime is beyond the Luttinger liquid description, except when approaching the Mott transition.

We recover the velocities mentioned in [Carleo et al., 2014]. Note however, that the propagation velocity of the maxima should not be assimilated to the light-cone velocity, as we already highlighted in Sec. 2.1.2.

2.2.2 Strongly correlated phases at unit filling

We now focus on the strongly correlated regime $\gamma \sim 1$ at fixed unit filling in both phases. In the SF, we quench from $(U/J)_\mathrm{i} = 1$ to $(U/J)_\mathrm{f} < (U/J)_\mathrm{c} \simeq 3.3$ below the critical point (open purple points and arrow in Fig. 2.7). In the MI, we quench from $(U/J)_\mathrm{i} = \infty$ to $(U/J)_\mathrm{f} > (U/J)_\mathrm{c}$ (full purple points and arrow in Fig. 2.7). We display in Fig. 2.10 our t-MPS results for the spreading of two different correlators: G_1 (upper row, index 1) and G_2 (lower row, index 2). Quenches are performed in the SF (to $(U/J)_\mathrm{f} = 0.5$, panel a) and in the MI slightly beyond the transition (to $(U/J)_\mathrm{f} = 8$, panel b) and in the strongly interacting regime (to $(U/J)_\mathrm{f} = 24$, panel c). In all cases, except for G_2 in the strongly interacting MI (panel c2, see discussion in Sec. 2.2.3), we find

[2]Putting back the lattice spacing a, the correspondence between the Lieb-Liniger and the Bose-Hubbard model in the long wavelength limit where the lattice becomes irrelevant gives $Ja^2 = \hbar^2/2m$. Expanding ε_k at low momenta (*i.e.* taking the lattice spacing to zero), we recover $\varepsilon_k = (\hbar k)^2/2m$.

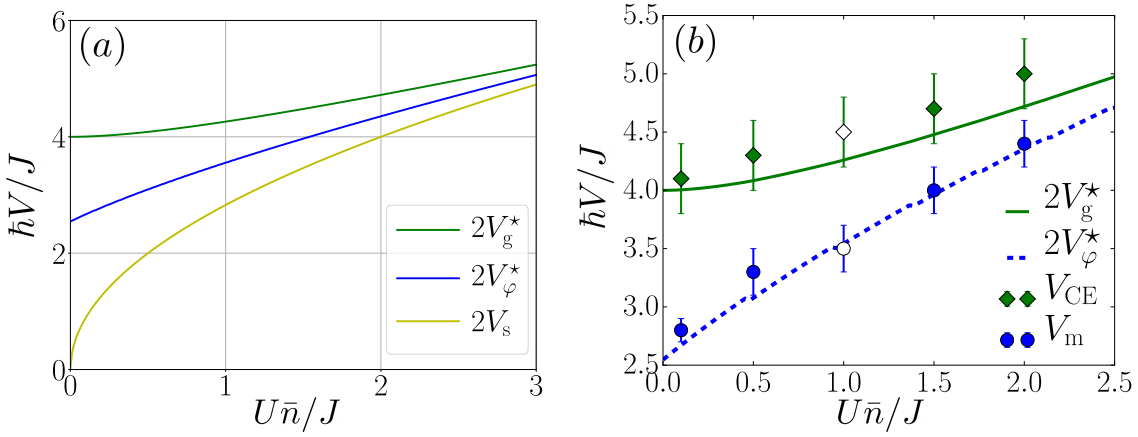

Fig. 2.9 Mean-field SF regime ($\bar{n} = 5$ so $\gamma_f < 3/50 \ll 1$ for $(U/J)_f < 3$). (a) Predicted values for twice the maximum group velocity of the quasiparticles $2V_g^\star$, twice their associated phase velocity $2V_\varphi^\star$ and comparison with twice the sound velocity $2V_s$ in the mean-field (Bogoliubov) regime. (b) Comparison between the extracted velocities from the fits and the microscopic predictions from the excitation spectrum $V_{CE} \simeq 2V_g^\star$ (green) and $V_m \simeq 2V_\varphi^\star$ (blue). The white points correspond to a different initial value $(U\bar{n}/J)_i = 2$ (1 for the other points, all for $\bar{n} = 5$). The good agreement within errorbars confirms the quasiparticle picture in this regime. Adapted from [Despres et al., 2019].

a twofold spike-like structure. The velocities V_m and V_{CE} extracted from linear fits as before (blue and green points respectively), are plotted in panels d both for G_1 and G_2 and show similar results. Again this is consistent with the prediction that these velocities only depend on the microscopic excitation spectrum and not the specific observable under consideration.

In the SF regime at unit filling for $(U/J)_f < (U/J)_c$ the results compare very well with the predictions $2V_\varphi^\star$ and $2V_g^\star$ found from the Bogoliubov dispersion relation (Fig. 2.10, panels d for $(U/J)_f \leq 3.5$). Surprisingly, the agreement is fair up to the critical point where $\gamma_c \simeq 1.6$ far beyond the validity condition of Bogoliubov theory $\gamma \ll 1$. We interpret this agreement for rather high values of γ by noting that $k^\star$ decreases from $\pi/2 \simeq 1.6$ down to $\simeq 1$ at the critical point with unit filling. The physics is then increasingly dominated by long wavelengths which are soundlike modes, as confirmed in Fig. 2.9(a) where all velocities converge towards a single value given by the speed of sound.

Moreover, the speed of sound at $\gamma \sim \gamma_c$ is well approximated by its Bogoliubov expression as we show now. In the long wavelength limit, the lattice discretisation of the Bose-Hubbard model may be disregarded and the latter maps onto the continuous Lieb-Liniger model which we recall has the following Hamiltonian

$$\hat{H}_{LL} = \frac{\hbar^2}{2m}\left[-\sum_{i=1}^{N}\frac{\partial^2}{\partial x_i^2} + 2c\sum_{i<j}\delta(x_i - x_j)\right]. \tag{2.9}$$

The many-body wave function $\psi(x_1, \cdots, x_N)$ can be discretised on an infinitesimal lengthscale (the lattice spacing) $a \ll x_i$ such that from a Taylor expansion

$$\frac{\partial^2\psi}{\partial x_i^2} \simeq \frac{1}{a^2}\left[\psi(x_i + a) + \psi(x_i - a) - 2\psi(x_i)\right]. \tag{2.10}$$

We recover the Bose-Hubbard Hamiltonian by taking the limit $a \to 0$ at fixed $Ja^2 = \hbar^2/2m$. Indeed, the first two terms from the right hand side of Eq. (2.10) represent the tunnelling of the particle i at x_i to one of its neighbour distant of a, and the last term may be reabsorbed in the definition of the chemical potential. The delta interaction of the Lieb-Liniger model for $|x_{i\pm1} - x_i| = a \to 0$ becomes the on-site interaction of the Bose-Hubbard model, with $U =$

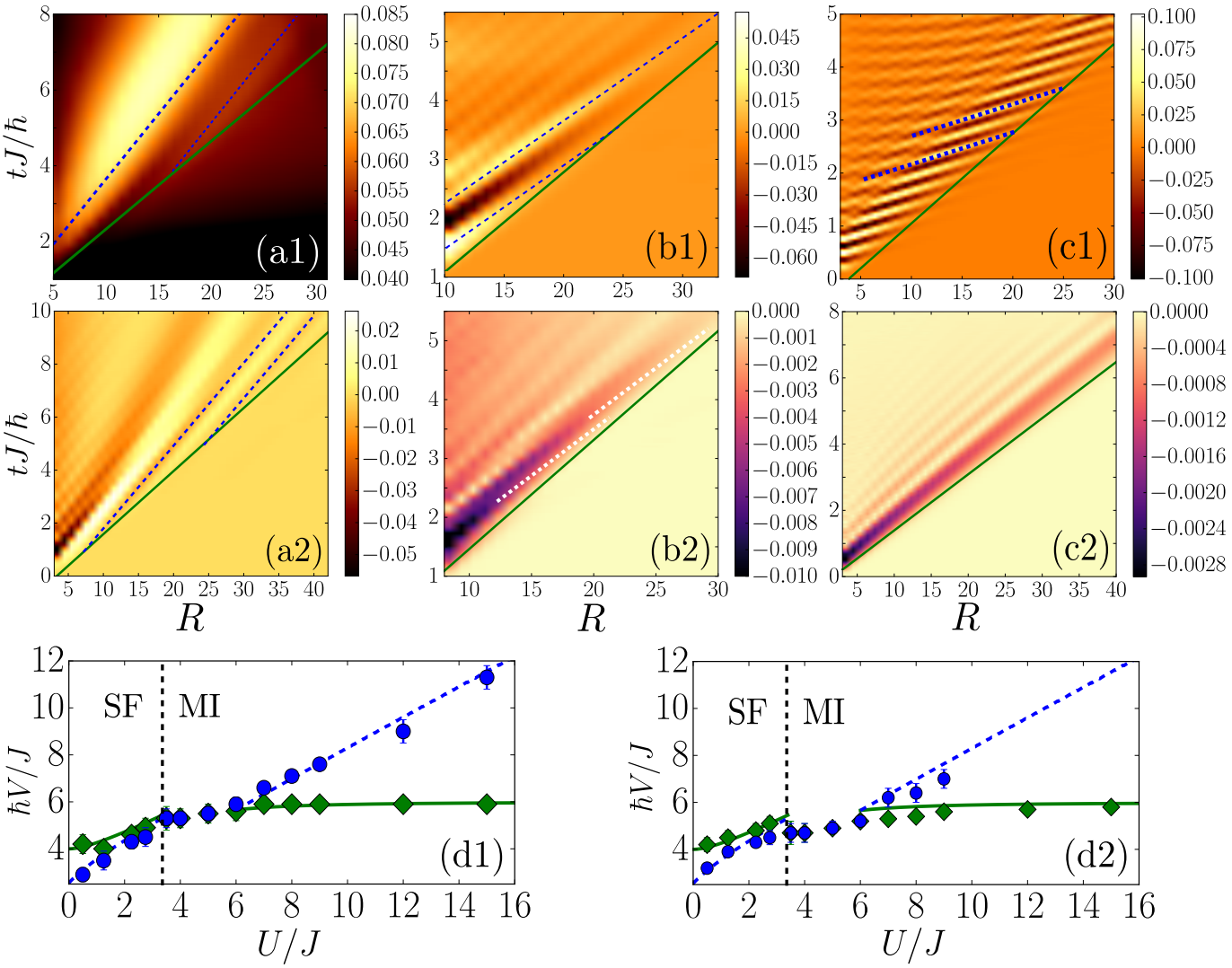

Fig. 2.10 Correlation spreading for $\bar{n} = 1$ of $G_1(R,t)$ (panels 1) and $G_2(R,t)$ (panels 2), respectively in (a) the SF regime to $(U/J)_\mathrm{f} = 0.5$, and the MI regime to (b) $(U/J)_\mathrm{f} = 8$ and (c) $(U/J)_\mathrm{f} = 24$. Initial values are $(U/J)_\mathrm{i} = 1$ for the SF and $(U/J)_\mathrm{i} = \infty$ for the MI. (d) The extracted velocity of the correlation edge (green, full line) matches with twice the group velocity of the fastest quasiparticles computed from the known dispersion relation, and the velocity of the local maxima (dashed blue lines) with twice the phase velocity of the fastest quasiparticles, irrespective of the observable. From [Despres et al., 2019].

$\hbar^2 c/ma = g/a$. As we have detailed in Appendix 1.A, the Lieb-Liniger model is exactly solvable from the Bethe ansatz and its thermodynamic sound velocity may be conveniently expressed from the dimensionless function $e(\gamma)$ as

$$v_\mathrm{s} := \sqrt{\frac{L}{mn}\frac{\partial^2 E_\mathrm{GS}}{\partial L^2}\bigg|_{N,S}} = \frac{\hbar n}{m}\sqrt{3\,e(\gamma) - 2\gamma e'(\gamma) + \frac{1}{2}\gamma^2 e''(\gamma)}, \tag{2.11}$$

which using the small γ expansion[3] becomes $e(\gamma) = \gamma[1 - (4/3\pi)\sqrt{\gamma}]$ such that[4]

$$v_\mathrm{s} \simeq \frac{\hbar n}{m}\sqrt{\gamma}(1 - \sqrt{\gamma}/4\pi). \tag{2.12}$$

[3]Surprisingly, this simpler expression gives an excellent approximation of the exact numerical Bethe ansatz result up to $\gamma \simeq 10$ (see Fig. 1.23 from Appendix 1.A).

[4]This result can be recovered by Taylor expanding to lowest order the expression (i) from Eq. (2.1).

Using the correspondence between the two models, $\gamma = U/(2J\bar{n})$ and $V_\mathrm{s} = v_\mathrm{s}/a$ is given by

$$\frac{\hbar V_\mathrm{s}}{J} \simeq \sqrt{2J\bar{n}U}\left(1 - \frac{1}{4\pi}\sqrt{\frac{U}{2J\bar{n}}}\right). \tag{2.13}$$

Up to the critical point, the lowest order correction to the mean-field result $V_\mathrm{s} = \sqrt{2J\bar{n}U}$ is less than 10%. This can explain the good agreement between the exact numerical simulations and the analytic formula, valid in the mean-field regime. Close the critical point, where the results from conformal field theory apply, the physics is dominated by soundlike modes and the numerical results for V_m and V_CE are consistent with the exact Bethe ansatz value (or the mean-field result) given at $(U/J)_\mathrm{f} = 3.5$ by $2V_\mathrm{s} \simeq 4.7$ (5.3) consistent with what we observed from the fits where $V_\mathrm{m} \simeq V_\mathrm{CE} \simeq 4.7$ for G_2 (5.3 for G_1).

The spreading velocities do not show any divergence when crossing the Mott-U transition and numerically we cannot distinguish the two features for $(U/J)_\mathrm{f} \in [3.5; 6]$ (Fig. 2.10, panels d). Deeper in the MI however, we recover the double structure on the observable G_1 where this time $V_\mathrm{m} > V_\mathrm{CE}$ in contrast to the SF regime. Such observations can be interpreted from the fact that the known excitations in the strongly interacting MI are pairs of a d-Bogoliubon and a h-Bogoliubon (approximately doublon-holon pairs). The pair has a dispersion relation for $\bar{n} = 1$ given by[5]

$$2E_k = \sqrt{(U - 6J\cos k)^2 + 32J^2 \sin^2 k}. \tag{2.14}$$

The value of $k^\star$ is monotonously increasing from 0 at $U/J = 6$ to $\pi/2$ at $U/J = \infty$. From the analytical expression of the dispersion relation we once again compute the predicted values for $2V_\varphi^\star$ and $2V_\mathrm{g}^\star$, and the comparison with the spreading velocities V_m and V_CE fitted from the t-MPS results yields very good agreement for both observables (Fig. 2.10, panels d for $(U/J)_\mathrm{f} \geq 6$). This agreement validates the quasiparticle picture also in this strongly interacting regime.

Yet, the G_2 correlations behave surprisingly in the Mott phase. For not too strong interactions above the transition $(U/J)_\mathrm{f} \in [6; 9]$, we find a twofold structure consistent with that found for G_1. In contrast, the signal for G_2 blurs when entering deeper in the MI regime, and we are not able to identify two distinct features for $(U/J)_\mathrm{f} \geq 9$. We discuss this peculiar situation in Sec. 2.2.3.

2.2.3 Loss of the double structure

The density-density correlation G_2 in the strongly interacting Mott phase provides an explicit example for the rare situation where the twofold structure disappears by reducing to a single one. This example is insightful since it can be fully explained analytically by resorting to a strong coupling expansion of the correlation functions. Following [Barmettler et al., 2012] (to which we refer for more details), within the strongly interacting Mott phase the density-density correlation function is of the form

$$G_2(R,t) \simeq -2\left(\left|g_2^{+,+}(R,t)\right|^2 + \left|g_2^{+,-}(R,t)\right|^2\right), \tag{2.15}$$

where both terms involve a correlator between the fermionic doublons and holons

$$\begin{aligned} g_2^{+,+}(R,t) &= \frac{1}{2\pi}\int_\mathrm{BZ} \mathrm{d}k\, \mathrm{e}^{-ikR}\langle \hat{c}^\dagger_{k,+}\hat{c}_{k,+}\rangle \simeq \frac{8J^2}{\pi U^2}\int_\mathrm{BZ} \mathrm{d}k\, \mathrm{e}^{-ikR}\sin^2(k)\left[\cos(2E_k t) - 1\right], \\ g_2^{+,-}(R,t) &= \frac{1}{2\pi}\int_\mathrm{BZ} \mathrm{d}k\, \mathrm{e}^{-ikR}\langle \hat{c}_{k,+}\hat{c}_{-k,-}\rangle \simeq \frac{\sqrt{2}J}{\pi U}\int_\mathrm{BZ} \mathrm{d}k\, \mathrm{e}^{-ikR}\sin(k)\left[\mathrm{e}^{-2iE_k t} - 1\right], \end{aligned} \tag{2.16}$$

[5] The derivation of this expression can be found in Appendix 1.D. Note that it differs by a constant factor of $32J^2$ under the square root from the expression (ii) given in Eq. (2.1).

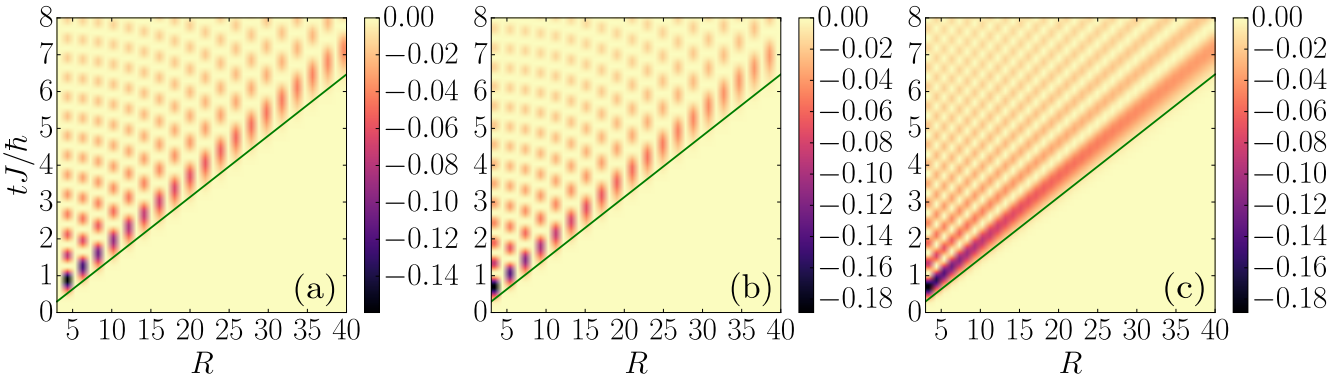

Fig. 2.11 Analytical space-time pattern expected for $G_2(R,t)$ in the strongly interacting regime. (a) $-2\,\mathrm{Re}(g_2^{+,-})^2$. (b) $-2\,\mathrm{Im}(g_2^{+,-})^2$. (c) $-2\left|g_2^{+,-}\right|^2 = -2\,\mathrm{Re}(g_2^{+,-})^2 - 2\,\mathrm{Im}(g_2^{+,-})^2$. The maxima "propagating" with $V_\mathrm{m} \simeq 0$ can be seen in (a) and (b) (vertical lines), but are much harder to detect on the full correlation function in (c). In this rare situation, a onefold structure is observed [compare with the simulation Fig. 2.10(c2)]. From [Despres et al., 2019].

where $2E_k \simeq U - 6J\cos k$ for $\bar{n} = 1$ by Taylor expanding Eq. (2.14) to first order in J/U. Note that the two correlators in Eq. (2.16) have a different scaling with J/U. Since their square is involved in the correlation function, when U/J is large enough, one has to a very good approximation $G_2(R,t) \simeq -2\left|g_2^{+,-}(R,t)\right|^2$. The expression for $g_2^{+,-}(R,t)$ can be rewritten by recognising the derivative of a Bessel function, and using their properties we can simplify it as

$$g_2^{+,-}(R,t) \propto \frac{J}{U}\frac{R}{t}\int_{\mathrm{BZ}} \frac{\mathrm{d}k}{2\pi}\left(\mathrm{e}^{i(2E_k t + kR)} + \mathrm{e}^{i(2E_k t - kR)}\right). \tag{2.17}$$

Because of the square modulus involved in the correlation function, the gap ($2E_k = \mathrm{gap} + 2E_{k,\mathrm{eff}}$) becomes irrelevant and everything goes as if the dispersion relation was the effective gapless one $2E_{k,\mathrm{eff}} \simeq -6J\cos k$. Thus $k^\star \simeq \pi/2$ so that first, $2V_\mathrm{g}^\star = 6J/\hbar$ in excellent agreement with the fitted values of V_CE [Fig. 2.10(d2)]. Second, this yields $2V_\varphi^\star \simeq 0$, also consistent with the fact that we do not observe a double structure. It is difficult to notice that $V_\mathrm{m} \simeq 0$ in the full correlation function because the maxima of the (square of the) real and imaginary part of g_2 are exactly shifted by $\pi/2$, such that we lose this signature in the modulus squared $G_2 \simeq -2\left|g_2^{+,-}\right|^2$. This disappearance of the vertical lines in the full space-time pattern can be observed in Fig. 2.11. In the intermediate regime where $(U/J)_\mathrm{f} \in [6;9]$, the contribution of $\left|g_2^{+,+}\right|^2$ increases and the double structure reappears.

2.2.4 Strongly interacting superfluid regime at low filling

Last but not least, we investigate the strongly interacting SF regime where $0 < \bar{n} < 1$ and $\gamma \gg 1$. At equilibrium, the low-energy physics is known to be well-captured by the Luttinger liquid theory. This bosonisation method describes the system as harmonic oscillator modes which all propagate with the same characteristic sound velocity V_s. For various fillings between 0 and 1, we once again quench the interaction parameter to $(U/J)_\mathrm{f} = 50$ (pink arrow in Fig. 2.7), and simulate using t-MPS the resulting dynamics. By extracting the relevant velocities from the observed dynamics, represented in Fig. 2.12, we observe that they do not coincide (especially at low-filling) in contrast to the harmonic fluid description. Therefore we observe an out-of-equilibrium signature in the dynamics beyond the Luttinger liquid description. Since the latter is only valid at low-energies, one may wonder if this could be attributed to a strong quench effect which excited higher energy modes. To verify this, we extracted the velocities starting from two different initial states, either at $(U/J)_\mathrm{i} = 1$ (full points) or $(U/J)_\mathrm{i} = 40$ (empty points). Within errorbars, we observe a similar behaviour. This suggests that the dynamics always involves the full excitation branch and

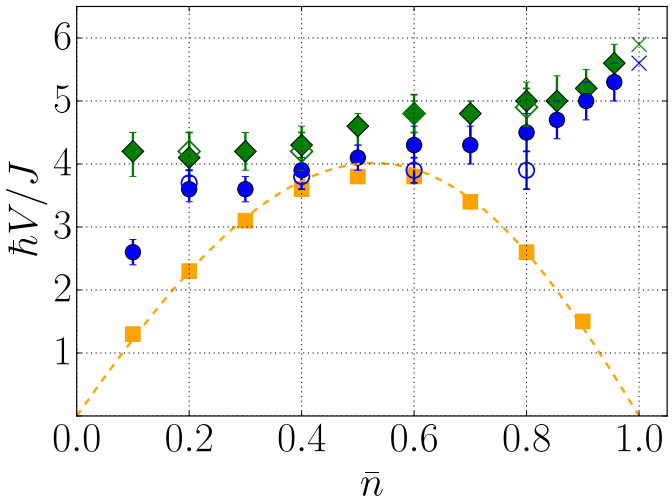

Fig. 2.12 Velocities extracted from the correlation spreading of G_2 in the strongly interacting SF regime at low filling. Filled points start from $(U/J)_\mathrm{i} = 1$ and open ones from $(U/J)_\mathrm{i} = 40$ and both end up at $(U/J)_\mathrm{f} = 50$. We represent the velocity of the correlation edge (green), the local maxima (blue) as well as (twice) the sound velocity given by Eq. (2.18) (dashed yellow line) or directly computed from MPS (yellow squares). From [Despres et al., 2019].

in particular the high momentum part which lies beyond the phonon regime. As suggested by the observation of two different velocities, the low-energy description of the Luttinger liquid is insufficient to capture the after quench dynamics.

It is also fruitful to compare our result with the precise value for the sound velocity of the harmonic fluid description, which can be computed by mapping the Bose-Hubbard model in the strongly interacting limit to a model to spinless fermions with attractive interactions [Cazalilla, 2003, 2004]. The derivation of both the fermionic mapping and the calculation of the speed of sound is detailed in Appendix 2.C. We only quote here the result[6]

$$2V_\mathrm{s} \simeq \frac{4Ja}{\hbar} \sin(\pi\bar{n}) \left[1 - \frac{8J}{U}\bar{n}\cos(\pi\bar{n})\right], \tag{2.18}$$

represented by the dashed yellow line in Fig. 2.12. We have independently checked the validity of this approximation from the energy of the first excited state in our exact MPS simulations (yellow squares) and found excellent agreement. At low filling, the two characteristic velocities V_CE and V_m strongly differ, which suggests that the usual Luttinger approach is insufficient to describe the spreading of correlations even upon renormalisation of the effective sound velocity. Close to half-filling, all velocities merge, consistent with the early observations by [Läuchli and Kollath, 2008]. Finally, the two velocities extracted from the dynamics almost coincide in the vicinity of the commensurate-incommensurate transition to the MI and reach the value $6J/\hbar$ but strongly differ from the speed of sound. This is consistent with the observed disappearance of the twofold structure and the value we found deep in the MI exactly at $\bar{n} = 1$.

We will come back to the question about the nature of the excitations in the strongly interacting SF regime clearly beyond the phononic regime in Sec. 3.2.2.2.

2.2.5 Extension to long-range systems

We conclude this chapter by briefly discussing related works and extensions, especially concerning the spreading of correlations in long-range models. The analysis discussed until now also applies to long-range models especially spin chains in regimes where linear spin wave theory captures

[6] Note that a typo slipped into the expression mentioned in the text of [Despres et al., 2019], but the expression used for the figure of that publication and in the thesis is the correct one.

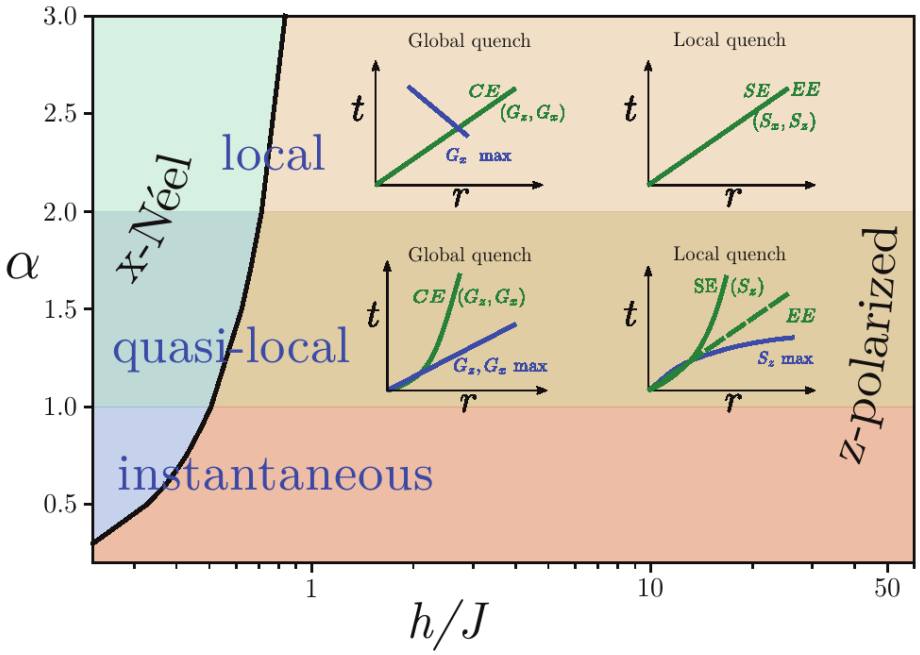

Fig. 2.13 Correlation spreading regimes in the long-range transverse-field Ising chain for two-point correlators (global quenches), local observables (local quenches) and the bipartite entanglement entropy (EE) throughout the phase diagram. All situations appear from sub-ballistic, ballistic, and super-ballistic spreading (see main text). From [Schneider et al., 2021].

the relevant dynamical behaviour, for instance the long-range transverse-field Ising chain (the tunnelling term is replaced by $\sum_{R<R'} J/|R-R'|^{\alpha}$) [Buyskikh et al., 2016; Cevolani et al., 2018], or spin models in higher dimensions such as XXZ [Frérot et al., 2017] or XX [Frérot et al., 2018].

We focus now on the long-range transverse-field Ising chain. For $\alpha > 2$ (causal regime), the system is effectively short-ranged and the previously discussed quasiparticle picture is unchanged: the correlations spread ballistically with $V_{\mathrm{CE}} = 2V_{\mathrm{g}}^{\star}$ and $V_{\mathrm{m}} = 2V_{\varphi}^{\star}$. However other regimes display different physics. First, for $\alpha < 1$ (instantaneous regime), E_k features an infrared divergence ($k \to 0$) and therefore $V_{\mathrm{g}}^{\star} = \infty$ leading to an instantaneous spreading of correlations. Second, when $1 < \alpha < 2$ (quasilocal regime), E_k is bounded but its derivative diverges as $k^{\alpha-2}$. Nonetheless, a weak form of causality emerges: the spin-spin two-point correlators display a quasilocal cone with algebraic leaks (instead of the exponential decay for short-range systems) and a complex internal structure. A correlation edge separating the causal and non-causal regions can still be defined, but the cone is "bending" with its boundaries defined by $t \sim R^{\beta_{\mathrm{CE}}}$ with $\beta_{\mathrm{CE}} > 1$ leading to a sub-ballistic correlation spreading. Local maxima are also found close to the cone edge, and propagate ballistically according to $t \sim R^{\beta_{\mathrm{m}}}$ with $\beta_{\mathrm{m}} = 1$. Therefore in long-range systems, richer behaviours can be observed. The recent investigation of [Schneider et al., 2021] showed that single-point functions *i.e.* local observables such as the local magnetisation $\langle \hat{S}^z(R,t) \rangle$ possess an edge that generally spreads sub-ballistically ($\beta_{\mathrm{CE}} > 1$). In contrast, the local maxima spread super-ballistically ($\beta_{\mathrm{m}} < 1$) and not ballistically like for the two-point spin-spin correlators. A summary of all cases is shown in Fig. 2.13.

Finally, even though we have not mentioned it yet, the propagation of entanglement (often the bipartite Von-Neumann entropy or more general measures defined by Rényi entropies) is also interesting to investigate. Recent observations from [Schneider et al., 2021] always find a ballistic propagation in the quasi-local regime, independently of the interaction regime.

Overall, it is found that correlation spreading is generally twofold, and the physical information propagates at the velocity given by the edge of the cone. For short-range systems, the latter can be related to the group velocity of the excitations. Although we investigated the widely used short-

ranged Bose-Hubbard chain, we emphasise that our results equally apply to many other models with arbitrary statistics, including long-range ones and in higher dimensions. This suggests that using quenches, one is able to link a measurement following the dynamics (the velocity of the edge and of the local maxima close to it) to a fundamental property of the excitations. Indeed, a single point from the excitation spectrum can be extracted from the analysis close to the cone (see insets in Fig. 2.5). Can we extract more information from the internal cone dynamics or do the interferences between the quasiparticles created through dephasing erase any interesting physics? Extracting such information is possible, and we extensively discuss how to perform such quench spectroscopies to probe the properties of the excitations in the following chapters.

Appendices

2.A Phase and group velocities and the wake-pattern in classical physics

2.A.1 General comments on dispersion

Definition of phase and group velocities. A physical signal (or a quasiparticle) may be described in terms of a wave packet of the form (in complex notation)

$$s(x,t) = \int_{-\infty}^{\infty} \mathcal{F}(k)\, \mathrm{e}^{i(kx-\omega t)}\, \mathrm{d}k, \tag{2.19}$$

where $\varphi_{x,t}(k) = kx - \omega t$ is the phase of a single wavelength component of $s(x,t)$ and it is important to stress that ω is implicitly dependent on k (dispersion relation). Phase and group velocities are general notions from the physics of waves. Two neighbouring points in (x,t) and $(x+\mathrm{d}x, t+\mathrm{d}t)$ have the same phase at a given k if $\varphi_{x+\mathrm{d}x,t+\mathrm{d}t} = \varphi_{x,t}$ which yields $k\,\mathrm{d}x - \omega\,\mathrm{d}t = 0$. We thus define the phase velocity as

$$v_\varphi = \frac{\mathrm{d}x}{\mathrm{d}t} = \frac{\omega}{k}, \tag{2.20}$$

which is the velocity of a single frequency component constituting the wave packet. It refers to the abstract concept of a Fourier component, however since only the wave packet has a physical reality, the phase velocity does not correspond to the speed at which an information propagates. Transporting information requires a modulation of the signal, where the information is encoded on a carrier.

In a dispersive medium, the wave packet gets deformed through the propagation, but it is nonetheless possible to define a quantity to characterise at what speed information spreads: this is the group velocity. Assume that the wave packet is maximum around the value $(k^\star, \omega^\star)$. Expanding around the maximum we write $k \simeq k^\star + \Delta k$ and $\omega \simeq \omega^\star + \Delta k \left.\frac{\mathrm{d}\omega}{\mathrm{d}k}\right|_{k=k^\star}$ such that

$$s(x,t) \simeq \mathrm{e}^{i(k^\star x - \omega^\star t)}\, \mathcal{F}(k^\star) \int_{\mathcal{D}(k^\star)} \exp\left(i\Delta k \left[x - t \left.\frac{\mathrm{d}\omega}{\mathrm{d}k}\right|_{k=k^\star} \right] \right) \mathrm{d}(\Delta k), \tag{2.21}$$

where $\mathcal{D}(k^\star)$ is a small region centered around $k^\star$. The interpretation of this equation is that the crest of the wave packet propagates at the speed (group velocity)

$$v_\mathrm{g} = \left.\frac{\mathrm{d}\omega}{\mathrm{d}k}\right|_{k^\star}. \tag{2.22}$$

This notion is only well-defined if the expansion of the wave packet around its maximum can be restricted to first order, which requires that $v_\mathrm{g} \gg \frac{\Delta k}{2} \left.\frac{\mathrm{d}^2\omega}{\mathrm{d}k^2}\right|_{k^\star}$. This condition can be satisfied by considering a sufficiently narrow wave packet, and/or if the medium itself in which the waves propagate is not very dispersive with respect to the given wave packet (centred around $k^\star$).

Saddle point approximation of the signal. We wish to approximate Eq. (2.19) at long time and long distances with fixed ratio x/t. The biggest contribution to the integral is given by the stationary value $\partial_k \varphi|_{k=k^\star} = 0$. Expanding around the maximum we get

$$\varphi(k) = \varphi(k^\star) + \sigma^2 \qquad \text{with} \qquad \sigma^2 = \frac{1}{2}(k-k^\star)^2 \left.\frac{\partial^2\varphi}{\partial k^2}\right|_{k=k^\star} \tag{2.23}$$

and therefore the real-part of the signal is given by

$$s(x,t) \approx \sqrt{\frac{2}{\left|\left.\frac{\partial^2\varphi}{\partial k^2}\right|_{k=k^\star}\right|}} \int_{-\infty}^{\infty} \mathcal{F}(k^\star) \cos\!\big(\varphi(k^\star) + \sigma^2\big)\, \mathrm{d}\sigma = \sqrt{\frac{2\pi}{\left|\left.\frac{\partial^2\varphi}{\partial k^2}\right|_{k=k^\star}\right|}} \mathcal{F}(k^\star) \cos\left[\varphi(k^\star) + \frac{\pi}{4}\right]. \tag{2.24}$$

Noting that $\frac{\partial^2\varphi}{\partial k^2}\Big|_{k=k^\star} = -t\,\frac{\partial^2\omega}{\partial k^2}\Big|_{k=k^\star}$ we recover Eq. (4) from [Cevolani et al., 2018].

In the situation where $\frac{\partial^2\omega}{\partial k^2}\Big|_{k=k^\star} = 0$ (this happens for instance when the dispersion relation is cosine like), the expansion should be performed to the next non-zero order such that

$$\varphi(k) = \varphi(k^\star) + \tilde{\sigma}^3 \qquad \text{with} \qquad \tilde{\sigma}^3 = \frac{1}{6}(k-k^\star)^3\,\frac{\partial^3\varphi}{\partial k^3}\Big|_{k=k^\star} \tag{2.25}$$

such that the real-part of the signal is given by

$$s(x,t) \approx \left(\frac{6}{\left|\frac{\partial^3\varphi}{\partial k^3}\Big|_{k=k^\star}\right|}\right)^{1/3} \int_{-\infty}^{\infty} \mathcal{F}(k^\star)\cos\Big(\varphi(k^\star)+\tilde{\sigma}^3\Big)\,\mathrm{d}\tilde{\sigma} = \frac{\Gamma(1/3)}{\sqrt{3}}\left(\frac{6}{\left|\frac{\partial^3\varphi}{\partial k^3}\Big|_{k=k^\star}\right|}\right)^{1/3} \mathcal{F}(k^\star)\cos\varphi(k^\star). \tag{2.26}$$

2.A.2 The wake pattern in classical hydrodynamics in 2D

The observed space-time correlation pattern in the quantum case is reminiscent of the wake pattern which can be observed if a disturbance [a boat or a duck, see Fig. 2.14(a)] moves at constant speed on top of the water. This analogy with classical 2D hydrodynamics, may be thought of as the result of a mapping between a D dimensional quantum system and a $D+1$ dimensional classical one. The hydrodynamical wake pattern was discovered and explained by Kelvin, by introducing the stationnary phase approximation of integrals [Havelock, 1908; Kelvin, 1887]. To my knowledge, the quantum analogy sparked interest only very recently [Kolomeisky and Straley, 2018; Wampler et al., 2020].

As a small aside, let us comment a bit more this analogy. Lengthy calculations of fluid dynamics can be avoided by making use of an intuitive geometrical derivation proposed by [Crawford, 1984]. We recall that the dispersion relation of water waves in deep water is $\omega = \sqrt{gk}$ where g is the acceleration by gravity, from which we get $v_{\mathrm{g}}/v_\varphi = 1/2$. Now suppose that a duck, initially at the point B_1 [see Fig. 2.14(b) for all the notations used below], emits at $t = 0$ a wave packet centred around the wavelength λ. The duck then moves at a constant speed and when it reaches the point B_2, the wave packet that was emitted when the duck was in B_1 travelled and reached the point W. Where will we observe the strongest signal? Because $v_{\mathrm{g}}/v_\varphi = 1/2$, the answer is at the point G in the middle of $\mathrm{B}_1\mathrm{W}$ where constructive interferences appear. The position of G, and thus the dominant wake angle can be found by maximising the value of θ with respect to the distance $\mathrm{B}_1\mathrm{G}$ at fixed $\mathrm{B}_2\mathrm{W}$. The angle ϕ can be obtained as a side product in order to characterise the full wake-pattern (see [Crawford, 1984] for details).

Note that this complex wake-pattern is the consequence of the non-linear dispersion relation of water waves in deep water, and is reminiscent of the one observed in the quantum case. However,

(a) (b)

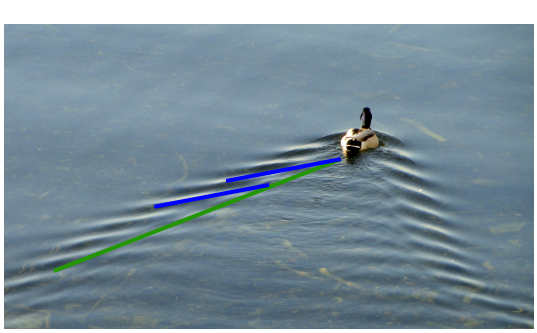

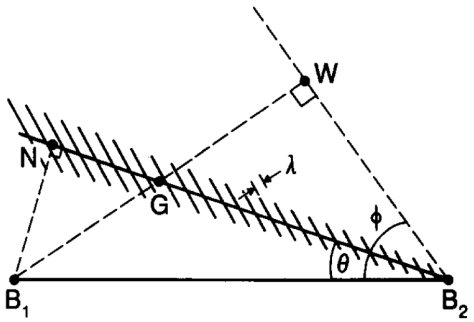

Fig. 2.14 (a) Observation of the wake-pattern. Note the wave crests towards the edge of the cone. From Wikipedia. (b) Scheme of the wake-pattern and definition of the angles (θ, ϕ) used in the text. The duck swims along the line $\mathrm{B}_1\mathrm{B}_2$. From [Crawford, 1984].

let us point out some important differences with the quantum case. In the classical case the perturbation is generated from a single point moving on the medium. In the referential of the duck, the pressure point is fixed at any time and the medium is moving. But this is different from the quantum case, where after the global quench, quasiparticle pairs are emitted from all points in the system, then interfere and give the spike-like structure of correlation spreading. The next difference is that the angles do not quite have the same interpretation. On water, the edge (formed by the transverse wave crests) propagates with a speed (in units of the velocity of the duck) of $\tan(\theta)$ where $\theta = \arctan\left(\sqrt{2}\right) - \arctan\left(1/\sqrt{2}\right) \simeq 19.3\,^\circ$ and the maxima (formed by the diverging wave crests close to the edge) propagates at $1/\tan(\phi - \theta)$ with $\phi - \theta = \arctan\left(1/\sqrt{2}\right) \simeq 35.3\,^\circ$. Therefore, the obtained ratio reads as

$$\frac{V_{\mathrm{CE}}}{V_{\mathrm{m}}} = \frac{1}{\sqrt{2}} \tan\left(\arctan\left(\sqrt{2}\right) - \arctan\left(1/\sqrt{2}\right)\right) = \frac{1}{4}. \tag{2.27}$$

If the picture were the same as in the quantum case, we would have

$$\frac{V_{\mathrm{CE}}}{V_{\mathrm{m}}} = \frac{v_{\mathrm{g}}}{v_{\varphi}} = \frac{1}{2}. \tag{2.28}$$

2.B Convergence of the MPS results

We summarise here the discussion that can be found in the Supplementary Material of [Despres et al., 2019] about the convergence of the MPS results, especially in gapless phases where the convergence of the numerical results needs to be checked in each case.

Two cutoff parameters are particularly important: the dimension of the local Hilbert space, which relates to the maximum of bosons allowed on each site, and the bond dimension, which limits the entanglement allowed between each subpart of the system. The lower the bond dimension, the smallest the region of the full Hilbert space gets represented, the faster the simulation but the lower the accuracy of the results. It can be formally defined as the maximum rank of the Schmidt matrix decomposition of the many-body state represented as a tensor product.

Concerning the local Hilbert space dimension, the mean-field SF is the most demanding regime. A good estimator for the maximum number of bosons allowed per site is given by $1-\sum_{m=0}^{n_{\max}} P(m) \leq 10^{-2}$ where $P(m)$ is the probability that m bosons occupy a given lattice site, which is nearly Poissonian so that $P(m) \simeq \bar{n}^m \mathrm{e}^{-\bar{n}}/m!$. For the filling $\bar{n} = 5$ we used, this requires $n_{\max} \geq 12$. In the SF phase at unit filling close to the transition, this yields $n_{\max} = 5$. In the strongly interacting phases, both for the MI phase with $U/J \geq 15$ and the strongly interacting SF at low fillings, the value $n_{\max} = 2$ proves sufficient.

About the bond dimension, the calculations are run for several values of χ until the correlation functions $G_1(R,t)$ and $G_2(R,t)$ do not sensibly vary upon increasing χ. Unless otherwise specified, values of $\chi = 300$ are always used, except for the strongly interacting phases (MI and SF at low filling) where $\chi = 100$ is enough.

2.C Mapping the Bose-Hubbard model to a Luttinger liquid

In this Appendix, we recall the steps required to map the strongly interacting Bose-Hubbard Hamiltonian for a filling $\bar{n} < 1$ to spinless fermions with attractive interactions and how to compute the sound velocity from the latter model. Such results have been obtained by [Cazalilla, 2003, 2004], here we detail some important steps of the derivation. We choose the notations such that

$$\hat{H}_{\mathrm{BH}} = \sum_R -J\left(\hat{a}_R^\dagger \hat{a}_{R+1} + \mathrm{h.c.}\right) + \frac{U}{2}\hat{n}_R(\hat{n}_R - 1), \tag{2.29}$$

where $\hat{a}_R$ and $\hat{a}_R^\dagger$ are respectively the annihilation and creation operators of a boson on site R. We will show that for $\bar{n} < 1$ and $U/J \gg 1$, this model maps to

$$\hat{H}_{\mathrm{F}} = \sum_R -J\left(\hat{c}_{R+1}^\dagger \hat{c}_R - \frac{2J}{U}\hat{c}_{R+1}^\dagger \hat{n}_R \hat{c}_{R-1} + \mathrm{h.c.}\right) - \frac{4J^2}{U}\hat{n}_{R+1}\hat{n}_R + O\left(\frac{J^3}{U^2}\right), \tag{2.30}$$

where $\hat{c}_R$ and $\hat{c}_R^\dagger$ are respectively fermionic annihilation and creation operators on site R.

2.C.1 The derivation of the effective fermionic Hamiltonian

In the strongly interacting regime and for $\bar{n} < 1$, the local Hilbert space can be restricted to two states, containing 0 or 1 boson (since a state with 2 bosons on a site would have a much higher energy U). We split the full Hilbert space into two complementary subspaces and call P the projector onto states where $\forall R, n_R \leq 1$ and $Q = 1 - P$ the orthogonal projector onto higher occupancy states. We have $PQ = QP = 0$, $P^2 = P$ and $Q^2 = Q$. We want to find the effective Hamiltonian within the subspace $\mathcal{H}_P$ such that $\hat{H}_{\mathrm{eff}} P|\psi\rangle := EP|\psi\rangle$. The Schrödinger equation reads as $(P+Q)\hat{H}(P+Q)|\psi\rangle = E|\psi\rangle$. Multiplying both sides on the left either by Q or by P yields to

$$\begin{aligned} \left(Q\hat{H}P + Q\hat{H}Q\right)|\psi\rangle &= EQ|\psi\rangle, \\ \left(P\hat{H}P + P\hat{H}Q\right)|\psi\rangle &= EP|\psi\rangle. \end{aligned} \tag{2.31}$$

Isolating $Q|\psi\rangle$ from the first equation gives $Q|\psi\rangle = \left(E - Q\hat{H}Q\right)^{-1} Q\hat{H}P|\psi\rangle$ and putting it back into the second equation in (2.31) we get

$$\hat{H}_{\mathrm{eff}} P|\psi\rangle := EP|\psi\rangle = \left[P\hat{H}P + P\hat{H}Q\left(E - Q\hat{H}Q\right)^{-1} Q\hat{H}P\right]|\psi\rangle. \tag{2.32}$$

To lowest order in energy ($E = 0$) we finally obtain

$$\hat{H}_{\mathrm{eff}} = P\hat{H}P - P\hat{H}Q\left(Q\hat{H}Q\right)^{-1} Q\hat{H}P, \tag{2.33}$$

which is Eq. (6) from [Cazalilla, 2003].

The highest order correction in $(Q\hat{H}Q)^{-1}$ is the lowest order correction from $Q\hat{H}Q$. But this lowest order correction to $\hat{H}$ belonging to the Q sector is coming from virtual processes where one site is occupied by two particles, and therefore to lowest order $Q\hat{H}Q \simeq U\,\mathbb{I}_Q$ such that

$$\hat{H}_{\mathrm{eff}} = P\hat{H}P - \frac{1}{U}P\hat{H}Q\hat{H}P. \tag{2.34}$$

It becomes apparent from Eq. (2.34) that P always projects $\hat{H}$ either to the left or to the right. The only term that can survive this process is the tunnelling which can be rewritten using periodic boundary conditions as

$$-J\sum_R \left[\hat{a}_{R+1}^\dagger \hat{a}_R + \hat{a}_R^\dagger \hat{a}_{R+1}\right] = -J\sum_R \left[\hat{a}_{R+1}^\dagger + \hat{a}_{R-1}^\dagger\right]\hat{a}_R, \tag{2.35}$$

such that the effective Hamiltonian is

$$\hat{H}_{\text{eff}} = -J\sum_R P\left(\hat{a}^\dagger_{R+1}\hat{a}_R + \hat{a}^\dagger_R\hat{a}_{R+1}\right)P - \frac{J^2}{U}\sum_R P\left[\hat{a}^\dagger_{R+1} + \hat{a}^\dagger_{R-1}\right]\hat{a}_R\, Q\, \hat{a}^\dagger_R\left[\hat{a}_{R+1} + \hat{a}_{R-1}\right]P, \quad (2.36)$$

which is valid up to first order in J/U. This is Eq. (7) from [Cazalilla, 2003]. Note that the virtual processes have a double occupancy on the site R. The other states with a local occupancy of 1 are already counted in the first term. To avoid overcounting, the projector Q has to select the states with double occupancy and remove single occupancies, so that $Q = \hat{n}_R - 1$. Using commutation relations, we rewrite $\hat{a}_R(\hat{n}_R - 1)\hat{a}^\dagger_R = \hat{n}_R(\hat{n}_R + 1)$ so that eventually the effective bosonic Hamiltonian becomes

$$\hat{H}_{\text{eff}} = -J\sum_R P\left(\hat{a}^\dagger_{R+1}\hat{a}_R + \hat{a}^\dagger_R\hat{a}_{R+1}\right)P - \frac{J^2}{U}\sum_R P\left[\hat{a}^\dagger_{R+1} + \hat{a}^\dagger_{R-1}\right]\left[\hat{a}_{R+1} + \hat{a}_{R-1}\right]\hat{n}_R(\hat{n}_R + 1)P. \quad (2.37)$$

Mapping to fermions. To get rid of the projector P, one maps the bosons to fermionic particles which can have either 0 or 1 local occupancies making use of the Jordan-Wigner transformation

$$\hat{a}_R = \exp\left(i\pi\sum_{R'<R}\hat{n}_{R'}\right)\hat{c}_R, \quad (2.38)$$

and $\hat{n}_R = \hat{a}^\dagger_R\hat{a}_R = \hat{c}^\dagger_R\hat{c}_R$. The tunneling term is not modified so that $P\hat{H}P = -J\sum_R\left(\hat{c}^\dagger_{R+1}\hat{c}_R + \hat{c}^\dagger_R\hat{c}_{R+1}\right)$. This is Eq. (8) from [Cazalilla, 2003].

> To see this, note that
>
> $$\hat{a}^\dagger_{R+1}\hat{a}_R = \hat{c}^\dagger_{R+1}\exp\left(-i\pi\sum_{R'<R+1}\hat{n}'_R\right)\exp\left(i\pi\sum_{R'<R}\hat{n}'_R\right)\hat{c}_R = \hat{c}^\dagger_{R+1}\exp\left(-i\pi\hat{n}_R\right)\hat{c}_R \quad (2.39)$$
>
> Expanding in power series the exponential shows that all terms with non zero power of $\hat{n}_R$ bring at least one $\hat{c}_R$ operator to the right. Then one has at least 2 operators $\hat{c}_R$ in $\hat{a}^\dagger_{R+1}\hat{a}_R$ to the right, which always gives zero because we restricted to the subspace where a state cannot be occupied more than once. This means that the exponential can be replaced by the identity operator, and therefore $\forall R,\ \hat{a}^\dagger_{R+1}\hat{a}_R = \hat{c}^\dagger_{R+1}\hat{c}_R$.

The remaining part can be simplified by noting that since $\hat{n}_R = 0$ or 1, $\hat{n}_R(\hat{n}_R+1) = 2\hat{n}_R$. Beware of the Jordan-Wigner phase which imposes that $\hat{a}^\dagger_{R+1}\hat{n}_R\hat{a}_{R-1} = -\hat{c}^\dagger_{R+1}\hat{n}_R\hat{c}_{R-1}$. Using translation invariance, the final Hamiltonian can be written in the form

$$\hat{H}_{\text{F}} = \sum_R -J\left(\hat{c}^\dagger_{R+1}\hat{c}_R - \frac{2J}{U}\hat{c}^\dagger_{R+1}\hat{n}_R\hat{c}_{R-1} + \text{h.c.}\right) - \frac{4J^2}{U}\hat{n}_{R+1}\hat{n}_R + O\left(\frac{J^3}{U^2}\right). \quad (2.40)$$

2.C.2 Calculating the Luttinger parameters from the effective Hamiltonian

The following part details the results from [Cazalilla, 2004]. We start from Eq. (2.40) and we want to compute the Luttinger parameter K and the speed of sound v_{s}, defined from the density stiffness v_N and the phase stiffness v_J as $K = \sqrt{v_J/v_N}$ and $v_{\text{s}} = \sqrt{v_J v_N}$ with

$$v_N = \frac{L}{\pi\hbar}\frac{\partial^2 E_{\text{GS}}}{\partial N^2}\bigg|_{\phi=0}, \qquad v_J = \frac{L\pi}{\hbar}\frac{\partial^2 E_{\text{GS}}}{\partial\phi^2}\bigg|_{\phi=0}. \quad (2.41)$$

Both derivatives are taken at fixed L, and E_{GS} is the energy of the ground state for the interacting Hamiltonian. However, restricting to first order in J/U, E_{GS} can be expressed as the sum of the average over the non-interacting ground state of the effective Hamiltonian.

The difficult part is to compute the average of the J/U component of $\hat{H}_{\mathrm{F}}$, called $\hat{H}_{\mathrm{int}}$,

$$\langle \hat{H}_{\mathrm{int}} \rangle_0 = \frac{2J^2}{U} \sum_R \left(\langle \hat{c}^\dagger_{R+1} \hat{c}^\dagger_R \hat{c}_R \hat{c}_{R-1} \rangle_0 + \langle \hat{c}^\dagger_{R-1} \hat{c}^\dagger_R \hat{c}_R \hat{c}_{R+1} \rangle_0 \right) - \frac{4J^2}{U} \sum_R \langle \hat{c}^\dagger_R \hat{c}_R \hat{c}^\dagger_{R+1} \hat{c}_{R+1} \rangle_0, \tag{2.42}$$

where we noted $\langle \cdot \rangle_0$ the average over the non-interacting ground state of $\hat{H}_0$. We can then use Wick's theorem, and say for $R = 1$ we get

$$\begin{aligned}
\langle \hat{c}^\dagger_2 \hat{c}^\dagger_1 \hat{c}_1 \hat{c}_0 \rangle_0 &= -\langle \hat{c}^\dagger_2 \hat{c}_1 \rangle_0 \langle \hat{c}^\dagger_1 \hat{c}_0 \rangle_0 + \langle \hat{c}^\dagger_2 \hat{c}_0 \rangle_0 \langle \hat{c}^\dagger_1 \hat{c}_1 \rangle_0 := f_2 f_0 - f_1^2, \\
\langle \hat{c}^\dagger_0 \hat{c}^\dagger_1 \hat{c}_1 \hat{c}_2 \rangle_0 &= \langle \hat{c}^\dagger_0 \hat{c}_2 \rangle_0 \langle \hat{c}^\dagger_1 \hat{c}_1 \rangle_0 - \langle \hat{c}^\dagger_0 \hat{c}_1 \rangle_0 \langle \hat{c}^\dagger_1 \hat{c}_2 \rangle_0 := f_{-2} f_0 - f_{-1}^2, \\
\langle \hat{c}^\dagger_0 \hat{c}_0 \hat{c}^\dagger_1 c_1 \rangle_0 &= \langle \hat{c}^\dagger_0 \hat{c}_0 \rangle_0 \langle \hat{c}^\dagger_1 \hat{c}_1 \rangle_0 - \langle \hat{c}^\dagger_0 \hat{c}_1 \rangle_0 \langle \hat{c}^\dagger_1 \hat{c}_0 \rangle_0 := f_0^2 - f_{-1} f_1.
\end{aligned} \tag{2.43}$$

We chose $R = 1$ but all the terms from 1 to L are the same due to translation invariance, thus

$$\langle \hat{H}_{\mathrm{int}} \rangle_0 = \frac{2J^2}{U} L \left[f_0 \left(f_2 + f_{-2} \right) - \left(f_1^2 + f_{-1}^2 \right) \right] - \frac{4J^2}{U} L \left[f_0^2 - f_1 f_{-1} \right], \tag{2.44}$$

where the lattice spacing is set to $a = 1$. To finally get E_{GS} (to lowest order) one adds the tight-binding contribution $-JL(f_1 + f_{-1})$. In the above equations we have defined

$$f_R = \langle \hat{c}^\dagger_{R+R'} \hat{c}_{R'} \rangle = \frac{1}{L} \sum_k \frac{\mathrm{e}^{-ikR}}{\mathrm{e}^{\beta(\varepsilon_0(k)-\mu)} + 1}, \tag{2.45}$$

where $\varepsilon_0(k) = -2J \cos k$ is the tight-binding dispersion relation. If we introduce a twist in the boundary conditions as $\hat{c}_{R+L} = \mathrm{e}^{i\phi} \hat{c}_R$, at zero temperature Eq. (2.45) simplifies into

$$f_R(\phi, T = 0) = \frac{\mathrm{e}^{-i\phi R/L}}{L} \frac{\sin(\pi \bar{n} R)}{\sin(\pi R/L)}. \tag{2.46}$$

Details of the calculation for v_N. We are only concerned about the thermodynamic limit $L \to \infty$, and in the end we will take the situation where $\phi = 0$ (no phase twist). To alleviate the notations, we denote by a dot the derivatives with respect to N (at fixed L, thus $\bar{n} = N/L$ varies). We have

$$f_R \sim \frac{\sin(\pi \bar{n} R)}{\pi R}, \qquad \dot{f}_R \sim \frac{\cos(\pi \bar{n} R)}{L}, \qquad \ddot{f}_R \sim -\pi R \frac{\sin(\pi \bar{n} R)}{L^2}, \tag{2.47}$$

such that

$$\begin{aligned}
\ddot{E}_{\mathrm{GS}} = \frac{2J^2}{U} L \Big[&\ddot{f}_0 (f_2 + f_{-2}) + 2\dot{f}_0 (\dot{f}_2 + \dot{f}_{-2}) + f_0 (\ddot{f}_2 + \ddot{f}_{-2}) - 2 f_1 \ddot{f}_1 - 2 f_{-1} \ddot{f}_{-1} - 2\dot{f}_1^2 - 2\dot{f}_{-1}^2 \Big] \\
&- \frac{4J^2}{U} L \left[2 f_0 \ddot{f}_0 + 2\dot{f}_0^2 - 2\dot{f}_1 \dot{f}_{-1} - f_1 \ddot{f}_{-1} - f_{-1} \ddot{f}_1 \right] - JL (\ddot{f}_1 + \ddot{f}_{-1}).
\end{aligned} \tag{2.48}$$

Putting everything together gives

$$\begin{aligned}
\ddot{E}_{\mathrm{GS}} &= \frac{2J^2}{U} L \left[\frac{4}{L^2} \cos(2\pi\bar{n}) - \frac{4\pi}{L^2} \bar{n} \sin(2\pi\bar{n}) + \frac{4}{L^2} \sin^2(\pi\bar{n}) - \frac{4}{L^2} \cos^2(\pi\bar{n}) \right] \\
&\quad - \frac{4J^2}{U} L \left[\frac{2}{L^2} - \frac{2}{L^2} \cos^2(\pi\bar{n}) + \frac{2}{L^2} \sin^2(\pi\bar{n}) \right] + \frac{2J\pi}{L} \sin(\pi\bar{n}), \\
&= \frac{2J\pi}{L} \sin(\pi\bar{n}) + \frac{8J^2}{UL} \left[\cos(2\pi\bar{n}) - 1 - \pi\bar{n} \sin(2\pi\bar{n}) \right].
\end{aligned} \tag{2.49}$$

Using trigonometric identities and the definition (2.41) we finally obtain

$$v_N = \frac{2Ja}{\hbar} \sin(\pi\bar{n}) \left(1 - \frac{8J}{U\pi} \left[\sin(\pi\bar{n}) + \pi\bar{n} \cos(\pi\bar{n}) \right] \right). \tag{2.50}$$

Details of the calculation for v_J. The steps are similar, we now denote by a dot the derivatives with respect to ϕ and taking after the derivatives $\phi = 0$ we get in the thermodynamic limit

$$f_R \sim \frac{\sin(\pi\bar{n}R)}{\pi R}, \qquad \dot{f}_R \sim \frac{-iR}{L} f_R, \qquad \ddot{f}_R \sim \frac{-R^2}{L^2} f_R. \tag{2.51}$$

We substitute into Eq. (2.48) the previous expressions and noting that $f_0 = \bar{n}$ thus $\dot{f}_0 = \ddot{f}_0 = 0$ it simplifies into

$$\ddot{E}_{\mathrm{GS}} = \frac{J}{L}(f_1 + f_{-1}) + \frac{2J^2}{UL}\left[-4\bar{n}(f_2 + f_{-2}) + 4(f_1^2 + f_{-1}^2)\right], \tag{2.52}$$

where the term in front of $4J^2/U$ cancels exactly. We end up with

$$\ddot{E}_{\mathrm{GS}} = \frac{2J}{L}\frac{\sin(\pi\bar{n})}{\pi} + \frac{16J^2}{UL}\left[-\frac{\bar{n}\sin(2\pi\bar{n})}{2\pi} + \frac{\sin^2(\pi\bar{n})}{\pi}\right]. \tag{2.53}$$

Using trigonometric formulas it simplifies into

$$\ddot{E}_{\mathrm{GS}} = \frac{2J}{\pi L}\sin(\pi\bar{n})\left(1 + \frac{8J}{U}\left[-\bar{n}\cos(\pi\bar{n}) + \sin(\pi\bar{n})\right]\right), \tag{2.54}$$

and finally using the definition in Eq. (2.41) we obtain

$$v_J = \frac{2Ja}{\hbar}\sin(\pi\bar{n})\left[1 - \frac{8J}{U\pi}\left(-\sin(\pi\bar{n}) + \pi\bar{n}\cos(\pi\bar{n})\right)\right]. \tag{2.55}$$

Final expressions for K and v_s. This last step is simply a Taylor expansion retaining only the highest order terms which gives

$$v_s = \sqrt{v_J v_N} \simeq \frac{2Ja}{\hbar}\sin(\pi\bar{n})\left[1 - \frac{8J}{U}\bar{n}\cos(\pi\bar{n})\right], \qquad K = \sqrt{\frac{v_J}{v_N}} \simeq 1 + \frac{8J}{U\pi}\sin(\pi\bar{n}). \tag{2.56}$$

3 Quench spectroscopy

Invaluable insights to characterise a system can be obtained from the low-energy physics. While the behaviour of the ground state characterises the phase diagram, the elementary excitations on top of it govern a variety of fundamental phenomena among which the electronic conductivity of metals, superconducting properties of type-I superconductors, superfluid properties and even quantum fluctuations leading to the absence of long-range order in one dimension. Low-lying excitations are often described in terms of quasiparticles. Just to name a few examples (see [Wölfle, 2018] for many others), we shall mention magnons and pairs of spinons in spin chains, Bogoliubov particle-hole pairs or doublon-holon pairs in the lattice Bose gas, phonons to describe thermal excitations on a lattice or the sound propagation in superfluids, to which we could add rotons in superfluids and Bose-Einstein condensates with spin-orbit coupling at higher momenta, and polaritons in strongly coupled optical cavities. Besides improving our fundamental understanding of quantum models, knowledge of the elementary excitations is paramount to the development of any quantum technology as they play a role as we have seen in the transport of quantum correlations and information.

Spectroscopy literally means observation of the (energy) spectrum, and is thus the principal technique for achieving this goal. From an experimental point of view, as discussed in Sec. 1.3.2.3, the generic method to measure the excitations properties is to weakly perturb the system by a pump and observe how it reacts using a probe. Such techniques include inelastic scattering experiments and photo-emission, Raman, Bragg or lattice modulation spectroscopies and will be generically referred to as pump-probe spectroscopies in the following. From a theoretical point of view, the elementary excitations describe the response of the system to a weak external perturbation and are captured within the linear response theory formalism. The weak coupling between the external probe and the system is essential to make sure that the measured properties are characteristic of the system and independent of the external perturbation. We briefly review the analytical framework of pump-probe spectroscopies in Sec. 3.1.

Our goal in this chapter is to introduce a novel method named quench spectroscopy, developed in Sec. 3.2 and 3.3. Quench spectroscopy uses the out-of-equilibrium dynamics following a quantum quench in order to unveil spectral properties about the excitations of the system. Importantly, in contrast to standard pump-probe spectroscopies, quench spectroscopy uses equal-time observables and grants access to *momentum-resolved* spectral properties through a series of snapshots. For convenience we will distinguish two complementary protocols for quench spectroscopy, depending whether a global or a local quench is performed. Alternatively as we will see, this choice can be made according to whether one has access to one-point functions or two-point correlators for the observable.

This alternative and versatile method is already accessible experimentally thanks to the considerable progress made recently in the time-resolved control and the out-of-equilibrium dynamics of ultracold many-body quantum systems. It also circumvents the formidable task of computing or measuring the dynamic structure factor or the single-particle Green's function, which both involve two-point correlators at different times in an equilibrium ensemble. In contrast as we will show below, quench spectroscopy advantageously uses the out-of-equilibrium dynamics in order to involve the simpler equal-time correlators. Out-of-equilibrium, we will define a generalised spectral function named the quench spectral function (QSF) which will be main tool to reveal the spectral properties among which the excitation spectrum.

3.1 Review of standard pump-probe spectroscopies

Before we jump into the uncharted territory of quench spectroscopy, we begin by reviewing the analytical foundations of pump-probe spectroscopies. We will focus on the points where the difference is most striking in order to emphasise in which way quench spectroscopy offers an alternative method. Alternatively, it is possible to begin directly by quench spectroscopy in Sec. 3.2 and Sec. 3.3 and finish by Sec. 3.1.

3.1.1 Response function in the linear regime

Many references exist for pump-probe spectroscopy and linear response theory. For this part I mainly used [Pitaevskii and Stringari, 2016; Pottier, 2012; Tong, 2012].

Close to equilibrium (Kubo formula). To observe the spectrum of a system characterised by the Hamiltonian $\hat{H}_0$ at $t \to -\infty$, one method is to introduce a weak perturbation $\hat{H}_{\text{pert}}(t)$. Let us see how an operator $\hat{O}$ in the Heisenberg picture changes when the Hamiltonian is modified from $\hat{H}_0$ to $\hat{H} = \hat{H}_0 + \hat{H}_{\text{pert}}$. For that we evaluate $\langle \hat{O}(t) \rangle_\phi = \text{Tr}\left(\rho_0(t)\hat{U}^\dagger(t)\hat{O}(t)\hat{U}(t)\right)$ where $\hat{U}(t)$ is the unitary time-evolution operator and $\phi(t)$ is called the source of the perturbation, say for instance a magnetic field. Restricting to first order in perturbation theory, the time evolution operator is

$$U(t, t_0) = \mathcal{T} \exp\left(-i \int_{t_0}^{t} \hat{H}_{\text{pert}}(t')\, \mathrm{d}t'\right) \simeq \hat{\mathbb{1}} - i \int_{t_0}^{t} \hat{H}_{\text{pert}}(t')\, \mathrm{d}t'. \tag{3.1}$$

We can use this to relate the expectation value of a probed observable $\hat{O}(t)$ in the presence of the linear perturbation to the one in its absence

$$\langle \hat{O}(t) \rangle_\phi \simeq \langle \hat{O}(t) \rangle_0 - i \int_{t_0}^{t} \langle \left[\hat{O}(t), \hat{H}_{\text{pert}}(t')\right] \rangle_0\, \mathrm{d}t'. \tag{3.2}$$

Now to make further progress, one has to assume a particular form of the perturbation, namely that it is proportional to the source

$$\hat{H}_{\text{pert}}(t) = \phi(t)\hat{P}(t), \tag{3.3}$$

where the operator $\hat{P}$ is called the pump and generates the perturbation. Within the linear response regime, the expectation value of an operator changes linearly with the source (in Fourier space) and the proportionality constant defines the response function tensor χ. Assuming time translation symmetry,

$$\langle \hat{O}(t) \rangle_\phi - \langle \hat{O}(t) \rangle_0 = \int_{-\infty}^{\infty} \chi_{\hat{O},\hat{P}}(t - t')\phi(t')\, \mathrm{d}t'. \tag{3.4}$$

Finally, making use of causality, Eq. (3.2) with Eq. (3.3) are compatible with Eq. (3.4) if

$$\chi_{\hat{O},\hat{P}}(t - t') = -i\theta(t - t')\langle \left[\hat{O}(t), \hat{P}(t')\right] \rangle_0. \tag{3.5}$$

This is the celebrated Kubo formula. The importance of this result comes from the fact that it links a non-equilibrium quantity (the response function on the left-hand side) with an equilibrium average (the expectation value of the non-equal time correlator on the right-hand side is evaluated in the absence of the perturbation, thus at equilibrium). This result only holds at first order in perturbation theory.

Spectral functions and the quantum fluctuation-dissipation theorem. Let us specify to the common situation where the equilibrium ensemble average $\langle\cdots\rangle_0$ previously mentioned is the canonical one. Before the perturbation is turned on, the system is thus at thermal equilibrium and described by the density matrix diagonal in the energy eigenbasis of $\hat{H}_0$ noted $\{|n\rangle\}$ such that $\hat{\rho}_0 = \mathrm{e}^{-\beta\hat{H}_0} = (1/Z)\sum_n \mathrm{e}^{-\beta E_n}|n\rangle\langle n|$ with $Z = \sum_n \mathrm{e}^{-\beta E_n}$ and β the inverse temperature. Note that since we are at equilibrium, $\left[\hat{\rho}_0, \hat{H}_0\right] = 0$. In the frequency domain, Eq. (3.5) becomes

$$\chi_{\hat{O},\hat{P}}(\omega) = -i\int_0^\infty \mathrm{d}t\, \mathrm{e}^{i\omega t}\,\mathrm{Tr}\left(\mathrm{e}^{-\beta\hat{H}_0}\left[\hat{O}(t), \hat{P}(0)\right]\right). \tag{3.6}$$

Using a completeness relation with the eigenbasis of $\hat{H}_0$ we get

$$\chi_{\hat{O},\hat{P}}(\omega) = -i\int_0^\infty \mathrm{d}t\, \mathrm{e}^{i\omega t}\sum_{m,n}\mathrm{e}^{-\beta E_n}\left[\langle n|\hat{O}|m\rangle\langle m|\hat{P}|n\rangle\,\mathrm{e}^{i(E_n-E_m)t} - \langle n|\hat{P}|m\rangle\langle m|\hat{O}|n\rangle\,\mathrm{e}^{-i(E_n-E_m)t}\right], \tag{3.7}$$

which can be rewritten as[1]

$$\mathrm{Im}\,\chi_{\hat{O},\hat{P}}(\omega) = -\pi\sum_{m,n}\langle n|\hat{O}|m\rangle\langle m|\hat{P}|n\rangle\,\delta(\omega+E_n-E_m)\,\mathrm{e}^{-\beta E_n}(1-\mathrm{e}^{-\beta\omega}). \tag{3.8}$$

The imaginary part of the response function diverges at the discrete resonant frequencies $\omega = E_m - E_n$. One usually defines the following quantity

$$S_{\hat{O},\hat{P}}(\omega) = 2\pi\sum_{m,n}\mathrm{e}^{-\beta E_n}\langle n|\hat{O}|m\rangle\langle m|\hat{P}|n\rangle\,\delta(\omega+E_n-E_m) \tag{3.9}$$

as the spectral function, which is proportional to the imaginary part of the response function

$$\mathrm{Im}\,\chi_{\hat{O},\hat{P}}(\omega) = -\tfrac{1}{2}(1-\mathrm{e}^{-\beta\omega})\,S_{\hat{O},\hat{P}}(\omega). \tag{3.10}$$

Equation (3.10) is a quantum fluctuation-dissipation theorem since the dissipation (captured by the imaginary part of the response function) in part created by intrinsic quantum fluctuations is proportional to the fluctuations in frequency space of the correlation function (see below how the spectral function is related to the dynamics). Because of causality, only the imaginary part is required to characterise the full response function (Kramers-Kronig relations). Therefore, spectral functions characterise the full response of the system in the linear regime. At zero temperature, spectral functions give access to the full energy spectrum of the model (at least if the choice of the pump and the probe is such that they can couple the eigenstates of the unperturbed system to its ground state).

3.1.2 Spectral functions, dynamics and excitations

Another insightful definition of spectral functions follows from the point of view of time-dependent correlation functions. The discussion below will be closely followed to define the quench spectral function (QSF) for quench spectroscopy (Sec. 3.2.1) which can be understood as the substitute for the spectral function in quench spectroscopy (3.9).

For now, we assume a system at equilibrium so that it is described by a generic density matrix $\hat{\rho}$ of the diagonal form $\hat{\rho} = \sum_n \rho^{nn}|n\rangle\langle n|$. We consider a generic non-equal time correlator $C_{\hat{O},\hat{P}}(\boldsymbol{x},\boldsymbol{y};t,t') = \mathrm{Tr}\left[\hat{\rho}\,\hat{O}(\boldsymbol{x},t)\hat{P}(\boldsymbol{y},t')\right]$ where $\boldsymbol{x}$ and $\boldsymbol{y}$ are spatial coordinates. To extract the time dependence, we expand the observables in the Heisenberg representation, for instance $\hat{O}(t) =$

[1] Use the Feynman prescription $\omega \to \omega + i\epsilon$ to remove divergences, then the formula $\lim_{\epsilon\to 0}(x-a+i\epsilon)^{-1} = \mathrm{p.v.}(x-a)^{-1} - i\pi\delta(x-a)$ with p.v. the principal value and rename the indices n and m in the second term.

$e^{i\hat{H}t}\,\hat{O}\,e^{-i\hat{H}t}$ where we write $\hat{O}(0) = \hat{O}$ and we assumed for simplicity that $\hat{H}$ does not depend explicitly on time. Then

$$\begin{aligned} C_{\hat{O},\hat{P}}(\boldsymbol{x},\boldsymbol{y};t,t') &= \sum_{n,m,p} \langle p|\,\rho^{nn}\,|n\rangle\,\langle n|\,e^{i\hat{H}t}\hat{O}(\boldsymbol{x})e^{-i\hat{H}t}\,|m\rangle\,\langle m|\,e^{i\hat{H}t'}\hat{P}(\boldsymbol{y})e^{-i\hat{H}t'}\,|p\rangle\,, \\ &= \sum_{n,m,p} \rho^{nn}\,\delta_{p,n}\,e^{i(E_n-E_m)t}\,e^{i(E_m-E_p)t'}\,\langle n|\,\hat{O}(\boldsymbol{x})\,|m\rangle\,\langle m|\,\hat{P}(\boldsymbol{y})\,|p\rangle\,, \\ &= \sum_{n,m} \rho^{nn}\,e^{i(E_n-E_m)(t-t')}\,\langle n|\,\hat{O}(\boldsymbol{x})\,|m\rangle\,\langle m|\,\hat{P}(\boldsymbol{y})\,|n\rangle\,. \end{aligned} \tag{3.11}$$

By taking the space-time Fourier transform, one recognises the definition of the spectral function (3.9), namely

$$\mathrm{FT}\left[C_{\hat{O},\hat{P}}(\boldsymbol{x}-\boldsymbol{y};t-t')\right] = S_{\hat{O},\hat{P}}(\boldsymbol{k};\omega). \tag{3.12}$$

The space-time Fourier transform of a non-equal time correlator is a spectral function. This highlights the importance of a non-equal time correlator for pump-probe spectroscopies. In Sec. 3.2.1, we will show that the simpler equal time correlators are sufficient in quench spectroscopy.

> Alternatively, the need for a non-equal time correlator can be observed by noting that
>
> $$C_{\hat{O},\hat{P}}(t,t) := \mathrm{Tr}\left(\hat{\rho}\hat{U}^\dagger\hat{O}\hat{U}\hat{U}^\dagger\hat{P}\hat{U}\right) = \mathrm{Tr}\left(\hat{U}\hat{\rho}\hat{U}^\dagger\hat{O}\hat{P}\right) = \mathrm{Tr}\left(\hat{\rho}\hat{O}\hat{P}\right) := C_{\hat{O},\hat{P}}(0,0) \tag{3.13}$$
>
> where in the second equality we used that $\hat{U}\hat{U}^\dagger = 1$ and the cyclicity of the trace, and in the third we used that at equilibrium $\left[\hat{\rho},\hat{H}\right] = 0 \Rightarrow \left[\hat{\rho},\hat{U}\right] = 0$.

Finally, we note that the interpretation of the spectral functions simplifies at zero temperature, where only the ground state $|n\rangle = |0\rangle$ is populated. In practice, the choice $\hat{P} = \hat{O}^\dagger$ is very common[2]. When a system can be described by a translation invariant Hamiltonian, the total momentum $\hat{\boldsymbol{P}}$ is a conserved quantity, and thus commutes with the Hamiltonian $\left[\hat{H},\hat{\boldsymbol{P}}\right] = 0$. Each energy eigenstate has a well defined momentum $\hat{\boldsymbol{P}}\,|n\rangle = \boldsymbol{P}_n\,|n\rangle$, thus for any operator $\hat{O}$ translation invariance of the system imposes that $\langle n|\,\hat{O}(\boldsymbol{R})\,|m\rangle = e^{i(\boldsymbol{P}_m-\boldsymbol{P}_n)\boldsymbol{R}}\,\langle n|\,\hat{O}(\boldsymbol{0})\,|m\rangle$. Therefore for a translational invariant system the spectral function becomes

$$S(\boldsymbol{k};\omega)_{T=0} = (2\pi)^{D+1}\sum_m |\langle 0|\,\hat{O}(\boldsymbol{0})\,|m\rangle|^2\,\delta(E_m-\omega)\delta(\boldsymbol{P}_m-\boldsymbol{k}). \tag{3.14}$$

The spectral function is sharply peaked at each resonant energy E_m and each momentum $\boldsymbol{P}_m$ corresponding to the energy and momentum $(\omega,\boldsymbol{k})$ injected by the pump. By scanning in $(\omega,\boldsymbol{k})$, this technique can be used to reconstruct the excitation spectrum. To observe a signal, the choice of the operator $\hat{O}$ (therefore the pump and the probe) is crucial to couple the eigenstates $|m\rangle$ to the vacuum. We stress that in Eq. (3.14), the eigenstates refer to the unperturbed Hamiltonian (the one at equilibrium, before the perturbation was adiabatically turned on), and the probed transition energies refer to the eigenvalues of this unperturbed Hamiltonian. This is only the case because we restricted to the linear regime.

Two particular spectral functions, corresponding to two choices of the pump and the probe are very important from a practical point of view. To write down the expressions in their most familiar form, we specify to the canonical ensemble.

[2] If $\hat{P}$ is a unitary operator, the probe should be chosen so as to contain a term which "reverses the pump", namely $\hat{O} \sim \hat{P}^{-1}$. As we will see in Sec. 3.3.2.1, the same strategy will apply to quench spectroscopy where the role of the pump is played by the local quench.

Single-particle spectral function. The single-particle spectral function is defined by choosing $\hat{O} = \hat{a}_{\boldsymbol{k}}$ the annihilation operator of a single particle and $\hat{P} = \hat{a}^\dagger_{\boldsymbol{k}}$ the creation operator of a single particle

$$A(\boldsymbol{k}, \omega) = 2\pi \sum_{n,m} \frac{\mathrm{e}^{-\beta E_n}}{Z} |\langle m| \hat{a}_{\boldsymbol{k}} |n\rangle|^2 \delta(\omega - E_m + E_n). \tag{3.15}$$

It corresponds to the space-time Fourier transform of the imaginary part of the retarded Green's function (up to an irrelevant constant prefactor of -2). Importantly, for any quadratic Hamiltonian of the form $\hat{H} = \sum_k E_k \hat{\gamma}^\dagger_k \hat{\gamma}_k$, the retarded Green's function can be computed exactly and the associated spectral function is given by $A(k, \omega) = 2\pi\delta(\omega - E_k)$. Any broadening relates to the behaviour of the interactions beyond the quadratic regime.

Dynamical structure factor. The dynamical structure factor is defined by the choice $\hat{O} = \hat{n}_{\boldsymbol{k}} = \sum_{\boldsymbol{q}} \hat{a}^\dagger_{\boldsymbol{k}+\boldsymbol{q}} \hat{a}_{\boldsymbol{q}}$ and $\hat{P} = \hat{n}^\dagger_{\boldsymbol{k}} = \hat{n}_{-\boldsymbol{k}}$, and is associated to a two-particle process

$$S(\boldsymbol{k}, \omega) = 2\pi \sum_{n,m} \frac{\mathrm{e}^{-\beta E_n}}{Z} |\langle m| \hat{n}_{\boldsymbol{k}} |n\rangle|^2 \delta(\omega - E_m + E_n). \tag{3.16}$$

It corresponds to the space-time Fourier transform of the density-density correlation function.

Excitations in many-body systems. A distinction is sometimes made in the literature between individual single-particle excitations and many-body collective ones. This distinction is useful from a practical point of view, since by their choice of observables, photo-emission spectroscopies are only sensitive to single-particle excitations while neutron scattering experiments or Bragg spectroscopies are sensitive to two-particle excitations. Also generally speaking, the dynamical structure factor probes the response at low momentum (large distances, hence the collective excitations) while the single-particle spectral function probes the higher momentum part (response at short distances, hence single-particle excitations). However, this distinction should not be understood at the formal level. For instance, a magnon can be understood as a single localised defect on an polarised spin chain or alternatively as a delocalised spin wave.

Another reason behind this distinction comes from solid-state physics (and in general fermionic systems, especially Fermi liquids), where the quasiparticle excitations are often restricted to be individual *fermionic* excitations while collective excitations refer to the *bosonic* ones. Throughout the thesis we deal with bosonic systems where the distinction is not very useful. Both types of excitations are elementary excitations that can be represented by quasiparticles with arbitrary statistics, and will thus be detectable using quench spectroscopy.

3.2 Global quench spectroscopy

The following section is mostly based on our publication [Villa et al., 2019], where we show how the full low-lying excitation spectrum of a correlated quantum system can be extracted from equal-time correlators following a global quench. To the best of our knowledge, the first idea of quench spectroscopy dates back to the work of [Gritsev et al., 2007] who proposed to use quenches to identify the transition energies in the frequency domain alone. Our work importantly extends such study by linking the resonances in momentum to the ones in frequency. We aim at providing a complete framework of the technique, by generalising previous results using power spectrum analysis of density ripples in one-dimensional quasicondensates [Schemmer et al., 2018] and spin correlations in two-dimensional models with flatbands [Menu and Roscilde, 2018]. This global quench spectroscopy project has been a collaboration with J. Despres, to whom I am in particular indebted for the t-MPS numerical simulations reproduced below.

3.2.1 The quench spectral function (QSF)

We begin by defining the quench spectral function (QSF), which probes spectral properties following the dynamics after a quantum quench. Here we focus on global quenches, where a parameter of the Hamiltonian is changed instantaneously at $t = 0$ from $\hat{H}_\mathrm{i}$ to $\hat{H}$.

In quench spectroscopy, the initial state (immediately after the quench) is an out-of-equilibrium excited state. As a consequence, the initial density matrix is no longer equivalent to a Gibbs ensemble and thus ρ_i^{nm} is not proportional to δ_{nm} anymore. This has to be contrasted with standard pump-probe spectroscopies where the correlation functions are evaluated (at linear order) with reference to an *equilibrium* ensemble in the absence of the external perturbation (the pump). We will show that this additional difficulty is actually what makes quench spectroscopy capable of dealing with the simpler equal-time correlators to unveil spectral properties.

Definition. The initial state is out of equilibrium, and the off-diagonal coherences $\rho_\mathrm{i}^{n'n}$ with $n \neq n'$ are now non-vanishing. An arbitrary two-point correlator then reads as[3]

$$\begin{aligned} G(\boldsymbol{x},\boldsymbol{y};t,t') &:= \mathrm{Tr}\left[\hat{\rho}_\mathrm{i}\hat{O}_1^\dagger(\boldsymbol{x},t)\hat{O}_2(\boldsymbol{y},t')\right], \\ &= \sum_{n,n',m,p} \langle p|\,\rho_\mathrm{i}^{n'n}\,|n'\rangle\,\langle n|\,\mathrm{e}^{i\hat{H}t}\hat{O}_1^\dagger(\boldsymbol{x})\mathrm{e}^{-i\hat{H}t}\,|m\rangle\,\langle m|\,\mathrm{e}^{i\hat{H}t'}\hat{O}_2(\boldsymbol{y})\mathrm{e}^{-i\hat{H}t'}\,|p\rangle\,, \\ &= \sum_{n,n',m} \rho_\mathrm{i}^{n'n}\,\mathrm{e}^{i(E_nt-E_{n'}t')}\,\mathrm{e}^{-iE_m(t-t')}\,\langle n|\,\hat{O}_1^\dagger(\boldsymbol{x})\,|m\rangle\,\langle m|\,\hat{O}_2(\boldsymbol{y})\,|n'\rangle\,. \end{aligned} \tag{3.17}$$

Note that the basis $\{|n\rangle\}$ used above is the one of the post-quench Hamiltonian $\hat{H}$ governing the dynamics. In Eq. (3.17) we may set $t = t'$ and still probe non-trivial dynamical properties from equal-time correlators. Extracting explicitly the spatial dependence, it becomes

$$G(\boldsymbol{x},\boldsymbol{y};t,t) = \sum_{n,n',m} \rho_\mathrm{i}^{n'n}\,\mathrm{e}^{i(E_n-E_{n'})t}\,\mathrm{e}^{i\boldsymbol{P}_m(\boldsymbol{x}-\boldsymbol{y})}\,\mathrm{e}^{i(\boldsymbol{P}_{n'}\boldsymbol{y}-\boldsymbol{P}_n\boldsymbol{x})}\,\langle n|\,\hat{O}_1^\dagger\,|m\rangle\,\langle m|\,\hat{O}_2\,|n'\rangle\,. \tag{3.18}$$

To make use of translation invariance of the system (we consider a clean system and assume periodic boundary conditions[4]), we move to relative coordinates $\boldsymbol{R} = \boldsymbol{x} - \boldsymbol{y}$ and $\boldsymbol{r} = (\boldsymbol{x} + \boldsymbol{y})/2$. Importantly, the initial state is also translational invariant, because the state immediately after the quench is the ground state of the initial (pre-quench) Hamiltonian which is translational invariant, so that

$$G(\boldsymbol{R},\boldsymbol{r};t,t) = \frac{1}{L^D}\int \mathrm{d}\boldsymbol{r}\, G(\boldsymbol{r}+\tfrac{\boldsymbol{R}}{2},\boldsymbol{r}-\tfrac{\boldsymbol{R}}{2};t,t) = G(\boldsymbol{R};t,t), \tag{3.19}$$

which simplifies as

$$\begin{aligned} G(\boldsymbol{R};t,t) &= \frac{1}{L^D}\sum_{n,n',m} \rho_\mathrm{i}^{n'n}\,\langle n|\,\hat{O}_1^\dagger\,|m\rangle\,\langle m|\,\hat{O}_2\,|n'\rangle\,\mathrm{e}^{i(E_n-E_{n'})t}\,\mathrm{e}^{i(2\boldsymbol{P}_m-\boldsymbol{P}_{n'}-\boldsymbol{P}_n)\boldsymbol{R}/2}\int \mathrm{d}\boldsymbol{r}\,\mathrm{e}^{i(\boldsymbol{P}_{n'}-\boldsymbol{P}_n)\boldsymbol{r}} \\ &= \left(\tfrac{2\pi}{L}\right)^D \sum_{n,n',m} \rho_\mathrm{i}^{n'n}\,\langle n|\,\hat{O}_1^\dagger\,|m\rangle\,\langle m|\,\hat{O}_2\,|n'\rangle\,\mathrm{e}^{i(E_n-E_{n'})t}\,\mathrm{e}^{i(\boldsymbol{P}_m-\boldsymbol{P}_n)\boldsymbol{R}}\,\delta(\boldsymbol{P}_{n'}-\boldsymbol{P}_n). \end{aligned} \tag{3.20}$$

We observe that translation invariance of both the system and the initial state is crucial to fix the unknown momentum of the intermediate state $\boldsymbol{P}_m$ as a function of a single momentum $\boldsymbol{P}_n$

[3] We now note G for the two-point correlator instead of C to highlight the difference with the previous situation in pump-probe spectroscopies where the correlation functions were evaluated with respect to an equilibrium ensemble.

[4] In the thermodynamic limit, the specific choice of boundary conditions is irrelevant as the boundary effects are negligible.

(equivalently $\boldsymbol{P}_{n'}$). By now taking a space-time Fourier transform, we define the quench spectral function (QSF) after global quenches in homogeneous systems as

$$\begin{aligned} G(\boldsymbol{k};\omega) &:= \int \mathrm{d}\boldsymbol{R}\,\mathrm{d}t\,\mathrm{e}^{-i(\boldsymbol{k}\boldsymbol{R}+\omega t)}\,G(\boldsymbol{R};t,t) \\ &= \frac{(2\pi)^{2D+1}}{L^D}\sum_{n,n',m}\rho_{\mathrm{i}}^{n'n}\,\langle n|\,\hat{O}_1^\dagger\,|m\rangle\,\langle m|\,\hat{O}_2\,|n'\rangle\,\delta(E_n-E_{n'}-\omega)\delta(\boldsymbol{P}_m-\boldsymbol{P}_n-\boldsymbol{k})\delta(\boldsymbol{P}_{n'}-\boldsymbol{P}_n). \end{aligned} \tag{3.21}$$

The expression (3.21) is at the core of the global quench spectroscopy technique. The dynamical selection rule in energy $\omega = E_n - E_{n'}$ applies regardless of the nature of the eigenstates, provided that the operators $\hat{O}_1^\dagger$ and $\hat{O}_2$ couple the eigenstates $|n\rangle$ and $|n'\rangle$ indirectly through $|m\rangle$. The transition energies $E_n - E_{n'}$ are identified with the resonance frequencies ω, as in standard spectroscopy. Importantly, the link between the excitation momentum and its energy allows to reconstruct spectral features with momentum resolution as we show in the following.

Weak global quenches. We are mostly interested in the low-lying excitations of the system. To this end, it will prove sufficient to consider weak quenches, where the initial state remains sufficiently close to the ground state such that

$$\hat{\rho}_{\mathrm{i}} \simeq \rho_{\mathrm{i}}^{00}\,|0\rangle\langle 0| + \sum_{n\neq 0}\rho_{\mathrm{i}}^{0n}\,|0\rangle\langle n| + \rho_{\mathrm{i}}^{n0}\,|n\rangle\langle 0|\,. \tag{3.22}$$

We stress that $|0\rangle$ is the vacuum of quasiparticle excitations, *i.e.* the ground state of the post-quench Hamiltonian $\hat{H}$. It should not to be confused with the ground state of $\hat{H}_{\mathrm{i}}$, which for a global quench we always take as our initial state $|\psi_{\mathrm{i}}\rangle$ (Fig. 1.7). For a pure initial state close to the ground state, $|\psi_{\mathrm{i}}\rangle \simeq |0\rangle + \sum_{n\neq 0}\epsilon_n\,|n\rangle$, and in Eq. (3.22) we have $\rho_{\mathrm{i}}^{n0} = (\rho_{\mathrm{i}}^{0n})^* = \epsilon_n \ll 1$. The weak quench assumption requires the ground state of the initial Hamiltonian to be "not too far from" the ground state of the final Hamiltonian (up to a finite number of low-energy excitations). It is clearly violated if the quench crosses a phase transition, a situation avoided throughout the manuscript. For weak quenches, the lowest order terms $\rho_{\mathrm{i}}^{n'n}$ correspond to either $n=0$ or $n'=0$ and the QSF given by Eq. (3.21) simplifies into

$$\begin{aligned} G(\boldsymbol{k};\omega) \simeq{}& (2\pi)^{D+1}\sum_m \rho_{\mathrm{i}}^{00}\,\langle 0|\,\hat{O}_1^\dagger\,|m\rangle\,\langle m|\,\hat{O}_2\,|0\rangle\,\delta(\omega)\delta(\boldsymbol{P}_m-\boldsymbol{k}) \\ &+ \frac{(2\pi)^{2D+1}}{L^D}\sum_{n,m}\rho_{\mathrm{i}}^{n0}\delta(\boldsymbol{P}_n)\,\langle 0|\,\hat{O}_1^\dagger\,|m\rangle\,\langle m|\,\hat{O}_2\,|n\rangle\,\delta(E_n+\omega)\delta(\boldsymbol{P}_m-\boldsymbol{k}) \\ &+ \frac{(2\pi)^{2D+1}}{L^D}\sum_{n,m}\rho_{\mathrm{i}}^{0n}\delta(\boldsymbol{P}_n)\,\langle n|\,\hat{O}_1^\dagger\,|m\rangle\,\langle m|\,\hat{O}_2\,|0\rangle\,\delta(E_n-\omega)\delta(\boldsymbol{P}_m-\boldsymbol{k}). \end{aligned} \tag{3.23}$$

For symmetry reasons, the momentum of the ground state is $\boldsymbol{P}_0 = \boldsymbol{0}$. The first term in Eq. (3.23) is space and time independent and thus irrelevant for the dynamics. The last two terms include a resonance at negative and positive frequencies, respectively, associated to the Dirac distributions $\delta(E_n \pm \omega)$. In the following, we focus on the positive frequency sector where only the last term is relevant.

Probing the excitation spectrum. We now detail how Eq. (3.23) allows to probe the excitation spectrum in a momentum-resolved manner in a single shot. The goal is to remove the dependence in n, m and refer to quantities that depend on $\boldsymbol{k}$ or ω only. To do so, we use the fact that the excitations above the ground state can be cast in terms of quasiparticles. Most operators of interest only create or annihilate a single quasiparticle excitation, and as a consequence the

intermediate states $|m\rangle$ can also be restricted to single quasiparticle excitations. We will provide specific examples in the last part of this section.

The term $\delta(\boldsymbol{P}_m - \boldsymbol{k})$ then imposes that $|m\rangle = \hat{\gamma}^\dagger_{\boldsymbol{k}}|0\rangle \equiv |\boldsymbol{k}\rangle$, where $\hat{\gamma}^\dagger_{\boldsymbol{k}}$ is the creation operator of a quasiparticle of momentum $\boldsymbol{k}$. Owing to the term $\delta(\boldsymbol{P}_n)$, the first non-zero contribution is given by states $|n\rangle$ composed of two quasiparticles[5] with opposite momenta such that $|n\rangle = \hat{\gamma}^\dagger_{\boldsymbol{q}}\hat{\gamma}^\dagger_{-\boldsymbol{q}}|0\rangle$. For now $\boldsymbol{q}$ is arbitrary, and neglecting the interactions between the quasiparticles $E_n = E_{\boldsymbol{q}} + E_{-\boldsymbol{q}}$. By decomposing the action of the operators at low energy as (see examples below) $\hat{O}_1 = \sum_{\boldsymbol{k}_1}(\alpha_{\boldsymbol{k}_1}\hat{\gamma}_{\boldsymbol{k}_1} + \bar{\alpha}_{\boldsymbol{k}_1}\hat{\gamma}^\dagger_{\boldsymbol{k}_1})$ and similarly $\hat{O}_2 = \sum_{\boldsymbol{k}_2}(\beta_{\boldsymbol{k}_2}\hat{\gamma}_{\boldsymbol{k}_2} + \bar{\beta}_{\boldsymbol{k}_2}\hat{\gamma}^\dagger_{\boldsymbol{k}_2})$, the positive frequency component of the QSF (3.23) reads as

$$G(\boldsymbol{k};\omega>0) = \sum_{\boldsymbol{q},\boldsymbol{k}_1,\boldsymbol{k}_2} \rho_{\mathrm{i}}^{0;(\boldsymbol{q},-\boldsymbol{q})}\bar{\alpha}_{\boldsymbol{k}_1}\bar{\beta}_{\boldsymbol{k}_2}\langle 0|\,\hat{\gamma}_{\boldsymbol{q}}\hat{\gamma}_{-\boldsymbol{q}}\hat{\gamma}^\dagger_{\boldsymbol{k}_1}\hat{\gamma}^\dagger_{\boldsymbol{k}}|0\rangle\langle 0|\,\hat{\gamma}_{\boldsymbol{k}}\hat{\gamma}^\dagger_{-\boldsymbol{k}_2}|0\rangle\,\delta(E_{\boldsymbol{q}} + E_{-\boldsymbol{q}} - \omega). \tag{3.24}$$

Using (anti-)commutation rules $\hat{\gamma}_{\boldsymbol{u}}\hat{\gamma}^\dagger_{\boldsymbol{v}} = \delta_{\boldsymbol{u},\boldsymbol{v}} \pm \hat{\gamma}^\dagger_{\boldsymbol{v}}\hat{\gamma}_{\boldsymbol{u}}$ (for bosonic and fermionic quasiparticles respectively), we get

$$G(\boldsymbol{k};\omega>0) = \rho_{\mathrm{i}}^{0;(\boldsymbol{k},-\boldsymbol{k})}\bar{\beta}_{\boldsymbol{k}}\,(\bar{\alpha}_{-\boldsymbol{k}} + \bar{\alpha}_{\boldsymbol{k}})\,\delta(E_{\boldsymbol{k}} + E_{-\boldsymbol{k}} - \omega). \tag{3.25}$$

If the excitation branch is symmetric for the exchange $\boldsymbol{k} \to -\boldsymbol{k}$ (parity symmetry), then $E_n = 2E_{\boldsymbol{k}}$ and finally

$$G(\boldsymbol{k};\omega>0) = \mathcal{F}(\boldsymbol{k})\,\delta(2E_{\boldsymbol{k}} - \omega), \tag{3.26}$$

where the coefficient $\mathcal{F}(\boldsymbol{k})$ depends on the operators $\hat{O}_1$ and $\hat{O}_2$, and on the quench through the initial density matrix coefficients between the ground state and the first excited states [see Eq. (3.25)]. Eq. (3.26) justifies the interpretation of the QSF as a direct probe of the excitation spectrum, through the resonance frequencies $\omega = 2E_{\boldsymbol{k}}$. Through the QSF, the study of the correlation spreading after a global quench allows to unravel the excitation spectrum of the post-quench Hamiltonian. We will present numerical evidence of this statement in Sec. 3.2.2.

Specific examples of operators. We argue below that the form of the operators $\hat{O}_1$ and $\hat{O}_2$ used to derive the simple form (3.26) of the QSF encapsulates most of the situations of practical interest and we provide a (non-exhaustive) list of examples.

First, consider the one-body correlation function

$$G_1(\boldsymbol{R},t) = \langle\hat{a}^\dagger(\boldsymbol{R},t)\hat{a}(\boldsymbol{0},t)\rangle = \frac{1}{L^D}\sum_{\boldsymbol{x}}\langle\hat{a}^\dagger(\boldsymbol{x}+\boldsymbol{R},t)\hat{a}(\boldsymbol{x},t)\rangle = \sum_{\boldsymbol{k}}\mathrm{e}^{-i\boldsymbol{k}\boldsymbol{R}}\langle\hat{a}^\dagger_{\boldsymbol{k}}(t)\hat{a}_{\boldsymbol{k}}(t)\rangle, \tag{3.27}$$

where $\hat{a}_{\boldsymbol{k}} = \sum_{\boldsymbol{x}}\mathrm{e}^{-i\boldsymbol{k}\boldsymbol{x}}\hat{a}_{\boldsymbol{x}}$ is the annihilation operator of a particle with momentum $\boldsymbol{k}$. This observable is the Fourier transform of the momentum distribution and can be measured by the time-of-flight and absorption imaging methods discussed in Sec. 1.3.2.1. The function $G_1(\boldsymbol{R},t)$ is an example of the equal-time correlator $G(\boldsymbol{R};t,t)$ where $\hat{O}_1 = \hat{O}_2 = \hat{a}_{\boldsymbol{k}}$. Let us now discuss how the operators $\hat{O}_j$ may be represented in terms of the single-quasiparticle operators. For instance, the Bogoliubov quasiparticles representing the collective excitations of a Bose-Einstein condensate are related to the particle operators by

$$\hat{a}_{\boldsymbol{k}} = u_{\boldsymbol{k}}\hat{\gamma}_{\boldsymbol{k}} + v_{\boldsymbol{k}}\hat{\gamma}^\dagger_{-\boldsymbol{k}}, \tag{3.28}$$

where $u_{\boldsymbol{k}}$ and $v_{\boldsymbol{k}}$ are the solutions of the Bogoliubov-De Gennes equations [Pitaevskii and Stringari, 2016] (Appendix 1.E). A similar linear expression relating single-particle operators to single-quasiparticle operators also holds for the elementary excitations in the strongly interacting Mott

[5] The quasiparticle statistics can be arbitrary, but for fermions in order to obey Pauli's exclusion principle, an additional spin index σ should be introduced. To lighten the notations, such index is kept implicit here.

phase of the Bose-Hubbard model (Appendix 1.D). In both cases, a quasiparticle of momentum $\boldsymbol{k}$ representing a particle excitation dressed by other particles or holes is associated to an annihilation operator $\hat{\gamma}_{\boldsymbol{k}}$, which is a linear combination of the operators $\hat{a}_{\boldsymbol{k}}$ and $\hat{a}^\dagger_{\boldsymbol{k}}$. Reciprocally, the operators $\hat{a}_{\boldsymbol{k}}$ are linear combinations of the operators $\hat{\gamma}_{\boldsymbol{k}}$ and $\hat{\gamma}^\dagger_{\boldsymbol{k}}$. Hence, the operator $\hat{O}_j$ can only create or annihilate a single quasiparticle as assumed to derive Eq. (3.26).

More generally, higher-order operators can be cast in a similar form with generic hydrodynamic formulations. Consider for instance the two-body correlation function

$$G_2(\boldsymbol{R},t) = \langle \hat{n}(\boldsymbol{R},t)\hat{n}(\boldsymbol{0},t)\rangle = \frac{1}{L^D}\sum_{\boldsymbol{x}}\langle \hat{n}(\boldsymbol{x}+\boldsymbol{R},t)\hat{n}(\boldsymbol{x},t)\rangle = \sum_{\boldsymbol{k}} \mathrm{e}^{-i\boldsymbol{k}\boldsymbol{R}}\langle \hat{n}_{\boldsymbol{k}}(t)\hat{n}_{-\boldsymbol{k}}(t)\rangle. \tag{3.29}$$

The latter expression can also be written as $\sum_{\boldsymbol{k}} \mathrm{e}^{i\boldsymbol{k}\boldsymbol{R}}\langle \hat{n}^\dagger_{\boldsymbol{k}}(t)\hat{n}_{\boldsymbol{k}}(t)\rangle$ and shows that $G_2(\boldsymbol{R},t)$ is another example of equal-time correlator $G(\boldsymbol{R};t,t)$ with $\hat{O}_1 = \hat{O}_2 = \hat{n}_{\boldsymbol{k}}$. In the superfluid phase, the density operator may be expanded as $\hat{n} = n_0 + \delta\hat{n}$ where n_0 is a classical field and $\delta\hat{n}$ represents the density fluctuations. The operator $\delta\hat{n}$ can be written, in momentum space as [Pitaevskii and Stringari, 2016]

$$\delta\hat{n}_{\boldsymbol{k}} = A_{\boldsymbol{k}}\left(\hat{b}_{\boldsymbol{k}} + \hat{b}^\dagger_{\boldsymbol{k}}\right). \tag{3.30}$$

Similar to the one-body correlation function, the two-body correlation function can be decomposed in quasiparticle operators. To give a concrete example, the hydrodynamic formulation may be used to describe a weakly interacting Bose gas, where within Bogoliubov theory one finds

$$A_{\boldsymbol{k}} = u_{\boldsymbol{k}} + v_{\boldsymbol{k}}, \tag{3.31}$$

and the quantities $u_{\boldsymbol{k}}$ and $v_{\boldsymbol{k}}$ are again solutions of the Bogoliubov-De Gennes equations. This applies to both condensates [Pitaevskii and Stringari, 2016] and quasi-condensates [Mora and Castin, 2003; Popov, 2001]. More generally, the hydrodynamic formulation may be applied to many correlated systems. For instance, a similar form holds for 1D Luttinger liquids [Giamarchi, 2004]. We finally note that the phase operator, conjugate of the density operator, can also be expanded in terms of single-quasiparticle operators. We refer to Appendix 1.E for further details.

Finally, for spin models in a polarised phase, the Holstein-Primakoff transformation can be used to map each spin operator onto bosonic operators if the deviation of the spin with respect to the mean-field ground state remains small ($\langle \hat{a}^\dagger_{\boldsymbol{R}}\hat{a}_{\boldsymbol{R}}\rangle \ll 1$ for a spin 1/2). In the direction orthogonal to the polarisation axis the mapping is [Auerbach, 1994; Holstein and Primakoff, 1940]

$$\hat{S}^x_{\boldsymbol{R}} \simeq \tfrac{1}{2}\left(\hat{a}_{\boldsymbol{R}} + \hat{a}^\dagger_{\boldsymbol{R}}\right). \tag{3.32}$$

In terms of these bosonic variables, the Hamiltonian is quadratic and can therefore be diagonalised by introducing the linear Bogoliubov transformation in the form of Eq. (3.28). To conclude, in many situations the relevant operators are linear in the quasiparticle annihilation and creation operators. The quench spectral function associated to $G_1(\boldsymbol{R},t)$ in quench spectroscopy and the single-particle spectral function used in pump-probe spectroscopies both correspond to the choice of the operator $\hat{a}_{\boldsymbol{k}}$ (both for the quench/pump and the probe). The same remark applies to the QSF of $G_2(\boldsymbol{R},t)$ and the dynamical structure factor with the choice of $\hat{n}_{\boldsymbol{k}}$.

Quench spectroscopy therefore offers an alternative technique to probe the spectrum. Its main advantage over standard spectroscopies is that it uses the simpler equal-time correlators that can be measured in a single snapshot of the dynamics. By repeating the same quench but capturing the dynamics at a different time, the space-time pattern can be reconstructed, and a space-time Fourier transform then yields the full momentum reconstruction of the excitation spectrum over the Brillouin zone. This avoids the tedious scan over the momentum and each individual calibration for instance of the angle between the mirrors in two-photon Bragg spectroscopy.

3.2.2 Probing excitation spectra from global quench dynamics

In this section, we test numerically quench spectroscopy. We simulate the post-quench dynamics of the system and then compute the associated QSF to detect the full low-lying excitation spectrum. We demonstrate the method on one-dimensional lattice models (bosonic and spin chains) with short and long-range interactions, however it equally applies in higher dimensions, on different models such as continuous ones, or for different statistics such as correlated fermions. In addition to the results presented in our publication [Villa et al., 2019], I included some exact diagonalisation simulations (mainly for comparison purposes).

3.2.2.1 Benchmarks on the Bose-Hubbard chain

We begin by benchmarking quench spectroscopy in two regimes where the excitation spectrum is known, the mean-field superfluid regime and the strongly interacting Mott insulator.

Superfluid in the mean-field regime (Bogoliubov). We initialise the system in its ground state computed with DMRG at fixed $\bar{n} = 5$, and at $t = 0$ we suddenly quench the interaction strength from $(U/J)_\mathrm{i} = 0.2$ to $(U/J)_\mathrm{f} = 0.1$. Here and in the following, the t-MPS simulation parameters are $L = 96$ lattice sites, and an evolution time of $tJ/\hbar = 10$, comparable to state-of-the-art experiments on this model [Trotzky et al., 2012]. To put some numbers, with a typical tunnelling rate of $J/\hbar \sim 100\,\mathrm{Hz}$ this requires the system to remain isolated during at least 100 ms. The bond dimension and the local dimension of the Hilbert space are increased until convergence of the numerical results (Appendix 2.B). This phase corresponds to the mean-field SF ($U/(2J\bar{n}) \ll 1$), where elementary excitations are Bogoliubov quasiparticles with the following dispersion relation

$$E_k = 2J\sqrt{2\sin^2(\tfrac{k}{2})\left[2\sin^2(\tfrac{k}{2}) + \bar{n}\tfrac{U}{J}\right]}, \tag{3.33}$$

gapless and linear for $k \to 0$. The after-quench dynamics is displayed in Fig. 3.1, for the connected density-density correlation function $G_2(R,t)$ and the one-body density matrix $G_1(R,t)$, both averaged over the initial state. The twofold structure for the correlation spreading can be observed, especially in $G_2(R,t)$ as discussed in Sec. 2.2.1. By taking the Fourier transform of each space-time pattern we obtain the associated QSF. Here and throughout the thesis, we show its normalised modulus. To improve visibility, we sometimes remove the $\omega = 0$ component (time-independent part) irrelevant for the dynamics, and cut off the colorbars after a fraction of their maximum value [*e.g.* Fig. 3.1(d)]. Each QSF displays a sharp resonance along the line $\omega = 2E_k$, in excellent agreement with the prediction of Eq. (3.26) where the excitation spectrum E_k is given by Eq. (3.33).

In the space-time pattern of $G_1(R,t)$, the linear cone is barely visible. Nonetheless, the QSF is also capable of extracting the excitation spectrum E_k with a reasonable accuracy. This shows the efficiency of quench spectroscopy to probe the excitation spectrum in a many-body quantum system, for different choices of the observable.

Strongly interacting Mott insulator. We again initialise the system in its ground state for $\bar{n} = 1$ at $(U/J)_\mathrm{i} = 25$, and at $t = 0$ we quench the interaction ratio to $(U/J)_\mathrm{f} = 26$. We probe G_1 and the following dynamics is represented in Fig. 3.2(a) (the double structure discussed in Chap. 2 is visible in the inset). Taking the space-time Fourier transform we compute the QSF and display the result in Fig. 3.2(b), where we rescaled the energies ω by U rather than J for convenience. The resonance of the QSF is in excellent agreement with twice the expected excitation spectrum as predicted by Eq. (3.26), the latter of which in the strongly interacting MI can be simply understood as a superposition of doublon-holon pairs with dispersion relation (Appendix 1.D)

$$2E_k \simeq J\sqrt{\left(\tfrac{U}{J} - 6\cos k\right)^2 + 32\sin^2 k}. \tag{3.34}$$

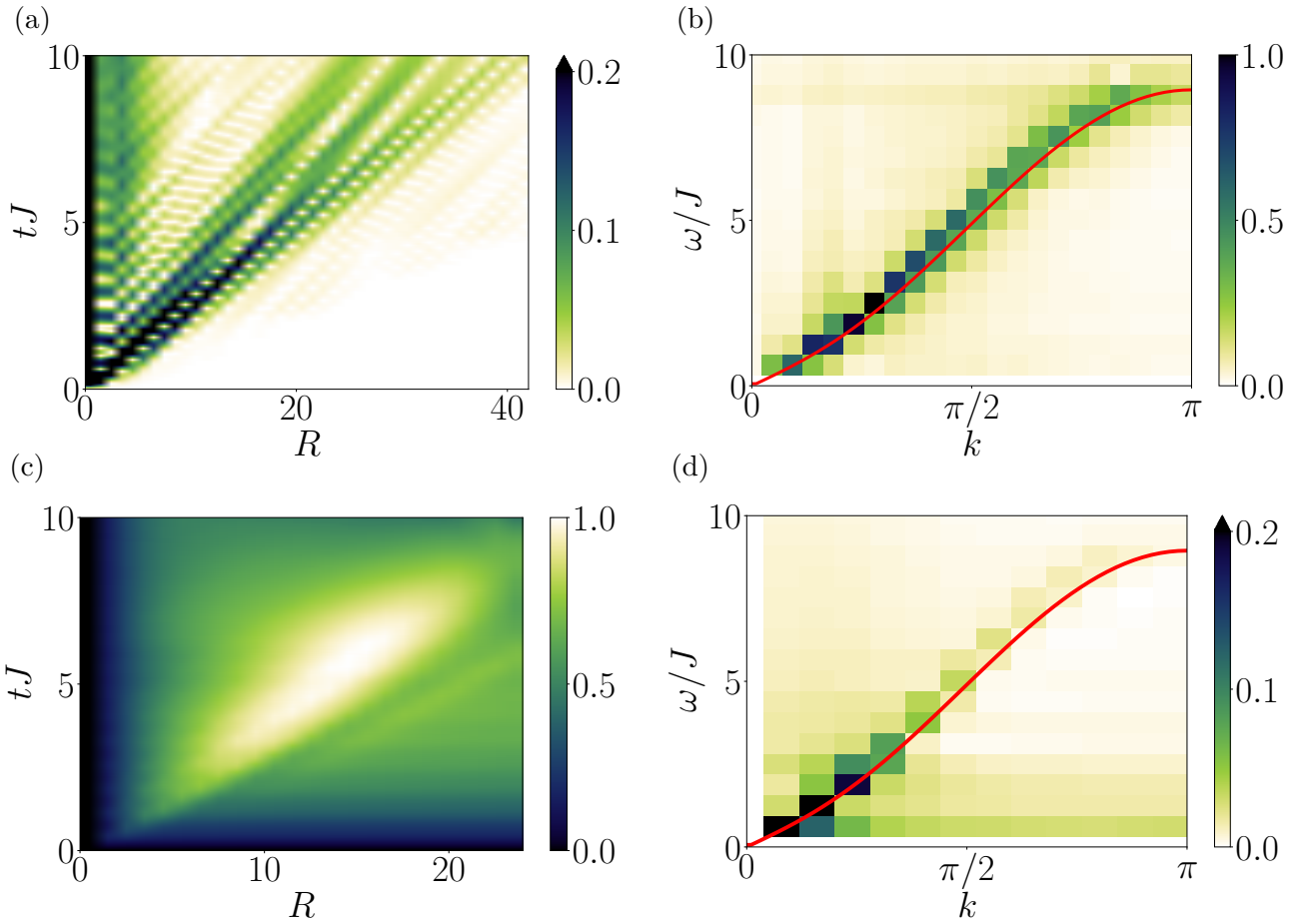

Fig. 3.1 (a) Space-time pattern of $G_2(R,t)$ (absolute value) following a global quench in the mean-field SF at fixed $\bar{n} = 5$ from $(U/J)_\mathrm{i} = 0.2$ to $(U/J)_\mathrm{f} = 0.1$. (b) Modulus of the associated QSF (normalised) and comparison with twice the expected Bogoliubov spectrum Eq. (3.33) (red line). Same for (c) and (d) with $G_1(R,t)$ instead. The space-time pattern is more blurred, but the excitation spectrum can still be reconstructed from the QSF (note however the cutoff on the colorbar to 20% of the maximum to improve visibility). The $\omega = 0$ component (irrelevant for the dynamics) and the spatial average $k = 0$ have been removed to improve visibility. Adapted from [Villa et al., 2019].

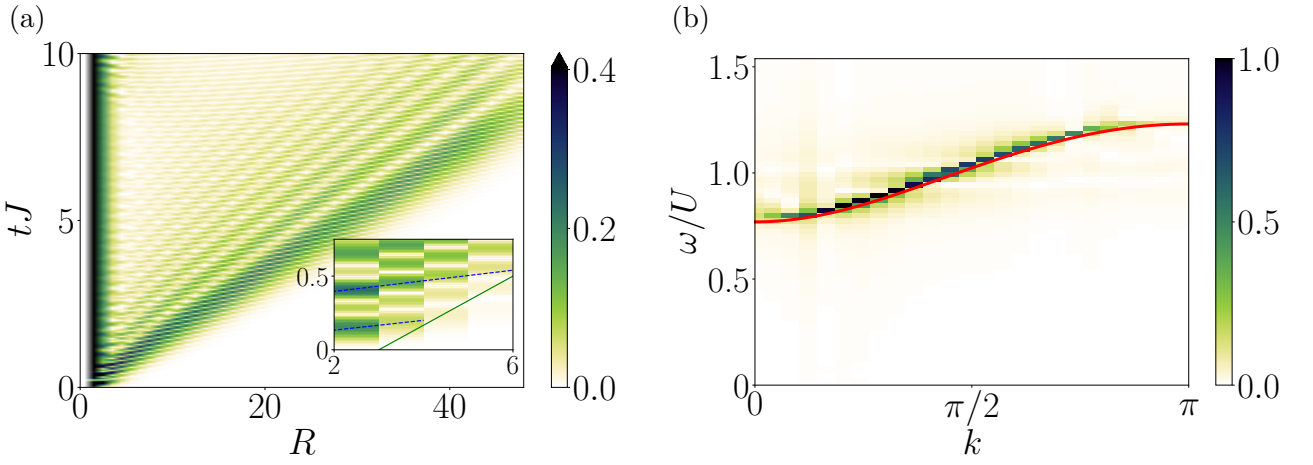

Fig. 3.2 Strongly interacting MI from $(U/J)_\mathrm{i} = 25$ to $(U/J)_\mathrm{f} = 26$ at fixed $\bar{n} = 1$. (a) Signal observed for G_1. (b) Associated QSF modulus, and comparison with dispersion relation for a pair of excitations (3.34) (red line). Adapted from [Villa et al., 2019].

It is important to stress here that due to the global quench, a pair of excitations with opposite momenta is emitted. To ensure particle number conservation, these reduce in the strongly inter-

acting regime to a doublon and a holon excitation. The QSF computed after a global quench is not sensitive to the individual excitations, but rather to their indissociable pair [Eq. (3.26)]. This will contrast to local quench spectroscopy which follows the dynamics after local quenches, as discussed in Sec. 3.3.

In this regime, we note that probing $G_1(R,t)$ is essential because $G_2(R,t)$ leads to a faint signal in real space. This can be understood qualitatively since the ground state in the strongly interacting MI is nearly an eigenstate of the local density operator. Thus the couplings with the excited states $\langle m|\,\hat{n}\,|0\rangle$ in the last line of Eq. (3.23) (positive frequency component of the QSF) are strongly suppressed. For the detailed discussion of the suppression of density fluctuations in this phase, we refer back to Sec. 2.2.3.

3.2.2.2 The strongly interacting superfluid regime

Having validated the approach in well-known regimes, we now explore using quench spectroscopy the more involved strongly interacting superfluid phase with $U/J \gg 1$ and non-integer filling, where the excitation spectrum is not known analytically. More precisely, the model may be mapped to an effective fermionic model and the speed of sound evaluated (Appendix 2.C), but as we have discussed previously in Sec. 2.2.4, the speed of sound does not match with the velocities extracted from the dynamics. Therefore, the excitation spectrum possesses modes beyond the phononic regime which are beyond the Luttinger regime, and another approach needs to be developed to understand such higher energy modes. We will show how for low fillings and strong interactions, an approximate Bethe ansatz approach may be used to describe the observed spectrum.

To reach the strongly interacting regime, we quench the interaction parameter from $(U/J)_\mathrm{i} = 40$ to $(U/J)_\mathrm{f} = 50$ at fixed fillings between $0 < \bar{n} < 1$. We display in Fig. 3.3 the modulus of the QSF for four characteristic values, with fillings $\bar{n} = 0.1$, 0.2, 0.5 and 0.9 respectively. The speed of sound predicted by the effective Luttinger theory (Appendix 2.C) is represented by the dashed blue line, and the result obtained from the approximate Bethe ansatz approach is represented by the red dash-dotted envelope. We already note that at small fillings, the approximate Bethe ansatz approach accounts very well for the resonances observed in the QSF, and therefore captures correctly the observed excitation spectrum. Surprisingly, the prediction remains acceptable for $\bar{n} \lesssim 0.5$, but becomes worse and worse as the filling increases, as shown for $\bar{n} = 0.9$. We will interpret this in the following by explaining how the approach is built.

Approximate Bethe ansatz. The Lieb-Liniger model (continuum counterpart of the Bose-Hubbard model) can be solved exactly using the Bethe ansatz and the excitation spectrum computed (Appendix 1.A). However, in a lattice some positions at the local minima of the lattice potential are privileged, and this breaks integrability. More precisely, the integrability breaking can be related to the presence of triply occupied sites allowed by the bosonic statistics and which cannot be properly accounted for by the Bethe ansatz [Choy and Haldane, 1982; F. Haldane, 1980; Sutherland, 2004]. However, for strong interactions and low filling, such highly occupied sites become less probable, and one can hope to evaluate approximately thermodynamic quantities using the Bethe ansatz. We focus here on the essential elements of the approach and postpone the technical details to Appendix 3.A. It was first noted by [Krauth, 1991] that for $0 < \bar{n} < 1$ and $U/J \gg 1$ this approximate Bethe ansatz method could accurately describe ground state properties, assuming the following approximate Bethe equations to hold

$$k_j L = 2\pi I_j + \sum_{l=1}^{N} \theta\left(\sin k_j - \sin k_l\right), \tag{3.35}$$

with the two-particle phase shift defined by $\theta(k) = -2\arctan\left(\frac{2J}{U}k\right)$. In Eq. (3.35), k_j refers to the quasimomentum of the particle j, and I_j its quantum number, which is an integer assuming N is

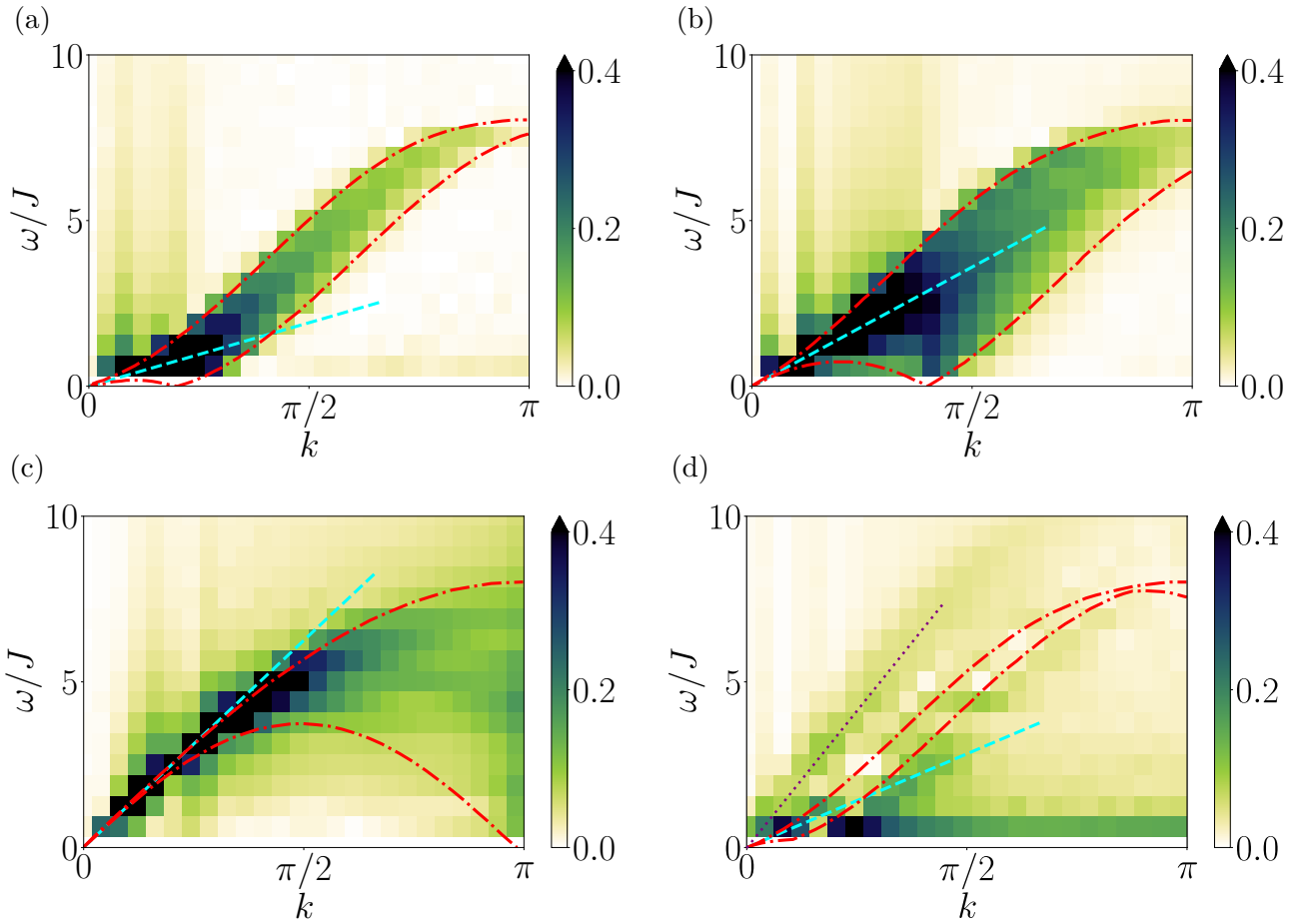

Fig. 3.3 Normalised QSF modulus of G_2 in the strongly interacting superfluid regime for a quench from $(U/J)_\mathrm{i} = 40$ to $(U/J)_\mathrm{f} = 50$ with (a) $\bar{n} = 0.1$ (b) $\bar{n} = 0.2$, (c) $\bar{n} = 0.5$ and (d) $\bar{n} = 0.9$. The dashed dotted red line marks the envelope predicted by the approximate Bethe ansatz approach and the blue line gives the speed of sound predicted by the effective Luttinger model. A dotted violet line highlights the phononic mode appearing at high filling. Adapted from [Villa et al., 2019].

odd. In the ground state, the particles are ordered such that the quantum numbers I_j are real, equidistant and monotonously increasing with j.

What we propose is to take the approximation further in order to describe the behaviour of the excitations. The latter require to add and remove particles from the ground state, so we can already expect that the validity regime found above for the ground state properties will be more restricted, typically $\bar{n} \ll 1$ and $U/J \gg 1$ so that the triply occupied sites are almost irrelevant also for the excitations in the thermodynamic limit. Similarly to the Lieb-Liniger model, the excitations can be built by moving a particle (denoted by the index $j = \alpha$) from within the Fermi sea above it. The Fermi level in quasimomentum space has quasimomentum k_F. To build an excitation, the distribution of quantum numbers I_j is unchanged compared to the ground state $\forall j \neq \alpha$, except that $I_{j=\alpha}$ becomes $I^\star_\alpha \neq I_\alpha$ (the label "$\star$" marks the excitation). After this move, all quasimomenta redistribute in quasimomentum space due to interactions between the particles, such that $\forall j \neq \alpha$, $\Delta k_j = k^\star_j - k_j$. We want to compute the energy and momentum difference between the excited state and the ground state, defined by

$$\begin{aligned} P &= \sum_{j=1}^{N} k^\star_j - k_j \\ \Delta E &= \sum_{j=1}^{N} \left[-2J\cos k^\star_j\right] - \left[-2J\cos k_j\right]. \end{aligned} \tag{3.36}$$

Taking the difference of Eq. (3.35) for the ground state and the first excited state, and restricting to lowest order in $\Delta k_j \ll k_j$, we can show that in the thermodynamic limit[6]

$$2\pi J(k) = \frac{U}{J}\int_{-k_\mathrm{F}}^{k_\mathrm{F}} \frac{J(k')\cos k'\,\mathrm{d}k'}{\left(\frac{U}{2J}\right)^2 + [\sin k - \sin k']^2} + \theta(\sin k - \sin k^\star_\alpha) - \theta(\sin k - \sin k_\alpha), \tag{3.37}$$

where $J(k_j) = \Delta k_j/(k_{j+1} - k_j)$. This function, called the backflow, accounts for the relative redistribution due to interactions (at lowest order) in the excited state compared to the original spacing in the ground state. Equation (3.37) can be solved numerically to obtain the backflow for a given interaction value and particle number. This function can then be used to compute the energy and momentum since by expanding Eq. (3.36) to lowest order in Δk_j, using the backflow definition and moving to the thermodynamic limit

$$\begin{aligned} P &= k^\star_\alpha - k_\alpha + \int_{-k_\mathrm{F}}^{k_\mathrm{F}} J(k)\,\mathrm{d}k \\ \frac{\Delta E}{J} &= -2\left[\cos(k^\star_\alpha) - \cos(k_\alpha)\right] + 2\int_{-k_\mathrm{F}}^{k_\mathrm{F}} J(k)\sin k\,\mathrm{d}k. \end{aligned} \tag{3.38}$$

These particle-hole excitations form a continuum $\Delta E(P)$ for $-k_\mathrm{F} < k_\alpha < k_\mathrm{F}$ and $k_\mathrm{F} < k^\star_\alpha < \pi$ (by symmetry $-\pi < k^\star_\alpha < -k_\mathrm{F}$ for $P < 0$). The envelope of $2\Delta E(P)/J$ is represented by the dash-dotted red line in Fig. 3.3 for the associated parameters, and shows excellent agreement with the resonances observed in the QSF at low filling. The excitations after the global quench can therefore be thought of as pairs of particle-hole excitations (*i.e.* pairs of pairs) propagating through the lattice. It appears that the backflow contribution is relatively small in the strongly interacting regime, so that, to a good approximation, the pairs of excitations do not interact much with each other (fermionised regime). At half-filling, the excitation continuum of the particle-hole pair merges into a single branch near the origin, whose velocity coincides with the speed of sound $V_\mathrm{s} = 2Ja/\hbar$ found by mapping the Bose-Hubbard chain in this regime to an effective Luttinger liquid model (Appendix 2.C). For higher fillings, typically $\bar{n} \gtrsim 0.5$, the agreement with the approximate Bethe ansatz breaks down. This is expected as three-body (or more than three) collisions become relevant and considerably alter the quasi-integrability of the model. A sound-like mode also emerges at high filling (see Fig. 3.3(d), dotted violet line) but its velocity $2V \simeq 4.8Ja/\hbar$ is significantly different from the one of the phonon pair $2V_\mathrm{s} = 1.4Ja/\hbar$ predicted by the mapping to the effective fermionic model (see Appendix 2.C for the derivation and the expression of the speed of sound). While the physical nature this branch remains to be determined, we note that its observation is consistent with the emergence of a unique characteristic velocity, faster that the speed of sound, in the vicinity of the causal cone (Fig. 2.12).

Effect of the lattice on the dynamics. It is fruitful to compare the previous results with the continuum limit corresponding to the integrable Lieb-Liniger model. This comparison allows to understand to what extent the lattice affects the underlying dynamics of the excitations.

In Fig. 3.4 we superimpose the excitation spectrum predicted by the previously discussed approximate Bethe ansatz approach on the lattice model (dash-dotted red line), together with the equivalent continuum excitation spectrum ($\gamma = U/(2J\bar{n})$, dashed blue line) discussed in Appendix 1.A. As expected, the comparison highlights that the lattice is crucial to the system dynamics, whatever the filling, especially to reproduce the breaking of convexity of the excitation continuum at higher momenta.

[6]For the full derivation, see Appendix 3.A.

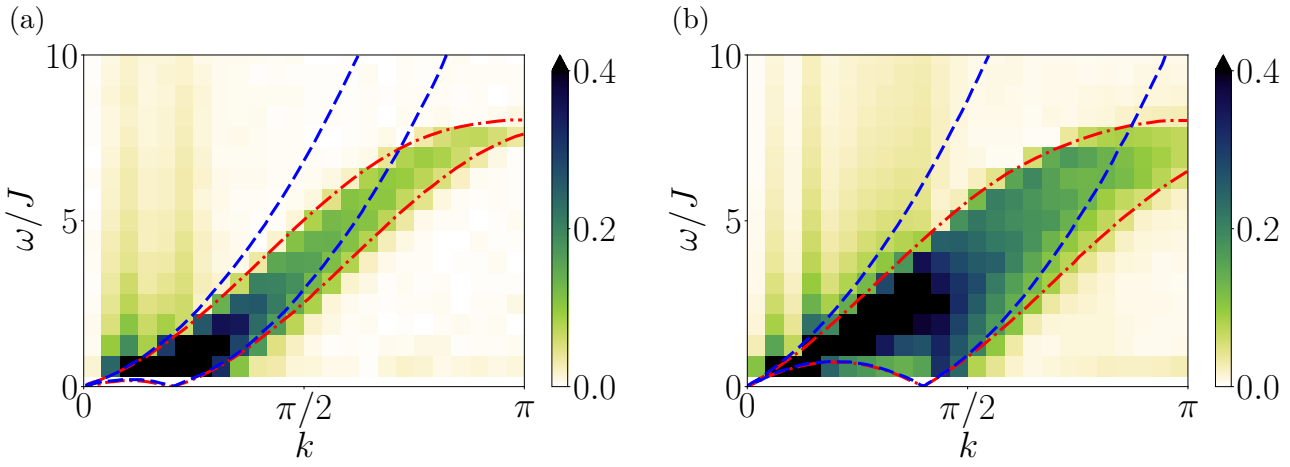

Fig. 3.4 Same as Fig. 3.3(a) and 3.3(b) with a comparison between the predicted excitation spectrum from the Bethe ansatz on the Lieb-Liniger model (blue) and the approximate Bethe ansatz on the Bose-Hubbard chain (red). Adapted from [Villa et al., 2019].

3.2.2.3 Spin chains

Quench spectroscopy can be used to unravel spectral properties in various models, here we investigate the transverse-field Ising chain, first with short-ranged interactions where an exact analytical solution for the excitation spectrum is known, and then we will discuss the challenging quasi-local regime in the presence of long-range interactions. In both cases, we show that quench spectroscopy can reconstruct the excitation spectrum efficiently.

Transverse-field Ising chain (short-ranged). This model has been already discussed in Sec. 1.1.3 to which we refer for details. We simply recall its Hamiltonian[7]

$$\hat{H} = J \sum_{R<R'} \hat{\sigma}^x_R \hat{\sigma}^x_{R'} - h \sum_R \hat{\sigma}^z_R \tag{3.39}$$

and its exact excitation spectrum

$$E_k = 2J\sqrt{1 + (\tfrac{h}{J})^2 + \tfrac{2h}{J}\cos k}. \tag{3.40}$$

This model offers a simple example because we can guess the observables that yield the excitation spectrum. From the Holstein-Primakoff transformation in the strongly z-polarised phase, we know that $\hat{S}^{\pm}_R = \hat{a}^{(\dagger)}_R/2$ such that $\hat{\sigma}^x_R = \hat{a}^\dagger_R + \hat{a}_R$ and $\hat{\sigma}^y_R = i\left(\hat{a}^\dagger_R - \hat{a}_R\right)$ are both linear in the quasiparticle operators and can be used to unravel the excitation spectrum. We report in Fig. 3.5 the space-time pattern of the observable $\langle \hat{\sigma}^y(R,t)\hat{\sigma}^y(L/2,t)\rangle$ from a quench within the z-polarised phase where $h_\mathrm{i} = 3.3$ to $h_\mathrm{f} = 3$, and $J = \pm 1$. This simulation is performed on a chain of length $L = 17$ sites using exact diagonalisation. The spectral maxima visible in the QSF match well with the expected excitation spectrum (red line). Despite visible finite size effects, an accurate reconstruction of the excitation spectrum is possible from the QSF. Choosing the observable $\langle \hat{\sigma}^x(R,t)\hat{\sigma}^x(L/2,t)\rangle$ also yields similar results (not shown), as expected from the mapping above.

Long-range interactions. In the long range case, the Hamiltonian reads[8]

$$\hat{H} = \sum_{R<R'} \frac{J}{|R-R'|^\alpha} \hat{\sigma}^x_R \hat{\sigma}^x_{R'} - h \sum_R \hat{\sigma}^z_R. \tag{3.41}$$

[7] I apologise for changing the sign of the nearest-neighbour interaction term throughout this part. Beware that it changes a sign below the square root for the excitation spectrum, and thus its concavity.

[8] As the notations used here differ from [Villa et al., 2019] by a factor of 2 in front of the nearest-neighbour interaction term J, I have redrawn the figures to match the notations in the thesis.

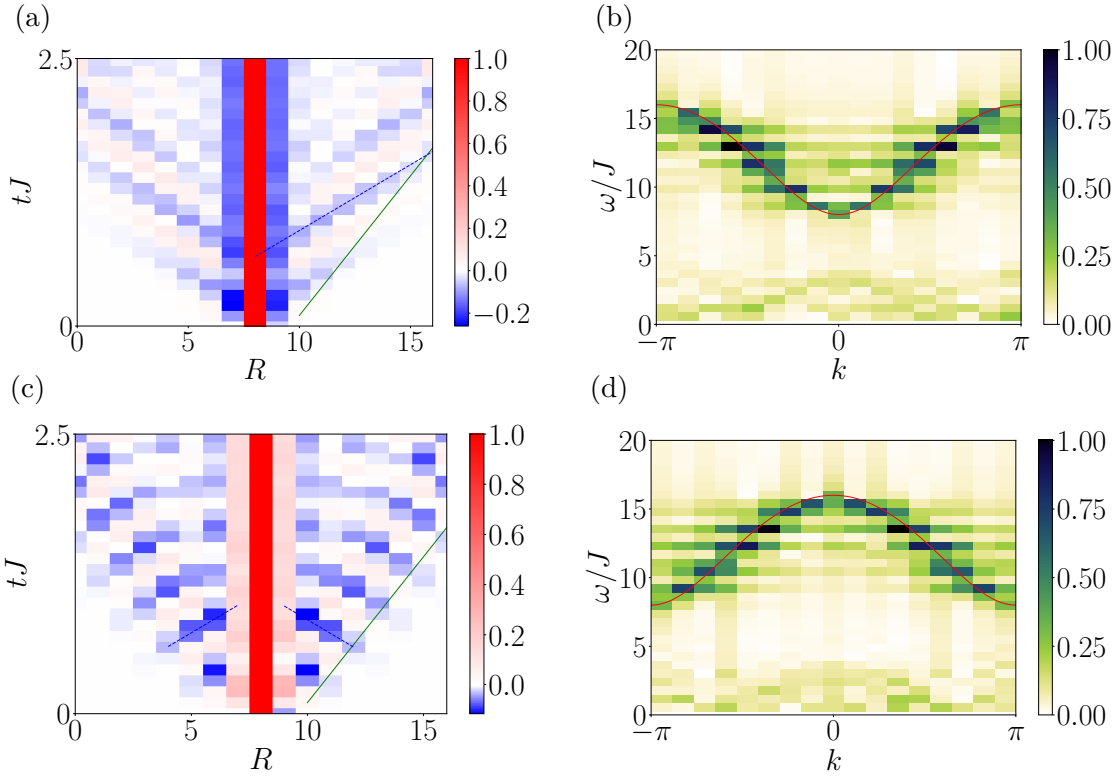

Fig. 3.5 (a) Space-time pattern of $\langle \hat{\sigma}^y(R,t)\hat{\sigma}^y(L/2,t)\rangle$ computed by exact diagonalisation on a short-range transverse-field Ising chain with $L = 17$ and periodic boundary conditions. The global quench performed, using the conventions of Eq. (3.41) is with $J = -1$ and $h_\mathrm{i} = 3.3$ to $h_\mathrm{f} = 3$. Only a fourth of the total evolution time is represented to highlight the different velocities for the propagation of the local maxima (dashed blue) and of the correlation edge (green). The associated slopes represent $2v^\star_\varphi$ and $2v^\star_\mathrm{g}$ from the quasiparticle picture. (b) Associated QSF and comparison with twice the analytical excitation spectrum (red) of Eq. (3.41). (c) and (d) are identical but with $J = 1$ (antiferromagnetic order). Note the different propagation fronts of the local maxima close to the edge compared to $J = -1$ (ferromagnetic order).

For $h/J \gg 1$, using linear spin-wave theory one can show that [Cevolani et al., 2016; Hauke and Tagliacozzo, 2013]

$$E_k \simeq 2J\sqrt{\tfrac{h}{J}\left[\tfrac{h}{J} + 2P_\alpha(k)\right]}, \tag{3.42}$$

where $P_\alpha(k) = \mathrm{FT}\left[\frac{1}{|R|^\alpha}\right]$. We numerically simulate using t-MPS the dynamics of the transverse spin-spin correlation function $\langle \delta\hat{S}^x(R,t)\delta\hat{S}^x(0,t)\rangle$ with $\delta\hat{S}^x(R,t) = \hat{S}^x(R,t) - \langle\hat{S}^x(R,t)\rangle$ for a $L = 48$ sites chain after global quenches in the quasi-local regime with the interaction power-law coefficient $\alpha = 1.8$, from $(h/J)_\mathrm{i} = 100$ to $(h/J)_\mathrm{f} = 40$ and to $(h/J)_\mathrm{f} = 2$. We then take the space-time Fourier transform to compute the QSF and we display our results in Fig. 3.6. Similar results are obtained for $\langle \delta\hat{S}^y(R,t)\delta\hat{S}^y(0,t)\rangle$ (not shown). We observe an excellent agreement between $2E_k$ computed from linear spin-wave theory in the strongly polarised regime and the resonances of the QSF. Closer to the critical point, where the polarisation along z is not as pronounced, a sharp line is still observed in the QSF, suggesting that well-defined quasiparticles can still be defined in this regime. Even though the spectrum strongly deviates from the linear spin-wave result of Eq. (3.42), especially close to the edges of the Brillouin zone, one may compare with a guess based on the exact short-range result given by $E_k \simeq 2J\sqrt{1 + (\frac{h}{J})^2 + \frac{2h}{J}P_\alpha(k)}$, which shows good agreement with the QSF. A deviation only appears at short k, which is to be expected considering the finite size of the system. This suggests a small change in the linear spin-wave excitation spectrum that becomes relevant near the critical point.

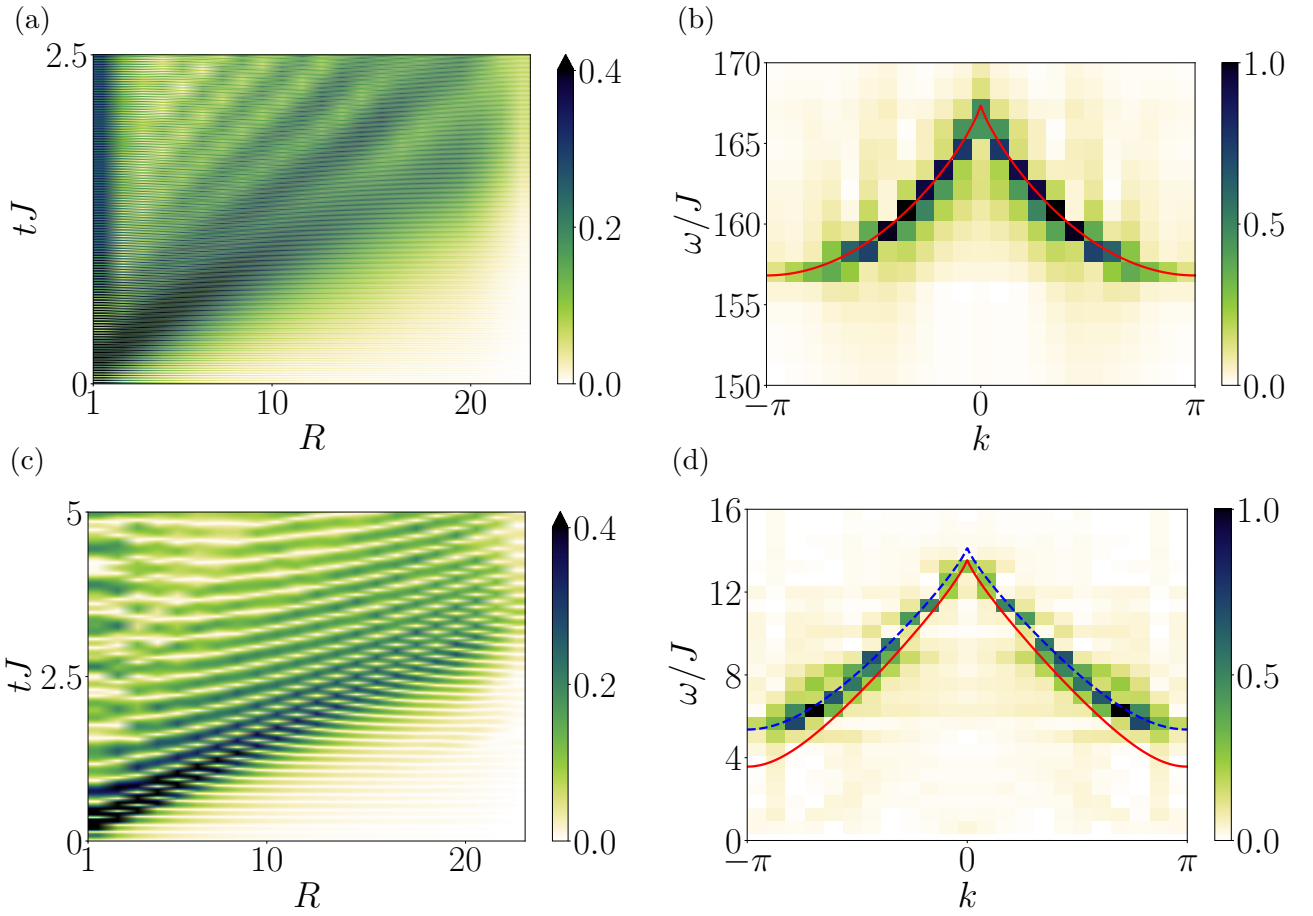

Fig. 3.6 (a) Space-time pattern of the absolute value of the spin-spin connected correlation function $\langle \delta\hat{S}^x(R,t)\delta\hat{S}^x(0,t)\rangle$ with $\delta\hat{S}^x(R,t) = \hat{S}^x(R,t) - \langle\hat{S}^x(R,t)\rangle$ computed from t-MPS with $L = 48$ for the long-range transverse-field Ising model for a quench in the quasi-local regime $\alpha = 1.8$ from $(h/J)_\mathrm{i} = 100$ to $(h/J)_\mathrm{f} = 40$. (b) Normalised modulus of the QSF, in excellent agreement with twice the excitation spectrum (3.41) (red line). (c) and (d) are similar but for a quench from $(h/J)_\mathrm{i} = 100$ to $(h/J)_\mathrm{f} = 2$ (the critical point is slightly below $(h/J)_\mathrm{c} \simeq 1.4$ in our units [Koffel et al., 2012]). The maximum of the QSF does not agree well with twice the expected linear-spin wave spectrum (red line), but is in rather good agreement with a guess based on the exact short-range result (dashed blue). Adapted from [Villa et al., 2019].

An aside on the weak quench hypothesis. One may wonder whether the weak quench assumption (necessary to explain why the QSF was able to unravel the excitation spectrum) is still valid for the quenches used in Fig. 3.6 (especially the second one). We have tested this assumption using exact diagonalisation by comparing with quenches having a lower amplitude, from $(h/J)_\mathrm{i} = 44$ to $(h/J)_\mathrm{f} = 40$ and from $(h/J)_\mathrm{i} = 2.2$ to $(h/J)_\mathrm{f} = 2$. We display our results in Fig. 3.7. Even though the system size used is small ($L = 13$ sites) and finite size effects are important, the results found for the QSF are similar to the ones obtained using DMRG. By comparing the weak and strong quenches, only very small differences can be found, barely visible for the quench closer to the critical point. This highlights the important property that the QSF is not very sensitive to the initial state, as expected since it probes the excitation spectrum of the final Hamiltonian (the one governing the time evolution). Of course, this is also because we normalise it and the numerical errors are negligible. In experiments, the stronger the quench, the easier it will be to detect a signal and thus the lower the uncertainty on the QSF. This also shows that the weak quench hypothesis is not a binding assumption. As long as we do not cross any phase transition, in most cases the initial state (ground state of the pre-quench Hamiltonian) remains close to the ground state of the post-quench Hamiltonian governing the dynamics, and the weak quench hypothesis holds.

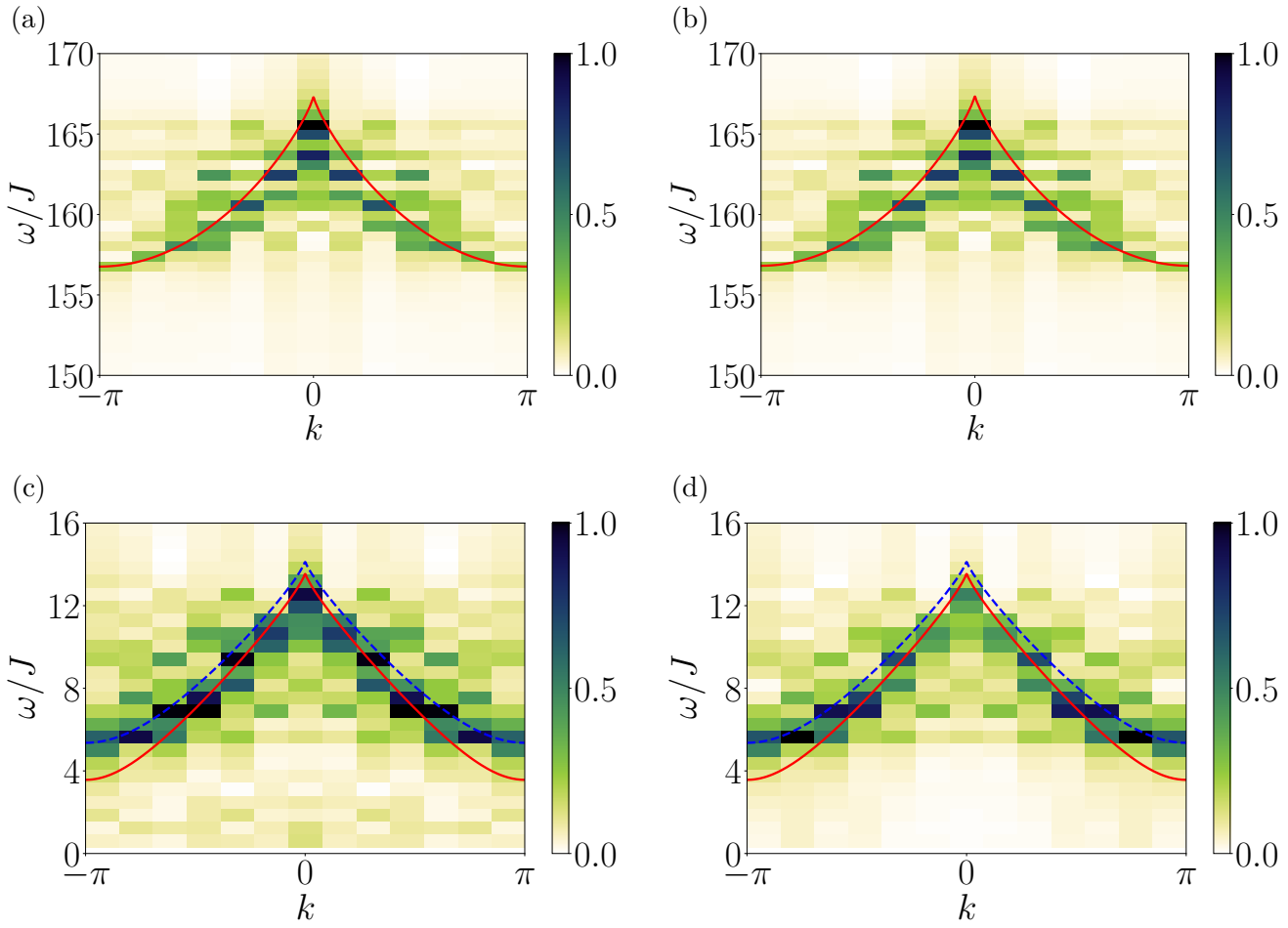

Fig. 3.7 QSF computed from exact diagonalisation simulations on a chain of size $L = 13$. (a) Same parameters as Fig. 3.6(b) and (b) for a weaker quench starting from $(h/J)_{\mathrm{i}} = 44$. (c) Same parameters as Fig. 3.6(d) and (d) for a weaker quench from $(h/J)_{\mathrm{i}} = 2.2$ to $(h/J)_{\mathrm{f}} = 2$.

3.2.3 Link with the generic form of two-point correlators after a global quench

Last but not least, we conclude this part about global quench spectroscopy by highlighting the connection between the QSF and the generic form of equal-time two-point correlators after a global quench which we recall reads as

$$G(\boldsymbol{R},t) = g(\boldsymbol{R}) - \int \frac{\mathrm{d}\boldsymbol{k'}}{(2\pi)^D}\, \mathcal{F}(\boldsymbol{k'}) \frac{\mathrm{e}^{i(\boldsymbol{k'}\boldsymbol{R}+2E^{\mathrm{f}}_{\boldsymbol{k'}}t)} + \mathrm{e}^{i(\boldsymbol{k'}\boldsymbol{R}-2E^{\mathrm{f}}_{\boldsymbol{k'}}t)}}{2}. \tag{3.43}$$

The generality of such form was realised by [Cevolani et al., 2015, 2016; Cevolani et al., 2018], demonstrated on translation invariant quadratic models after a global quench and expected to be more generally valid. Our previous discussion of the QSF explains why such form captures well the dynamics after global quenches. Indeed, taking the space-time Fourier transform of Eq. (3.43) immediately yields (up to an irrelevant term for the dynamics only modifying the $\omega = 0$ behaviour of the QSF)

$$\begin{aligned} G(\boldsymbol{k},\omega) &\propto \int \mathrm{d}\boldsymbol{k'}\, \delta(\boldsymbol{k'}-\boldsymbol{k})\, \mathcal{F}(\boldsymbol{k'}) \left[\delta(2E^{\mathrm{f}}_{\boldsymbol{k'}}-\omega) + \delta(2E^{\mathrm{f}}_{\boldsymbol{k'}}+\omega)\right] \\ &\propto \mathcal{F}(\boldsymbol{k}) \left[\delta(2E^{\mathrm{f}}_{\boldsymbol{k}}-\omega) + \delta(2E^{\mathrm{f}}_{\boldsymbol{k}}+\omega)\right], \end{aligned} \tag{3.44}$$

which is simply Eq. (3.26). The previous discussion of the QSF also reveals in which regimes the generic form can be expected to hold, since the QSF and the generic form are two sides of the

same coin. First, the initial state has to be translation invariant (implicitly assumed by [Cevolani et al., 2016] since the initial state was the ground state of the translation invariant pre-quench Hamiltonian). But it is also important that the observables $\hat{O}_1$ and $\hat{O}_2$ linearly couple to the quasiparticle excitations. As we argued, this is very often (but not always) the case.

Resolution of quench spectroscopy. Equation (3.43) has another practical advantage, somehow allowing for an easier discussion of the resolution of our method both in space and time. Indeed, the signal probed in experiments or numerical simulations is finite, in contrast to the generic form which is valid in the thermodynamic limit. To account for finite size effects both in space and time, we may convolve the QSF with a step function both in space and in time such that the quench spectral function we probe is rather[9]

$$\tilde{G}(k,\omega) = \mathrm{e}^{\frac{i\omega T}{2}} \int_{-L/2}^{L/2} \mathrm{d}R \int_0^T \mathrm{d}t\, G(R,t)\, \mathrm{e}^{-i(kR+\omega t)}. \tag{3.45}$$

Inserting Eq. (3.43) in (3.45) and making use of standard properties of the Fourier transform we end up with

$$\tilde{G}(k,\omega) = \int_{\mathcal{B}} \mathrm{d}q\, \frac{\mathcal{F}(q)}{2}\, L\, \mathrm{sinc}\left(\tfrac{(k-q)L}{2}\right) \left[\mathrm{e}^{-iE_qT}\, T\, \mathrm{sinc}\left(\tfrac{(\omega+2E_q)T}{2}\right) + \mathrm{e}^{iE_qT}\, T\, \mathrm{sinc}\left(\tfrac{(\omega-2E_q)T}{2}\right)\right]. \tag{3.46}$$

This expression allows to estimate the resolution of quench spectroscopy from the typical width of the sinc function, close to π. Therefore the resolution of the method is about $\Delta k \simeq 2\pi/L$ in momentum and similarly $\Delta\omega \simeq 2\pi/t_{\mathrm{max}}$ in frequency [Villa et al., 2019]. For the values given in Sec. 3.2.2, $t_{\mathrm{max}} = 10\hbar/J$ and $J/\hbar = 100\,\mathrm{Hz}$, this gives a frequency resolution for the spectrum of about 10 Hz.

3.3 Local quench spectroscopy

In Sec. 3.2, we showed how the excitation spectrum of a translation invariant many-body quantum system could be obtained from the dynamics of equal-time correlators following a global quench. After the sudden weak global quench, the system generates a bunch of low-lying quasiparticle excitations and follows an out-of-equilibrium dynamics. Spectral properties of the elementary excitations can be uncovered by Fourier transforming the two-point equal-time correlator which defines the quench spectral function (QSF) and displays divergences in frequency at twice the excitation spectrum. Importantly, a global quench preserves translation invariance such that the use of two-point correlators was required to probe the excitation spectrum.

In contrast, local quenches break the translation invariance of the initial state. We will show that spectral properties can still be revealed, this time by following the dynamics of the simpler one-point observables (acting on a single lattice site). This makes local quench spectroscopy an experimentally promising technique, already within the reach of current-generation experiments [Fukuhara, Kantian, et al., 2013; Fukuhara, Schauß, et al., 2013]. A particularly interesting point is that despite the fact that the excitations can be extended, the full dynamical pattern of a well-chosen local probe can prove sufficient to reconstruct spectral properties throughout the full Brillouin zone. This avoids to explicitly construct the excitation site by site in order to measure its properties, as performed recently by [Jurcevic et al., 2015]. We will benchmark the approach on a variety of spin and particle one-dimensional models, but as for global quench spectroscopy, the method applies equally well to different models or higher-dimensional systems.

This local quench spectroscopy project is the result of a collaboration, and I would like to particularly thank S.J. Thomson who performed all the t-MPS numerical simulations presented

[9] The factor $\mathrm{e}^{\frac{i\omega T}{2}}$ compensates the shift due to the non-symmetric time integration domain. It will not matter in the final expression where we compute the modulus of the QSF.

below. Throughout this section, we closely follow our publication [Villa et al., 2020]. In Sec. 3.3.1 we highlight the differences between local and global quench spectroscopies, which lead us to a redefinition of the QSF. We show that the non-equilibrium dynamics following a *single* local quench out of the ground state is sufficient to unveil spectral properties. As in any spectroscopic method, the choice of the observable is crucial, and the local quench protocol required to probe the spectrum is discussed in Sec. 3.3.2. The next three sections explicitly use local quench spectroscopy on various models to probe different properties of the excitations: the excitation spectrum in Sec. 3.3.3, the transition energies in Sec. 3.3.4 and additional information on higher energy excited states with different types of excitations in Sec. 3.3.5.

3.3.1 The need for a new definition of the QSF for local quenches

Motivations and differences with the global quench. We first recall that in a local quench, the Hamiltonian of the system is unchanged but the initial state is modified at $t = 0$ by a local operator $\hat{L}$ acting on the ground state of the Hamiltonian such that for $t = 0^+$, $|\psi_\mathrm{i}\rangle = \hat{L}\,|0\rangle$. For the moment, the specific operator $\hat{L}$ under consideration does not matter. However, it is important to note that the quench spectral function (QSF) introduced in Sec. 3.2.1 for global quantum quenches is not suited to local quenches since the initial state is no longer translational invariant. We first extend the derivation of the QSF without assuming translational invariance of the initial state to an equal-time correlator between the operators $\hat{O}_1(\boldsymbol{x}, t)$ and $\hat{O}_2(\boldsymbol{y}, t)$ such that

$$\begin{aligned} G(\boldsymbol{x}, \boldsymbol{y}; t) :&= \langle \hat{O}_1(\boldsymbol{x}, t)\hat{O}_2(\boldsymbol{y}, t)\rangle \\ &= \sum_{n,n',m} \rho_\mathrm{i}^{n'n}\, \mathrm{e}^{i(E_n - E_{n'})t}\, \mathrm{e}^{i(\boldsymbol{P}_m - \boldsymbol{P}_n)\boldsymbol{x}}\, \mathrm{e}^{i(\boldsymbol{P}_{n'} - \boldsymbol{P}_m)\boldsymbol{y}}\, \langle n|\, \hat{O}_1\, |m\rangle\, \langle m|\, \hat{O}_2\, |n'\rangle\,. \end{aligned} \tag{3.47}$$

Assuming only translation invariance of the system, we change to relative variables $\boldsymbol{R} = \boldsymbol{x} - \boldsymbol{y}$ and $\boldsymbol{r} = (\boldsymbol{x} + \boldsymbol{y})/2$, such that

$$G(\boldsymbol{R}, \boldsymbol{r}; t) = \sum_{n,n',m} \rho_\mathrm{i}^{n'n}\, \mathrm{e}^{i(E_n - E_{n'})t}\, \mathrm{e}^{i(\boldsymbol{P}_{n'} - \boldsymbol{P}_n)\boldsymbol{r}}\, \mathrm{e}^{i(2\boldsymbol{P}_m - \boldsymbol{P}_n - \boldsymbol{P}_{n'})\boldsymbol{R}/2}\, \langle n|\, \hat{O}_1\, |m\rangle\, \langle m|\, \hat{O}_2\, |n'\rangle\,. \tag{3.48}$$

Importantly, as the initial state breaks translation invariance, we no longer have $\frac{1}{L^D}\int \mathrm{d}\boldsymbol{r}\, G(\boldsymbol{r}, \boldsymbol{R}; t) = G(\boldsymbol{R}; t)$. Taking the Fourier transform would give

$$\begin{aligned} G(\boldsymbol{k}, \boldsymbol{k'}; \omega) :&= \int \mathrm{d}\boldsymbol{R}\, \mathrm{d}\boldsymbol{r}\, \mathrm{e}^{-i(\boldsymbol{k}\boldsymbol{R} + \boldsymbol{k'}\boldsymbol{r})}\, \mathrm{d}t\, \mathrm{e}^{i\omega t}\, G(\boldsymbol{R}, \boldsymbol{r}; t) \\ &= (2\pi)^{2D+1} \sum_{n,n',m} \rho_\mathrm{i}^{n'n} \delta(E_n - E_{n'} + \omega)\, \langle n|\, \hat{O}_1\, |m\rangle\, \langle m|\, \hat{O}_2\, |n'\rangle \\ &\quad \times \delta(\boldsymbol{P}_m - \tfrac{\boldsymbol{P}_{n'}}{2} - \tfrac{\boldsymbol{P}_n}{2} - \boldsymbol{k})\, \delta(\boldsymbol{P}_{n'} - \boldsymbol{P}_n - \boldsymbol{k'}). \end{aligned} \tag{3.49}$$

Equation (3.49) is valid for an arbitrary quench, as long as the system is translation invariant. For a global quench, the initial state is usually taken to be the ground state of the initial Hamiltonian and is therefore also translational invariant. Therefore we can integrate over $\boldsymbol{r}$ so as to remove the dependence over $\boldsymbol{k'}$ [formally $\boldsymbol{k'} = 0$ in Eq. (3.49)]. This imposes the additional selection rule $\boldsymbol{P}_n = \boldsymbol{P}_{n'}$ and Eq. (3.49) reduces to Eq. (3.21) which is the QSF obtained in the global quench case. In striking contrast, for a local quench, the translation invariance of the initial state is broken, the crucial selection rule which links $\boldsymbol{P}_{n'}$ with the momentum of the intermediate state $\boldsymbol{P}_m$ is missing due to the presence of an additional momentum $\boldsymbol{k'}$, and the excitation spectrum generally cannot be obtained in a simple manner from two-point correlators.

QSF for local quenches. The issue previously mentioned can be circumvented if we define the QSF using one-point functions instead of two-point correlators. We study the post-quench

dynamics of a one-point observable $\hat{O}(\boldsymbol{x},t)$ at a given position $\boldsymbol{x}$ and time $t>0$, and compute the expectation value $G(\boldsymbol{x};t)=\langle\hat{O}(\boldsymbol{x},t)\rangle=\mathrm{Tr}\left[\hat{\rho}_{\mathrm{i}}\hat{O}(\boldsymbol{x},t)\right]$ which, using translation invariance of the system, becomes

$$G(\boldsymbol{x};t)=\sum_{n,n'}\rho_{\mathrm{i}}^{n'n}\,\mathrm{e}^{i(E_n-E_{n'})t}\,\mathrm{e}^{i(\boldsymbol{P}_{n'}-\boldsymbol{P}_n)\boldsymbol{x}}\,\langle n|\,\hat{O}\,|n'\rangle\,. \tag{3.50}$$

The QSF for local quenches is defined by the space-time Fourier transform of Eq. (3.50) as

$$\begin{aligned}G(\boldsymbol{k},\omega)&:=\int\mathrm{d}\boldsymbol{x}\,\mathrm{d}t\,\mathrm{e}^{-i(\boldsymbol{k}\boldsymbol{x}-\omega t)}\,G(\boldsymbol{x};t)\\&=(2\pi)^{D+1}\sum_{n,n'}\rho_{\mathrm{i}}^{n'n}\,\langle n|\,\hat{O}\,|n'\rangle\,\delta(E_{n'}-E_n-\omega)\,\delta(\boldsymbol{P}_{n'}-\boldsymbol{P}_n-\boldsymbol{k}).\end{aligned} \tag{3.51}$$

Equation (3.51) will be the basis of the following analysis. We recover the key elements from spectroscopy, that is the emergence of frequency and momentum resonances corresponding to elementary excitations between two eigenstates $n\leftrightarrow n'$ with resonances in frequency at $\omega=E_{n'}-E_n$ and in momentum at $\boldsymbol{k}=\boldsymbol{P}_{n'}-\boldsymbol{P}_n$, corresponding to the Dirac functions in Eq. (3.51).

Why didn't we use a one-point function for the global quench? For a global quench, a one-point observable is not able to probe the excitation spectrum for $k\neq 0$ because of translation invariance (of both the system and the initial state) which cancels any position dependence. The proof follows the one used to derive Eq. (3.50). Translation invariance of the system imposes that $G(\boldsymbol{x},t)=(1/L^D)\int\mathrm{d}\boldsymbol{x}\;G(\boldsymbol{x},t)$ is independent of $\boldsymbol{x}$. It yields the selection rule $\delta(\boldsymbol{P}_n-\boldsymbol{P}_{n'})$ and the exponential term giving the momentum dependence vanishes.

3.3.2 Choosing the initial state and the observable

3.3.2.1 General strategy

As for global quench spectroscopy, the local quench spectroscopy strategy follows from the expression of the QSF in Eq. (3.51), and is easier to understand for weak quenches which generate only low-energy excitations. Starting from the ground state, we apply a local operator $\hat{L}$ which acts on a single site chosen to be the centre of the chain. The system being translational invariant, the eigenstates have a well-defined momentum ($\left[\hat{H},\hat{P}\right]=0$). This localisation in momentum space translates into a delocalisation of eigenstates in real space over the full system. Reciprocally, the action of the operator $\hat{L}$ being local in real space, it acts over various eigenstates in momentum space. The initial state created is therefore a superposition of all low-lying excited states $|\psi_{\mathrm{i}}\rangle=\hat{L}\,|0\rangle=\sum_m c_m\,|m\rangle$.

The excitation spectrum may be probed under two main conditions. First, the initial state must overlap with both the ground state and the low-lying excited states, such that the coherences $\rho_{\mathrm{i}}^{n'0}$ (or ρ_{i}^{0n}) are non-zero. This condition reads as

$$\rho_{\mathrm{i}}^{n'0}=\langle n'|\psi_{\mathrm{i}}\rangle\,\langle\psi_{\mathrm{i}}|0\rangle=\langle n'|\,\hat{L}\,|0\rangle\,\langle 0|\,\hat{L}^\dagger\,|0\rangle\neq 0. \tag{3.52}$$

The condition $\rho_{\mathrm{i}}^{n'0}\neq 0$ was generally satisfied by performing a weak global quench in global quench spectroscopy. In the local quench case the initial state has to be constructed explicitly with this condition in mind, and the operator $\hat{L}$ has to be picked accordingly. We will show below that it is particularly easy for a spin chain where the rotation of a single spin to satisfy this condition, but it can become quite involved for a particle model. Second, the delta distributions in energy and momentum from Eq. (3.51) must select the transition between the ground state and the excited states. Assuming that $|n\rangle=|0\rangle$ is the ground state ($\boldsymbol{P}_n=0$ and $E_n=0$), we want that for each

eigenstate $|n'\rangle$, the QSF displays a resonance at $\boldsymbol{k} = \boldsymbol{P}_{n'}$ and $\omega = E_{n'}$. This condition can be satisfied using an observable such that

$$\langle 0|\,\hat{O}\,|n'\rangle \neq 0. \tag{3.53}$$

From Eq. (3.52) and (3.53), we can derive a general simple rule to explain how to choose the observable to probe the spectrum. Since the system is isolated, we may naturally expect the operations on the quantum state to be unitary ($\hat{L}^\dagger = \hat{L}^{-1}$). We will encounter more subtle cases in the following, but for now we restrict to such simple case. The ground state can then be decomposed as $|0\rangle = \hat{L}^\dagger\,|\psi_\mathrm{i}\rangle = \sum_m c_m \hat{L}^\dagger\,|m\rangle$ and substituting it into Eq. (3.53) gives

$$\langle 0|\,\hat{O}\,|n'\rangle = \sum_m c_m^\star\,\langle m|\,\hat{L}\hat{O}\,|n'\rangle \neq 0. \tag{3.54}$$

A sufficient condition is to choose $\hat{O}$ such that it contains $\hat{L}^{-1}$, i.e. the observable contains a term which corresponds to an operator which "reverses" the quench we performed with the local operator $\hat{L}$. This is reminiscent of the common choice in pump-probe spectroscopy where the pump and the probe are related by $\hat{P}^\dagger = \hat{O}$, although here we established this argument on a stronger footing. In order to choose $\hat{L}$ now, we need to remind ourselves that the density matrix coherences $\rho_\mathrm{i}^{n'0}$ in Eq. (3.52) must be non-vanishing. Again a sufficient condition is to take $\hat{L} \propto \hat{\mathbb{1}} + \hat{\mathcal{P}}$, where $\hat{\mathcal{P}}$ couples the ground state to the first excited manifold of states $|n'\rangle$, namely $\langle 0|\,\hat{L}^\dagger\,|0\rangle \propto 1$ and $\langle n'|\,\hat{L}\,|0\rangle \propto \langle n'|\,\hat{\mathcal{P}}\,|0\rangle \neq 0$. This corresponds to the initial state being the superposition of the ground state and the first excited states.

If the local quench cannot be described by the action of a unitary operator, the same argument applies by substituting $\hat{L}$ with $(\hat{L}^{-1})^\dagger$ in Eq. (3.54). The simple condition for $\hat{O}$ becomes $\left((\hat{L}^{-1})^\dagger\right)^{-1}$ and is less intuitive. This condition is sufficient but not unique, and we will show in the following that the general intuition that the observable should reverse the quench remains valid with only minor modifications.

3.3.2.2 Examples of local quench protocols

We now discuss experimentally realistic quenches suitable for local quench spectroscopy, applicable to both spin and particle models.

Spin models. A single spin 1/2 may be pictured in three equivalent ways: as a point on the complex circle (Hilbert space representation)

$$|\psi\rangle = \cos\!\left(\tfrac{\theta}{2}\right)|\uparrow\rangle_z + \mathrm{e}^{i\phi}\sin\!\left(\tfrac{\theta}{2}\right)|\downarrow\rangle_z\,; \tag{3.55}$$

as a unitary vector $\boldsymbol{u} = (\sin\theta\cos\phi, \sin\theta\sin\phi, \cos\theta)$ living on the Bloch sphere [Fig. 3.8(a)]; finally by a matrix from the $SU(2)$ algebra

$$M = \boldsymbol{u}\cdot\hat{\boldsymbol{\sigma}} = \begin{pmatrix} \cos\theta & \mathrm{e}^{-i\phi}\sin\theta \\ \mathrm{e}^{i\phi}\sin\theta & -\cos\theta \end{pmatrix}, \tag{3.56}$$

where $\hat{\boldsymbol{\sigma}}$ is the vector of Pauli matrices. The last two representations are convenient in order to represent the action of a local operator (particularly the Bloch sphere picture for visualisation and the $SU(2)$ matrix representation for computations using Pauli matrices). We represent a local quench by the rotation of a single spin on the site $\mathcal{S}$ (we choose the centre of the chain), with an angle α around an arbitrary axis $\boldsymbol{n}$. After such a rotation, the state of the spin is described on the Bloch sphere by the vector

$$\boldsymbol{u'} = \cos\alpha\,\boldsymbol{u} + (1-\cos\alpha)(\boldsymbol{n}\cdot\boldsymbol{u})\,\boldsymbol{n} + \sin\alpha\,(\boldsymbol{n}\times\boldsymbol{u}). \tag{3.57}$$

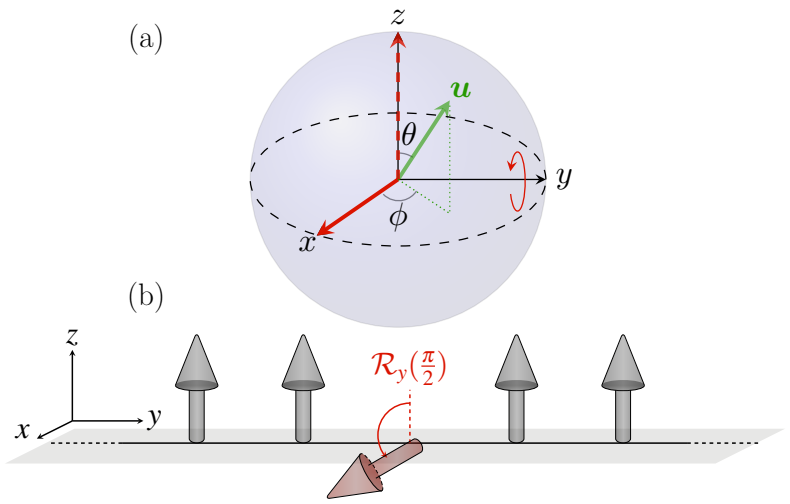

Fig. 3.8 (a) Parametrisation on the Bloch sphere of an arbitrary spin-1/2 state pointing along $\boldsymbol{u}$ (green) with the polar and azimuthal angles (θ, ϕ). (b) Example of a local quench for a spin model. Initially aligned along z, the central spin (red arrow) is rotated around the axis y by an angle $\pi/2$ to point along x. From [Villa et al., 2020].

Since Pauli matrices are the generators of rotations and using the properties of the $SU(2)$ algebra, a rotation of an angle α around $\boldsymbol{n}$ can be represented by the action of the following operator

$$\hat{\mathcal{R}}_{\mathbf{n}}(\alpha) = \mathrm{e}^{-i\frac{\alpha}{2}\boldsymbol{n}\cdot\hat{\boldsymbol{\sigma}}} = \cos\left(\tfrac{\alpha}{2}\right)\hat{\mathbb{1}} - i\sin\left(\tfrac{\alpha}{2}\right)\boldsymbol{n}\cdot\hat{\boldsymbol{\sigma}}, \tag{3.58}$$

where $\hat{\mathbb{1}}$ the identity matrix operator. In this representation, the rotated state (initial state) is represented by $M' = \hat{\mathcal{R}}_{\boldsymbol{n}}(\alpha) M \hat{\mathcal{R}}_{\boldsymbol{n}}^{-1}(\alpha)$. For any angle $\alpha \neq \pi$, the rotation operator satisfies both Eq. (3.52) and (3.53): this is our operator $\hat{L}$. In the transverse-field Ising and Heisenberg chains discussed below, we will rotate the central spin around the axis y by an angle $\theta = \pi/2$, which corresponds to $\phi = 0$ and $\theta = \alpha$ in Eq. (3.55) and (3.56). On the Ising chain, for $h \gg J$ the ground state is z-polarised and to a good approximation [Fig. 3.8(b)]

$$\begin{aligned} |0\rangle &\simeq |\uparrow\rangle^{\otimes N_\mathrm{s}} \\ |\psi_\mathrm{i}\rangle = \hat{L}\,|0\rangle &\simeq |\uparrow\rangle^{\otimes \mathcal{S}-1} \otimes \left[\cos\left(\tfrac{\theta}{2}\right)|\uparrow\rangle_{\mathcal{S}} + \sin\left(\tfrac{\theta}{2}\right)|\downarrow\rangle_{\mathcal{S}}\right] \otimes |\uparrow\rangle^{\otimes N_\mathrm{s}-\mathcal{S}}, \end{aligned} \tag{3.59}$$

where N_s is the total number of spins. Since in this regime the elementary excitations are superposition of single spin flips, by rotating the central spin by $\pi/2$ we build the initial state as a coherent superposition of the ground state and the low-lying excitations. In the ferromagnetic Heisenberg model [Eq. (1.9)], the ground state is highly degenerate due to global rotational invariance. To break this degeneracy in order to define a unique ground state, we numerically add a small magnetic field along z with strength $h_z = -10^{-2}J$ to the first site of the chain. Then the post-quench initial state is also well approximated by Eq. (3.59).

Particle models In particle models, such as the Bose-Hubbard chain, local quenches consist in introducing defects at a single site. In contrast to spin models, these quenches are non-unitary as they do not conserve the total particle number. In the superfluid we start from the ground state and then remove all particles in the centre. In the Mott insulating phase, we also start from the ground state (close to the homogeneous state with $\bar{n}$ particles per site when $U/J \gg 1$), and remove or add one particle in the centre.

3.3.3 Extracting excitation spectra

We now demonstrate how local quench spectroscopy can be used to obtain the excitation spectrum. We begin with the analytical insight from the quasiparticle picture and then discuss the numerical

simulation results.

Analytical insight We investigate weak quenches which populate the low-lying excited states of the system, such that $|n'\rangle = \hat{\gamma}^\dagger_{\boldsymbol{q}} |0\rangle$ contains a single quasiparticle excitation over the ground state $|0\rangle$ with momentum $\boldsymbol{q}$. At this point, $\boldsymbol{q}$ is arbitrary and may even represent the ground state if $\boldsymbol{q} = 0$. Quasiparticles can be indifferently fermionic or bosonic, with $[\hat{\gamma}_{\boldsymbol{q}}, \hat{\gamma}^\dagger_{\boldsymbol{q}'}]_\pm = \delta_{\boldsymbol{q},\boldsymbol{q}'}$ respectively. For simplicity, we assume that a single type of excitations can be created by the system, but the following expressions can be easily adapted to the case of multiple types of excitations (for instance as in the Mott-insulating phase of the Bose-Hubbard model) by adding an extra index σ with $[\hat{\gamma}_{\boldsymbol{q},\sigma}, \hat{\gamma}^\dagger_{\boldsymbol{q}',\sigma'}]_\pm = \delta_{\boldsymbol{q},\boldsymbol{q}'}\delta_{\sigma,\sigma'}$. The QSF in Eq. (3.51) can be simplified by noting that the delta distribution in momentum sets $\boldsymbol{P}_n = \boldsymbol{q} - \boldsymbol{k}$ such that

$$G(\boldsymbol{k};\omega) = 2\pi \int \rho_{\mathrm{i}}^{\boldsymbol{q};\boldsymbol{q}-\boldsymbol{k}} \langle \boldsymbol{q}-\boldsymbol{k}| \hat{O} |\boldsymbol{q}\rangle \, \delta(E_{\boldsymbol{q}-\boldsymbol{k}} - E_{\boldsymbol{q}} + \omega) \, \mathrm{d}\boldsymbol{q}, \tag{3.60}$$

where we switched to an integral representation valid in the thermodynamic limit. This expression shows that all transitions between quasiparticles with momentum difference $\pm\boldsymbol{k}$ are probed at low-energy. To probe the excitation spectrum, the transition $n' \leftrightarrow 0$ (or $n \leftrightarrow 0$) should be targeted, and only one of the two eigenstates should contain one quasiparticle, the other one being the vacuum. Just as for the global quench, a non-zero QSF is obtained if the observable couples linearly to the quasiparticles, namely

$$\hat{O} = \sum_{\boldsymbol{p}} A_{\boldsymbol{p}} \hat{\gamma}_{\boldsymbol{p}} + \bar{A}_{\boldsymbol{p}} \hat{\gamma}^\dagger_{\boldsymbol{p}}. \tag{3.61}$$

This observable is the simplest choice for coupling the ground state to the low-lying excitations, and therefore is expected to capture the low-energy physics. Substituting the expression (3.61) in the term $\langle \boldsymbol{q}-\boldsymbol{k}| \hat{O} |\boldsymbol{q}\rangle$, we obtain as expected a non-zero contribution only if $\boldsymbol{q} = \boldsymbol{0}$, in which case

$$\langle \boldsymbol{q}-\boldsymbol{k}| \hat{O} |\boldsymbol{q}\rangle = \sum_{\boldsymbol{p}} \bar{A}_{\boldsymbol{p}} \langle 0| \hat{\gamma}_{-\boldsymbol{k}} \hat{\gamma}^\dagger_{\boldsymbol{p}} |0\rangle = \bar{A}_{-\boldsymbol{k}}, \tag{3.62}$$

or if $\boldsymbol{q} = \boldsymbol{k}$, in which case

$$\langle \boldsymbol{q}-\boldsymbol{k}| \hat{O} |\boldsymbol{q}\rangle = \sum_{\boldsymbol{p}} A_{\boldsymbol{p}} \langle 0| \hat{\gamma}_{\boldsymbol{p}} \hat{\gamma}^\dagger_{\boldsymbol{q}} |0\rangle = A_{\boldsymbol{k}}. \tag{3.63}$$

Finally, the QSF simplifies into

$$G(\boldsymbol{k};\omega) = 2\pi \left[A_{\boldsymbol{k}} \, \rho_{\mathrm{i}}^{\boldsymbol{k};0} \delta(\omega - E_{\boldsymbol{k}}) + \bar{A}_{-\boldsymbol{k}} \, \rho_{\mathrm{i}}^{0;-\boldsymbol{k}} \delta(\omega + E_{-\boldsymbol{k}}) \right]. \tag{3.64}$$

The positive frequency component displays resonances at the energy $E_{\boldsymbol{k}}$ for an observable of the form (3.61). If several types of excitation σ are present, an additional sum over σ is added to Eq. (3.64) showing that the local QSF is sensitive to individual excitations.

Numerical simulations results We now demonstrate local quench spectroscopy on the various models introduced in Sec. 1.1. We use t-MPS based algorithms with open boundary conditions to simulate the local quench in the centre of the chain. This choice minimises boundary effects, but is not a strict requirement as we have obtained similar results on different sites. We then probe the following dynamics after a total evolution time $t_{\max} J/\hbar = 10$. Since the frequency resolution of quench spectroscopy is inversely proportional to the maximum evolution time, a better resolution can be obtained by increasing the latter. We choose a bond dimension $\chi = 256$ and system size $L = 47$ sites. Convergence of the numerical result has been checked by varying the bond dimension and the system size similarly as in Appendix 2.B. Note that while our simulations display small finite size effects in the form of reflections at the boundaries in the real-space data, we find that a small number of reflections are not an issue and do not qualitatively alter the QSF.

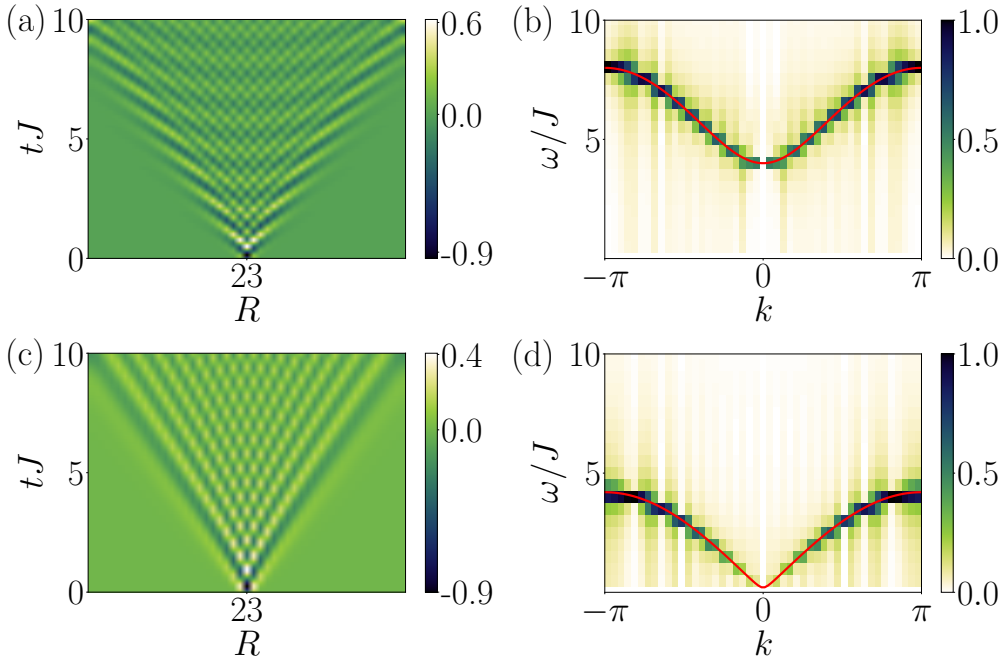

Fig. 3.9 (a) Space-time pattern of $\langle\hat{\sigma}^y(R,t)\rangle$ in the short-ranged transverse-field Ising chain after the rotation of the central spin by $\theta = \pi/2$ around y with $h/J = 3$ (z-polarised phase). (b) Corresponding normalised modulus of the QSF, whose maxima are in excellent agreement with the exact excitation spectrum given by Eq. (1.15) (red line). (c) and (d) are identical except that $h/J = 1.1$, close to the critical point. From [Villa et al., 2020].

TFI chain We follow the local quench protocol discussed in Sec. 3.3.2.2 and rotate the central spin around y by $\theta = \pi/2$ such that the spin points along x (Fig. 3.8). Because $\hat{\sigma}^y$ is the generator of the rotation around y, we probe $\langle\hat{\sigma}^y(R,t)\rangle$ where the average is over the initial state. We display in Fig. 3.9 the space-time pattern and the corresponding QSF after a local quench in the z-polarised phase, first with $h/J = 3$ and then with $h/J = 1.1$ (the critical point is at $(h/J)_c = 1$). In both cases the spectrum given by Eq. (1.15) with the Hamiltonian (1.14) can be accurately reconstructed.

In the x-polarised phase, the low-lying excitations are known to be non-local domain walls, and as such their excitation branch cannot be probed using local quench spectroscopy. In this regime, global quench spectroscopy is more appropriate to probe the properties of the low-lying excitations. However, the duality mapping (Sec. 1.1.3) reveals that a single spin flip is equivalent to a pair of domain walls, and therefore local quench spectroscopy is sensitive to pairs of excitations, as we will show in Sec. 3.3.5.1.

Interestingly, similar results can be obtained by probing $\langle\hat{\sigma}^x(R,t)\rangle$. This highlights that the criterion we discussed in Sec. 3.3.2.1 to pick the observable for observing the spectrum gives an insight but is not necessarily the only valid choice. The fact that $\langle\hat{\sigma}^x(R,t)\rangle$ also leads to the observation of the spectrum can be understood following the same argument as for the global quench spectroscopy (Sec. 3.2.2.3). To probe the spectrum, an observable of the form (3.61) has to be found. In the strongly polarised phase along z, corresponding to $h/J \gg 1$, linear spin-wave theory and the Holstein-Primakoff transformation tell us that the transverse magnetisations $\hat{\sigma}^x$ or $\hat{\sigma}^y$ are good choices. Indeed, spin-wave excitations are created by the spin raising operator $\hat{\sigma}^+ = \hat{\sigma}^x + i\hat{\sigma}^y$ which couples the ground state to the first excited state, while the spin lowering operator $\hat{\sigma}^- = \hat{\sigma}^x - i\hat{\sigma}^y$ destroys an excitation and annihilates the ground state. Therefore their linear combination formed by the transverse magnetisations are of the form (3.61) and thus can probe the excitation spectrum. The numerics and the argument for the observable reversing the quench show that the argument remains beyond the regime $\langle\hat{\gamma}^\dagger\hat{\gamma}\rangle \ll 1$, even very close above the critical point for $h/J \to (h/J)_c = 1$.

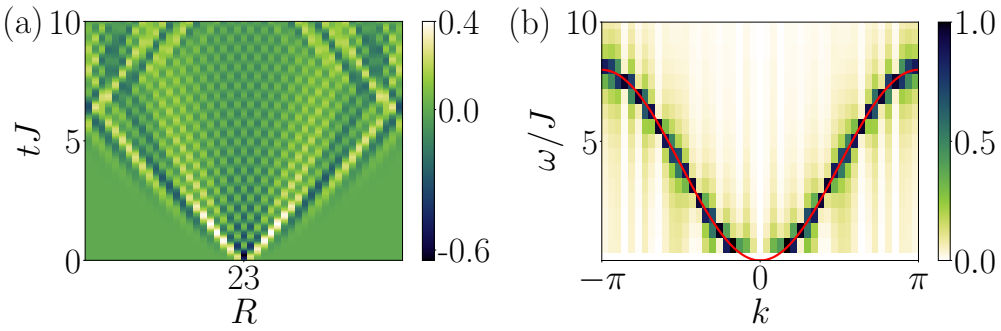

Fig. 3.10 (a) Space-time pattern of $\langle \hat{\sigma}^y(R,t)\rangle$ in the Heisenberg ferromagnetic chain after the rotation of the central spin by $\theta = \pi/2$ around y. (b) Corresponding normalised modulus of the QSF, whose maxima are in excellent agreement with the exact magnon excitation spectrum $E_k = 4J(1-\cos k)$ (red line) for $\hat{H} = -J\sum_R \hat{\boldsymbol{\sigma}}_R \cdot \hat{\boldsymbol{\sigma}}_{R+1}$. From [Villa et al., 2020].

The Holstein-Primakoff representation also explains why the longitudinal magnetisation $\hat{\sigma}^z$ cannot probe the spectrum. It can be cast as $\hat{\sigma}^z = 2\hat{\gamma}^\dagger\hat{\gamma} - 1$ and therefore is not of the required form (3.61) to probe the spectrum. However, we will show in Sec. 3.3.4 that it can be used to probe the transition energies between energy levels within the same manifold.

Heisenberg chain The Heisenberg chain is interesting for studying local quench spectroscopy for various reasons. First, its excitation spectrum is exactly known from the Bethe ansatz, and consists of magnons in the ferromagnetic regime. The spectrum has been obtained using pump-probe spectroscopies from the dynamical structure factor in inelastic neutron scattering experiments [Lake et al., 2013; Mourigal et al., 2013], but unless one adds an additional parameter to the Hamiltonian which the global quench sets to zero, it cannot be obtained from global quench spectroscopy (the Hamiltonian only has a single parameter, the nearest-neighbour exchange coupling J). Second, while the excitation spectrum is known, there is no explicit representation of the excitations in real-space, and therefore there is no *a priori* simple choice for the observable. Despite the latter issue, using the same quench protocol as for the transverse-field Ising chain, we are able to probe the magnon excitation branch as shown in Fig. 3.10. The resonances observed in the QSF are in excellent agreement with the exact dispersion relation of magnons predicted by the Bethe ansatz and represented by the red line. Since here once again the quench performed is a unitary operation, choosing an observable which reverses the quench probes the spectrum. This shows that the explicit construction of elementary excitations is not required for local quench spectroscopy to unveil the spectrum.

An exception to this rule is the Heisenberg antiferromagnet, as its low-lying excited states are pairs of spinons (non-local domain walls) and therefore cannot be probed by rotating a single spin. From a more fundamental point of view, such low-lying excited states are protected by a symmetry which cannot be broken by a unitary operation.

BH chain The Bose-Hubbard chain is insightful for two main reasons. First, as a particle model, the local quench protocol differs as the addition or removal of a particle is no longer a unitary operation and the criterion for the observable reversing the quench needs to be adapted. Second, deep in the Mott-insulating regime two types of excitations coexist. Global quench spectroscopy used two-point correlators and was only sensitive to the *pair* of excitations. In contrast, we will see that local quench spectroscopy which uses one-point functions can probe the excitations *individually*.

We start by investigating the mean-field SF regime which hosts Bogoliubov excitations with the excitation spectrum given by Eq. (3.33) for $\gamma = U/(2J\bar{n}) \ll 1$. As discussed in global quench spectroscopy, a hydrodynamic formulation in this regime shows that the density fluctuations

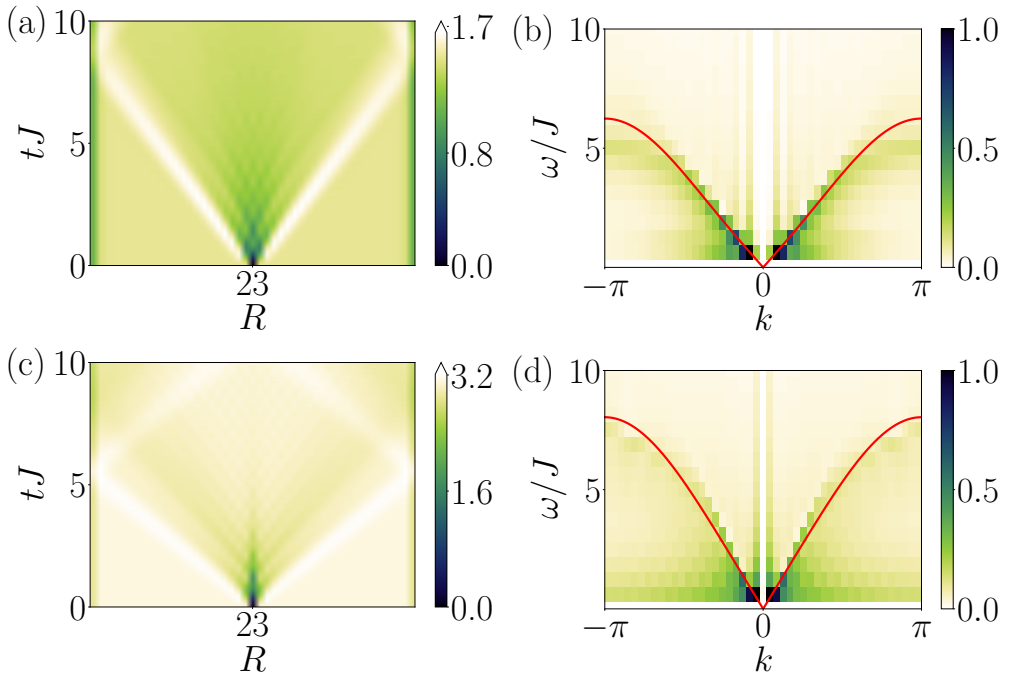

Fig. 3.11 (a) Space-time pattern of $\langle \hat{n}(R,t) \rangle$ in the Bose-Hubbard chain in the mean-field SF after preparing the system in the ground state with $U/J = 2$ and $\bar{n} \simeq 1.4$, then removing all particles from the centre. (b) Corresponding normalised modulus of the QSF, whose maxima are in good agreement with the Bogoliubov excitation spectrum (3.33) (red line). (c) and (d) are similar but the filling is $\bar{n} \simeq 3.0$. The strong signal around $k = 0$ signals quasi long-range order (the $k = 0$ component itself has been removed for visibility). From [Villa et al., 2020].

operator has the required form (3.61) to probe the spectrum, namely in momentum space $\delta\hat{n}_k \sim \hat{\gamma}_k + \hat{\gamma}_k^\dagger$. After initialising the system in its ground state, we remove all particles from the central site at $t = 0$. We display the following space-time evolution of the on-site density and its corresponding QSF for $\gamma \simeq 0.7$ and $\gamma \simeq 0.3$ in Fig. 3.11. The branches displayed by the QSF are in good agreement with the spectrum expected from Bogoliubov theory. For smaller values of γ, the agreement with the Bogoliubov spectrum improves but the convergence of the numerical results is more demanding.

We now move to the strongly interacting MI phase at $\bar{n} = 1$ which contains two types of excitations propagating with different velocities. Summarising Appendix 1.D, they can be understood by restricting the local Hilbert space to the three values $\{0; 1; 2\}$ and introducing the fermionic doublons and holons. The physical bosons on the chain are rewritten as superpositions of doublons and holons $\hat{a}_R^\dagger = \sqrt{\bar{n}+1}\, Z_{R,+} \hat{c}_{R,+}^\dagger + \sqrt{\bar{n}}\, Z_{R,-} \hat{c}_{R,-}$ with $Z_{R,\pm}$ the Jordan-Wigner phase factor preserving the commutation rules. In the strongly interacting regime where density fluctuations are small, the elementary excitations are Bogoliubov quasiparticles, linear combinations of the fermionic doublons and holons $\hat{\gamma}_{k,\pm}^\dagger = u(k)\hat{c}_{k,\pm}^\dagger \pm v(k)\hat{c}_{-k,\mp}$. At zero order in J/U, one has $u(k) = 1$ and $v(k) = 0$ such that the elementary excitations reduce to pure doublons and holons (and not linear combinations of them as in the more general case).

The most natural idea for a local quench would be to add or remove one particle from the central site, which would create both a doublon and a holon (see expression above for $\hat{a}_R^\dagger$). However, in the strongly interacting regime, the ground state is homogeneous (for unit filling $|111\cdots\rangle$) and thus a state such as $|1\cdots101\cdots\rangle$ or $|1\cdots121\cdots\rangle$ is orthogonal to it. The necessary condition (3.53) to probe the excitation spectrum is not satisfied. One cannot use either the local density $\hat{n}(R,t)$ in this regime, since it also does not satisfy the condition (3.53) to couple the ground state and the first excited state manifold. However, as we will show in Sec. 3.3.4, the density in this regime provides complementary information about the quasiparticles.

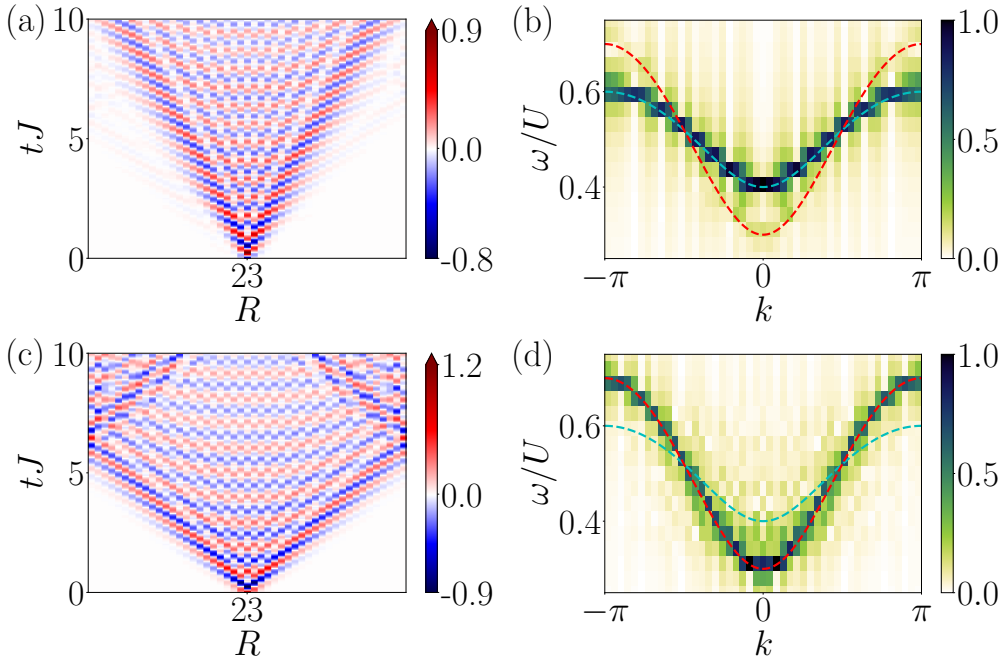

Fig. 3.12 (a) Space-time pattern of $\langle(\hat{a}+\hat{a}^\dagger)(R,t)\rangle$ in the Bose-Hubbard chain in the strongly interacting MI phase after preparing the system in its ground state and changing the central site to be a coherent superposition of Fock states $(|0\rangle+|1\rangle)/\sqrt{2}$ with $U/J=20$ at unit filling. (b) Corresponding normalised modulus of the QSF, whose maxima is in excellent agreement with holon-like band (dashed cyan). (c) and (d) are similar but the central site is prepared in the coherent superposition $(|1\rangle+|2\rangle)/\sqrt{2}$, which probes the doublon-like band instead (dashed red). From [Villa et al., 2020].

Just as for the rotation operator in spin systems, we have to prepare a superposition state using a local quench operator such that for instance $\hat{L}\,|111\cdots\rangle \propto |111\cdots\rangle + |101\cdots\rangle$ *i.e.* $\hat{L} \propto \hat{\mathbb{1}} + \hat{a}_{L/2}$. We then pick the observable to reverse the quench, so to add a particle in the centre (plus its hermitian conjugate for it to be hermitian) such that $\hat{O}(R,t) = \hat{a}(R,t) + \hat{a}^\dagger(R,t)$.

We numerically start from the ground state at unit filling and then change the central site to be in a coherent superposition of Fock states $(|0\rangle + |1\rangle)/\sqrt{2}$. The dynamics of the observable $\langle(\hat{a}+\hat{a}^\dagger)(R,t)\rangle$ together with the resulting QSF is displayed in Fig. 3.12(a,b). A sharp branch can be observed, which matches well with the holon branch (cyan line). The doublon line is represented for reference as the red line, which shows that the local QSF is only sensitive to the individual excitations. Alternatively, one can probe the doublon branch alone, by adding one particle such that the central site is in the coherent superposition of Fock states $(|1\rangle+|2\rangle)/\sqrt{2}$ as showed in Fig. 3.12(c,d).

As this procedure does not conserve the total number of particles in the system, both the preparation of the state and the measurement of the observable will be challenging. This can be experimentally realised in a double-species Bose-Hubbard model, where for instance the bosons have two different internal hyperfine states (labelled $|\uparrow\rangle$ and $|\downarrow\rangle$) which can be individually addressed. By applying an appropriate laser pulse, it is possible to locally prepare a boson in the required coherent superposition of both hyperfine states [Mandel et al., 2003; Trotzky et al., 2008; Trotzky et al., 2010]. Rather than measuring the bare creation or annihilation operator, the experiment will instead probe the "spin-flip" operator $(\hat{a}_\downarrow^\dagger\hat{a}_\uparrow + \hat{a}_\uparrow^\dagger\hat{a}_\downarrow)(R,t)$ associated to transitions between the two hyperfine states. This operator has previously been reconstructed from measurements [Trotzky et al., 2012]. As discussed in Sec. 1.3.1.3, the two-species Bose-Hubbard model is equivalent in the strongly interacting limit with unit filling to an effective pseudo-spin Hamiltonian. The previously mentioned local quench realises a unitary rotation of the pseudo-spin and the required operator again reduces to a transverse magnetisation, precisely as we discussed in

the case of spin chains.

3.3.4 Probing transition energies

Are there realistic examples of observables which are not in the form (3.61), and if they do not probe the excitation spectrum, can they reveal complementary information about the excitations? Extending the scope of local quench spectroscopy, we will indeed show how energy transitions between excited states within the same excitation manifold can also be probed. As previously, we begin by a general analytical argument and then demonstrate it using numerical simulations. We also highlight a possible pitfall: the observation of a well-defined branch does not imply that it is the excitation spectrum. This will be explained analytically when the dispersion relation possesses a generic cosine-like shape.

Analytical insight We still restrict to weak quenches populating the low-energy levels close to a given level (here for simplicity we specifically choose the ground state, but the argument could be generalised to an arbitrary state). Therefore we start back from the expression (3.60). If we want to probe the transition energies within the same manifold, now both $\boldsymbol{q}$ and $\boldsymbol{q}-\boldsymbol{k}$ must be non-zero, and the observable has to couple the energy levels. The simplest form (with the lowest possible number of quasiparticles) of such observable conserves the quasiparticle number and is

$$\hat{O} = \sum_{\boldsymbol{p},\boldsymbol{p}'\neq\boldsymbol{0}} B_{\boldsymbol{p},\boldsymbol{p}'}\hat{\gamma}^\dagger_{\boldsymbol{p}}\hat{\gamma}_{\boldsymbol{p}'}. \tag{3.65}$$

Therefore we get

$$\langle \boldsymbol{q}-\boldsymbol{k}|\,\hat{O}\,|\boldsymbol{q}\rangle = \sum_{\boldsymbol{p},\boldsymbol{p}'\neq\boldsymbol{0}} B_{\boldsymbol{p},\boldsymbol{p}'}\,\delta_{\boldsymbol{q},\boldsymbol{p}}\delta_{\boldsymbol{q}-\boldsymbol{k},\boldsymbol{p}'} = B_{\boldsymbol{q},\boldsymbol{q}-\boldsymbol{k}}, \tag{3.66}$$

where we discarded an irrelevant $\boldsymbol{k}=\boldsymbol{0}$ term. Substituting into the QSF (3.60) we obtain

$$G(\boldsymbol{k};\omega) = 2\pi\int B_{\boldsymbol{q},\boldsymbol{q}-\boldsymbol{k}}\,\rho_{\mathrm{i}}^{\boldsymbol{q};\boldsymbol{q}-\boldsymbol{k}}\,\delta(E_{\boldsymbol{q}-\boldsymbol{k}}-E_{\boldsymbol{q}}+\omega)\,\mathrm{d}\boldsymbol{q}. \tag{3.67}$$

If we define for convenience the function (we now restrict to one dimension for simplicity)

$$g_k(q,\omega) = E_{q-k}-E_q+\omega, \tag{3.68}$$

and write $q_k^\star(\omega)$ its ω-dependent zeros, we see that for $\forall q_k^\star(\omega), \partial_q g_k(q)|_{q=q_k^\star(\omega)} \neq 0$, we can rewrite Eq. (3.67) as

$$\begin{aligned} G(k,\omega) &= 2\pi\sum_{q_k^\star(\omega)} |\partial_q g_k(q_k^\star(\omega))|^{-1}\int B_{q,q-k}\,\rho_{\mathrm{i}}^{q;q-k}\,\delta(q-q_k^\star(\omega))\,\mathrm{d}q \\ &= 2\pi\sum_{q_k^\star(\omega)} B_{q^\star,q^\star-k}\,\rho_{\mathrm{i}}^{q^\star;q^\star-k}\,|\partial_q g_k(q_k^\star(\omega))|^{-1}\,. \end{aligned} \tag{3.69}$$

The function $g_k(q,\omega)$ refers to the energy differences, and is in general analytic, but a divergence in the QSF can be observed if $\partial_q g_k(q_k^\star(\omega))\to 0$. We show below that an algebraic divergence can appear along specific lines $k\to\omega(k)$, which are not to be confused with the excitation spectrum.

The special case of a cosine-like dispersion relation Let us consider a cosine-like dispersion relation, of the form

$$E_k = \Delta - v\cos k, \tag{3.70}$$

where $\Delta - v$ is the gap at $k=0$, and v the maximum group velocity. This form is very common in lattice models and is valid for instance for the ferromagnetic Heisenberg chain, for the transverse-field Ising chain far from the critical point ($h\ll J$ or $h\gg J$), or in the strongly interacting Mott

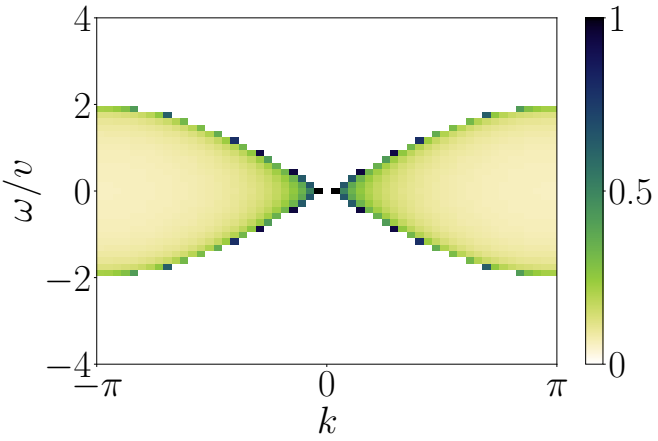

Fig. 3.13 Normalised modulus of the QSF predicted by Eq. (3.74). Algebraic divergences appear along the lines $\omega = \pm 2v \sin(k/2)$.

insulator for the Bose-Hubbard chain. For this form of excitation spectrum, Eq. (3.69) can be evaluated explicitly.

We first find the expression for $q_k^\star(\omega)$. Using trigonometric identities, the energy difference appearing in the energy selection rule of the QSF (3.67) can be rewritten as $E_q - E_{q-k} = -2v \sin\left(\frac{k}{2}\right) \sin\left(\frac{k}{2} - q\right)$. The zeros of $g_k(q,\omega)$ are then given by

$$\sin\left(\tfrac{k}{2}\right) \sin\left[\tfrac{k}{2} - q_k^\star(\omega)\right] = -\frac{\omega}{2v}. \tag{3.71}$$

This equation has solutions provided $\omega \leq |2v \sin\left(\frac{k}{2}\right)|$, and we find for $k \neq 0$

$$q_k^\star(\omega) = \frac{k}{2} + \arcsin\left(\frac{\omega/2v}{\sin(k/2)}\right). \tag{3.72}$$

Second, we evaluate the derivative of the argument of the delta energy selection rule at the points where this argument is zero

$$\partial_q g_k(q)|_{q=q_k^\star(\omega)} = -2v \sin\left(\tfrac{k}{2}\right) \cos\left[\arcsin\left(\frac{\omega/2v}{\sin(k/2)}\right)\right] = -2v \sin\left(\tfrac{k}{2}\right) \sqrt{1 - \left(\frac{\omega/2v}{\sin(k/2)}\right)^2}. \tag{3.73}$$

Using Eq. (3.69) we finally get

$$G(k,\omega) = \frac{B_{q_k^\star(\omega),q_k^\star(\omega)-k}\, \rho_{\mathrm{i}}^{q_k^\star(\omega);q_k^\star(\omega)-k}}{\left|2v \sin\left(\frac{k}{2}\right)\right| \sqrt{1 - \left(\frac{\omega/2v}{\sin(k/2)}\right)^2}} \sim \left[1 - \left(\frac{\omega}{2v \sin(k/2)}\right)^2\right]^{-1/2}. \tag{3.74}$$

Therefore, the QSF displays an algebraic divergence[10] along the lines

$$\omega = \pm 2v \sin\left(\tfrac{k}{2}\right). \tag{3.75}$$

For reference, we plot the QSF predicted by Eq. (3.74) with $B_{q_k^\star(\omega),q_k^\star(\omega)-k}\, \rho_{\mathrm{i}}^{q_k^\star(\omega);q_k^\star(\omega)-k} = 1$ as a contour plot in Fig. 3.13. We will explicitly observe this shape throughout the following numerical results when the spectrum is cosine-like [Eq. (3.70)] and the observable conserves the number of quasiparticles and is of the form (3.65).

[10] Except for pathological cases where the numerator cancels for all k and ω satisfying Eq. (3.75).

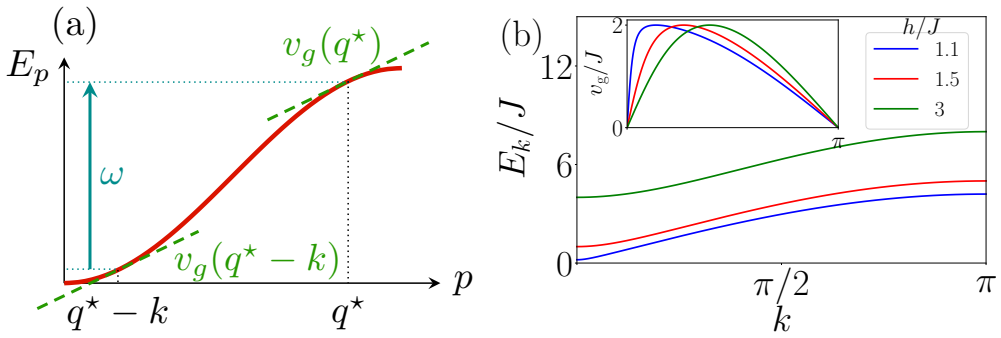

Fig. 3.14 (a) An algebraic divergence of the QSF can appear if the excitation spectrum (red line) changes convexity in the Brillouin zone. It results from the interference of two different wave packets propagating with the same group velocity (dashed green line), and corresponds to frequencies such that $\omega = E_{q^\star} - E_{q^\star - k}$ (blue arrow), where the notation $q^\star$ is short for $q_k^\star(\omega)$. (b) Excitation spectrum of the transverse-field Ising model far from the critical point $(h/J)_\mathrm{c} = 1$ where it is in good approximation cosine-like (green, also red) and close to it where it significantly deviates (blue). Even when the spectrum deviates from the cosine-like shape, it always changes convexity and there exists two points at different momenta with the same velocity satisfying Eq. (3.76). From [Villa et al., 2020].

Interpretation of the divergence The algebraic divergences of the QSF along the lines where $\partial_q g_k(q_k^\star(\omega)) = 0$ [Eq. (3.69)] can be interpreted using the quasiparticle picture. Going back to the definition (3.68) of the function g_k, and recalling that $v_\mathrm{g} = \partial_k E_k$ is the excitation group velocity, the algebraic divergences correspond to

$$v_\mathrm{g}^\star(q_k^\star(\omega) - k) = v_\mathrm{g}^\star(q_k^\star(\omega)). \tag{3.76}$$

This equality is satisfied if two different wave packets, formed by quasiparticles created by the quench, propagate which the same group velocity and interfere [Fig. 3.14(a)]. This situation can only happen if the excitation spectrum E_k changes its convexity somewhere in the Brillouin zone. The previously mentioned example of the cosine-like dispersion relation is a prime example of such situation where the convexity changes in the middle of the Brillouin zone for $k = \pi/2$. In this case, for any $k \in [-\pi; \pi]$, there always exists $q_k^\star(\omega) \in [0; \pi]$ (given by $q_k^\star(\omega) = \pi/2 + k/2$), which satisfies the condition (3.76). For a more general spectrum, this condition can be satisfied on a finite range of values, as showed in Fig. 3.14(b) for the transverse-field Ising spectrum even close to the critical point $(h/J)_\mathrm{c} = 1$ where the spectrum deviates from the cosine-like shape.

Numerical results We numerically test the previously discussed theory on various models, by choosing observables of the form (3.65). We now assume the excitation spectrum of the models to be known, obtained for instance from the procedure discussed in Sec. 3.3.3.

Heisenberg chain We start with the ferromagnetic Heisenberg chain, with the spectrum given by $E_k = 4J(1 - \cos k)$ which is an example of the cosine-like form (3.70). We still initialise the system in its ground state and rotate the spin around the axis y by an angle $\theta = \pi/2$, and now we probe the local magnetisation along z, $\langle \hat{\sigma}^z(R,t) \rangle$. The spin variables can conveniently be expanded into bosonic operators using the Holstein-Primakoff transformation, and to lowest-order $\hat{\sigma}_R^z = 2\hat{\gamma}_R^\dagger \hat{\gamma}_R - \hat{1}$. Such observable conserves the number of quasiparticles and obeys the form (3.65), up to an irrelevant constant term. The result of the numerical simulation is shown in Fig. 3.15, in excellent agreement with the expected divergences previously mentioned along $\omega = \pm 2v \sin(k/2)$ with $v = 4J$ (blue line). The excitation spectrum is represented in Fig. 3.15 (dashed red) in order to emphasise that the observed divergence of the QSF comes from the energy transitions, not the excitation spectrum.

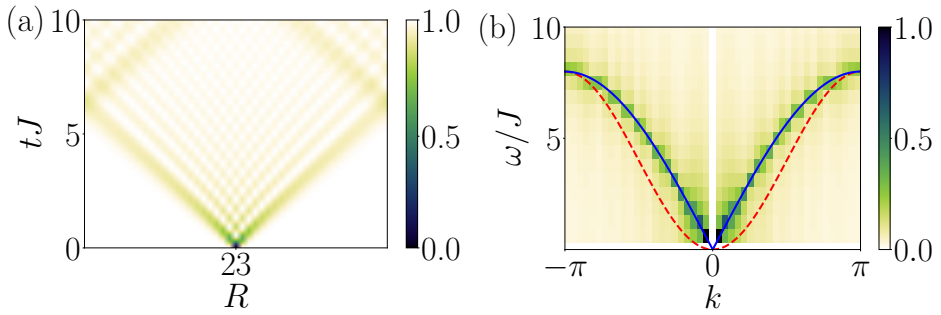

Fig. 3.15 (a) Space-time pattern of $\langle\hat{\sigma}^z(R,t)\rangle$ in the ferromagnetic Heisenberg chain after preparing the system in its ground state and rotating the central spin around y by $\pi/2$. (b) Corresponding normalised modulus of the QSF. An algebraic divergence probing energy transitions is observed along $\omega = 8J\sin(k/2)$ (blue line) in agreement with the prediction of Eq. (3.75). It differs from the excitation spectrum (dashed red line). From [Villa et al., 2020].

TFI chain We now investigate the transverse-field Ising chain, using the same local quench protocol and the same observable $\langle\hat{\sigma}^z(R,t)\rangle$, which also conserves the quasiparticle number and obeys the form (3.65). The result of the numerical simulation is represented in Fig. 3.16 for two typical values of h/J, one deep in the z-polarised phase where $h/J = 3$ and another closer to the critical point at $h/J = 1.1$. Far from the critical point, to lowest order in J/h the excitation spectrum (1.15) is cosine-like, with $v = 2J$ from Eq. (3.70). This explains the excellent agreement between the observed divergence of the QSF and the prediction of Eq. (3.75) represented by the solid blue line in Fig. 3.16(b).

Closer to the critical point, the spectrum deviates from the cosine-like form, however since the spectrum is known we can extract numerically the maxima of $E_{q-k} - E_q$ (which are the same as the ones of the function g_k introduced previously) with respect to q at fixed k. Such points are

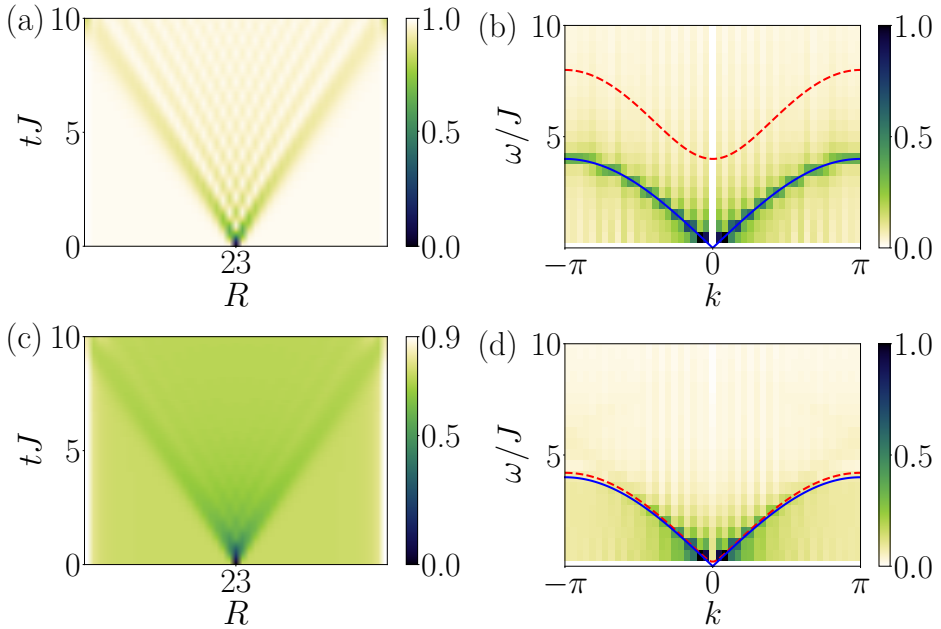

Fig. 3.16 (a) Space-time pattern of $\langle\hat{\sigma}^z(R,t)\rangle$ in the transverse-field Ising chain with $h/J = 3$ after preparing the system in its ground state and rotating the central spin around y by $\pi/2$. (b) Corresponding normalised modulus of the QSF, in excellent agreement with the algebraic divergence coming from energy transitions $\omega = \pm 4J\sin(k/2)$ (blue line). The excitation spectrum is given for reference (dashed red). (c,d) are similar to (a,b) but with $h/J = 1.1$ close to the critical point. In (d), Eq. (3.75) is indistinguishable from the numerical extraction of the maxima with respect to q of the function $g_k(q,\omega)$ (blue line). From [Villa et al., 2020].

responsible for the algebraic divergence observed in the QSF [Eq. (3.76)], and are represented by the blue line in Fig. 3.16(d). Incidentally, they are almost indistinguishable from the excitation spectrum itself (red line), as well as (perhaps even more surprisingly) Eq. (3.75). Once again, the excellent agreement obtained supports the validity of the more general expression (3.69).

BH chain We finally discuss the Bose-Hubbard model in the strongly interacting Mott insulating phase, where the excitations reduce to simpler doublons and holons. The density observable $\hat{n}(R,t) = \hat{a}_R^\dagger(t)\hat{a}_R(t)$ can be decomposed in terms of the doublon and holon excitations as $\hat{n}(R,t) = (\bar{n}+1)\hat{c}_{R,+}^\dagger(t)\hat{c}_{R,+}(t) + \bar{n}\hat{c}_{R,-}(t)\hat{c}_{R,-}^\dagger(t)$. Deep in the Mott phase, the true elementary excitations approximately reduce to the doublon and the holon, such that the density reduces to the form (3.65). Since the dispersion relation of each excitation is cosine-like, with the doublon propagating at twice the velocity of the holon for $\bar{n} = 1$ due to the Bose enhancement factor, we expect to observe two lines from the energy differences $\omega = \pm 2v\sin(k/2)$ with $v = 2J$ for the holon and $v = 4J$ for the doublon. This is indeed confirmed numerically by Fig. 3.17. To improve the visibility of the QSF, it is interesting to reduce the numerical noise when computing the space-time Fourier transform by multiplying the space-time signal by a filtering window (for instance the commonly chosen bell-shaped Hann function). This technique known in signal processing as apodisation can be used to improve the spectral features probed by the QSF. All credit for this idea goes to S.J. Thomson, I simply mention it here to show explicitly one striking example with Fig. 3.17(c) where the improvement is much visible. Even though we did not use them in the early publications [Villa et al., 2019; Villa et al., 2020], these filtering techniques can be efficiently used in quench spectroscopy to enhance the visibility of the signals.

3.3.5 Extracting additional information from the QSF

In addition to the excitation spectrum or transition energies, local quench spectroscopy can also be a tool to explore other less standard properties of excitations. This section highlights the versatility of local quench spectroscopy, especially the fact that in principle any transition can be targeted depending on the choice of the observable, including higher excited state manifolds.

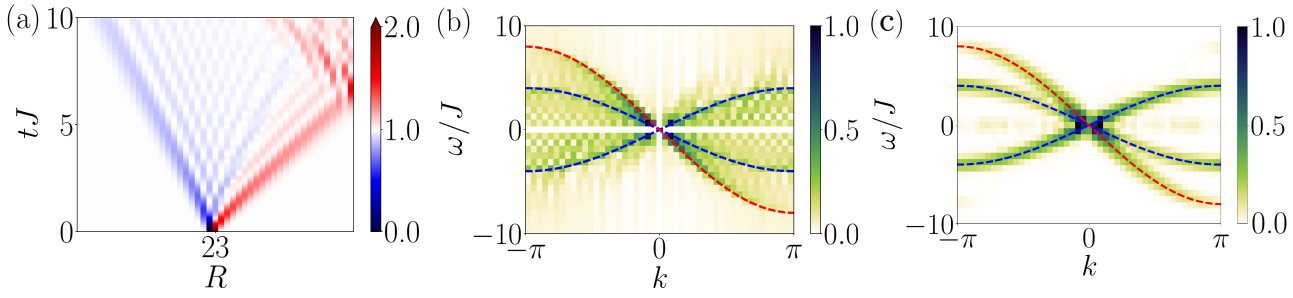

Fig. 3.17 (a) Space-time pattern of the density $\langle\hat{n}(R,t)\rangle$ in the Bose-Hubbard chain in the strongly interacting Mott phase with $U/J = 75$ and $\bar{n} = 1$. The initial state is the ground state where a particle has been displaced from the central site to its neighbour. (b) Corresponding normalised modulus of the QSF, whose algebraic divergences are in excellent agreement with the resonant energy transitions $\omega = \pm 2v\sin(k/2)$ with $v = 2J$ for the holon (dashed blue line) and $v = 4J$ for the doublon (dashed red line). The $\omega = 0$ component has been removed to improve visibility. From [Villa et al., 2020]. (c) Same as (b) but after an apodisation of the space-time pattern using a Hann window to reduce numerical artefacts of the numerical Fourier transform. The long-time average instead of the time average has been removed for visibility. I thank S.J. Thomson for this last figure.

3.3.5.1 Probing non-local excitations of the transverse-field Ising chain

Until now we have mainly focused on the z-polarised phase of the transverse-field Ising chain, where the low-lying excitations are represented by spin flips. Exploiting the self-duality of the model, we know that in the x-polarised phase, the excitations are spin flips in the reciprocal lattice, and correspond to pairs of counter-propagating domain walls (Sec. 1.1.3). While an individual domain wall is non-local and thus cannot be excited individually by a local quench, a *pair* corresponding to the second excited manifold can be probed using local quench spectroscopy.

Analytical insight To probe the properties of states containing two domain walls excitations, we should find an observable that couples the transitions $n \leftrightarrow 0$, with $|n'\rangle = |0\rangle$ the ground state and $\langle n|$ containing two quasiparticles with arbitrary momenta $\boldsymbol{k_1}$ and $\boldsymbol{k_2}$. The choice of the observable is dictated by the condition $\langle n|\,\hat{O}\,|n'\rangle \neq 0$, and the simplest form of observable satisfying such requirement is

$$\hat{O} = \sum_{\boldsymbol{p},\boldsymbol{p'}} C_{\boldsymbol{p},\boldsymbol{p'}} \hat{\gamma}^\dagger_{\boldsymbol{p}} \hat{\gamma}^\dagger_{\boldsymbol{p'}}. \tag{3.77}$$

The same argument applies by reversing the role of n and n', in which case the observable annihilates two quasiparticles instead of creating them. From the QSF given in Eq. (3.51), the momentum selection rule sets $\boldsymbol{P}_n = -\boldsymbol{k}$, such that without loss of generality we may choose $\boldsymbol{k_1} = -\boldsymbol{k} - \boldsymbol{q}$ and $\boldsymbol{k_2} = \boldsymbol{q}$ with $\boldsymbol{q}$ being arbitrary for now. The matrix elements of the observable simplify as

$$\langle n|\,\hat{O}\,|n'\rangle = \sum_{\boldsymbol{q},\boldsymbol{p},\boldsymbol{p'}} C_{\boldsymbol{p},\boldsymbol{p'}} \langle 0|\,\hat{\gamma}_{-\boldsymbol{k}-\boldsymbol{q}} \hat{\gamma}_{\boldsymbol{q}} \hat{\gamma}^\dagger_{\boldsymbol{p}} \hat{\gamma}^\dagger_{\boldsymbol{p'}}\,|0\rangle = \sum_{\boldsymbol{q},\boldsymbol{p},\boldsymbol{p'}} C_{\boldsymbol{p},\boldsymbol{p'}} \delta_{\boldsymbol{p},\boldsymbol{q}} \delta_{\boldsymbol{p'},-\boldsymbol{k}-\boldsymbol{q}} \pm (\boldsymbol{p} \leftrightarrow \boldsymbol{p'}), \tag{3.78}$$

where the sign depends on the quasiparticle statistics (+ for bosonic ones and - for fermionic ones), and $E_n = E_{-\boldsymbol{k}-\boldsymbol{q}} + E_{\boldsymbol{q}}$. The QSF finally becomes

$$G(\boldsymbol{k};\omega) = 2\pi \int \left(C_{\boldsymbol{q},-\boldsymbol{k}-\boldsymbol{q}}\, \rho_{\mathrm{i}}^{0;(-\boldsymbol{k}-\boldsymbol{q},\boldsymbol{q})} \pm C_{-\boldsymbol{k}-\boldsymbol{q},\boldsymbol{q}}\, \rho_{\mathrm{i}}^{0;(\boldsymbol{q},-\boldsymbol{k}-\boldsymbol{q})} \right) \delta(E_{-\boldsymbol{k}-\boldsymbol{q}} + E_{\boldsymbol{q}} + \omega)\, \mathrm{d}\boldsymbol{q}. \tag{3.79}$$

The alternative choice for the observable annihilating two quasiparticles (with the roles of n and n' reversed) can be obtained by changing $(\boldsymbol{k},\omega) \to (-\boldsymbol{k},-\omega)$ and the energy selection rule becomes $\delta(E_{\boldsymbol{k}-\boldsymbol{q}} + E_{\boldsymbol{q}} - \omega)$.

To understand the nature of the divergences that may appear in Eq. (3.79), and owing to the similarities with Eq. (3.67) for the transitions energies, we follow a similar derivation as in Sec. 3.3.4 and study the behaviour of the function $\tilde{g}_k(q,\omega) = E_{-k-q} + E_q + \omega$ (equivalently one may use $E_{k-q} + E_q - \omega$ which eventually leads to the same conclusion). We write the zeros of the function $\tilde{g}_k(q,\omega)$ as $\tilde{g}_k(\tilde{q}^\star_k(\omega)) = 0$, which for a spectrum of the form $E_k = \Delta - v\cos k$ are

$$\tilde{q}^\star_k(\omega) = -\frac{k}{2} + \arccos\left(\frac{\omega + 2\Delta}{2v\cos(k/2)}\right), \tag{3.80}$$

and exist within the interval $\omega \in [2\Delta - 2v\cos(k/2); 2\Delta + 2v\cos(k/2)]$. Equation (3.69) still holds for $\tilde{g}_k(q,\omega)$ now, and the algebraic divergence of the QSF appear for $\partial_q \tilde{g}_k|_{q=\tilde{q}^\star_k(\omega)}$ explicitly given for the cosine-like spectrum by

$$\partial_q \tilde{g}_k|_{q=\tilde{q}^\star_k(\omega)} = -2v\cos\left(\tfrac{k}{2}\right)\sqrt{1 - \left(\frac{\omega + 2\Delta}{2v\cos(k/2)}\right)^2}. \tag{3.81}$$

Therefore we observe a continuum bounded by sharp upper and lower boundaries defined for positive frequencies by

$$\omega = 2\Delta \pm 2v\cos\left(\tfrac{k}{2}\right). \tag{3.82}$$

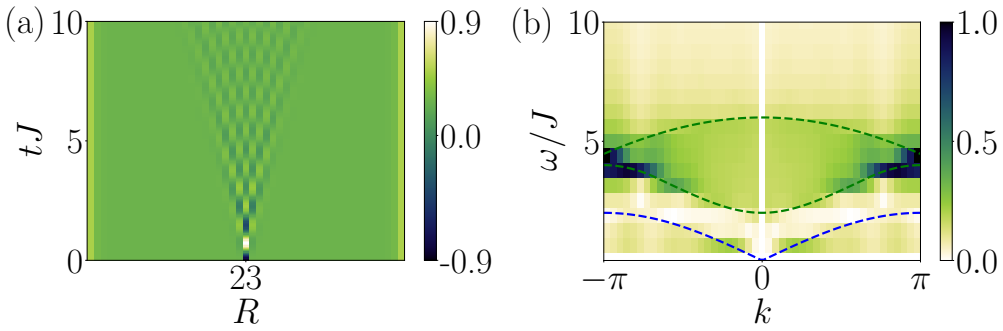

Fig. 3.18 (a) Space-time pattern of the transverse magnetisation $\langle\hat{\sigma}^z(R,t)\rangle$ in the x-polarised phase. The initial state is the ground state where the central spin as been rotated around y by $\theta = \pi/2$. (b) Corresponding normalised modulus of the QSF displaying a sharp signal within the energy continuum $E_q + E_{q-k}$ with arbitrary q (envelope in dotted green). A weak signal resulting from the energy transitions $E_q - E_{q-k}$ (dotted blue) is also barely visible. From [Villa et al., 2020].

This result is well known for instance for the isotropic Heisenberg chain, where the 2-magnon continuum computed from the Bethe ansatz lies within a continuum with boundaries $2J[1 \pm \cos(k/2)]$ [Karbach and Müller, 1997], consistently with the picture above since the excitation spectrum is given by a cosine-like form with $\Delta = v = J$. The boundaries of this continuum can also be obtained from a geometrical point of view as a consequence of the global concavity of the single magnon dispersion relation, and are given by $2E_{k/2}$ (lower boundary) and $2E_{\pi-k/2}$ (upper boundary) [Barnes, 2003].

Numerical results We keep the same local quench protocol, but since the ground state is within the x-polarised phase when we rotate the central spin around y by $\pi/2$, it points along $-z$. To avoid numerical issues with the degeneracy of the ground state, we apply a small symmetry-breaking field on the first site of the chain with amplitude $h_x = -10^{-2}J$ in the x-direction.

For $h/J = 0.5$, we probe the transverse magnetisation $\langle\hat{\sigma}^z(R,t)\rangle$ and compute the associated QSF in Fig. 3.18. The boundaries observed in the QSF for the two-excitation continuum matches very well with the ones predicted by evaluating numerically the derivative with respect to q of $\tilde{g}_k(q,\omega)$ at $q = \tilde{q}_k(\omega)$ (dashed green line). It turns out that for $h/J = 0.5$, we are sufficiently far from the critical point such that the spectrum is approximately given by $E_k \simeq 2h - 2J\cos(k)$. Therefore the continuum boundaries can be approximated by Eq. (3.82) with $\Delta = 2J$ and $v = 2h$ (recall that in the dual phase the roles of h and J are reversed, see below). This is even more visible if we move further away from the critical point, as shown in Fig. 3.19(b) for $h/J = 0.2$. Let us now explain why $\hat{\sigma}^z$ can probe such 2-excitations continuum. We will make use of the self-duality mapping of the model already discussed in Sec. 1.1.3. We start from the Hamiltonian of the form $\hat{H} = \sum_j -J\hat{\sigma}^x_j\hat{\sigma}^x_{j+1} - h\hat{\sigma}^z_j$. Thanks to the duality mapping, we may write $\hat{\sigma}^z_j = \hat{\mu}^x_{\alpha+1}\hat{\mu}^x_\alpha$ in the reciprocal lattice, where the $\hat{\mu}$'s are Pauli matrices. Using the linearised Holstein-Primakoff transformation, $\hat{\mu}^x_j = \hat{a}_j + \hat{a}^\dagger_j$ such that $\hat{\sigma}^z_j = \left(\hat{a}_j + \hat{a}^\dagger_j\right)\left(\hat{a}_{j+1} + \hat{a}^\dagger_{j+1}\right)$. Moving to momentum-space, such observable contains a term of the form (3.77) which reveals the 2-excitation continuum. Note that it also contains a term of the form (3.65) which probes the energy differences and that we already discussed in Sec. 3.3.4. One last subtlety is that the Hamiltonian now reads in terms of the new Pauli matrices as $\hat{H} = \sum_\alpha -h\hat{\mu}^x_\alpha\hat{\mu}^x_{\alpha+1} - J\hat{\mu}^z_\alpha$. Therefore it is the same Hamiltonian as the original one, but with the roles of h and J reversed. The 2-excitation boundaries in the x-polarised phase are therefore given (far from the critical point) by $4J \pm 4h\cos(k/2)$ for the upper and lower edge of the continuum respectively. Similarly, the continuum from energy differences, barely visible in Fig. 3.18 has an upper edge given by $2v\sin(k/2)$ with $v = 2h$. Closer to the critical point, the continuum envelope gets distorted compared to the simple form (3.82), but it

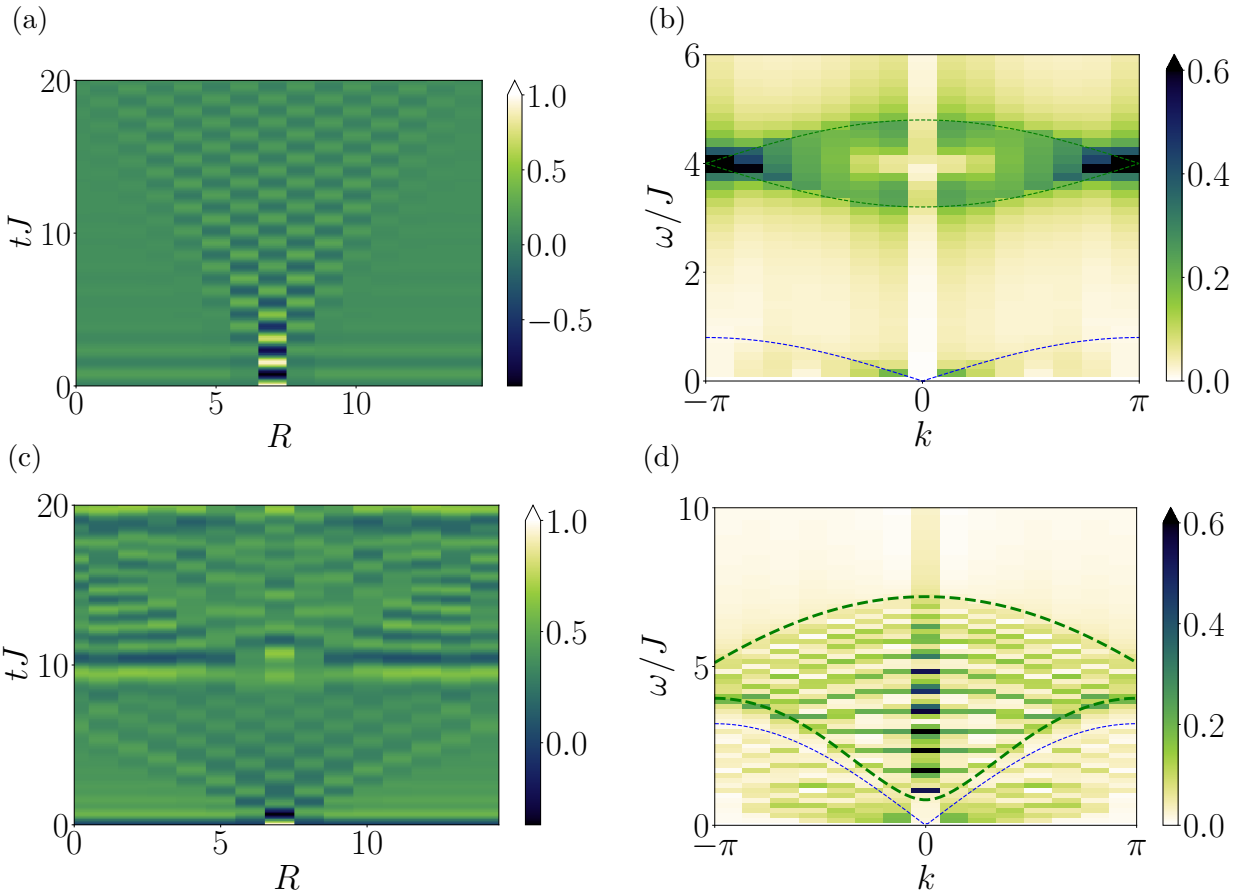

Fig. 3.19 (a) Space-time pattern of $\langle\hat{\sigma}^z(R,t)\rangle$ after preparing the system in its ground state for $h/J = 0.2$ and rotating the central spin by $\theta = -\pi/2$ around y (such that it points along $+z$). Periodic boundary conditions are used and $L = 15$ sites. (b) Associated normalised QSF modulus. The 2-excitation continuum is well approximated by Eq. (3.82) since far from the critical point the spectrum is almost cosine-like. (c,d) Are similar but with $h/J = 0.8$. Closer to the critical point, the continuum envelope of $E_q + E_{q-k}$ deviates from the previous simple analytical form but can be determined numerically (dashed green). The energy transitions are also visible below the continuum.

can still be obtained numerically since the spectrum is exactly known. We show such an example in Fig. 3.19(d) for $h/J = 0.8$ (dashed green). Several lines from the energy transitions are also visible below the 2-excitation continuum.

It proves interesting to compare the results obtained for the probe $\langle\hat{\sigma}^z(R,t)\rangle$ with the ones that can be obtained from the dynamical structure factor in pump-probe spectroscopy at both zero and finite temperature. However, to keep our focus purely on quench spectroscopy, we postpone this discussion to Appendix 3.B.

3.3.5.2 Two-excitation continuum in the Bose-Hubbard chain

The observation of the signal from the 2-excitation continuum is not restricted to the transverse-field Ising model, and can also be observed on the Bose-Hubbard chain. In the strongly interacting Mott insulating phase, the true elementary excitations (see Appendix 1.D) are the Bogoliubons

$$\hat{\gamma}^\dagger_{k,\pm} = u_k \hat{c}^\dagger_{k,\pm} \pm v_k \hat{c}_{-k,\mp}, \tag{3.83}$$

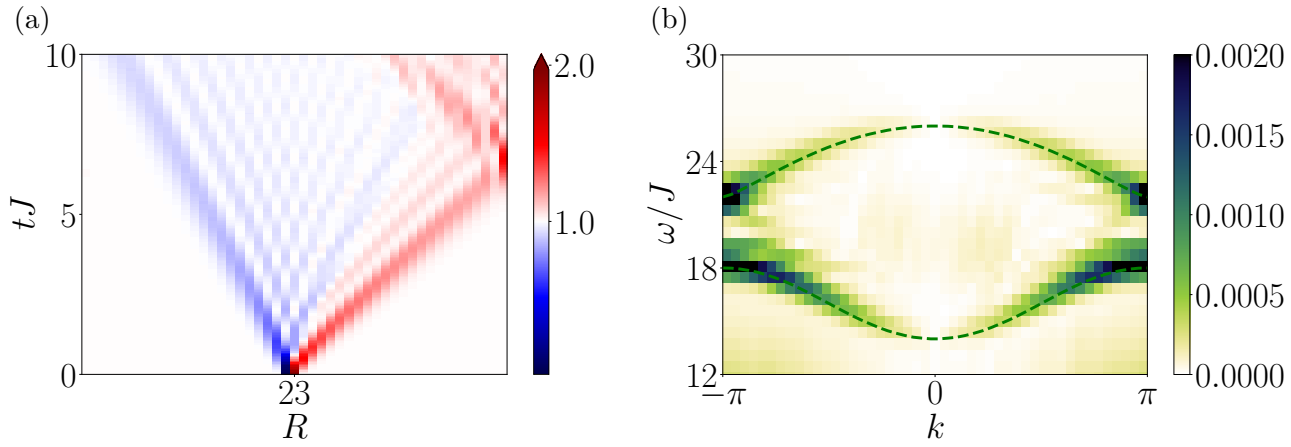

Fig. 3.20 (a) Space-time pattern of the density $\langle \hat{n}(R,t) \rangle$ in the Bose-Hubbard chain in the Mott phase with $U/J = 20$ and $\bar{n} = 1$. The initial state is the ground state where a particle has been moved from the central site to its neighbour. (b) Corresponding normalised modulus of the QSF on the region showing the 2-excitation continuum whose boundaries are in excellent agreement with the predicted algebraic divergences (dashed green). This signal is extremely weak (see cutoff on the colorbar).

and the full expression of the density is (removing the time dependence to lighten the notations)

$$\begin{aligned}\hat{n}(R) = \hat{a}_R^\dagger \hat{a}_R &= (\bar{n}+1)\hat{c}_{R,+}^\dagger \hat{c}_{R,+} + \bar{n}\,\hat{c}_{R,-}\hat{c}_{R,-}^\dagger \\ &= (\bar{n}+1)\sum_{p,p'} \mathrm{e}^{i(p'-p)R}\left[u_p u_{p'}\hat{\gamma}_{p,+}^\dagger\hat{\gamma}_{p',+} - v_p v_{p'}\hat{\gamma}_{-p,-}\hat{\gamma}_{-p',-}^\dagger + u_p v_{p'}\hat{\gamma}_{p,+}^\dagger\hat{\gamma}_{-p',-}^\dagger - v_p u_{p'}\hat{\gamma}_{-p,-}\hat{\gamma}_{p',+}\right] \\ &\quad + \bar{n}\sum_{p,p'} \mathrm{e}^{i(p-p')R}\left[u_p u_{p'}\hat{\gamma}_{p,-}\hat{\gamma}_{p',-}^\dagger - v_p v_{p'}\hat{\gamma}_{-p,+}^\dagger\hat{\gamma}_{-p',+} - u_p v_{p'}\hat{\gamma}_{-p,+}^\dagger\hat{\gamma}_{p',-}^\dagger + v_p u_{p'}\hat{\gamma}_{p,-}\hat{\gamma}_{-p',+}\right],\end{aligned} \tag{3.84}$$

where we inverted Eq. (3.83) to write $\hat{c}_{k,\pm}^\dagger = u_k\hat{\gamma}_{k,\pm}^\dagger \mp v_k\hat{\gamma}_{-k,\mp}$. By relabelling a few indices we conveniently rewrite the on-site density in the compact form

$$\hat{n}(R) = \sum_{p,p'} C_{pp'}^{uu}\hat{\gamma}_{p,+}^\dagger\hat{\gamma}_{p',+} + C_{pp'}^{vv}\hat{\gamma}_{-p,-}\hat{\gamma}_{-p',-}^\dagger + C_{pp'}^{uv}\hat{\gamma}_{p,+}^\dagger\hat{\gamma}_{-p',-}^\dagger + C_{pp'}^{vu}\hat{\gamma}_{-p,-}\hat{\gamma}_{p',+}, \tag{3.85}$$

where the prefactors are interaction dependent through the Bogoliubov-De Gennes functions u and v. In Sec. 3.3.4, we focused on the very strongly interacting regime ($U/J = 75$ in Fig. 3.17) such that $u_p \simeq 1$ and $v_p \simeq 0$ in excellent approximation. Thus, only $C_{pp'}^{uu} \neq 0$ in Eq. (3.85) and we recover the form (3.65) probing energy differences. When the interactions are a little less strong, $v_p = O(J/U)$ and the coefficients $C_{pp'}^{uv}$ and $C_{pp'}^{vu}$ start to become relevant. Since these terms are of the form (3.77), the density also probes a signal coming from the pair of two different excitations.

The signal observed in the QSF can be understood by generalising Eq. (3.51) to this specific situation. We take $|n'\rangle$ to be the ground state, while $\langle n|$ contains two elementary excitations with momentum k_1 and k_2. For simplicity, we focus on the contribution $\sum_{p,p'} C_{p,p'}^{uv}\hat{\gamma}_{p,+}^\dagger\hat{\gamma}_{-p',-}^\dagger$. (The same reasoning applies to $\sum_{p,p'} C_{pp'}^{vu}\hat{\gamma}_{p,-}\hat{\gamma}_{-p',+}$ by reversing the role of n and n'). The momentum selection rule on the eigenstate $\langle n|$ imposes only the momentum of the pair of the excitations $k_1 + k_2$ to be $-k$, so without loss of generality we choose $k_1 = -k - q$ and $k_2 = q$ with q being arbitrary. The matrix elements of the observable are given by

$$\langle n|\,\hat{O}\,|n'\rangle = \sum_{q,p,p'} \langle 0|\,\hat{\gamma}_{-k-q,+}\hat{\gamma}_{q,-}C_{p,p'}^{uv}\hat{\gamma}_{p,+}^\dagger\hat{\gamma}_{-p',-}^\dagger\,|0\rangle = \sum_{q,p,p'} C_{p,p'}^{uv}\delta_{-k-q,p}\delta_{q,-p'} = C_{-k-q,q}^{uv}, \tag{3.86}$$

and since the energy of the eigenstate n is $E_n = E_{-k-q}^+ + E_q^-$, finally the QSF is

$$G(k,\omega) \propto \int \rho_{\mathrm{i}}^{0;(-k-q,q)} C_{-k-q,q}^{uv}\,\delta(E_{-k-q}^+ + E_q^- - \omega)\,\mathrm{d}q. \tag{3.87}$$

The contribution of the term C^{vu} is similar by changing $n \leftrightarrow n'$. The consequence of Eq. (3.87) is that a continuum (q is arbitrary) appears around the gap U, with a sharply defined envelope that corresponds to the lines where the function $E^{+}_{-k-q} + E^{-}_{q} - \omega$ tends to zero. These algebraic divergences of the QSF are similar to the ones discussed from Eq. (3.69). We display the result of the numerical post-quench dynamics of $\langle \hat{n}(R,t) \rangle$ together with the corresponding QSF in Fig. 3.20. Since the expressions for $E_{\pm}(k)$ are known [for $\bar{n} = 1$, see by Eq. (1.113)], we can evaluate the boundaries of the predicted continuum and we represent them by the dashed green lines. They show an excellent agreement with the QSF. The amplitude of such signal is extremely weak, which shows the sensitivity of the QSF and the predictive power of a careful quench spectroscopy analysis. Indeed here, the smallness of the signal in comparison with the energy differences comes from the fact that $C^{uv}_{pp'} \ll C^{uu}_{pp'}$ in the expression of the density (3.85) since $U \gg J$.

In conclusion, we have proposed in this chapter a general scheme to study the spectral properties of the excitations by following the out-of-equilibrium dynamics after a quantum quench in translation invariant systems. As for any spectroscopic technique, in quench spectroscopy the choice of the observable determines the spectral properties that can be studied: excitation spectrum, energy transitions or higher excited states. The probed quantity can be understood by decomposing the observable in terms of quasiparticles. The common example to many lattice models of a cosine-like excitation spectrum has been detailed analytically, since it offers a simple interpretation of the observed continua.

After a global quench, since translation invariance of the initial state is preserved, two-point correlators are necessary to probe spectral properties. After a local quench which break the translation invariance of the initial state, the simpler one-point functions can be used. In both cases, and in contrast to standard pump-probe spectroscopies, the study of the out-of-equilibrium dynamics allows to probe equal-time correlators, such that the quench spectral function can be reconstructed from snapshots of the dynamics. This grants a momentum-resolved spectroscopy over the full Brillouin zone without requiring any external calibration for each value of the momentum. Another advantage of the method is its simplicity: after a global quench, a bunch of excitations are automatically generated throughout the system. Local quenches also offer a simpler tool compared to alternative methods by avoiding to explicitly construct the excitation, here only a *single* local quench can probe the entire spectrum.

Here we focused on one-dimensional systems to make use of efficient tensor network numerical simulations in order to benchmark the method, but the technique should equally apply to higher dimensions and different models (especially fermions, not considered here). We chose our dynamical parameters to match with the resolution that can already be accessed by state-of-the-art experiments either using local quenches [Fukuhara, Kantian, et al., 2013; Fukuhara, Schauß, et al., 2013; Jurcevic et al., 2015] or global ones [Trotzky et al., 2012]. We note however that values up to $t_{\max} = 100\hbar/J$ are now being used in experiments [Kohlert et al., 2019; Rispoli et al., 2019], which would probe spectral properties with an unprecedented resolution.

Appendices

3.A Approximate Bethe ansatz for the Bose-Hubbard model

While the Lieb-Liniger model is integrable and can be solved exactly using the Bethe ansatz (Appendix 1.A), its lattice counterpart, the Bose-Hubbard model, breaks integrability for a finite value of the interaction parameter U/J [Sutherland, 2004]. Nonetheless, we discuss below how in the strongly interacting regime at low filling, an approximate approach based on the Bethe ansatz can reasonably describe the dynamics of the low-energy excitations.

3.A.1 Validity regime of the Bethe ansatz approach

The integrability breaking of the Bose-Hubbard chain for finite interactions can be related to the presence of multiply occupied states containing at least 3 bosons on a single site [Choy and Haldane, 1982; F. Haldane, 1980]. Such states, allowed by the bosonic statistics, violate the consistency condition that three-body scattering can be decomposed into a product of two-body scattering independently of the ordering. The model is not integrable, Bethe ansatz states do not cover the full Hilbert space. Worse, the states described by the ansatz may be unphysical, in the sense that they may not obey the Schrödinger equation.

Regardless, in a pioneering work [Krauth, 1991] argued that the Bethe ansatz gives an approximative but acceptable solution for thermodynamic quantities if $\bar{n} < 1$. He interpreted the agreement by noting that for sufficiently strong interactions, the density fluctuations are small enough such that the states containing more than two particles on a single site become less and less probable and therefore do not contribute significantly to the thermodynamic properties. On small systems, we may estimate the contribution of such states using exact diagonalisation (Fig. 3.21). At low filling $\bar{n} \ll 1$ and sufficiently strong interactions $U \gg J$, states involving multiply-occupied sites with three bosons or more are very unlikely. To give a number, we will show below that the approximate Bethe ansatz approach gives an acceptable approximation for thermodynamic quantities in the ground state if $U > 8J$ with $\bar{n} < 1$.

3.A.2 Bethe equations and thermodynamic properties

The strategy to derive the Bethe equations for the Bose-Hubbard chain is very similar to the one detailed for the Lieb-Liniger case (Sec. 1.A.1.3). We first obtain the two-particle phase shift, from which we express the approximate Bethe equations for $U \gg J$ and $\bar{n} \ll 1$. We then explain how to extract thermodynamic quantities and test the approximation by comparing to other methods.

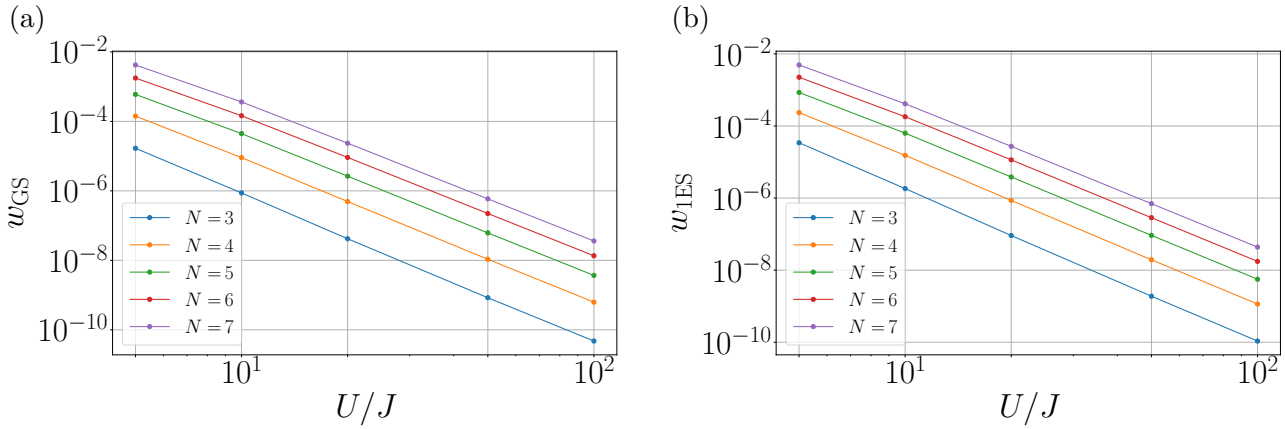

Fig. 3.21 Contribution $w_n = \sum_\alpha |\langle n|\alpha\rangle|^2$ of the Fock states $|\alpha\rangle$ with at least 3 bosons on at least one site to the eigenstate $|n\rangle$ which refers to (a) the ground state and (b) the first excited state. This result has been computed using ED on a $L = 10$ sites system for the interaction values $U/J = 5, 10, 20, 50, 100$. For all but the weakest interactions, such highly occupied states do not contribute much to the low-energy physics.

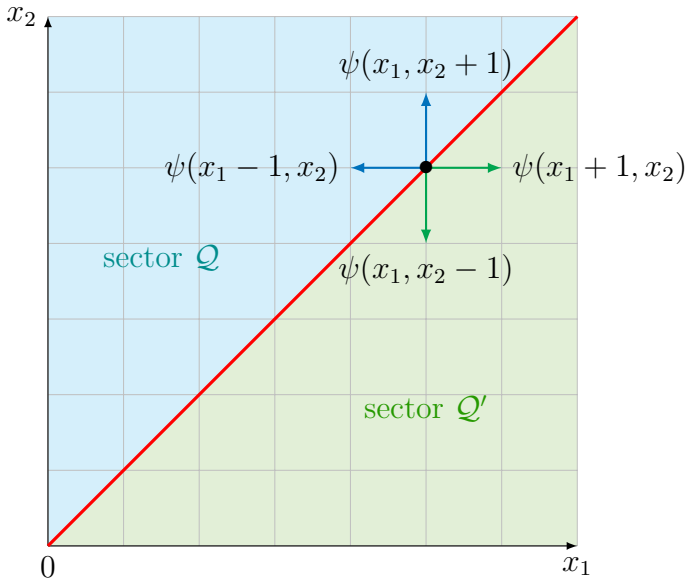

Fig. 3.22 Representation of the different sectors in the plane (x_1, x_2). The frontier between the two sectors (red line) represents the interaction region. The tunnelling term of the Hamiltonian can induce a move in the sector $\mathcal{Q}$ (blue) or the sector $\mathcal{Q}'$ (green). In these two regions the wave function is given by the ansatz (3.89).

3.A.2.1 The two-particle phase shift

The goal of this subsection is to derive the two-particle phase shift θ_{12} initially obtained by [Krauth, 1991]. The result is given by Eq. (3.94). We focus on the simplest case of two particles, labelled by an index $j = 1, 2$ and located at the sites x_j. The Schrödinger equation reads as

$$\begin{aligned}\hat{H}_{\rm BH}\,\psi(x_1,x_2) = &-J\left[\psi(x_1+1,x_2)+\psi(x_1-1,x_2)+\psi(x_1,x_2+1)+\psi(x_1,x_2-1)\right]\\ &+\tfrac{U}{2}\left[\delta(x_1-x_2)+\delta(x_2-x_1)\right]\psi(x_1,x_2) = E\,\psi(x_1,x_2).\end{aligned} \tag{3.88}$$

We denote by $f_{\mathcal{Q},\mathcal{Q}'}$ the restriction of the wave function to one of the two sectors $\mathcal{Q} = \{x_1 < x_2\}$ or $\mathcal{Q}' = \{x_1 > x_2\}$ and we make the following ansatz for the reduced wave function in each sector

$$\begin{aligned}f_{\mathcal{Q}} &= A_{\mathcal{Q}}(k_1,k_2)\,\mathrm{e}^{i(k_1x_1+k_2x_2)} + A_{\mathcal{Q}}(k_2,k_1)\,\mathrm{e}^{i(k_2x_1+k_1x_2)},\\ f_{\mathcal{Q}'} &= A_{\mathcal{Q}'}(k_1,k_2)\,\mathrm{e}^{i(k_1x_2+k_2x_1)} + A_{\mathcal{Q}'}(k_2,k_1)\,\mathrm{e}^{i(k_2x_2+k_1x_1)}.\end{aligned} \tag{3.89}$$

The continuity of the wave function imposes that on the boundary $x_1 = x_2$, $f_{\mathcal{Q}} = f_{\mathcal{Q}'}$. We then determine whether the wave function belongs to the sector $\mathcal{Q}$ or $\mathcal{Q}'$ (Fig. 3.22) and write

$$\begin{aligned}\hat{H}_{\rm BH}\psi = -J\Big[&A_{\mathcal{Q}'}(k_1,k_2)\,\mathrm{e}^{ik_2}\,\mathrm{e}^{i(k_1x_2+k_2x_1)} + A_{\mathcal{Q}'}(k_2,k_1)\,\mathrm{e}^{ik_1}\,\mathrm{e}^{i(k_2x_2+k_1x_1)}\\ &+ A_{\mathcal{Q}'}(k_1,k_2)\,\mathrm{e}^{-ik_1}\,\mathrm{e}^{i(k_1x_2+k_2x_1)} + A_{\mathcal{Q}'}(k_2,k_1)\,\mathrm{e}^{-ik_2}\,\mathrm{e}^{i(k_2x_2+k_1x_1)}\\ &+ A_{\mathcal{Q}}(k_1,k_2)\,\mathrm{e}^{-ik_1}\,\mathrm{e}^{i(k_1x_1+k_2x_2)} + A_{\mathcal{Q}}(k_2,k_1)\,\mathrm{e}^{-ik_2}\,\mathrm{e}^{i(k_2x_1+k_1x_2)}\\ &+ A_{\mathcal{Q}}(k_1,k_2)\,\mathrm{e}^{ik_2}\,\mathrm{e}^{i(k_1x_1+k_2x_2)} + A_{\mathcal{Q}}(k_2,k_1)\,\mathrm{e}^{ik_1}\,\mathrm{e}^{i(k_2x_1+k_1x_2)}\Big]\\ &+ U\left(A_{\mathcal{Q}}(k_1,k_2)\,\mathrm{e}^{i(k_1x_1+k_2x_2)} + A_{\mathcal{Q}}(k_2,k_1)\,\mathrm{e}^{i(k_2x_1+k_1x_2)}\right).\end{aligned} \tag{3.90}$$

Our goal is now to determine the amplitude coefficients. Since we work with bosons, the global wave function must be symmetric under the exchange of two particles which imposes that $A_{\mathcal{Q}}(k_1,k_2) = A_{\mathcal{Q}'}(k_1,k_2)$ (which we now simply write A_{12}) and $A_{\mathcal{Q}}(k_2,k_1) = A_{\mathcal{Q}'}(k_2,k_1)$ (which we now simply write A_{21}). Furthermore, we are only interested in the value of the wave function on

the boundary $x_1 = x_2$ where the interaction term is non-vanishing, so we take $x_1 = x_2 = \bar{x}$. Up to an irrelevant phase factor $\mathrm{e}^{i(k_1+k_2)\bar{x}}$, Eq. (3.90) simplifies into

$$\hat{H}_{\mathrm{BH}}\psi = -J\left[A_{12}\,\mathrm{e}^{-i(k_1-k_2)} + A_{21}\,\mathrm{e}^{i(k_1-k_2)} + A_{12}\,\mathrm{e}^{-i(k_1-k_2)} + A_{21}\,\mathrm{e}^{i(k_1-k_2)}\right] + U\left(A_{12}+A_{21}\right). \quad (3.91)$$

Now we impose that the energy is of the form $-2J[\cos(k_1)+\cos(k_2)]$ (which corresponds to the hard core limit where $U \to \infty$ and the model can be mapped to free fermions) such that

$$E\psi = -J\left[\mathrm{e}^{ik_1} + \mathrm{e}^{-ik_1} + \mathrm{e}^{ik_2} + \mathrm{e}^{-ik_2}\right]\left(A_{12}+A_{21}\right). \quad (3.92)$$

To satisfy the Schrödinger equation (Eq. (3.91) and (3.92) are equal), the following constraint has to be satisfied

$$A_{12}\left[U + J\left(\mathrm{e}^{ik_1} - \mathrm{e}^{-ik_1}\right) - J\left(\mathrm{e}^{ik_2} - \mathrm{e}^{-ik_2}\right)\right] = A_{21}\left[-U + J\left(\mathrm{e}^{ik_1} - \mathrm{e}^{-ik_1}\right) - J\left(\mathrm{e}^{ik_2} - \mathrm{e}^{-ik_2}\right)\right], \quad (3.93)$$

which can be expressed as

$$\frac{A_{12}}{A_{21}} = \frac{i(\sin k_1 - \sin k_2) - \frac{U}{2J}}{i(\sin k_1 - \sin k_2) + \frac{U}{2J}} := -\mathrm{e}^{i\theta_{12}}, \quad \text{with} \quad \theta_{12} = -2\arctan\left[\tfrac{2J}{U}(\sin k_1 - \sin k_2)\right]. \quad (3.94)$$

As mentioned by [Krauth, 1991], this expression can be obtained directly by using the phase-shift of the Lieb-Liniger model $\theta_{12} = -2\arctan((k_1-k_2)/c)$ and the mapping $c = U/(2Ja)$; $k \to \sin k$. The explicit derivation above ensures that no factor such as $\cos k$ appear (this will be the case for the excitations where the result cannot be simply derived from the continuum limit).

3.A.2.2 Approximate Bethe equations

For strong interactions and at low filling, we may neglect the integrability breaking and assume that the N-particles system can be described approximately by the following Bethe equations

$$\mathrm{e}^{ik_jL} = (-1)^{N-1}\prod_{l=1}^{N}\mathrm{e}^{i\theta_{jl}}. \quad (3.95)$$

Taking the logarithm, we write it as

$$k_jL = 2\pi I_j + \sum_{l=1}^{N}\theta_{jl}, \quad (3.96)$$

with $I_j = \tilde{I}_j - \left(\frac{N-1}{2}\right) \in \mathbb{N}$ for N odd (half-integers for N even) and $\tilde{I}_j \in [0;N]$ in the ground state. Importantly, just as in the continuum case, the ground state can be described by the ordered and equidistant quantum numbers $\tilde{I}_j$. To describe the thermodynamic properties, we define the counting function

$$y(k_j) := k_j - \frac{1}{L}\sum_{l=1}^{N}\theta_{jl}, \quad (3.97)$$

so that

$$\begin{aligned}\frac{\mathrm{d}y}{\mathrm{d}k_j} &= 1 - \frac{1}{L}\sum_{l=1}^{N}\frac{-2\times\frac{2J}{U}\cos k_j}{1+\left[\frac{2J}{U}(\sin k_j - \sin k_l)\right]^2} = 1 + \frac{U}{J}\cos k_j\frac{1}{L}\sum_{l=1}^{N}\frac{1}{\left(\frac{U}{2J}\right)^2 + (\sin k_j - \sin k_l)^2} \\ &:= \frac{y(k_{j+1})-y(k_j)}{k_{j+1}-k_j} = \frac{\frac{2\pi}{L}(I_{j+1}-I_j)}{k_{j+1}-k_j} = 2\pi\rho(k_j).\end{aligned} \quad (3.98)$$

Therefore in the thermodynamic limit we obtain

$$2\pi\rho(k) = 1 + \frac{U}{J}\cos k \int_{-k_\mathrm{F}}^{k_\mathrm{F}} \frac{\rho(k')\,\mathrm{d}k'}{\left(\frac{U}{2J}\right)^2 + (\sin k - \sin k')^2}. \tag{3.99}$$

Introducing the reduced variables

$$\alpha = \frac{U}{2Jk_\mathrm{F}a}\,, \qquad \gamma = \frac{U}{2Jna}\,, \tag{3.100}$$

the set of coupled equations we need to solve numerically is

$$\frac{\alpha}{\gamma} = \int_{-1}^{1} g(x)\,\mathrm{d}x \tag{3.101a}$$

$$g(x) = \frac{1}{2\pi} + \frac{\alpha}{\pi}\cos(k_\mathrm{F}x)\int_{-1}^{1} \frac{g(y)\,\mathrm{d}y}{\alpha^2 + \frac{1}{k_\mathrm{F}^2}\left[\sin(k_\mathrm{F}x) - \sin(k_\mathrm{F}y)\right]^2}. \tag{3.101b}$$

In the continuum limit $a \to 0$, we recover the equations of the Lieb-Liniger model.

3.A.2.3 Generating function of thermodynamic properties

In the Lieb-Liniger model, only a single parameter, $\alpha = c/k_\mathrm{F}$, was required to solve the Bethe equations (1.71). Equivalently but more conveniently, we chose the parameter γ. In the discrete case now, we need to specify independently two parameters $\{\alpha; k_\mathrm{F}\}$ to solve the set of equations (3.101). This additional parameter comes from the additional length scale due to the discretisation (the lattice spacing, set to one in the following). Physically, it proves more convenient to specify independently the two parameters $\{U/J; k_\mathrm{F}\}$. By analogy with the generating function $e(\gamma)$, defined by Eq. (1.68), we define the generating thermodynamic function $e(U/J; k_\mathrm{F})$ as[11]

$$e(U/J; k_\mathrm{F}) = \frac{E_0/J}{\bar{n}^3} = \frac{-2k_\mathrm{F}}{\bar{n}^3}\int_{-1}^{1} \cos(k_\mathrm{F}x)g(x)\,\mathrm{d}x. \tag{3.102}$$

From this choice of variables we can express in a compact form all thermodynamic quantities, since they are defined at fixed U/J and system size L. To lighten the notations, we write $e = e(U/J; k_\mathrm{F})$ and all derivatives below are implicitly taken at fixed U/J and L such that

$$\mu/J = \frac{\partial(E_0/J)}{\partial\bar{n}} = 3n^2 e + n^3\frac{\partial e}{\partial k_\mathrm{F}}\left(\frac{\partial n}{\partial k_\mathrm{F}}\right)^{-1} \tag{3.103a}$$

$$\kappa_\mathrm{phys}^{-1} = n^2\frac{\partial\mu}{\partial n} = 6n^3 e + 6n^4\frac{\partial e}{\partial k_\mathrm{F}}\left(\frac{\partial n}{\partial k_\mathrm{F}}\right)^{-1} + n^5\left(\frac{\partial n}{\partial k_\mathrm{F}}\right)^{-2}\left\{\frac{\partial^2 e}{\partial k_\mathrm{F}^2} - \frac{\partial e}{\partial k_\mathrm{F}}\frac{\partial^2 n}{\partial k_\mathrm{F}^2}\left(\frac{\partial n}{\partial k_\mathrm{F}}\right)^{-1}\right\}. \tag{3.103b}$$

To compute $e(U/J, k_\mathrm{F})$ numerically, we fix some initial parameters $(U/J, k_\mathrm{F})$ and immediately obtain α. We then solve the Bethe equations by successive iterations to obtain the rescaled quasimomentum density $g(x)$, and then the filling $\bar{n}$. From there we can compute the generating thermodynamic function $e(U/J, k_\mathrm{F})$, and then any thermodynamic function in particular the chemical potential μ and the compressibility κ. The algorithm used is adapted from the one discussed for the Lieb-Liniger model, and its basic steps are represented in Fig. 3.23.

[11] In the continuum limit, one recovers the definition (1.68) up to a factor $2/\bar{n}^2$. This is because the ground state energies between the two models are shifted by $2J$. Also note that $e(U/J; k_\mathrm{F})$ remains only a function of $\gamma = U/2J\bar{n}$, but γ now depends on both variables U/J and k_F.

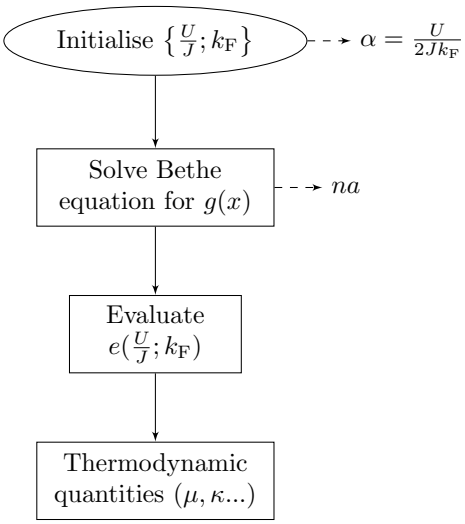

Fig. 3.23 Flowchart of the algorithm used to compute thermodynamic quantities in the Bose-Hubbard chain. The equations used are (3.101), (3.102) and (3.103).

3.A.3 Numerical results using the Bethe ansatz

Once the parameters $(U/J, k_F)$ are fixed, we can solve iteratively the approximate Bethe equations to evaluate the dimensionless quasimomentum density $g(x)$ and the filling $\bar{n}$. The correspondence between k_F and $\bar{n}$ is shown in Fig. 3.24(a). As expected, in the strongly interacting regime we recover the fermionised result $k_F \simeq \pi\bar{n}$. A physically acceptable solution of the Bethe equations is obtained if $n(k_F)$ is a strictly monotonic function such that $n(k_F) = k_F \int_{-1}^{1} g(x)\,dx$ is bijective. A pathological region appears for high fillings $\bar{n} \simeq 1$ and weak interactions $U/J < (U/J)_c$. The interaction value threshold below which the approximate Bethe ansatz breaks down at $\bar{n} = 1$ can be determined analytically as $(U/J)_c = 2\sqrt{3} \simeq 3.46$ [Krauth, 1991]. This is confirmed by our numerical results, where for interactions below this threshold value, negative values of the (rescaled) quasimomentum density $g(x)$ can be observed [Fig. 3.24(b)].

Of course requiring that the (rescaled) quasimomentum density is positive for all values is a necessary but not sufficient condition for the results to be physically meaningful. To assess

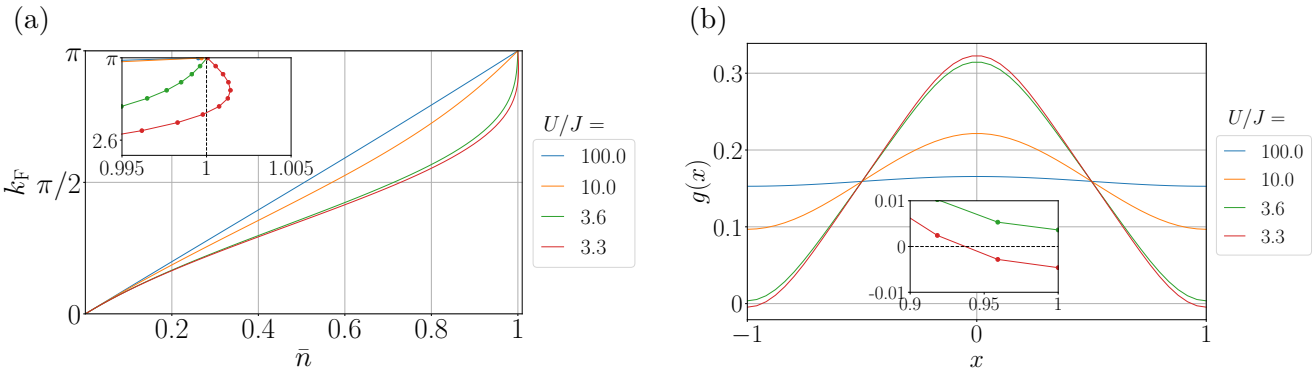

Fig. 3.24 (a) By specifying the Fermi quasimomentum k_F, we obtain a unique value of the filling $\bar{n}$ only if $U/J > (U/J)_c$ and $\bar{n} < 1$. Otherwise, the solution given by the approximate Bethe ansatz is not physically acceptable. While the precise value of $(U/J)_c$ can be determined to an arbitrary accuracy, here we simply show that $3.3 < (U/J)_c < 3.6$ (see inset). (b) Rescaled quasimomentum density $g(x) := \rho(k/k_F)$ for different interaction values, close to $\bar{n} = 1$. For very large interactions, $g(x) \simeq 1/2\pi$ (fermionised regime). Generally, the quasiparticles localise in quasimomentum space around $k = 0$. Below $(U/J)_c$, the approximate Bethe ansatz breaks down as the quasimomentum density takes negative values (see inset).

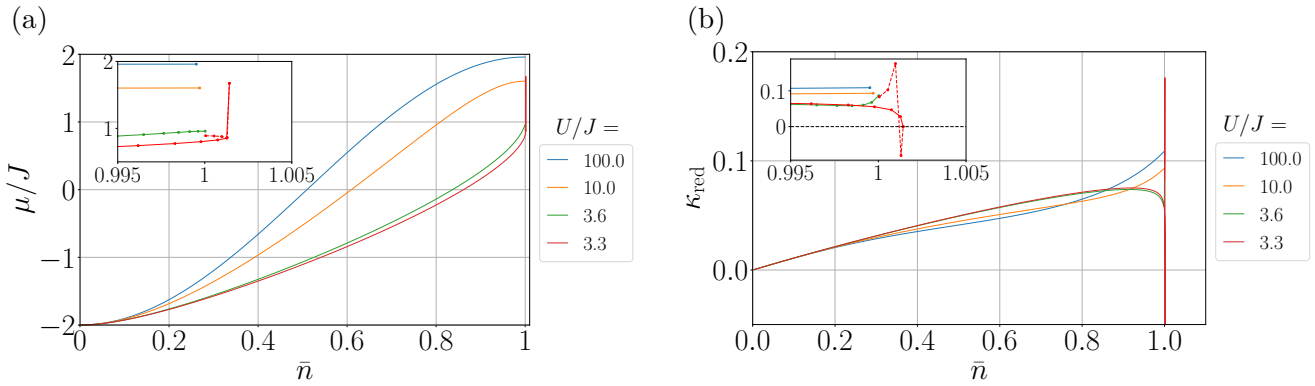

Fig. 3.25 (a) Chemical potential and (b) reduced compressibility as a function of the filling for different interaction values. The plateau around $\bar{n} = 1$ does not refer to the Mott transition. As shown by the inset, it corresponds to a region where the approximate Bethe ansatz approach is no longer valid. Such states yield a negative compressibility (inset in b).

the quality of the approximation, we need to compare to known exact results. In the regime where the Bethe ansatz can *a priori* be used, we obtain the equation of state of the system $\mu = f(\bar{n})$ [Fig. 3.25(a)] and other thermodynamic quantities, for instance the reduced compressibility [Fig. 3.25(b)]. For $(U/J)_c = 2\sqrt{3} \simeq 3.46$ at $\bar{n} = 1$, the compressibility diverges and crosses zero. Negative compressibilities are not physical, and this shows that such divergence does not signal the SF-MI phase transition (found using exact methods to be at $(U/J)_c = 3.3(1)$ [Ejima et al., 2011; Ejima et al., 2012; Kashurnikov and Svistunov, 1996]), as it appears inside the unphysical regime with negative quasimomentum densities.

3.A.4 Assessing the quality of the approximation

Since the model is not integrable, we want to know how good the approximate Bethe ansatz is for calculating thermodynamic quantities. We expect the approach to become worse at high filling where the multiply occupied sites play an increasingly important role (Sec. 3.A.1). The most binding criterion is for $\bar{n} = 1$, where we collect the value of the chemical potential for each value of the interaction $U/J > (U/J)_c$ and reconstruct the lower part of the first Mott lobe from the approximate Bethe ansatz. The structure of the lobe is well established and allows for a comparison with exact results (Fig. 3.26).

We compare our result to two models: first, a troncated model where at most two bosons per site are allowed [Kashurnikov and Svistunov, 1996; Kashurnikov et al., 1998] and second the full model[12]. As expected, the truncation of the Hilbert space has a dramatic effect especially at high filling and low interactions. For instance, the critical point of the SF-MI transition $(U/J)_c$ at $\bar{n} = 1$ is lowered by a factor of 5 in the reduced model [Kashurnikov et al., 1998], and the Mott lobe structure is strongly modified compared to the full model close to the tip of the lobe (Fig. 3.26). A discrepancy shows that multiply occupied states contribute significantly to the thermodynamic properties of the system. We first note that in the region $\bar{n} < 1$ and $U/J > 8$, the predictions of the full and reduced model become equivalent, and they further agree with the approximate Bethe ansatz result. The model is "quasi integrable", in the sense that the ansatz form describes well the solutions that are relevant for the ground state thermodynamic properties of the system.

When the interactions are reduced, the ansatz misses physical solutions of the Schrödinger equation that contribute significantly to the thermodynamic properties. More surprisingly, a discrepancy is also visible with the reduced model. This suggests that the form of the ansatz does not capture all the relevant solutions with at most two particles per site. In this regime where

[12] Any DMRG data is obtained by imposing a cutoff on the dimension of the local Hilbert space. The full model means that increasing the cutoff yields the same result.

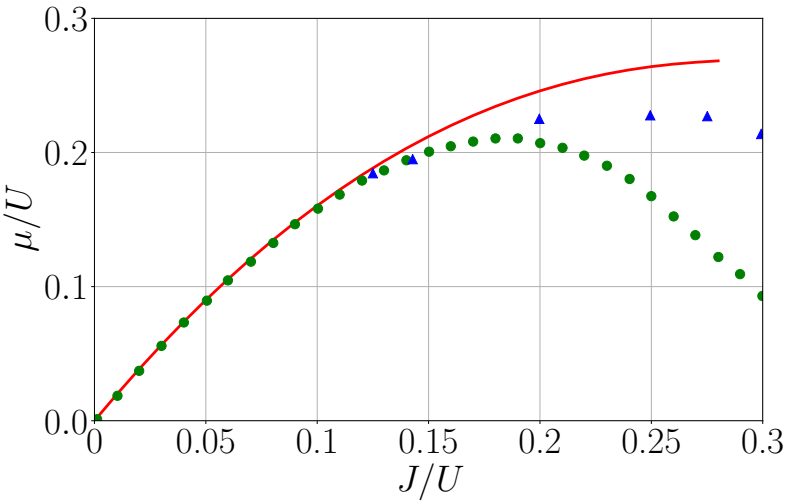

Fig. 3.26 First Mott lobe obtained by the approximate Bethe ansatz (full red line) compared with the Quantum Monte-Carlo data from [Kashurnikov et al., 1998] (blue triangles) for the reduced model and the DMRG data from [Kühner et al., 2000] (green circles) for the full model. On the region of strong interactions ($U/J > 8$) all approaches coincide. For weaker interactions, significant discrepancies between the predictions appear.

$\bar{n} \simeq 1$ and $U/J < 8$, the approximate Bethe ansatz should not be used.

3.A.5 Excitations and the excitation spectrum

Now that we have studied the ground state properties in the thermodynamic limit, we investigate the low-lying excited states. Following the procedure described for the Lieb-Liniger model, we describe how the quasimomenta redistribute when an excitation is created. Our goal is to obtain an equation for the backflow function $J(k)$ and use it to express the predicted excitation spectrum.

3.A.5.1 Derivation of the backflow equation

Physically, an excitation which conserves the particle number corresponds to the removal of a particle α from within the Fermi sea in quasimomentum space, and its placement above it. By definition, the equations for the N-particle ground state and the N-particle excited state are[13]

$$\begin{aligned} k_j L &= 2\pi I_j + \sum_{l=1}^{N} \theta\left(\sin k_j - \sin k_l\right), \\ k_j^\star L &= 2\pi I_j^\star + \sum_{l=1}^{N} \theta\left(\sin k_j^\star - \sin k_l^\star\right). \end{aligned} \tag{3.104}$$

We now want to know how the other quasimomenta k_j with $j \neq \alpha$ redistribute after this move of the particle α. Thus we define $\Delta k_j = k_j^\star - k_j$, assuming that $\Delta k_j \ll k_j$, and look for an equation on Δk_j. Since we only create one excitation, $I_j^\star = I_j$ for $j \neq \alpha$. Then, for $j \neq \alpha$, by taking the difference between the two equations (3.104) we get

$$\begin{aligned} \Delta k_j L &= \sum_{l=1}^{N} \left[\theta(\sin k_j^\star - \sin k_l^\star) - \theta(\sin k_j - \sin k_l)\right], \\ &\simeq \sum_{l\neq\alpha} \left[\Delta k_j \cos k_j - \Delta k_l \cos k_l\right] K(\sin k_j - \sin k_l) \\ &\quad + \theta(\sin k_j - \sin k_\alpha^\star) + \Delta k_j \cos k_j \, K(\sin k_j - \sin k_\alpha^\star) + \theta(\sin k_j - \sin k_\alpha), \end{aligned} \tag{3.105}$$

[13] From a technical point of view, we consider below Yang-Yang like excitations, and not Lieb like ones (see details in Sec. 1.A.3 on the Lieb-Liniger model).

where we defined

$$K(\sin k_j - \sin k_l) := \frac{-U/J}{\left(\frac{U}{2J}\right)^2 + \left[\sin k_j - \sin k_l\right]^2}. \tag{3.106}$$

To first order, we have $\Delta k_j \cos k_j \, K(\sin k_j - \sin k_\alpha^\star) \simeq \Delta k_j \cos k_j \, K(\sin k_j - \sin k_\alpha)$. We include this term so as to complete the sum over l in Eq. (3.105), and by regrouping the terms in Δk_j on the left-hand side we get

$$\begin{aligned}\Delta k_j L \left[1 - \frac{\cos k_j}{L} \sum_{l=1}^{N} K(\sin k_j - \sin k_l)\right] = &- \sum_{l \neq \alpha} \Delta k_l \cos k_l \, K(\sin k_j - \sin k_l) \\ &+ \theta(\sin k_j - \sin k_\alpha^\star) - \theta(\sin k_j - \sin k_\alpha).\end{aligned} \tag{3.107}$$

The term inside the brackets on the left is equal to $2\pi\rho(k_j)$ from the Bethe equation (3.98). In the thermodynamic limit, we finally get

$$2\pi J(k) = \frac{U}{J} \int_{-k_\mathrm{F}}^{k_\mathrm{F}} \frac{J(k') \cos k' \, \mathrm{d}k'}{\left(\frac{U}{2J}\right)^2 + \left[\sin k - \sin k'\right]^2} + \theta(\sin k - \sin k_\alpha^\star) - \theta(\sin k - \sin k_\alpha), \tag{3.108}$$

which can be written in dimensionless form by setting $\alpha = \frac{U}{2Jk_F}$ as

$$\begin{aligned}J(x) = &\frac{\alpha}{\pi} \int_{-1}^{1} \frac{\cos(k_\mathrm{F} y) J(y) \, \mathrm{d}y}{\alpha^2 + \frac{1}{k_\mathrm{F}^2} \left[\sin(k_\mathrm{F} x) - \sin(k_\mathrm{F} y)\right]^2} \\ &+ \frac{1}{\pi} \arctan\left[\frac{\sin(k_\mathrm{F} x_\alpha^\star) - \sin(k_\mathrm{F} x)}{\alpha k_\mathrm{F}}\right] - \frac{1}{\pi} \arctan\left[\frac{\sin(k_\mathrm{F} x_\alpha) - \sin(k_\mathrm{F} x)}{\alpha k_\mathrm{F}}\right].\end{aligned} \tag{3.109}$$

This is the backflow equation we were looking for. Note that, up to a global shift of $\pm\pi$ when one adds or remove a particle in quasimomentum space, the Lieb-like excitations can be described by setting either $x_\alpha = 1$ with $x_\alpha^\star \in]-\pi; -1[\cup]1; \pi[$ (type-I) or $x_\alpha^\star = 1$ and $-1 \leq x_\alpha < 1$ (type-II).

3.A.5.2 Expression of the momentum and energy of the excited state

The momentum and energy difference between the first excited state and the ground state can be written as functions of the backflow function. The momentum difference is

$$P := \sum_{j=1}^{N} k_j^\star = \sum_{j \neq \alpha} (k_j + \Delta k_j) + k_\alpha^\star \xrightarrow{\mathrm{TL}} k_\alpha^\star - k_\alpha + \int_{-k_\mathrm{F}}^{k_\mathrm{F}} J(k) \, \mathrm{d}k, \tag{3.110}$$

where we have used that $\sum_{j=1}^{N} k_j = 0$ in the ground state, and the energy difference is

$$\begin{aligned}\Delta E := &-2J \sum_{j=1}^{N} \cos k_j^\star + 2J \sum_{j=1}^{N} \cos k_j \simeq -2J(\cos k_\alpha^\star - \cos k_j) + 2J \sum_{j \neq \alpha} \Delta k_j \sin k_j \\ \xrightarrow{\mathrm{TL}} &-2J \left(\cos k_\alpha^\star - \cos k_\alpha\right) + 2J \int_{-k_\mathrm{F}}^{k_\mathrm{F}} J(k) \sin k \, \mathrm{d}k,\end{aligned} \tag{3.111}$$

where we neglected a second order term in the energy redistribution. In dimensionless form we finally have

$$\begin{aligned}P &= k_F \left[(x_\alpha^\star - x_\alpha) + \int_{-1}^{1} J(x) \, \mathrm{d}x\right], \\ \frac{\Delta E}{J} &= -2\left[\cos(k_\mathrm{F} x_\alpha^\star) - \cos(k_\mathrm{F} x_\alpha)\right] + 2k_\mathrm{F} \int_{-1}^{1} J(x) \sin(k_\mathrm{F} x) \, \mathrm{d}x.\end{aligned} \tag{3.112}$$

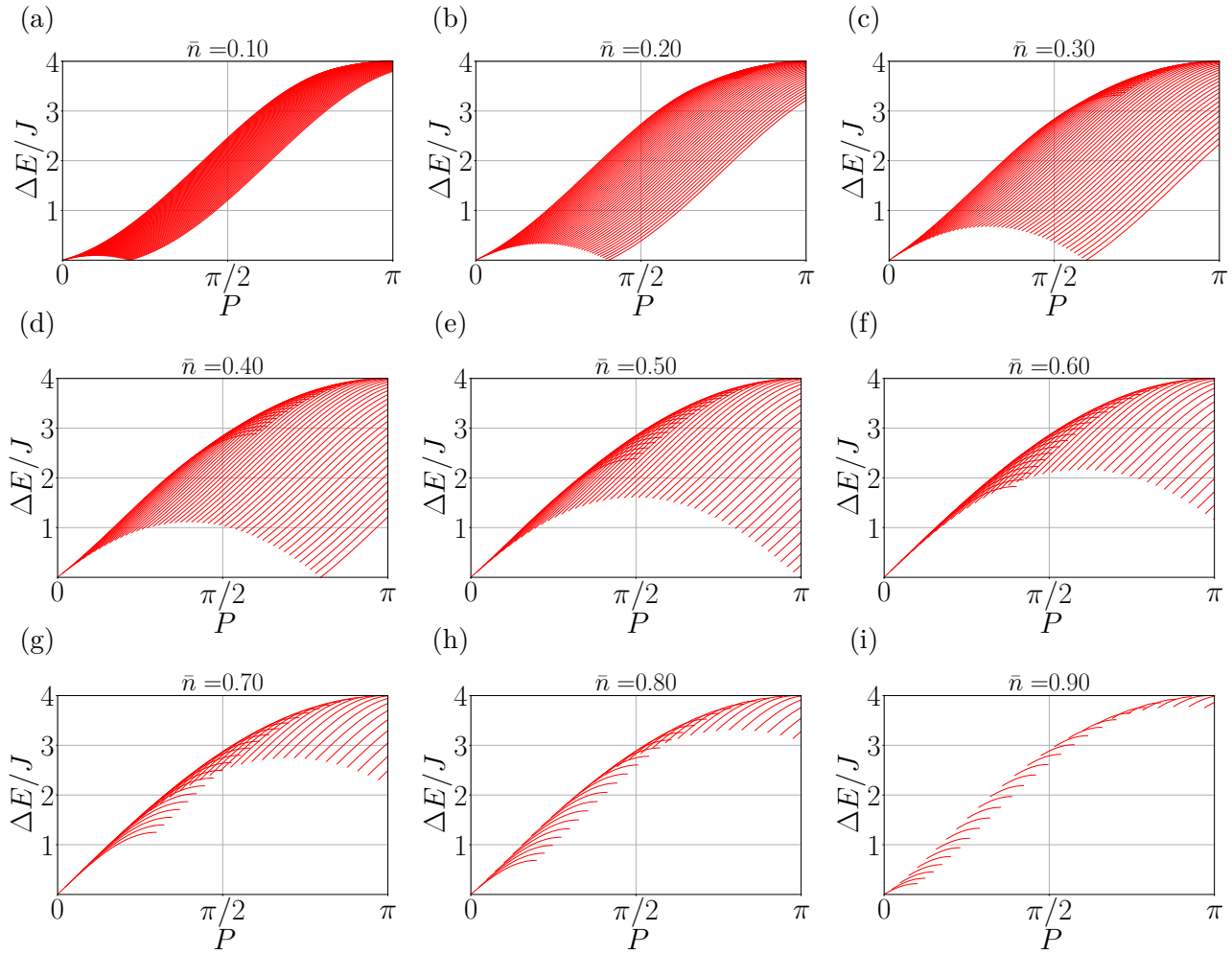

Fig. 3.27 Excitation spectrum continuum predicted by the approximate Bethe ansatz for the Bose-Hubbard chain, with $U/J = 10$ for different values of the filling $\bar{n}$.

We can numerically obtain the excitation spectrum $\Delta E = f(P)$ with $x_\alpha^\star \in]-\frac{\pi}{k_F}; -1[\cup]1; \frac{\pi}{k_F}[$ and $-1 < x_\alpha < 1$. We solve the backflow equation (3.109) for a given set $\{U/J; k_F\}$ and then reconstruct the full excitation continuum from Eq. (3.112). The result is shown in Fig. 3.27. As discussed in Sec. 3.2.2.2, the envelope of the obtained continuum is in excellent agreement at low filling with the spectral intensities observed in global quench spectroscopy (Fig. 3.3).

3.B Comparison between the dynamical structure factor and the QSF

The dynamical structure factor is defined for a finite temperature T (with $k_B = 1$) as

$$S(k,\omega) = 2\pi \sum_{n,m} \frac{e^{-E_n/T}}{Z} \left| \langle m| \hat{S}^z_k |n\rangle \right|^2 \delta(\omega - E_m + E_n), \tag{3.113}$$

with $Z = \sum_n e^{-E_n/T}$. At zero temperature it reduces to

$$S(k,\omega) = 2\pi \sum_{m} \left| \langle m| \hat{S}^z_k |0\rangle \right|^2 \delta(\omega - E_m), \tag{3.114}$$

where the ground state energy has been chosen such that $E_0 = 0$. Equivalently, for a spin model it represents the space-time Fourier transform of the non-equal time spin-spin correlator (here along z). To evaluate Eq. (3.113), we decompose the eigenstates of the system (Latin indices $\{|n\rangle\}$ on the basis where the spin value along z on each site is fixed as either $1/2$ or $-1/2$ (Greek indices $\{|\alpha\rangle\}$), such that $|n\rangle = \sum_\alpha \langle \alpha|n\rangle |\alpha\rangle := \sum_\alpha c_{\alpha,n} |\alpha\rangle$. Such basis is advantageous since

$$\langle \alpha| \hat{S}^z_R |\beta\rangle = \langle \left\{ S^z_1 \cdots S^z_{\dim(\mathcal{H})} \right\}_\alpha | \hat{S}^z_R | \left\{ S^z_1 \cdots S^z_{\dim(\mathcal{H})} \right\}_\beta \rangle = \delta_{\alpha,\beta} S^z_R(\alpha), \tag{3.115}$$

which is simply the expectation value of the spin along z on site R for the state α. Furthermore, by diagonalising the Hamiltonian numerically, we get all overlaps $c_{\alpha,n}$ exactly and we may evaluate the matrix elements of the observable as [Roth and Burnett, 2004]

$$\langle m| \hat{S}^z_k |n\rangle = \sum_{R=1}^{L} e^{-2i\pi kR/L} \sum_{\alpha}^{\dim(\mathcal{H})} c^\star_{\alpha,n} c_{\alpha,m} S^z_R(\alpha). \tag{3.116}$$

For a spin-1/2 chain, this overlap coefficient requires the evaluation of $L \times 2^L$ terms. In addition, we need to evaluate this overlap 2^L times at $T = 0$ and $2^L \times 2^L$ times at finite temperature to compute the dynamical structure factor. The brute-force computation is therefore numerically very costly and since we only aim at a qualitative comparison we shall restrict to small sizes where exact diagonalisation can be used. Numerically, we also replace the delta distribution by a smooth Gaussian function $\delta(x) \to \frac{1}{\sqrt{2\pi\sigma^2}} e^{-\frac{x^2}{2\sigma^2}}$ and we choose the variance σ such that the full width at half maximum (FWHM) $2\sqrt{2\ln(2)}\,\sigma$ coincides with the resolution of quench spectroscopy $2\pi/t_{\max}$. Combining all the steps above, we evaluate first Eq. (3.114) and display our results in Fig. 3.28 at zero temperature for $L = 8$.

Comparing with the result obtained in quench spectroscopy using the QSF (Fig. 3.19), we see that the dynamical structure factor also allows to reconstruct the 2-particle continuum (its boundaries are represented by the same dashed green lines). A striking difference however with the QSF is that the signal from the energy differences is not visible at all, despite the observable being the same. This is because at zero temperature, there is a single sum over the Hilbert space and only the transitions to the ground state are allowed, so the energy transitions between two excited levels $E_m - E_n$ are absent and we only have $E_m - E_0$. The fact that the dynamical structure factor is not sensitive to such transitions is due to its vanishing off-diagonal coherences, and thus the fact that such quantity is defined with respect to an equilibrium ensemble, in contrast to the QSF where the initial state is out of equilibrium in the eigenbasis that controls the dynamics. As we have discussed for quench spectroscopy, the observable $\hat{S}^z_k$ cannot couple to the first excited state manifold, so the spectrum is not observed and the signal we see here comes from the coupling between the second excited manifold with two quasiparticle excitations and the ground state.

We also compute the dynamical structure factor at finite temperatures from $T = 10^{-2}J$ to $10J$ with $L = 5$ using Eq. (3.113). We represent our results in Fig. 3.29.

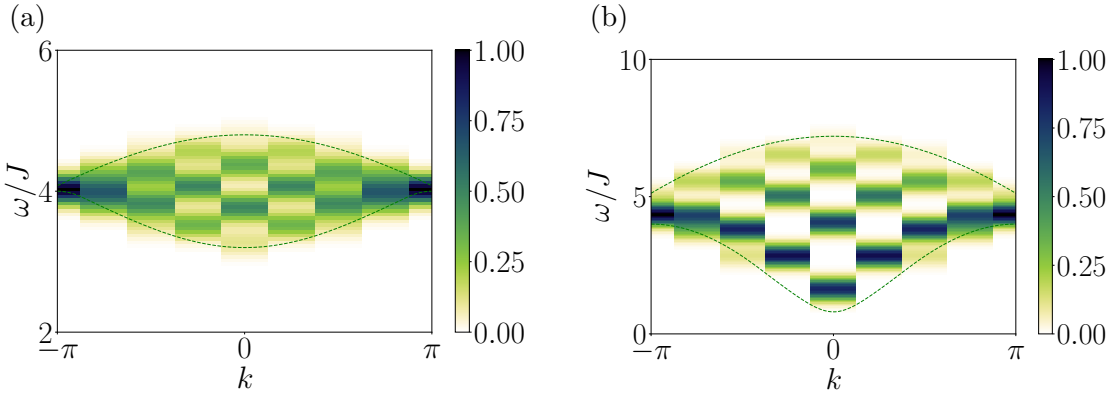

Fig. 3.28 Normalised dynamical structure factor at $T = 0$ computed using exact diagonalisation for the TFI model with periodic boundary conditions and $L = 8$ sites (a) $h/J = 0.2$ and (b) $h/J = 0.8$. The direct ground state transition has been forbidden numerically to enhance visibility. To facilitate comparison with quench spectroscopy, the frequency broadening of the delta function approximated by a Gaussian with variance σ is chosen such that its full width at half maximum (FWHM) equal to $2\sqrt{2\ln(2)}$ coincides with the resolution of quench spectroscopy $2\pi/t_{\max}$, with (a) $t_{\max} = 20J^{-1}$ and (b) $t_{\max} = 10J^{-1}$.

When the temperature increases, the transitions between two excited levels $E_m - E_n$ become possible, and just as for the QSF we observe a signal below the 2-excitation continuum coming from such energy transitions. The higher the temperature, the more transition lines are observed. This suggests that the role played by temperature in pump-probe spectroscopy is similar to the role played by the strongness of the quench in quench spectroscopy, stronger quenches exciting more and more energy levels and allowing additional transition lines to appear in the QSF.

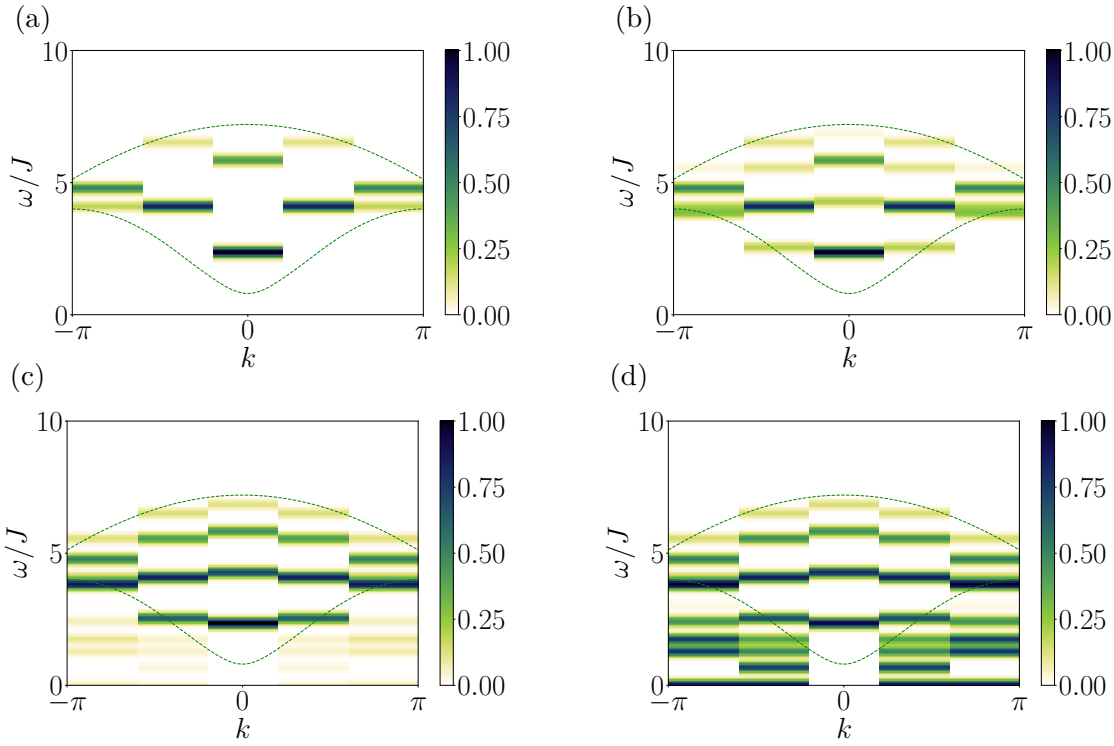

Fig. 3.29 Normalised dynamical structure factor at finite temperature T for $h/J = 0.8$ computed using exact diagonalisation for the TFI model with periodic boundary conditions and $L = 5$ sites. The temperatures are (a) $T = 0.01J$ (b) $T = 0.1J$ (c) $T = 1J$ and (d) $T = 10J$. The transitions between identical eigenstates (which contribute to the $\omega = 0$ signal) have been forbidden numerically to improve visibility.

4 Quench spectroscopy for disordered systems

In the previous chapters, we have only discussed translation invariant clean systems. On the one hand, they constitute an approximation to the physical reality – albeit a very good one in ultracold atoms where the system can be very well isolated from external perturbations and prepared so as to contain almost no defect. On the other hand, thanks to the degree of control ultracold systems offer, this platform can simulate solid state systems where disorder is almost impossible to avoid. Including disorder leads to the emergence of new physical effects, including for instance the existence of new phases of matter and a modification of the behaviour of the excitations which tend to localise in real-space. We introduce briefly the physics of disordered systems and its motivations in Sec. 4.1. We then specialise to a prime example of a disordered system, the Bose-Hubbard chain with on-site disorder. We detail the properties of the new phase of matter named the Bose glass which competes with the Mott insulator (Sec. 4.2). This phase has resisted unambiguous detection, in particular from the experimental point of view. We discuss the already obtained achievements and existing detection methods. Finally we investigate the generalisation of quench spectroscopy to disordered systems where translation invariance is broken (Sec. 4.3). We first expose the general strategy for a quench spectroscopy in the presence of disorder, and then we apply it to the disordered Bose-Hubbard chain. We will explain how the spectral properties are affected in comparison to the clean case discussed in the previous chapter. Using numerical simulations, we demonstrate that quench spectroscopy can be used in particular to unambiguously detect the Bose glass phase using a single probe. We show how to extract information about the underlying excitations of the system within each phase across various regimes, and eventually reconstruct the phase diagram of the model.

Throughout the following we focus on time-independent random potentials[1] affecting the system as a whole. This excludes the presence of controlled localised defects which can be understood as local quenches performed on clean systems (Sec. 3.3). While we focus on random disorder, we will also briefly mention quasi-random potentials due to their practical relevance, as they can be engineered using bichromatic optical lattices with incommensurate wavelengths.

4.1 Why are disordered systems interesting?

Many reviews exist on disordered systems, throughout the following I mainly used [Abanin et al., 2019; Alet and Laflorencie, 2018; Nandkishore and Huse, 2015; Sanchez-Palencia and Lewenstein, 2010]. In the following, we will call a system disordered if it can be described by a Hamiltonian model that has at least one parameter that is a time-independent random variable with a probability distribution. Arguably the key physical notion for disordered systems is localisation, which ambiguously refers to at least three distinct concepts. At low energy, in the absence of disorder but in the presence of interactions, particles on a lattice can localise to the minima of the potential created by the optical lattice. This Mott transition, as discussed in previous chapters, has nothing to do with disorder. Below, we discuss two other localisation concepts which only appear in the presence of disorder: Anderson localisation in non-interacting systems at low energies (Sec. 4.1.1) and many-body localisation in interacting systems at high energies (Sec. 4.1.2).

[1] Sometimes referred to as quenched (or frozen-in) random disorder. We will avoid this terminology to avoid confusion with the quantum quenches performed.

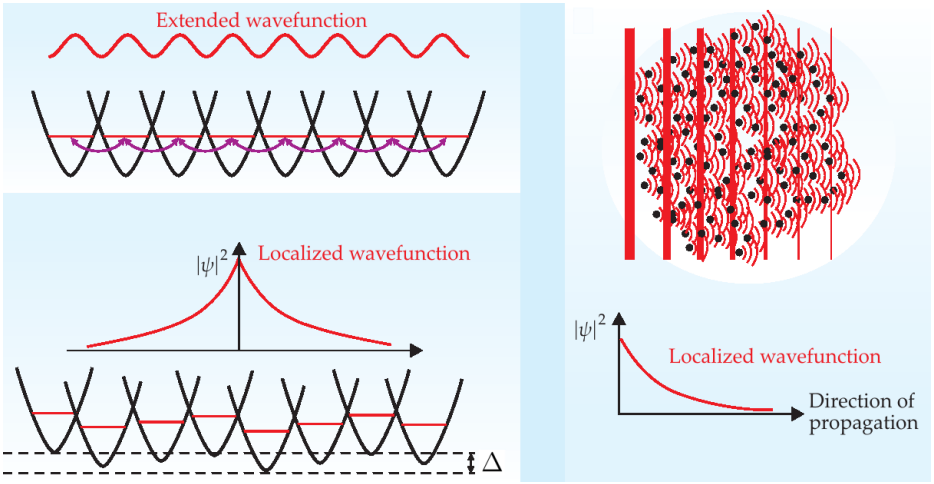

Fig. 4.1 In the sole presence of disorder (no interaction), the global wave function localises on a finite region in real space, and decays exponentially fast from the centre of such region (Anderson localisation). This phenomenon leads to the absence of diffusive transport on large distances, which can be interpreted from a semi-classical picture of random scatterers leading to a dephasing of the global wave function. From [Aspect and Inguscio, 2009].

4.1.1 Anderson localisation

Since the seminal work of [Anderson, 1958], disorder is known to be able to affect dramatically quantum systems. The phenomenon of Anderson localisation refers to the exponential decay of the single-particle wave function (non-interacting system) in the presence of a random potential such that $|\psi(\boldsymbol{r})|^2 \sim \exp(-r/l_{\mathrm{loc}})$ with $r = \|\boldsymbol{r}\|$. The disorder localises the single-particle wave function in real space on a finite region of typical linear size l_{loc} called the localisation length. Diffusive transport is suppressed for distances larger than the localisation length and the system becomes globally insulating. This phenomenon is not restricted to quantum physics and is ubiquitous in the physics of waves, and can be interpreted from a semi-classical picture where random scatterers prevent the propagation of the wave (function) [Fig. 4.1].

Localisation originates from constructive interferences at short distances and destructive ones at long distances. In a disordered medium, a wave gets scattered on the impurities. The rescattered wavelets lead to a constructive interference that increase the probability of return to the origin emission point, thus decreasing global transport. It can be demonstrated rigorously from renormalisation theory that the transport stops completely in one and two dimensions, and in three dimensions at sufficiently low energy. In one dimension, localisation surprisingly appears even for an infinitesimal amount of disorder[2]. Within ultracold atoms, a significant boost occurred after realising that Anderson localization can be directly observed and the localisation length measured in the expansion of a Bose-Einstein condensate, taking advantage of the bounded momentum distribution in the Thomas-Fermi regime [Lugan et al., 2009; Piraud et al., 2011; Sanchez-Palencia et al., 2007]. The Anderson localisation was thus unambiguously observed for the first time by [Billy et al., 2008; Roati et al., 2008] in 1D and by [Jendrzejewski et al., 2012; Semeghini et al., 2015] in 3D.

Reliable methods are therefore required to distinguish localised from delocalised states and characterise the properties of the underlying quantum phases. A particularly pressing question (especially in the presence of interactions, see below) concerns the characterisation of the localisation-delocalisation transition induced by the disorder. Are all the states from the energy spectrum localised or is there a finite energy threshold (called the mobility edge) which separates localised from delocalised states? If so, how does the mobility edge varies with the system

[2]For weak disorder, the localisation length l_{loc} is generally large and can be larger than the system size. The system then appears delocalised, and a larger system size is required to realise that it is not.

parameters, the type of disorder or the dimensionality? Such questions, stimulated by experiments [Lüschen et al., 2018; Sbroscia et al., 2020; Semeghini et al., 2015] regained theoretical interest recently in one [Li et al., 2017; H. Yao et al., 2019] and higher dimensions [Gautier et al., 2021; Szabó and Schneider, 2020].

4.1.2 Quantum glasses and many-body localisation

Do interactions always play with the disorder to reinforce localisation? As insulators are more the exception than the rule, we already expect that combining interactions with disorder will lead to non-trivial effects. The interplay between disorder and interactions is pivotal to understand transport properties in solid-state materials, where electrons interact via the Coulomb interaction (and with phonons at finite temperature). The study of this question led to the discovery of new phases of matter and physical effects which are still active fields of modern research.

First of all, given a certain disordered interacting many-body system, does it always have localised excited states? When they exist, such states are insulators at finite temperature and are said many-body localised (MBL). MBL phases are intriguing because they do not thermalise. This is reminiscent of integrable systems which escape thermalisation because their dynamics is constrained by an extensive set of quasi-local conserved quantities that prevent energy redistribution. Similarly, MBL phases exhibit a form of integrability, where conserved quantities emerge from localised operators (l-bits) and explain the breakdown of thermalisation [Nandkishore and Huse, 2015]. The statistical properties of integrable models at long times can be described by a generalised Gibbs ensemble, as we discussed in Appendix 1.B. [Inglis and Pollet, 2016] provided evidence for a similar phenomenon with MBL states, where the ensemble is built using local integrals of motion from the l-bits. However there are some differences between MBL states and the ones accessible to integrable systems. Integrable systems are fragile with respect to perturbations, and they eventually thermalise in the presence of a weak term that breaks integrability (such as a harmonic trap used to confine ultracold atoms). In contrast, MBL phases are robust phases of matter (at least when isolated from the environment and in low dimension). They retain memory of their initial state at long times and may be good candidates for quantum storage devices. Finally, the thermal-MBL transition is dynamical, meaning that dynamical probes are necessary to observe it. It cannot be described by equilibrium statistical mechanics and strongly differs from standard localisation transitions like the Mott transition.

A second active topic is the one of quantum glasses, which are emergent phases in the presence of disorder[3]. The adjective "glassy" was originally used to describe a non-equilibrium phase whose Helmholtz free energy potential landscape is very complicated and includes many local minima where the system remains trapped into and thus never thermalises. We will study a specific example in the following on the disordered Bose-Hubbard model called the Bose glass. Although glassy phases share some properties with MBL ones (breaking of thermalisation, slow dynamics), the important difference is that quantum glasses are low temperature phases, thus in particular zero temperature ones, and therefore are accessible to the ground state of the system. They do not possess any clear spatial order (exponential decay of correlation functions) and do not break any physical symmetry and thus prove challenging to detect unambiguously experimentally. Quantum glasses often possess intriguing properties, for instance by being simultaneously insulating and admitting gapless excitations. This is rather uncommon, because usually transport is ensured by the elementary excitations and if the latter can be created at arbitrarily low energies, the system is not expected to be insulating. The twist is that transport is suppressed globally, but not locally.

Glassy phases often exhibit rare spatial domains referred to as Griffiths regions. The probability of appearance of such regions decays exponentially with their size, and they are characterised by

[3]Disorder is a necessary condition, although it may not be sufficient (for instance in spin glasses, frustration is also known to play a role).

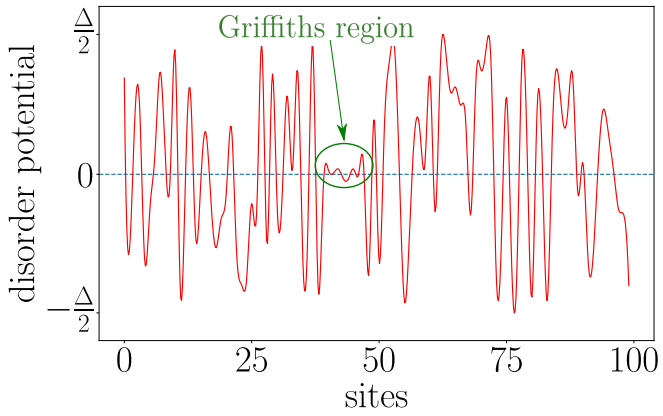

Fig. 4.2 For rare disorder realisations, Griffiths regions might occur. Here we considered random-box disorder (uniform probability distribution where $\Delta_j \in [-\frac{\Delta}{2}; \frac{\Delta}{2}]$). A weakly coupled region (compared to the typical average regions) can be observed towards the centre.

the fact that they strongly differ from the typical regions by being either more strongly coupled or more weakly coupled than them. An example of such rare region in a particular disorder realisation is illustrated in Fig. 4.2. These regions, first discovered on classical spin systems, lead to non-analytic behaviours in certain thermodynamic quantities (for instance the free energy) even *below* the critical point [Griffiths, 1969; McCoy, 1969]. Their occurrences are essentially equivalent to a strongly-coupled localised defect, which governs the relaxation time and thus controls the dynamics. Since some properties of disordered systems are dictated by very rare events, it becomes necessary to consider a large number of disorder realisations (samples) in order to capture the correct physics. Indeed, the behaviour of a single disorder realisation may differ from the typical behaviour of the system and therefore averaging over the disorder samples is necessary. Lastly, some systems are said self-averaging, which means that essentially considering a system of double linear size $2L$ is equivalent to considering two disorder realisations of a system of linear size L. This is formally the case if for a large number of disorder realisations N_s, the relative variance of the disorder average $\overline{X}$ of the quantity X goes to zero, *i.e.* $(\overline{X^2} - \overline{X}^2)/\overline{X}^2 \to 0$. This enables us to replace numerically the costly large system size limit with a large number of disorder samples for a smaller system. Such property is usually ensured far from critical points.

Last but not least, it has been suggested recently that the two topics of MBL and quantum glasses may be in fact intertwined: the glassy ground state and the excitations atop being adiabatically connected (when the temperature is increased) to the MBL of highly excited states [Abanin et al., 2019]. We certainly hope that the development of additional spectral techniques such as disordered quench spectroscopy can help to shed light on this question.

4.2 The disordered Bose-Hubbard model

We now focus on the disordered Bose-Hubbard model, especially in one dimension, and discuss the properties of the new quantum glassy phase that appears called the Bose glass.

4.2.1 The Bose glass

The disordered Bose-Hubbard model is a prototypical example of a disordered system. The most common type of disorder affects the on-site energy levels, such that the one dimensional Hamiltonian reads as

$$\hat{H} = \sum_j \left[-J\left(\hat{a}_j^\dagger \hat{a}_{j+1} + \text{h.c.}\right) + \frac{U}{2}\hat{n}_j\left(\hat{n}_j - 1\right) + V_j \hat{n}_j \right]. \tag{4.1}$$

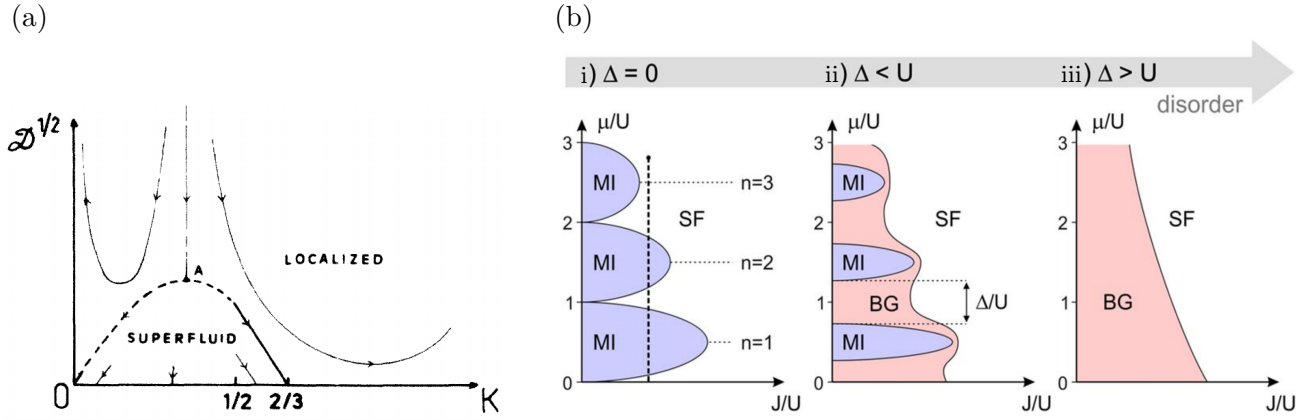

Fig. 4.3 (a) Renormalisation group flow in the presence of disorder on the bosonic chain, and the separatrix between the two localised phases and the delocalised superfluid. From [Giamarchi and Schulz, 1987]. (b) Sketch of the phase diagram in the grand canonical ensemble for increasing disorder strength Δ. Each frontier of the lobe shrinks as $\Delta/2U$, such that for $\Delta \geq U$ the Mott lobes disappear entirely. From [Fallani et al., 2007].

There exists two main types of disorder, corresponding to different choices for the distribution of variables V_j. Random box disorder corresponds to the choice $V_j = -\mu + \Delta_j$ in the grand-canonical ensemble (and simply Δ_j in the canonical one), where Δ_j is a random number on every site picked within the uniform distribution $\left[-\frac{\Delta}{2}; \frac{\Delta}{2}\right]$. The value Δ will be referred to as the disorder strength. This type of disorder can be approximated experimentally from light speckle patterns [Billy et al., 2008; Clément et al., 2005; Clément et al., 2006; Sanchez-Palencia and Lewenstein, 2010] or engineered exactly using a spatial light modulator [Choi et al., 2016]. Another common choice of disorder is the quasi-random disorder, generated from quasiperiodic potentials, for instance using two optical lattices with an incommensurate[4] wavevector ratio $r = k_1/k_2$. The disorder distribution is in this case symmetric and given by $V_j = (\Delta/2)\cos(2\pi r j + \phi)$, where ϕ is a random phase in $[-\pi; \pi[$.

[Giamarchi and Schulz, 1987] showed from a renormalisation group analysis of the bosonised chain that the presence of disorder implies the existence of two localised phases. The shape of the phase diagram from the flow equations of the renormalisation group picture is represented in Fig. 4.3(a), where K is the Luttinger parameter which controls the asymptotic power-law decay of the correlation functions (and is interaction dependent) and $\mathscr{D}$ is the disorder strength. The disorder is responsible for the appearance of a new localised phase called the "charge-density glass", which is a strongly disordered phase as the solutions of the renormalisation group equations flow towards infinite disorder. This phase was later named Bose glass (BG) and further investigated in the milestone paper by [Fisher et al., 1989]. They argued on general grounds that the BG always intervenes between the MI and the superfluid (SF) if the disorder is random and its associated probability distribution is bounded. A sketch of the phase diagram in the grand canonical ensemble where the number of particles is not fixed is represented in Fig. 4.3(b) for different increasing disorder values. The fact that a direct MI-SF transition is prevented for random bounded disorder distributions was later on formalised by [Pollet et al., 2009] and is now known as the "theorem of inclusions". The Griffiths regions mentioned previously prevent the direct SF-MI transition, as close to the critical region, arbitrarily large SF puddles appear in the system. An intuitive physical picture for the BG is the one of isolated SF puddles on top of a MI uniform background. In dimensions higher than one, the transition from the BG to either the SF or the MI is a percolation transition: SF puddles are starting to connect each other and when they do, long-range coherence is restored and the system becomes superfluid.

Similarly to a true superfluid, the BG possesses gapless excitations, a finite compressibility and

[4] Probably from aesthetic considerations, the irrational number r is often chosen in theoretical works as a precious mean $r(n) = (\sqrt{n^2+4} - n)/2$, with $n = 1$ the golden mean being the most common.

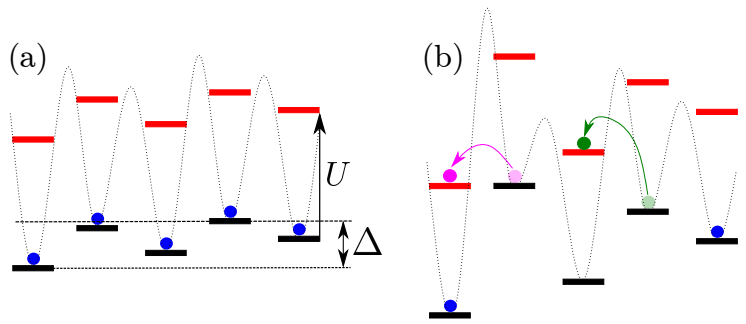

Fig. 4.4 Sketch in the atomic limit ($J = 0$) for (a) weak and (b) strong disorder. Each site is represented by a two-level system (black, red) separated by an energy U. (a) MI ground state at $\bar{n} = 1$ in the absence of weak disorder $\Delta < U$. The excitations are gapped and cost an energy $U - \Delta > 0$. (b) For stronger disorder $\Delta \geq U$ at $\bar{n} = 1$, gapless excitations start to appear for $U = \Delta$ (magenta) together with gapped ones still present (green). In this regime, the MI is always destroyed in favour of the BG. From [Villa et al., 2021a].

(very often) a finite but small condensate fraction. The existence of gapless excitations can be understood in the atomic limit from the following picture (Fig. 4.4). Start from the MI phase in the absence of disorder where all particles are localised and all sites are occupied by a single atom. Then increase the disorder: the on-site energies shift by $\Delta_j \in [-\frac{\Delta}{2}; \frac{\Delta}{2}]$, such that two arbitrary sites may have an energy mismatch within $[-\Delta; \Delta]$. When a boson is moved from the site with the highest on-site energy to the lowest one, such site becomes doubly occupied. If $\Delta = U$, the state considered initially and the one obtained with a double-occupancy have the same energy. Gapless excitations can be created, this localised state becomes a BG rather than staying a MI.

Similarly to a true MI, the BG is a localised phase, globally insulating. It also hosts gapped excitations, has a zero superfluid density and no long range order (its correlation function are decaying exponentially on a scale set by the correlation length). Thanks to its intriguing properties, summarised at zero temperature in Tab. 4.1, the BG can be distinguished from the SF and the MI. Note that a comparison between several probes is necessary to distinguish all three phases from thermodynamic quantities (the compressibility κ and the superfluid density ρ_s for instance are sufficient) . Nonetheless the corresponding phase diagram can be reconstructed, for instance from the measurement of standard probes such as the compressibility and the superfluid density, as we review below in Sec. 4.2.2.

	gapless excit.	κ	ρ_s	f_c	insulator
SF	✓	$O(1)$	$O(1)$	$O(1)$	✗
BG	✓	0^+	0	0^+	✓
MI	✗	0	0	0	✓

Tab. 4.1 Properties of the different phases in the disordered Bose-Hubbard model. The (reduced) compressibility $\kappa = \partial n/\partial\mu$ can be measured using quantum gas microscopes or via trap squeezing [Roscilde, 2009]. Time-of-flight absorption imaging is used to measure the condensate fraction f_c. The interference pattern of Bragg peaks reveals the quasi long-range order in the SF in one dimension $\langle\hat{\Psi}^\dagger(x)\hat{\Psi}(0)\rangle \sim |x|^{-1/2K}$ (in contrast to $\langle\hat{\Psi}^\dagger(x)\hat{\Psi}(0)\rangle \sim \mathrm{e}^{-|x|/\xi}$ in the MI), from which the superfluid density ρ_s can be extracted using $(\pi/K)^2 = m/(\rho_s\kappa)$. The BG is gapless but globally insulating: the excitations occur only locally and stay localised.

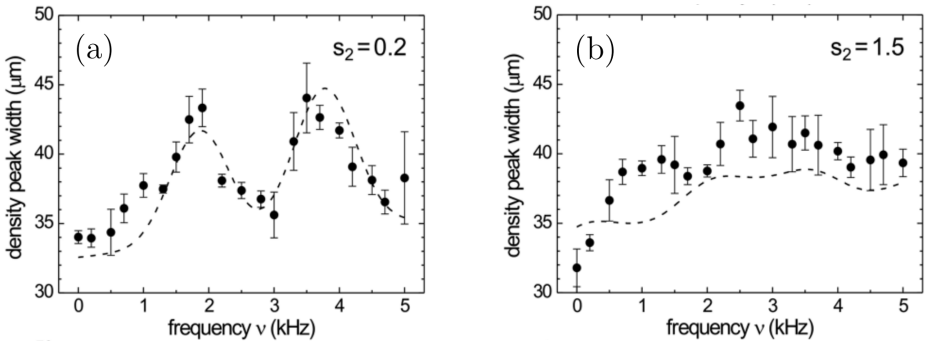

Fig. 4.5 (a) Excitation spectrum at $k = 0$ for a small disorder strength (equivalent to $\Delta/U = 0.14$) corresponding to the MI. The peak centred around $U/h \simeq 1.9\,\mathrm{kHz}$ corresponds to the frequency of the lattice modulation ν. A second peak at twice this frequency is also present. (b) Same for a larger disorder strength ($\Delta/U \simeq 1$), the excitation spectrum flattens which suggests the formation of a BG. The chemical potential is in both cases $\mu/U = 2.8$, such that domains with up to 3 atoms per sites are possible. The trapping frequency along the tubes is $\nu_x = 75\,\mathrm{Hz}$ such that $J/U \simeq 0.04$ (strongly interacting regime). The dashed line is a model predicting the inhomogeneous broadening of the MI resonances due to the disorder distribution. Adapted from [Fallani et al., 2007].

4.2.2 Detecting the Bose glass and probing the phase diagram

Before discussing the method we propose, we briefly review the existing literature. For convenience, we begin with experimental works before discussing theoretical ones.

Experimental signatures of the BG. [Fallani et al., 2007; Guarrera et al., 2007] experimentally investigated the Bose-Hubbard chain with quasi-random disorder by making use of a bichromatic lattice. The authors measured the excitation spectrum at zero momentum using lattice modulation spectroscopy[5]. The phase coherence properties were characterised from the interference pattern observed after the time-of-flight. Starting from the MI phase and increasing the disorder, the state reached possesses both vanishing long-range coherence and a flat density of excitations, which suggests the formation of a BG (Fig. 4.5).

[Meldgin et al., 2016] followed another route to detect the BG using quantum quenches of speckle disorder from an initial disorder strength Δ *slowly* ramped down to zero, at fixed U/J. This experiment investigates the SF-BG transition from the dynamical behaviour induced by the excitations. The authors investigated the 3D Bose-Hubbard model, at small interaction strength where the MI phase is not present. Because of the trap, the density varies throughout the system and the BG phase is expected to appear at the edges of the system for sufficiently high disorder. By quenching slowly across the BG-SF phase transition, both phases can be distinguished from the amount of vortex-type excitations created (none in the SF, rare ones in the BG). Such vortices modulate the optical density measured by a time-of-flight. A few points from the phase diagram have been reconstructed from this method, and qualitatively agree with QMC calculations. This method distinguishes the SF from the BG essentially from the long-range coherence properties, but remains to be adapted to also tell apart the BG from the MI.

Determination of the phase diagram. We now discuss theoretical approaches used to obtain the phase diagram of the disordered Bose-Hubbard chain. We discuss both random box disorder and quasi-random disorder, since the two phase diagrams are qualitatively different. Generally,

[5] We discussed it in Sec. 1.3.2.3 as it was used by [Stöferle et al., 2004] to investigate the excitation spectrum of the clean system. The amplitude modulation of the lattice was rather strong (30%), and t-DMRG simulations beyond the linear regime [Kollath et al., 2006] are necessary to quantitatively explain the experimental results.

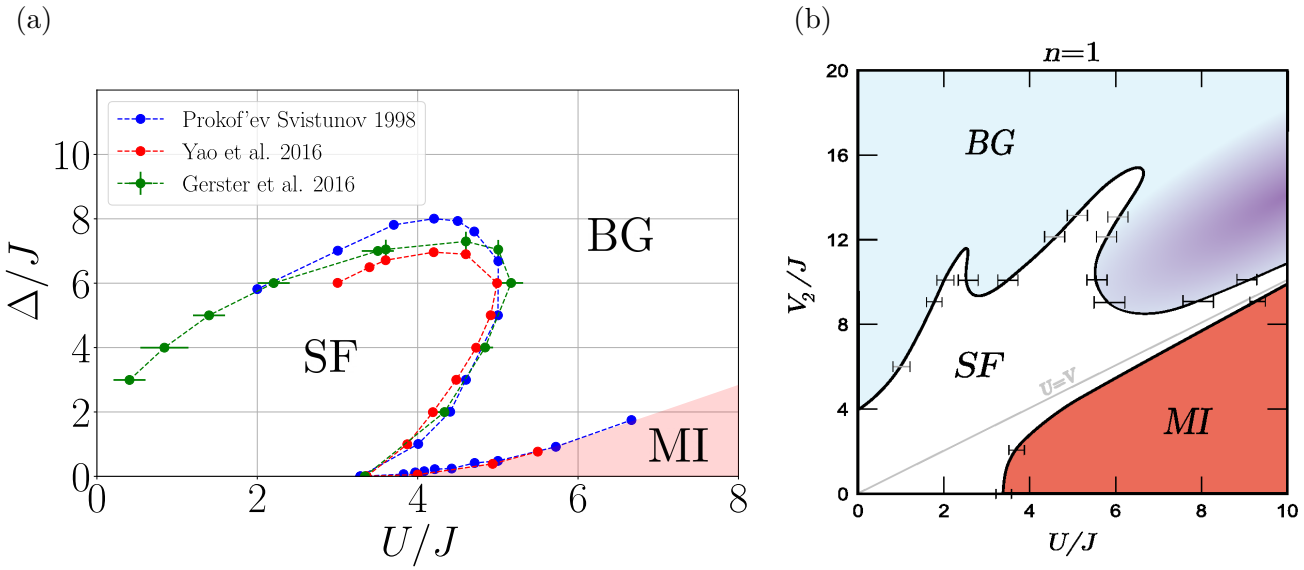

Fig. 4.6 (a) Phase diagram at $\bar{n} = 1$ for the disordered Bose-Hubbard chain with random box disorder drawn from $[-\Delta/2; \Delta/2]$ with the notations of Eq. (4.1). The BG-SF transition is identified from the points at which the Luttinger parameter is equal to its critical value $K_c = 3/2$ and the BG-MI transition is identified from $E_{gap} = \Delta$, where E_{gap} is obtained from the clean system. (b) Same with quasi-random disorder, from DMRG results ($L = 35$) from [Roux et al., 2008]. The purple area represents a localised region appearing as gapped, with a gap value below numerical resolution (finite size effects).

determining the full phase diagram is very costly numerically because it requires disorder averaging over a reasonable number of samples. To reduce the numerical cost by reducing the size of the Hilbert space, it is common to work in the canonical ensemble where the number of particles is fixed. We will focus on $\bar{n} = 1$ where three phases coexist: SF, BG and MI.

In the presence of random disorder, a piece of the phase diagram for $\bar{n} = 1$ was first[6] captured using quantum Monte-Carlo (QMC) simulations by [Prokof'ev and Svistunov, 1998] on a $L = 100$ sites system [Fig. 4.6(a), blue points]. Recent results from [Gerster et al., 2016] using tensor networks methods (green points, up to $L = 128$) and [Z. Yao et al., 2016] using a combination of QMC and the Giamarchi-Schulz renormalisation group flow equations (red points, up to $L = 192$) confirmed the obtained shape. The region for $U/J < 2$ is very costly numerically, since it requires to allow for a large maximal number of bosons per site, and therefore a large Hilbert space. A small discrepancy is visible around the tip of the SF lobe where the disorder is strongest. This is probably a finite size effect, since we expect the SF lobe to shrink for larger systems, as observed in Fig. 4.6(a).

Quasi-random disorder, which can be engineered experimentally using bichromatic lattices also allows for a BG phase. Reconstruction of the full phase diagram has been performed by [Roux et al., 2008] using DMRG simulations on a $L = 35$ sites chain, by comparing five different probes (Luttinger parameter, superfluid density, condensate fraction, correlation length, one-particle energy gap). The obtained phase diagram is represented in Fig. 4.6(b). Some differences with the random case are striking. First, the presence of quasi-random disorder (for which the theorem of inclusions is no longer valid) authorises a direct SF-MI transition. Second, at arbitrarily low interactions, there exists a disorder threshold $\Delta/J = 4$ that has to be overcome to destabilise the delocalised phase and induce localisation. Third, for fixed interactions around $U/J = 6$, increasing the disorder leads to consecutively MI-SF-BG-SF-BG phases, so there exists a rather unexpected

[6] A previous attempt was made using DMRG by [Pai et al., 1996], but the proposed phase diagram was not consistent with the theorem of inclusions and exact renormalisation group results from [Giamarchi and Schulz, 1987] by showing a direct SF-MI transition. A second attempt was made by [Rapsch et al., 1999] using DMRG ($L = 50$), but the predicted diagram significantly differs from the shape nowadays admitted [Fig. 4.6(a)].

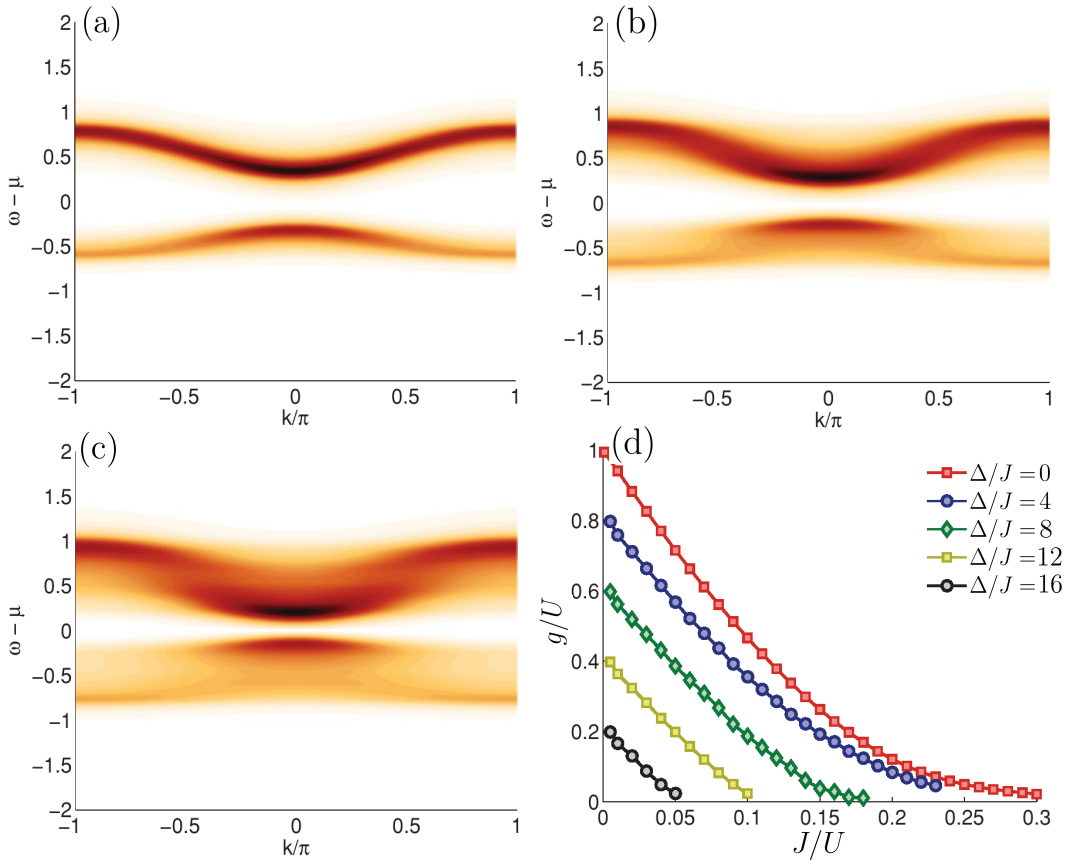

Fig. 4.7 Fourier transform of the single-particle Green's function in the strongly interacting regime $J/U = 0.05$ with $\mu/U = 0.45$ (inside the first Mott lobe, at $\bar{n} = 1$) in the presence of quasi-random disorder for different disorder strengths (a) $\Delta/J = 4$, (b) $\Delta/J = 8$, (c) $\Delta/J = 12$. The artificial broadening parameter was set to J. (d) Evolution of the gap g (lowest energy value of the spectral function) in units of U as a function of the interaction for different disorder strengths. A vanishing gap signals the BG. Adapted from [Knap et al., 2010].

"re-entrant" SF. To distinguish the SF from the BG or the MI, the authors propose to study the momentum distribution $n(k)$, easily obtained by a time-of-flight measurement. This probe was further investigated by [Roscilde, 2008] in trapped systems, who showed that to distinguish the BG from the SF, in addition to the momentum distribution, the noise correlations (Fourier transform of the density-density correlation function) could also be used in time-of-flight experiments. However such global probes cannot reveal the local structure of the BG phase and its superfluid puddles.

Excitations and localisation properties. We now briefly comment two early publications that analysed the BG from the point of view of the elementary excitations in quasimomentum space rather than from global thermodynamic properties.

[Knap et al., 2010] studied the behaviour of the single-particle spectral function, which is the Fourier transform of the single-particle Green's function (commonly abbreviated "spectral function") using a numerical variational cluster approach. The authors observed that increasing the disorder leads to a broadening of the spectral function, as shown in Fig. 4.7. The spectral function is sensitive to both types of excitations in the MI phase (approximately pure doublons and pure holons in the strongly interacting regime explored in the publication). When the disorder is increased, the value of the gap shrinks to zero, and most of the spectral weight accumulates towards $k = 0$, suggesting the progressive formation of a quasicondensate. By assessing the point at which gapless excitations occur, the value of the MI-SF transition can be estimated.

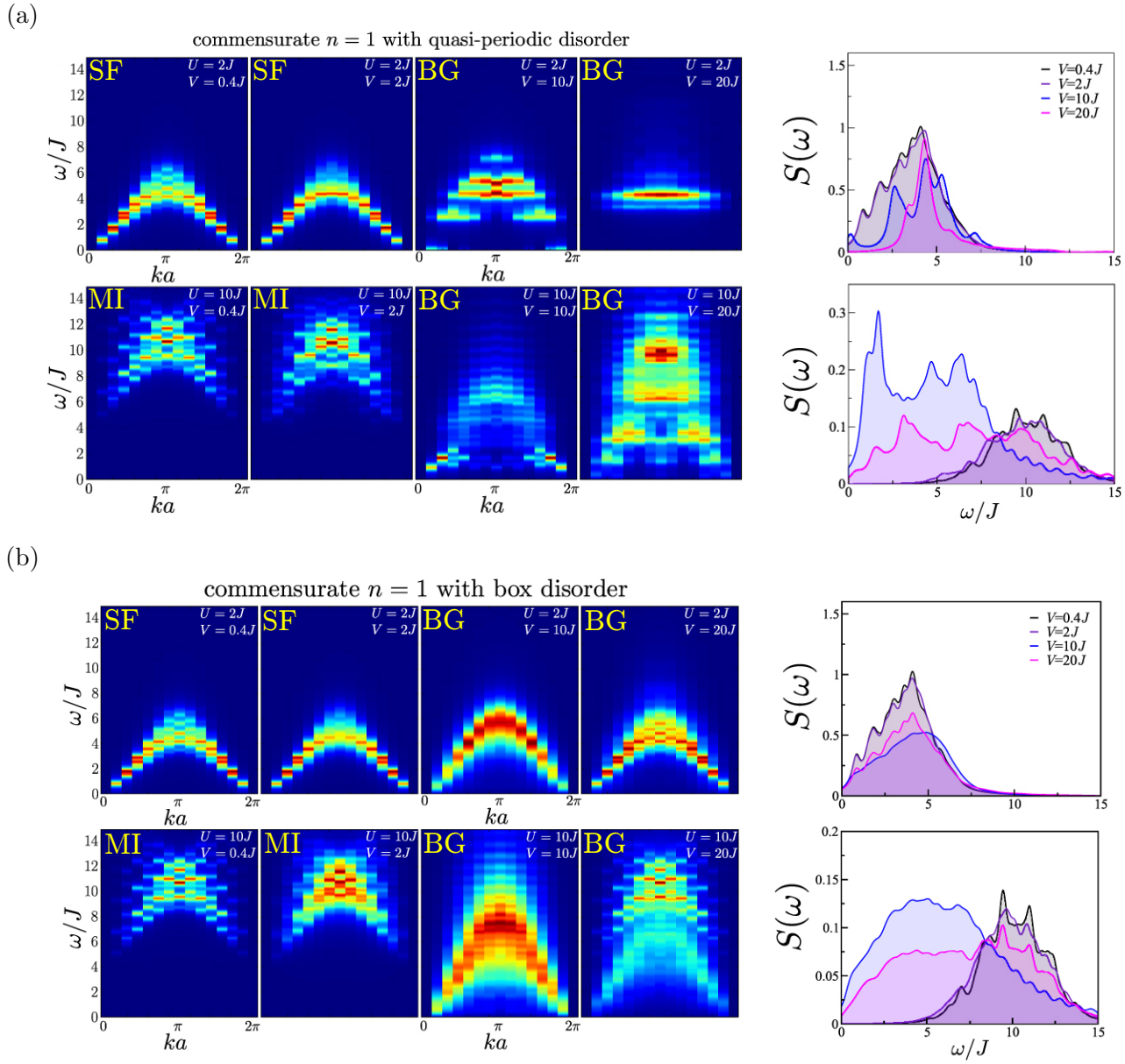

Fig. 4.8 Dynamical structure factor of the disordered Bose-Hubbard chain computed using exact diagonalisation on a $L = 14$ sites chain for unit filling at (a) quasi-random disorder and (b) random-box disorder. The expected phases from the phase diagrams in Fig. 4.6 have been added in the top-left corners (for the quasiperiodic potential at $V/J = 10$, the phase is expected to be BG but is very close to the SF boundary). Adapted from [Roux et al., 2013].

Another type of spectral function commonly used in pump-probe spectroscopies is the dynamical structure factor. As a momentum-resolved probe, it can reveal the presence of gapless excitations and their localisation properties inside the BG phase. [Roux et al., 2013] investigated such probe in both quasiperiodic potentials and random box disorder, commensurate and incommensurate fillings and various regimes of interaction and disorder. The authors showed that the dynamical structure factor reveals the localisation properties of the excitations, by leading to a broadening of spectral features in quasimomentum at large disorder strength and high energies. The situation at unit filling is represented in Fig. 4.8 for two interaction values ($U/J = 2$ and $U/J = 10$) and increasing disorder strengths ($V = \Delta$ with our notations). For a quasiperiodic potential, the main effect of localisation is to induce the formation of mini-gaps in the spectral features, while in the random disordered case it induces a broadening leading to blurred spectral features. This confirms that different localisation mechanisms are at play between random and quasi-random disorder [Roux et al., 2008]. For high disorder, the BG phase is entered. It possesses

a finite excitation weight at zero momentum (for $U/J = 2$ and $\Delta/J = 20$ in the quasi-disordered case, the gapless excitations have very little spectral weight but are nonetheless present [Roux et al., 2013]). The plot at $U/J = 10$ and $\Delta/J = 20$ shows the coexistence of SF-like features and MI-like features, in agreement with the intuitive picture of the BG phase being constituted of SF puddles on top of a MI background.

4.3 Disordered quench spectroscopy of the Bose-Hubbard chain

In this section, adapted from our recently submitted results [Villa et al., 2021a, 2021b], we extend quench spectroscopy to disordered systems. As an illustrative well-known example, we focus on the disordered Bose-Hubbard chain. This project is the result of a collaboration, and a special acknowledgment is due to S.J. Thomson who performed the DMRG and TDVP simulations presented below.

Two striking differences appear compared to the clean case, both related to the fact that the disorder is breaking translation invariance of the system. First, disordered systems are more involved numerically. Computing physical properties requires disorder averaging over $N_s \gg 1$ samples to obtain representative results of the disorder distribution including rare occurrences. Typically we take between 10 to 25 disorder samples. In the following, we simulate chains with $L = 47$ sites. Second, since translation invariance of the system is broken, we revise the quench protocol and the definition of the QSF in Sec. 4.3.1. In Sec. 4.3.2, we evaluate the phase diagram in the grand-canonical ensemble from standard probes, which will be useful in the following to independently verify our results obtained from quench spectroscopy. We show in Sec. 4.3.3 our numerical simulations and explain how quench spectroscopy can distinguish the three phases SF-BG-MI of the disordered Bose-Hubbard chain using a *single* probe, and discuss the behaviour of the excitations within each phase. Finally, we reconstruct the full phase diagram of the model using quench spectroscopy in Sec. 4.3.4.

4.3.1 Quench protocol and QSF for disordered systems

How can we adapt the quench protocol to disordered systems, *i.e.* what should we choose for the observable and for the type of quench? We still want to focus on the out-of-equilibrium dynamics of equal-time observables following a quench. If we are to investigate the excitations from their spectral properties, we already know that the BG is a Griffiths phase, constituted of local regions that can be either SF-like or MI-like. Performing global quenches is more intuitive as the system generates its own excitations, in contrast to local quenches where the excitations are targeted individually and the quench protocol for the initial state is more demanding. In clean systems, local quenches had the advantage of being able to probe spectral properties from one-point functions while global quenches required two-point correlators. The difference between the two was the breaking of translational invariance of the initial state (Sec. 3.3.1). In the presence of disorder, translation invariance of the system is broken, and we have to generalise the definition of the QSF. We show below that in the presence of disorder one gets the best of both worlds, allowing to use global quenches and any observable (one-point functions or two-point correlators) to probe spectral properties.

To gain insight on how the QSF definition should be extended, we again begin by emphasising the role played by translation invariance. For convenience, we denote by $\{|\nu\rangle\}$ (Greek indices) the disorder dependent eigenstates of the post-quench Hamiltonian and $\{|n\rangle\}$ (Latin indices) the corresponding eigenstates of the clean system ($\Delta = 0$). Let us consider that our observable is a one-point function $\hat{O}(\boldsymbol{x}, t)$. Translation invariance is broken by the disorder, such that $\left[\hat{H}, \hat{P}\right] \neq 0$, namely the energy eigenstates are no longer momentum eigenstates. For a single disorder

realisation, the dynamics are given by

$$\begin{aligned} G(\boldsymbol{x};t) &= \mathrm{Tr}\Big[\hat{\rho}_{\mathrm{i}}\,\hat{O}(\boldsymbol{x},t)\Big] = \mathrm{Tr}\Big[\hat{\rho}_{\mathrm{i}}\,\mathrm{e}^{i\hat{H}t}\mathrm{e}^{-i\hat{\boldsymbol{P}}\boldsymbol{x}}\,\hat{O}\,\mathrm{e}^{i\hat{\boldsymbol{P}}\boldsymbol{x}}\mathrm{e}^{-i\hat{H}t}\Big] \\ &= \mathrm{Tr}\Big[\mathrm{e}^{-i\hat{H}t}\hat{\rho}_{\mathrm{i}}\,\mathrm{e}^{i\hat{H}t}\mathrm{e}^{-i\hat{\boldsymbol{P}}\boldsymbol{x}}\,\hat{O}\,\mathrm{e}^{i\hat{\boldsymbol{P}}\boldsymbol{x}}\Big], \end{aligned} \tag{4.2}$$

where $\hat{O}$ is short for $\hat{O}(0,0)$ and we used the cyclicity of the trace in the last line. By decomposing on the energy eigenbasis and inserting a completeness relation we obtain without any approximation

$$G(\boldsymbol{x};t) = \sum_{\nu',\nu} \rho_{\mathrm{i}}^{\nu'\nu}\mathrm{e}^{i(E_\nu - E_{\nu'})t}\,\langle\nu|\,\mathrm{e}^{-i\hat{\boldsymbol{P}}\boldsymbol{x}}\,\hat{O}\,\mathrm{e}^{i\hat{\boldsymbol{P}}\boldsymbol{x}}\,|\nu'\rangle\,. \tag{4.3}$$

Importantly, while for a clean system we had that the energy eigenstates were also momentum eigenstates, and therefore

$$\langle n|\,\mathrm{e}^{i\hat{\boldsymbol{P}}\boldsymbol{x}}\,\hat{O}\,\mathrm{e}^{i\hat{\boldsymbol{P}}\boldsymbol{x}}\,|n'\rangle = \mathrm{e}^{i(\boldsymbol{P}_{n'}-\boldsymbol{P}_n)\boldsymbol{x}}. \tag{4.4}$$

Additionally, if the initial state is also translation invariant (as for a global quench), $G(\boldsymbol{x};t) = G(t)$ no longer depends on $\boldsymbol{x}$ and one-point functions cannot probe momentum-resolved properties for $\boldsymbol{k} \neq 0$ as discussed in Sec. 3.3.1. In the disordered case however, the equivalent of Eq. (4.4) does not hold, namely we do not obtain $\mathrm{e}^{i(\boldsymbol{P}_{\nu'}-\boldsymbol{P}_\nu)\boldsymbol{x}}\,\langle\nu|\,\hat{O}\,|\nu'\rangle$ because the energy eigenstates are no longer momentum eigenstates. Consequently, we no longer obtain the selection rule in momentum that associated the frequency resonances to the momentum ones and yielded the sharp spectral lines in the clean system. In the presence of disorder, the QSF can be defined for a one-point observable as

$$G(\boldsymbol{k};\omega) = 2\pi\sum_{\nu,\nu'}\rho_{\mathrm{i}}^{\nu'\nu}\,\delta(E_{\nu'}-E_\nu-\omega)\int \mathrm{d}\boldsymbol{x}\,\mathrm{e}^{-i\boldsymbol{k}\boldsymbol{x}}\,\langle\nu|\,\mathrm{e}^{-i\hat{\boldsymbol{P}}\boldsymbol{x}}\,\hat{O}\,\mathrm{e}^{i\hat{\boldsymbol{P}}\boldsymbol{x}}\,|\nu'\rangle\,, \tag{4.5}$$

where implicitly the eigenstates and the initial density matrix depend on the specific disorder realisation.

To gain further insight on the role played by the disorder, in the following we restrict to first order in perturbation theory assuming weak disorder ($\Delta \ll U$), such that the disorder dependent eigenstates and energies are related to their clean counterpart by

$$\begin{aligned} &|\nu\rangle = |n\rangle + \sum_{m\neq n}\mathcal{D}^\star_{nm}\,|m\rangle \qquad \text{with} \qquad \mathcal{D}_{nm} := \frac{\langle n|\,\hat{H}_{\mathrm{pert}}\,|m\rangle}{E_n - E_m} = -\mathcal{D}^\star_{mn}, \\ &E_\nu = E_n + \mathcal{D}_n \qquad \text{with} \qquad \mathcal{D}_n = \langle n|\,\hat{H}_{\mathrm{pert}}\,|n\rangle\,. \end{aligned} \tag{4.6}$$

Importantly, the clean eigenstates are translational invariant. We also assume that the initial density matrix can be decomposed as $\hat{\rho}_{\mathrm{i}} = \hat{\rho}_{\mathrm{i},(0)} + \delta\hat{\rho}_{\mathrm{i}}$ where $\hat{\rho}_{\mathrm{i},(0)}$ refers to the clean system. Making use of Eq. (4.6) and using that the *clean* energy eigenstates are also eigenstates of the momentum operator, the QSF (4.5) becomes

$$\begin{aligned} G(\boldsymbol{k};\omega) \simeq (2\pi)^{D+1}&\sum_{n',n}\delta\left(E_{n'}-E_n-\omega+\mathcal{D}_{n'}-\mathcal{D}_n\right) \\ &\times\Bigg[\delta(\boldsymbol{P}_{n'}-\boldsymbol{P}_n-\boldsymbol{k})\,\langle n|\,\hat{O}\,|n'\rangle\left(\delta\rho_{\mathrm{i}}^{n'n}+\sum_{m\neq n'}\rho_{\mathrm{i},(0)}^{mn}\mathcal{D}_{n'm}+\sum_{m\neq n}\rho_{\mathrm{i},(0)}^{n'm}\mathcal{D}^\star_{nm}\right) \\ &+\rho_{\mathrm{i},(0)}^{n'n}\left(\sum_{m\neq n'}\delta(\boldsymbol{P}_m-\boldsymbol{P}_n-\boldsymbol{k})\,\langle n|\,\hat{O}\,|m\rangle\,\mathcal{D}^\star_{n'm}+\sum_{m\neq n}\delta(\boldsymbol{P}_{n'}-\boldsymbol{P}_m-\boldsymbol{k})\,\langle m|\,\hat{O}\,|n'\rangle\,\mathcal{D}_{mn}\right)\Bigg]. \end{aligned} \tag{4.7}$$

For clarity, we regrouped on the second line the terms where the initial density matrix coherences are of first order in the disorder perturbation and in the last line the terms where the expectation value of the observable over the eigenstates is of first order. Note that Eq. (4.7) shows that a non-zero QSF may be obtained using one-point functions. This is because the addition of disorder, which breaks translation invariance of the initial state and of the system, prevents the momentum selection rules $\delta(\boldsymbol{P}_{n'} - \boldsymbol{P}_n - \boldsymbol{k})\,\delta(\boldsymbol{P}_{n'} - \boldsymbol{P}_n)$ as highlighted above. This is also the reason why the zeroth order term (disorder independent) vanishes and thus is not present in Eq. (4.7). The final step is to disorder average this result over several disorder samples. This last step cannot be derived analytically in full generality here, but we shall describe the qualitative features of the obtained QSF starting from the result obtained above for a single disorder realisation.

First, the resonances in energy are shifted compared to the clean system due to the additional terms $\mathcal{D}_{n'} - \mathcal{D}_n$ inside the energy selection rule. For a single disorder realisation, this results in a modification of the effective energy gap, visible in the numerical results. After disorder averaging, this results in a frequency broadening of the transitions. Second, the disorder dresses the initial density matrix coefficients for a single disorder realisation such that the intensity of each branch is randomly weighted. Indeed the momentum selection rule in the second line of Eq. (4.7) are not modified at first order in perturbation theory with respect to the clean system, but their prefactor is explicitly disorder dependent. After disorder averaging over a reasonable number of samples, we recover smooth spectral features (Fig. 4.11). Third and most importantly, the disorder broadens the spectral features in momentum space by modifying the momentum selection rule [last line in Eq. (4.7)]. Such terms depend on an intermediate state $|m\rangle$ whose momentum $\boldsymbol{P}_m$ is not specified. However, it should be noted that $\mathcal{D}_{nm}$ diverges as $(E_n - E_m)^{-1}$ so we generally expect to find the sharper features for $|m\rangle$ close in energy to $|n\rangle$ or $|n'\rangle$ for each term respectively. Making this argument more quantitative goes beyond the perturbative calculation presented here. Nonetheless, this simple calculation captures the essential features (shift of the effective energy gap, random weight of the spectral features for a single disorder realisation, broadening in momentum space) that will be observed in our numerical results.

What about two-point correlators? Choosing different types of observables is relevant since they lead to the observation of different spectral properties. Thus, let us briefly discuss equal-time two-point correlators which for a single disorder realisation may be cast in the form

$$\begin{aligned} G(\boldsymbol{x},\boldsymbol{y};t) &:= \mathrm{Tr}\big[\hat{\rho}_\mathrm{i}\,\hat{O}_1(\boldsymbol{x},t)\hat{O}_2(\boldsymbol{y},t)\big] \\ &= \sum_{\nu,\nu',\mu} \rho_\mathrm{i}^{\nu'\nu}\,\mathrm{e}^{i(E_\nu - E_{\nu'})t}\,\langle\nu|\,\mathrm{e}^{-i\hat{\boldsymbol{P}}\boldsymbol{x}}\,\hat{O}_1\,\mathrm{e}^{i\hat{\boldsymbol{P}}(\boldsymbol{x}-\boldsymbol{y})}\,|\mu\rangle\,\langle\mu|\,\hat{O}_2\,\mathrm{e}^{i\hat{\boldsymbol{P}}\boldsymbol{y}}\,|\nu'\rangle\,. \end{aligned} \tag{4.8}$$

Moving to the relative variables $\boldsymbol{x} = \boldsymbol{r} + \frac{\boldsymbol{R}}{2}$, $\boldsymbol{y} = \boldsymbol{r} - \frac{\boldsymbol{R}}{2}$ and taking the space-time Fourier transform we obtain the QSF as

$$\begin{aligned} G(\boldsymbol{k},\boldsymbol{k'};\omega) = 2\pi \sum_{\nu,\nu',\mu} \rho_\mathrm{i}^{\nu'\nu}\,\delta(E_{\nu'} - E_\nu - \omega) \\ \times \int \mathrm{d}\boldsymbol{R}\,\mathrm{e}^{-i\boldsymbol{k}\boldsymbol{R}} \int \mathrm{d}\boldsymbol{r}\,\mathrm{e}^{-i\boldsymbol{k'}\boldsymbol{r}}\,\langle\nu|\,\mathrm{e}^{-i\hat{\boldsymbol{P}}(\boldsymbol{r}+\frac{\boldsymbol{R}}{2})}\,\hat{O}_1\,\mathrm{e}^{i\hat{\boldsymbol{P}}\boldsymbol{R}}\,|\mu\rangle\,\langle\mu|\,\hat{O}_2\,\mathrm{e}^{i\hat{\boldsymbol{P}}(\boldsymbol{r}-\frac{\boldsymbol{R}}{2})}\,|\nu'\rangle\,. \end{aligned} \tag{4.9}$$

Starting from this expression, if we use again perturbation theory, the lowest order term where both the initial state and the system are translation invariant is reminiscent of the term obtained in the clean case and reads as[7]

$$\sum_{n,n',m} \rho_{\mathrm{i},(0)}^{n'n}\,\delta(E_{n'} - E_n - \omega + \mathcal{D}_{n'} - \mathcal{D}_n)\,\langle n|\,\hat{O}_1\,|m\rangle\,\langle m|\,\hat{O}_2\,|n'\rangle\,\delta(\boldsymbol{P}_m - \boldsymbol{P}_n - \boldsymbol{k})\,\delta(\boldsymbol{P}_{n'} - \boldsymbol{P}_n). \tag{4.10}$$

[7] When both the system and the initial state are translation invariant, the two-point correlator can only depend on $\boldsymbol{R} = \boldsymbol{x} - \boldsymbol{y}$ and not on $\boldsymbol{r} = (\boldsymbol{x} + \boldsymbol{y})/2$, which is equivalent to set the associated Fourier variable $\boldsymbol{k'} = 0$.

Assuming a weak quench such that $\boldsymbol{P}_n = 0$, the intermediate state can be restricted to a single-quasiparticle excitation $\boldsymbol{P}_m = \boldsymbol{k}$ and eventually we recover that the state $|n'\rangle$ contains a pair of quasiparticles with opposite quasimomentum such that $\boldsymbol{P}_{n'} = 0$ as well. This term is the one discussed in global quench spectroscopy displaying resonances at twice the excitation spectrum in the absence of disorder. Here the energy selection rule is modified but we still expect to observe a sharp signal around for $\omega \simeq 2E_{\boldsymbol{k}}$. Besides, the QSF also contains first order terms in the disorder such as

$$\sum_{n,n',m} \delta\rho^{n'n}_{\mathrm{i},(0)}\, \delta(E_{n'} - E_n - \omega + \mathcal{D}_{n'} - \mathcal{D}_n)\, \langle n|\, \hat{O}_1\, |m\rangle\, \langle m|\, \hat{O}_2\, |n'\rangle \\ \times\, \delta(\boldsymbol{P}_m - \tfrac{\boldsymbol{P}_{n'}}{2} - \tfrac{\boldsymbol{P}_n}{2} - \boldsymbol{k})\, \delta(\boldsymbol{P}_{n'} - \boldsymbol{P}_n - \boldsymbol{k'}). \tag{4.11}$$

Still for a weak quench such that $\boldsymbol{P}_n = 0$, we see that the intermediate state can no longer be restricted to a single-quasiparticle excitation $\boldsymbol{P}_m = \boldsymbol{k}$. This is because the disorder breaks explicitly translation invariance of the initial state such that the QSF is now a function of two quasimomenta $\boldsymbol{k}$ and $\boldsymbol{k'}$. When translation invariance is preserved, the spatial dependence only on $\boldsymbol{x}-\boldsymbol{y}$ ensures that the QSF depends on a single quasimomentum, $\boldsymbol{k}$. Note that this is also true after disorder averaging if one assumes that the disorder is homogeneous, *i.e.* its statistical properties are independent of the reference point. This eventually leads to the condition $\boldsymbol{P}_n = \boldsymbol{P}_{n'}$, whose consequence is that only pairs of excitations were observable after weak quenches. Now in the presence of disorder, the QSF contains terms that can probe the excitation spectrum directly (as opposed to twice the excitation spectrum).

In the following we will apply quench spectroscopy to the disordered Bose-Hubbard chain, and show how it can be used to distinguish between the three phases of the model (SF,BG,MI) and eventually reconstruct the full phase diagram using a single probe. Before, we briefly recall the standard numerical method used to reconstruct the phase diagram. The latter will be useful in the following to compare with quench spectroscopy.

4.3.2 A benchmark: the phase-diagram from standard probes

We shall restrict to diagonal box disorder with $\Delta_j \in [-\Delta/2; \Delta/2]$ and start our investigation by fixing the disorder strength to a weak/intermediate value $\Delta/U = 0.25$. We also work in the grand canonical ensemble where the number of particles can be varied via the chemical potential.

As we have discussed in Sec. 4.2.2, the phase diagram at fixed density $\bar{n} = 1$ in the $(\Delta/J, U/J)$ plane is by now well-established [Fig. 4.6(a)]. While the phase diagram of the Bose-Hubbard model in the $(\mu/U, J/U)$ plane (therefore for variable densities) in the presence of random-box disorder is also well-established in higher dimensions, the only investigation to our knowledge in one dimension is the one from [Scalettar et al., 1991] for $\Delta/U = 0.5$. The phase diagram can be obtained numerically by combining several standard probes that distinguish all three phases (Tab. 4.1). We computed it using DMRG for $\Delta/U = 0.25$ on a $L = 47$ sites chain with $N_{\mathrm{s}} = 15$ disorder samples and show the result in Fig. 4.9. This phase diagram will serve as a benchmark to the quench spectroscopy results.

The BG-SF transition is identified from the change in the spatial decay of the one-body correlator $g_1(i,j)$ averaged over distances $r = |i-j|$ from exponential to algebraic. If the decay is algebraic, in log-log scale this function matches an affine function. If the decay is exponential, the same applies in semi-log scale. To estimate the quality of a fit, we evaluate Pearson's correlation coefficient. This coefficient is computed from the ratio of the covariance of two variables divided by their respective standard deviation and in our case provides an estimate of the correlation between the data and the fit function. By definition, it is always between -1 and 1, an absolute value of 1 meaning that the fit function is perfectly correlated with the data. By comparing Pearson's correlation coefficient of the two fits, we can quantitatively assess whether the decay is algebraic or exponential and distinguish between the SF and the BG. The colorbar in Fig. 4.9 indicates

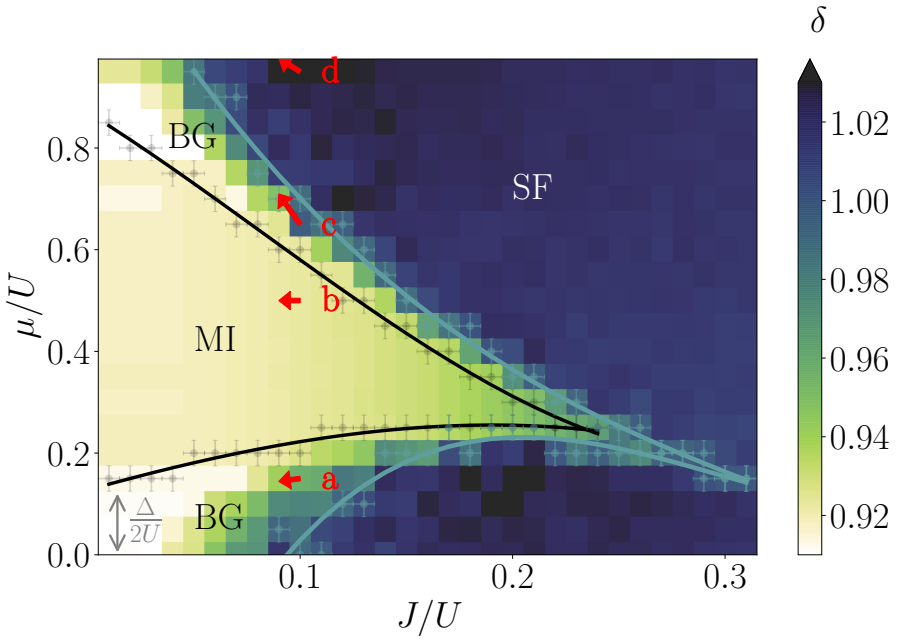

Fig. 4.9 Phase diagram of the disordered Bose-Hubbard chain in the grand-canonical ensemble for random-box disorder with a disorder strength $\Delta/U = 0.25$, computed by DMRG ($L = 47$, $N_s = 15$). The Bose glass phase surrounds the Mott insulator and the superfluid. The boundary of the MI-BG transition (black) is obtained by measuring the deviation from one of the average density (gray points), and the boundary of the BG-SF transition (cyan) from the spatial decay of the one-body correlator (algebraic in the SF, exponential in the BG). The colorbar indicates the ratio of the Pearson's correlation coefficients for an algebraic fit and an exponential one, and the cyan points indicate the closest value below 1. The red arrows represent the quenches considered in Fig. 4.10. From [Villa et al., 2021b].

the value of the ratio between the Pearson's correlation coefficients for an algebraic fit and an exponential fit, so that the BG-SF transition corresponds to a ratio of 1. Pearson's correlation coefficient had been used recently in our group [H. Yao et al., 2020] to distinguish the MI from the SF and the normal fluid at finite temperature. Finally, to detect the BG-MI transition, we use another probe: the behaviour of the averaged density which is integer only in the MI phase. Probing the compressibility (only zero in the MI) is also possible.

4.3.3 Spectral properties of the excitations within each phase

We now investigate the spectral properties throughout the phase diagram using quench spectroscopy. We perform a global quench of the tunnelling from J_i to $J_f = 0.9J_i$, at fixed disorder strength $\Delta/U = 0.25$ and while conserving the particle number throughout the quench (we move along iso-filling lines in the phase diagram, such that the chemical potential also varies between the pre-quench state and the post-quench one). We will explore different regimes for various densities and values of the on-site interaction U. We begin by discussing the one-body correlator before studying the on-site density.

The one-body correlator. In the clean system, the one-body correlator $g_1(R,t)$ unveils the excitation spectrum in both the SF and the MI. For weak disorder, we expect this observable to also probe the excitation spectrum in these phases, based on the perturbative arguments presented in Sec. 4.3.1. Following the quench protocol described above, we represent the QSF of $\langle \hat{a}^\dagger(R,t)\hat{a}(0,t)\rangle$ averaged over $N_s = 15$ disorder realisations at fixed $U = 10J_i$ in Fig. 4.10. The four quenches are represented schematically by the red arrows in Fig. 4.9, and the final values of the chemical potential are indicated within each panel.

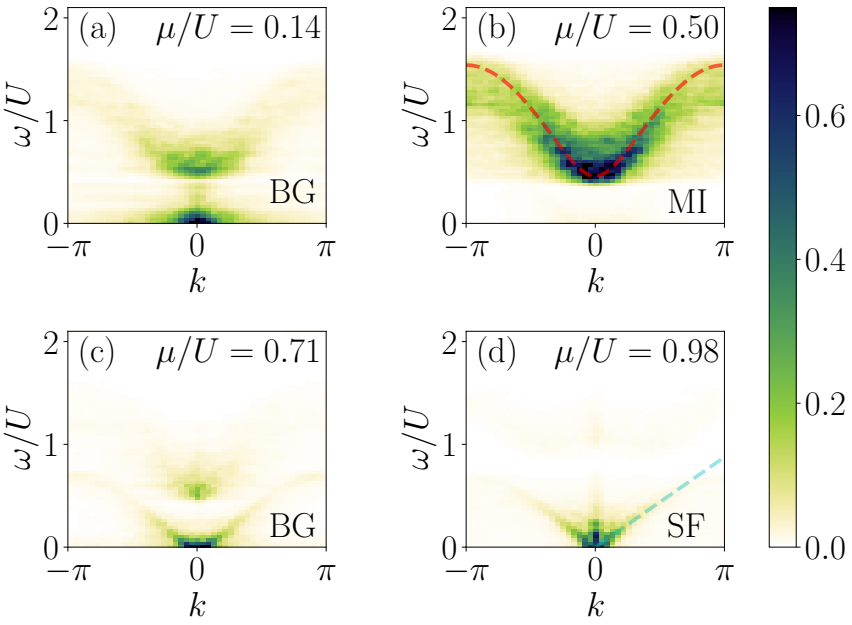

Fig. 4.10 QSF of $g_1(R,t)$ after a global quench of the tunnelling $J_\mathrm{f} = 0.9J_\mathrm{i}$ such that $U/J_\mathrm{i} = 10$ becomes U/J_f, at fixed disorder strength $\Delta/U = 0.25$ for four different initial values of the chemical potential (a) $\mu/U = 0.15$ (BG), (b) $\mu/U = 0.5$ (MI), (c) $\mu/U = 0.65$ (BG) and (d) $\mu/U = 0.95$ (SF). The *final* values of the chemical potential are indicated on each panel, and each quench is represented by a red arrow in Fig. 4.9. The excitation spectrum is revealed within each phase. In (b) the dashed red line represents the excitation spectrum from the pair of d-Bogoliubon and h-Bogoliubon (which reduce to pure doublon and holon respectively in the strongly interacting regime). In (d) the dashed cyan line is a linear fit of the lower edge of the QSF, whose value can be used to extract the speed of sound. From [Villa et al., 2021b].

In Fig. 4.10(b), we observe a gapped signal. The same parameters in the clean system would correspond to the middle of the Mott lobe. Since the disorder strength is rather weak, we may compare the signal with the excitation spectrum of the pair of elementary excitations (d-Bogoliubon and h-Bogoliubon which reduce to a pure doublon and a pure holon for strong interactions) $E_{k,+} + E_{-k,-} = 2E_k$, which we represent by the dashed red line. We find an good agreement with the observed spectral intensity, therefore we conclude that this region is still MI in the presence of disorder. This is consistent with the phase diagram given in Fig. 4.9. Interestingly, the energy-gap in units of U for the clean system is about $1 - 6J_\mathrm{f}/U$ in the strongly interacting regime (0.46 here) and matches well with the observation of the QSF in the presence of disorder. This is to be contrasted with the expected value $1 - \Delta/U$ (0.75 here) in the atomic limit.

This first simple example allows to illustrate many general features that we will encounter again in the following. The presence of random disorder causes broadening of the spectral features, similarly as for other spectroscopic techniques (Sec. 4.2.2) and analytical insights from first order perturbation theory (Sec. 4.3.1). Most of the spectral weight is also concentrated around $k = 0$. It appears that higher momenta are significantly more scattered and affected by the disorder. This is physically intuitive as the disorder affects the on-site energies of the system, and therefore plays an important role on small length scales (small spatial wavelengths) which translate into large momenta. Spectral features are less affected close to $k = 0$ (are thus more visible) because the global effect of the disorder is less important than the local one. For instance, a localised state on the clean system (MI) stays localised in the presence of disorder (MI or BG) and a delocalised one (SF) stays delocalised. The disorder does not modify the global behaviour of the system, but only its local properties (through the excitations for instance). This is, as we saw, what makes the BG so difficult to detect using global probes. Scattering is also known to be screened by the presence of

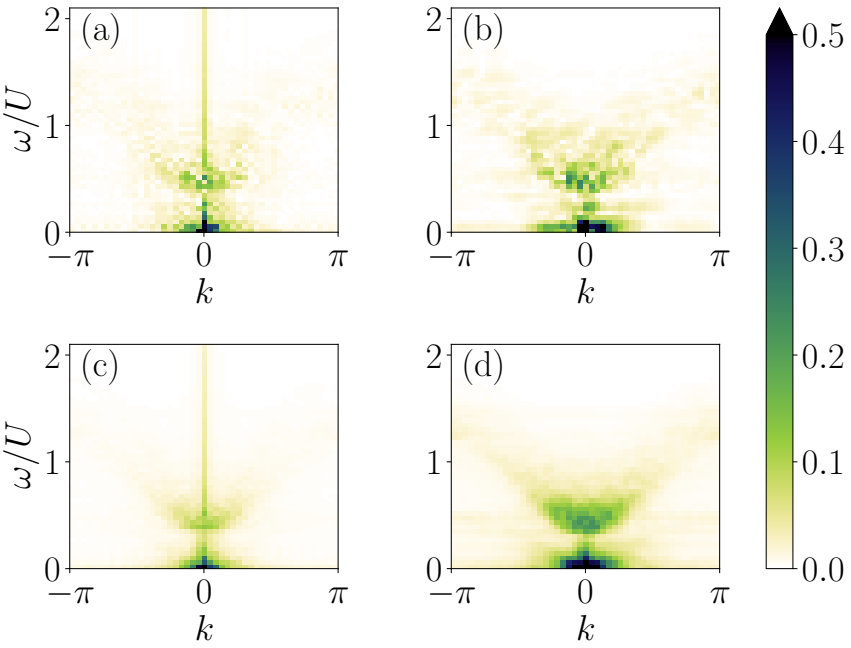

Fig. 4.11 QSF of the one-body correlator after a quench of the tunnelling $J_f = 0.9J_i$ at fixed $U/J_i = 7.5$ with $\mu/U = 0.15$ (BG phase). (a) Represents a single disorder realisation while (b) shows the same result after applying a window function (Hann) to the data before taking the Fourier transform. (c) and (d) are the result of (a) and (b) respectively after averaging over $N_s = 15$ samples. From [Villa et al., 2021a].

repulsive interactions in the phonon regime at low k which strongly suppresses localisation [Lugan et al., 2007; Lugan and Sanchez-Palencia, 2011]. This can explain why the spectral features at more strongly affected towards higher k.

We highlight that in all our numerical results, we remove the long-time average (in order to isolate the fluctuations due to the excitations from the time-independent background) before computing the QSF of a single disorder realisation. We also apply a bell-shaped Hann window so as to smooth the discontinuities from the start and the end of the sampled space-time data and reduce the associated numerical artefacts appearing in the numerical Fourier transform. Such apodisation method can also be used efficiently in quench spectroscopy for clean systems, as shown in Fig. 3.17. We finally take the modulus of the QSF and average over N_s samples and finally normalise the result. The full numerical procedure used in the disordered case can be viewed in Fig. 4.11, where we distinguish the effect of each processing step.

In Fig. 4.10(d), we observe a gapless signal linear close to the origin. In the clean system for the same parameters we would expect a SF phase, and this is still the case in the presence of disorder, in agreement with the phase diagram in Fig. 4.9. A strong signal appears along $k = 0$, suggesting the presence of quasi long-range order characteristic of the SF. We will further analyse this phase in the following, and in particular extract the velocity of the soundlike mode and compare it to the sound velocity of a related model. This will provide further evidence for a SF phase.

Lastly, Fig. 4.10(a) and Fig. 4.10(c) display intermediate spectral features, with the coexistence of gapped and gapless spectral weight and the absence of a well defined linear branch at low energy (particularly clear in the first case). In the clean system for the same parameters, this corresponds to a MI. In the presence of disorder, gapless excitations appear without signature of a soundlike mode, suggesting the formation of the BG phase. This identification, purely from the dynamics of the system using quench spectroscopy, is once again consistent with the phase diagram computed using standard thermodynamic probes in Fig. 4.9. Here, using a single probe and global quenches we are able to probe the properties of the excitations and qualitatively distinguish all three phases

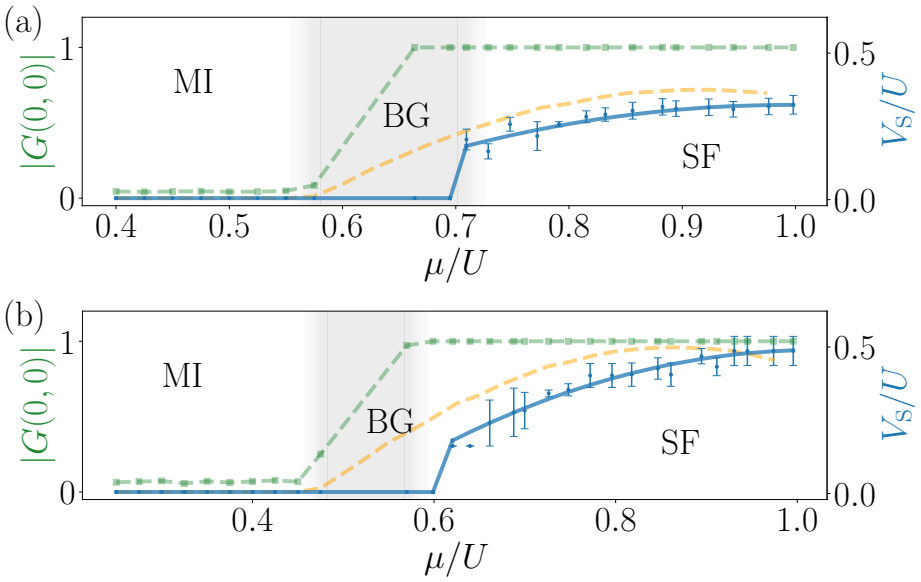

Fig. 4.12 Analysis of the QSF of g_1: the existence of gapless excitations through the modulus of $G(0,0)$ (green points, left axis) allows to precisely distinguish the MI from the BG and the finite velocity of a soundlike mode (blue points, right axis) allows to distinguish the BG from the SF phase. The blue line is a spline ajustement to guide the eye and the dashed yellow line is the comparison with Eq. (4.12) expected in the strongly interacting regime for the clean system (here in the region $1 < \bar{n} < 2$) with (a) $U/J_\mathrm{i} = 10$ and (b) $U/J_\mathrm{i} = 7.5$ after a quench of the tunneling to $J_\mathrm{f} = 0.9J_\mathrm{i}$ at fixed disorder strength $\Delta/U = 0.25$. From [Villa et al., 2021b].

from the behaviour of the elementary excitations probed by the QSF, as detailed below.

The MI-BG transition can be detected from the existence of gapless excitations which are present in the BG but absent in the MI. As emphasised by [Fallani et al., 2007], "rigorously speaking the BG phase should be characterised by a gapless spectrum, [but] detecting the absence of a gap is technically challenging [...]. It would require a measurement of excitability at arbitrarily small energies, [which] cannot be accomplished with the modulation technique that works well only for frequencies much larger than the reciprocal of the modulation time, starting from a few hundreds Hz". In quench spectroscopy, the resolution is set by the maximum evolution time available, and is ultimately limited by the time during which the system remains isolated. With current generation experiments, a resolution down to the Hz is possible, and would make a very accurate determination of the transition and circumvent such issue. Quench spectroscopy also probes spectral properties in the full momentum space, not only the $k = 0$ part, which helps to distinguish all phases. Detecting gapless excitations is indeed tantamount to distinguish a true BG from a strongly inhomogeneous MI.

Still choosing the one-body correlator as an observable, we extract the modulus of its QSF at the origin $|G(0,0)|$ for two vertical cuts through the phase diagram at $U/J_\mathrm{i} = 10$ and $U/J_\mathrm{i} = 7.5$ in Fig. 4.12 (green points, left axis). When $|G(0,0)|$ starts to significantly deviate from zero marks the transition from the gapped MI to the gapless BG. We find an excellent agreement with the size of the BG region obtained from the phase diagram in Fig. 4.9, reproduced as the gray area in Fig. 4.12.

The BG-SF transition can be detected by the existence of a finite soundlike mode close to $k = 0$ (present in the SF but not in the BG). The presence of weak disorder facilitates the fitting procedure as the broadening of the spectral features is less significant. We always fit the lower edge of the spectral signal obtained from the disorder averaged QSF by an affine function, and we extract its slope. We represent the velocity of such linear mode in Fig. 4.12 by the blue points (right axis). The fitted slope may be equal to zero, meaning that the signal is featureless at low energy and a soundlike mode is absent, suggesting a BG rather than a SF. The μ/U value for

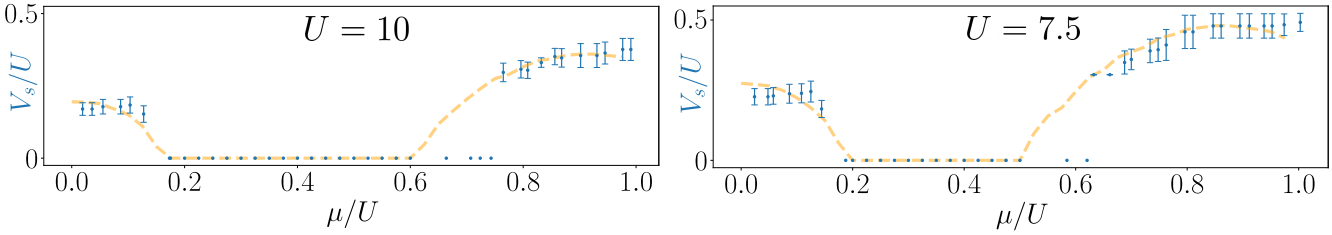

Fig. 4.13 Extracted velocities from the soundlike mode in the QSF of the one-body correlator in the *clean* system (blue points) and comparison with the speed of sound given by Eq. (4.12) (dashed yellow line), for two interaction values at $U/J_\mathrm{i} = 10$ and $U/J_\mathrm{i} = 7.5$. Below the first Mott lobe ($\mu/U \lesssim 0.2$, $0 < \bar{n} < 1$) while above it ($\mu/U \gtrsim 0.6$, $1 < \bar{n} < 2$). Aside from a few outliers around $\mu/U \simeq 0.6$ due to fitting difficulties, the agreement is excellent. This suggests that the small discrepancy with the model observed in the disordered case in Fig. 4.12 is caused by the disorder rather than the finite value of the interactions (recall that Eq. (4.12) is exact in the hard core limit). From [Villa et al., 2021b] (Supplemental Material).

which a linear mode appears matches very well with the predicted width of the BG region in Fig. 4.9 (again marked by the gray region for each panel in Fig. 4.12).

It proves interesting to compare the value of the extracted velocity from the QSF to a model predicting the behaviour of the sound velocity in the strongly interacting SF regime. As the effect of disorder is screened around $k = 0$, as a first approximation we may compare to a clean model. When the filling is smaller than 1, the expression of the sound velocity is found by the fermionic mapping detailed in Appendix 2.C, which in the hard core regime reads as $V_\mathrm{s} = 2J\sin(\pi\bar{n})$. However, we also explore a strongly interacting SF regime above the first lobe where the filling is higher than one. In the hard core regime, we apply a similar logic and reduce to the Hilbert space to two sites, so as to study an effective tight-binding model where the SF with filling $1 < \bar{n} < 2$ can be thought of as a uniform homogeneous background with $\bar{n} = 1$ on top of which lies fermionic excitations such that $0 < \bar{n}_\mathrm{f} < 1$ where $\bar{n}_\mathrm{f} = \bar{n} - 1$ is the average density of the spinless fermions ($\bar{n}_\mathrm{f} = \bar{n}$ if $0 < \bar{n} < 1$). The elementary excitations of this simpler model consist of particle-hole pairs, with individual momenta given by $k_\mathrm{p} \in]-\pi; -k_\mathrm{F}] \cup [k_\mathrm{F}; \pi[$ and $k_\mathrm{h} \in [-k_\mathrm{F}; k_\mathrm{F}]$ with $k_\mathrm{F} = \pi\bar{n}_\mathrm{f}$. The excitation spectrum can be constructed as $E(k_\mathrm{p}; k_\mathrm{h}) = -2bJ(\cos k_\mathrm{p} - \cos k_\mathrm{h})$ where we introduced b the Bose enhancement factor, given by $b = 1$ for $0 < \bar{n} < 1$ and $b = 2$ for $1 < \bar{n} < 2$. The spectrum can be rewritten by introducing $k = k_\mathrm{p} - k_\mathrm{h}$ using trigonometric formulas as $E(k; k_\mathrm{h}) = 4bJ\sin(k/2)\sin(k/2 + k_\mathrm{h})$. Close to the origin $k = 0$, we have $k_\mathrm{p} \simeq k_\mathrm{h} \simeq k_\mathrm{F}$. Therefore the spectrum is soundlike with a sound velocity generally given by $V_\mathrm{s} = 2bJ\sin(k_\mathrm{F})$ which reads as

$$\begin{aligned} V_\mathrm{s} &= 2J\sin(\pi\bar{n}) \qquad \text{if} \quad 0 < \bar{n} < 1, \\ V_\mathrm{s} &= 4J\sin(\pi(\bar{n} - 1)) \qquad \text{if} \quad 1 < \bar{n} < 2. \end{aligned} \tag{4.12}$$

We plot Eq. (4.12) as the dashed orange line in Fig. 4.12 and we find a good agreement with the velocities extracted from the linear mode observed in the QSF (blue points). The small discrepancy observed should be attributed to the disorder rather than the finite interaction value, although both effects are expected to renormalise the sound velocity towards lower values [Cazalilla, 2004; Gaul et al., 2009]. To check for this effect we compare the velocities given by Eq. (4.12) (derived in the hard core regime) with the velocities extracted from the QSF but this time in the *clean* system and we show the result in Fig. 4.13. Within the errorbars, the agreement is very good. This suggests that the observed reduction of the sound velocity visible in Fig. 4.12 is due to the presence of the disorder rather than the strong but finite value of the interactions.

Finally, we note that the strongest signal probed by the QSF of the one-body correlator in the disordered regime is the excitation spectrum E_k rather than twice the excitation spectrum $2E_k$ as in the clean system (even though the latter signal is still present). This has to do with the

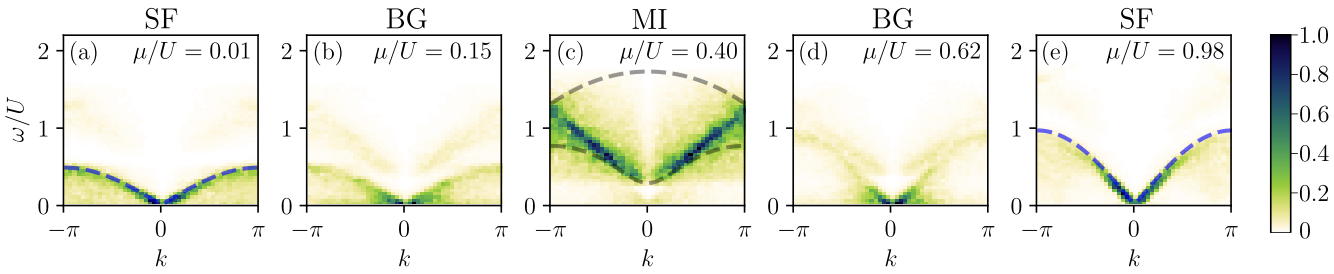

Fig. 4.14 QSF of $\hat{n}(R,t)$ after a global quench of the tunnelling from J_i to $J_\mathrm{f} = 0.9J_\mathrm{i}$ at fixed $U = 7.5J_\mathrm{i}$ and $\Delta/U = 0.25$, for different values of the final chemical potential indicated in each panel. Contrary to the one-body correlator presented in Fig. 4.10, here the QSF of the density reveals the energy transitions in the gapless phases and a continuum inside the two-excitation continuum in the MI. In (c) the dashed gray line represents the envelope of the pair of a d-Bogoliubon and a h-Bogoliubon with different momenta. In (a,e) the dashed blue line represents $\omega = 4bJ\sin(k/2)$ [Eq. (4.17)], with the Bose enhancement factor equal to $b = 1$ in (a) where the filling is $\bar{n} \sim 0.6$, and to $b = 2$ in (e) where the filling is $\bar{n} \sim 1.6$. From [Villa et al., 2021a].

fact that the disorder breaks translation invariance of both the system and the initial state, as discussed at the end of Sec. 4.3.1 based on the perturbative expression of the QSF.

The on-site density. We now change our observable and choose a one-point function, the simplest of which is the on-site density $\hat{n}(R,t)$ that can be measured experimentally using quantum gas microscopes with single-site resolution (Sec. 1.3.2.2). Following the same numerical procedure (quench of the tunnelling from J_i to $J_\mathrm{f} = 0.9J_\mathrm{i}$ at fixed disorder strength $\Delta/U = 0.25$ in the grand-canonical ensemble), we display the behaviour of the QSF of the density in Fig. 4.14 for $U = 7.5J_\mathrm{i}$ and different values of the chemical potential. The phases deduced from the previous analysis of g_1 (or from the following analysis of $\hat{n}$) are indicated for reference on top of each panel. Here the QSF of the density shows a gapped signal in the MI, and sharp gapless spectral features in the SF, which appear linear close to the origin. Once again, the spectral features in the BG are intermediate between both phases, with the signal similar to the SF more visible but significantly blurrier towards the origin.

Importantly, the spectral features observed in both the SF and the MI are *not* the excitation spectrum. As we discuss in the following, the signal in the SF is caused by resonances of energy transitions in the SF and energy sums in the MI. We already encountered a similar behaviour in local quench spectroscopy where translation invariance of the initial state was broken explicitly by the quench. The gapped signal in the MI phase can be understood from the quasiparticle picture detailed in Sec. 3.3.5.2. The signal observed is caused by the pair of two different excitations with different quasimomentum coupling to the ground state, and the predicted envelope from the clean system is represented by the dashed gray line in Fig. 4.14(c). It is satisfactory that the spectral intensity of the signal is well-contained within this envelope, up to the expected additional broadening caused by the disorder. However, a sharp feature is visible inside this continuum (that also differs from the excitation spectrum) whose nature remains to be elucidated and requires more investigation.

Similarly to the discussion presented in Sec. 3.3.4, we expect the QSF of the density in the SF phase to display resonances around the energy differences $\omega \simeq E_q - E_{q-k}$. Indeed, we intuitively expect the density to couple eigenstates with the same number of excitations. This interpretation is also in agreement with Eq. (4.7), where the condition $\omega = E_q - E_{q-k}$ is broadened by the disorder. This leads to algebraic divergences in the QSF, which are reminiscent of the ones we obtained from the energy transitions for a cosine-like dispersion relation in Sec. 3.3.4. Adopting the same notations, we define the function $g_k(q,\omega) = E_q - E_{q-k} - \omega$ and denote by $q_k^\star(\omega)$ its

ω-dependent zeros. We expect the divergences of the QSF to come from the values such that $\partial_q g_k(q_k^\star(\omega)) \to 0$ [Eq. (3.69)]. As discussed above, in the strongly interacting regime the excitation spectrum continuum can be approximated by

$$E_k = 4bJ \sin\left(\tfrac{k}{2}\right) \sin\left(\tfrac{k}{2} + k_\mathrm{h}\right), \tag{4.13}$$

where k_h is fixed and b is the Bose enhancement factor given by $b = 1$ for $0 < \bar{n} < 1$ and $b = 2$ for $1 < \bar{n} < 2$. First, using trigonometric identities, we rewrite the function g_k exactly as

$$g_k(q, \omega) = 4bJ \sin\left(\tfrac{k}{2}\right) \sin\left(q - \tfrac{k}{2} + k_\mathrm{h}\right) - \omega, \tag{4.14}$$

such that the zeros of $g_k(q, \omega)$ are given by

$$q_k^\star(\omega) - \tfrac{k}{2} + k_\mathrm{h} = \arcsin\left(\frac{\omega}{4bJ \sin(k/2)}\right). \tag{4.15}$$

Second, we evaluate the derivative of the argument of the delta energy selection rule at the points where this argument is zero

$$\partial_q g_k(q)|_{q=q_k^\star(\omega)} = 4bJ \sin\left(\tfrac{k}{2}\right) \cos\left(q_k^\star(\omega) - \tfrac{k}{2} + k_\mathrm{h}\right) = 4bJ \sin\left(\tfrac{k}{2}\right) \sqrt{1 - \left(\frac{\omega}{4bJ \sin(k/2)}\right)^2}. \tag{4.16}$$

So eventually the QSF is expected to display algebraic divergences along the lines

$$\omega = \pm 4bJ \sin\left(\tfrac{k}{2}\right). \tag{4.17}$$

We represent these lines in dashed blue in Fig. 4.14(a) where the filling is about $\bar{n} \simeq 0.6$ such that $b = 1$, and in Fig. 4.14(e) where the filling is about $\bar{n} \simeq 1.6$ such that $b = 2$. In both situations we find an excellent agreement with the observations from the QSF. Such sharp signals, linear close to $k = 0$ and with apparent velocity $2bJ$ (independent of the filling) should not be confused with the excitation spectrum with sound velocity $2bJ \sin(k_\mathrm{F})$ (explicitly dependent on the filling through k_F). This highlights once again the subtle role played by the observable in spectroscopy. We note that the BG phase shares spectral features of both the SF and the MI. However the well defined algebraic divergences in the SF phase are significantly blurrier in the BG. Consequently, the density can be used to distinguish the three phases, as we will show in Sec. 4.3.4.

Increasing the disorder strength. Finally, we investigate the effect of an increasing disorder strength on the observed spectral features. To retain only two variable parameters, we fix the filling to $\bar{n} = 1$. We recall that the phase diagram was given in Fig. 4.6(a). To briefly summarise the results obtained thus far, the QSF of the one-body correlator g_1 probes the excitation spectrum, while the QSF of the density $\hat{n}$ probes a gapped signal caused by the energy sum of a pair of excitations in the MI and a gapless signal caused by the energy transitions in the SF.

We perform quenches with a fixed tunnelling J and we vary the on-site interaction from $U_\mathrm{f} = 9J$ to $U_\mathrm{i} = 0.9U_\mathrm{f}$. We consider different disorder strengths (now measured in units of the tunnelling), and we represent the result for the QSF of both the density (top row) and the one-body correlator (bottom row) in Fig. 4.15. On the first panels with weak/intermediate disorder we recover the spectral features discussed previously. By increasing the disorder, we gradually observe the closing of the Mott gap and eventually the system becomes gapless and enters the BG phase. Within the same phase and for weak disorder (compare panels (a,b) in the MI for instance), we observe a broadening of the resonance in frequency due to the disorder in agreement with the perturbative expressions from Sec. 4.3.1 that broaden the energy selection rule after disorder averaging compared to the clean case due to the disorder dependent term $\mathcal{D}_{n'} - \mathcal{D}_n$.

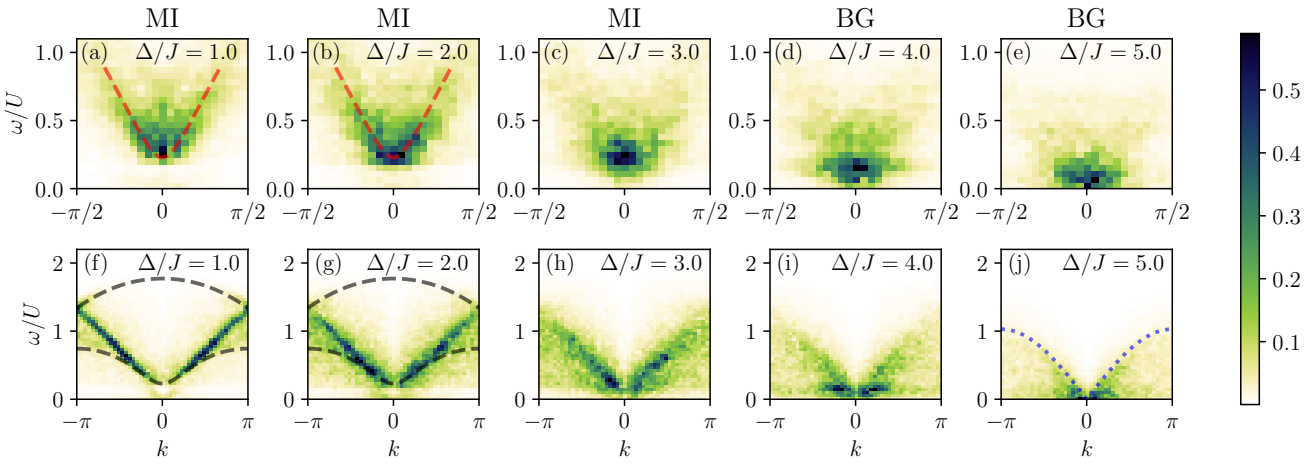

Fig. 4.15 QSF of the one-body correlator (top row) and of the density (bottom row) at fixed $\bar{n} = 1$ for increasing disorder strengths. The quench is performed on the interaction strength to $U_f/J = 9$ starting from the ground state at $U_i = 0.9U_f$. Spectral features broaden with increasing disorder, and the transition from gapped excitations in the MI to gapless ones in the BG is directly visible. The red dashed line indicates the excitation spectrum of the clean system in the MI, the dashed gray envelope indicates the two-excitation continuum in the MI and the dotted blue line marks the divergence observed in the SF and approximates well the outer envelope of the signal in the BG. From [Villa et al., 2021a].

We also note a gradual reduction of the gap, but ultimately the existence of the BG phase is a non-perturbative effect and perturbation theory is not expected to account for the existence of gapless excitations.

Qualitatively, the transition to the BG can be observed using either the QSF of g_1 as the excitation spectrum becomes gapless (top row in Fig. 4.15) or the QSF of $\hat{n}$ (bottom row in Fig. 4.15) which also becomes gapless at the transition as it contains the gapless energy transitions also observed in the SF phase instead of solely the gapped energy sums observed in the MI. Below, we show how to quantitatively use quench spectroscopy in order to reconstruct the full phase diagram of the model.

4.3.4 Reconstructing the phase diagram from the excitations dynamics

Using the QSF (momentum-space) We can use the previous results on the QSF of the one-body correlator g_1 to detect the MI-BG transition from the existence of gapless excitations (extracted from the value of $|G(0,0)|$) and the BG-SF transition from the existence of a finite speed of sound. We already demonstrated it in the grand canonical ensemble for two cuts at $U = 10J_i$ and $U = 7.5J_i$ in Fig. 4.12. The predicted boundaries agreed well within the errorbars with the ones predicted using the phase diagram computed from standard probes (Fig. 4.9). Reconstructing the entire phase diagram in the grand canonical ensemble using this method is computationally demanding. Furthermore, when the gap of excitations drops below our numerical resolution (which depends on the maximum time accessible to the dynamics), the BG-MI boundary becomes difficult to extract. This may be problematic close to the lobe tip. Here, we rather reconstruct the entire phase diagram in the canonical ensemble for $\bar{n} = 1$.

Quenching the on-site interaction U_f from $U_i = 0.9U_f$ at fixed tunnelling J (set to 1), we compute the QSF of the one-body correlator and extract the velocity of the lower edge of the signal. Examples of fits performed are shown in Fig. 4.16. For weak and intermediate disorder, we generally find that the procedure reliably distinguishes between the SF and the BG. The obtained boundary is in excellent agreement within the errorbars to the one obtained using standard methods [Fig. 4.6(a)]. However, for stronger disorder the fit procedure is more difficult and we

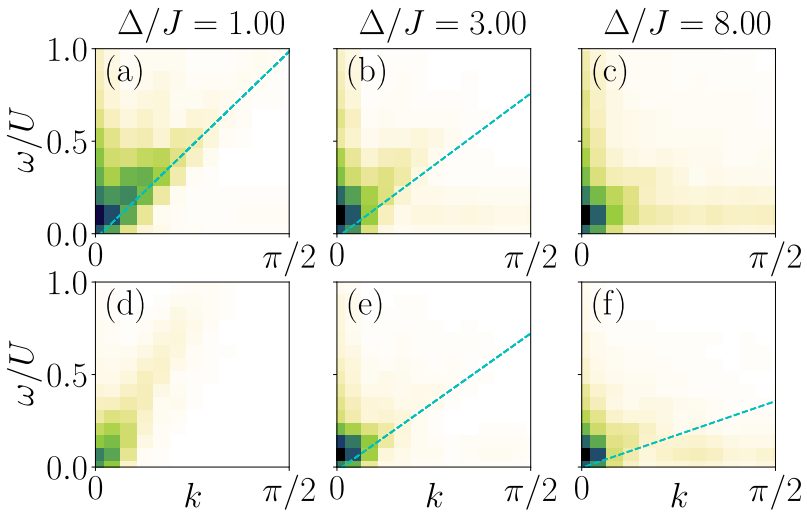

Fig. 4.16 Examples for the QSF of g_1 at $\bar{n} = 1$ at weak, intermediate and strong disorder, for (a-c) $U/J = 3$ and (d-f) $U/J = 4.5$. (d) is close to the MI-BG boundary and is not a SF phase ($V_s = 0$ due to the broadened signal around $\omega = 0$). (c) and (f) illustrates the difficulties in the fit of the lower edge at strong disorder. While (c) is identified as a BG with no speed of sound, (f) is very close to the transition and is identified as a SF.

may only estimate qualitatively the SF-BG boundary. Close to the SF-BG transition, the size of the superfluid puddles becomes of the order of the system size, and the spectral features in momentum space of the BG closely resemble the ones of the SF. Therefore, our fitting algorithm may incorrectly fit an existing finite soundlike mode and we expect to overestimate the size of the SF region. A larger time resolution would help to resolve more accurately the region close to the origin. A larger system size would also help to distinguish the spectral features between a SF and a BG in this region. Therefore we emphasise that the limiting factor here is the finite evolution time and finite size in our numerical simulations, and is not a fundamental limitation of the quench spectroscopy method. We display the shape of the obtained phase diagram in Fig. 4.17. The extracted BG-MI boundary is represented by a dark blue line, which is dotted whenever the energy gap in the disordered system drops below our numerical resolution such that we can no longer distinguish the existence of gapless excitations. When this is the case, we rather estimate the transition from the condition $E_{\text{gap}}(\Delta = 0) = \Delta$ where $E_{\text{gap}}(\Delta = 0)$ is obtained from the QSF analysis of the clean system. The predicted SF-BG boundary is represented by a light blue line, intended as a guide to the eye to the points which for the upper part of the lobe mark the first value of Δ/J at fixed U/J where a soundlike mode is present, and similarly the first value of U/J at fixed Δ/J for the lower part of the lobe. At strong disorder, the boundary is only in qualitative agreement with the expected transition represented by the magenta line based on the results obtained by [Gerster et al., 2016]. The fits of the lower-edge of the spectral features are very demanding at high disorder strength, making it difficult to reconstruct the full shape of the lobe using such method for the system size and finite evolution time we use in our numerical simulations. In the following, we propose an alternative approach, which is significantly less sensitive to finite size effects in order to reconstruct quantitatively the entire phase diagram using quench spectroscopy.

Using the local spectral function (real-space) The features in momentum space are almost identical close to the transition between the SF and the BG and in particular at strong disorder, however we expect the spectral features in real-space to be more distinguishable as the BG exhibits locally gapped MI regions or gapless SF regions. As we target local properties, we choose our observable to be the on-site density. Instead of computing the space-time Fourier transform of the

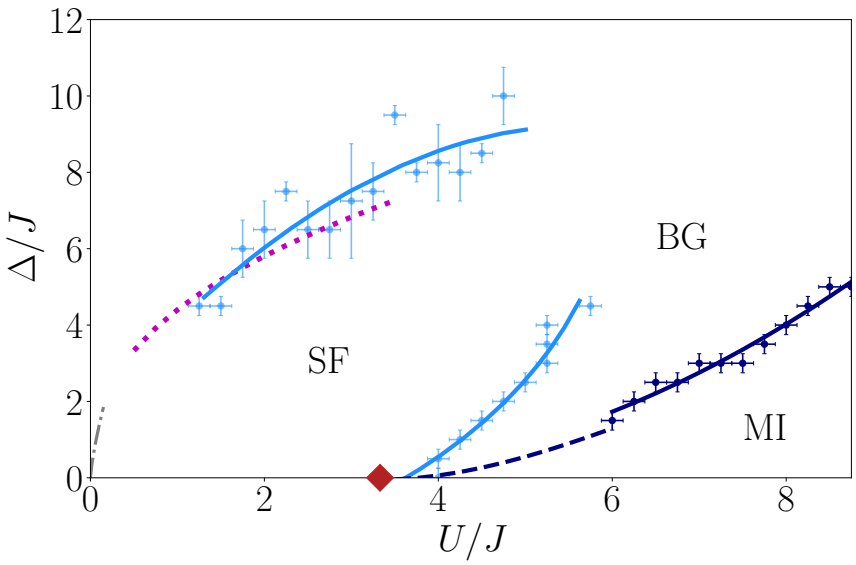

Fig. 4.17 Phase diagram of the Bose-Hubbard chain at $\bar{n} = 1$ reconstructed from the QSF of the one-body correlator. The MI-BG transition (dark blue line) is obtained from the closing of the energy gap of the QSF, and the dashed dark blue line is an estimate of the transition based on the condition $E_{\mathrm{gap}}(\Delta = 0) = \Delta$ (where the energy gap is measured from the QSF of the clean system) which we use when we can no longer clearly resolve the gap in the disordered system. The SF-BG transition is reconstructed from an interpolation of the first point after which we no longer find a finite soundlike mode (light blue line). The upper boundary of the SF-BG transition at strong disorder is only a qualitative estimate due to the fit difficulties to extract the speed of sound. The magenta dotted line represents the expected boundary based on the results from [Gerster et al., 2016] and the dashed gray line the scaling $\Delta \sim U^{3/4}$ expected in the weakly interacting regime. The red diamond indicates the transition in the clean system. From [Villa et al., 2021a].

dynamics, we only compute the Fourier transform in time, which leaves us with spatial information about the phases which constitute the system. This local spectral function (LSF) is defined as

$$G(R,\omega) = 2\pi \sum_{\nu,\nu'} \rho_{\mathrm{i}}^{\nu'\nu}\, \delta(E_{\nu'} - E_{\nu} - \omega)\, \langle \nu | \hat{O}(R) | \nu' \rangle \,. \tag{4.18}$$

While the LSF is not very informative for translational invariant clean systems, it reveals the inhomogeneous spatial structure when disorder is present. We begin the study in the weak disorder regime $\Delta/U = 0.25$, after a quench of the tunnelling from J_{i} to $J_{\mathrm{f}} = 0.9J_{\mathrm{i}}$ in the grand canonical ensemble. We take strong interactions $U = 10J_{\mathrm{i}}$ in order to distinguish all three phases by simply changing the initial value of the chemical potential. For a single disorder realisation, we display a cut of the LSF in the centre of the chain in Fig. 4.18(a-c) within each phase. In the MI, the density probes a signal from the two-excitation continuum and shows a maximum for non-zero energy reflecting the existence of locally gapped excitations. In the SF, we expect to probe a gapless signal from the QSF of the density, which is therefore gapless. The BG resembles the SF signal but shows secondary maxima at finite energy suggesting the coexistence of locally gapped and gapless excitations. Before extracting the excitation peak, we use a Gaussian convolution to smooth the observed signal (dashed green line). To identify the phases, we then identify the regions which are locally SF or locally MI by computing $G(R,\omega)$ for *each* lattice site. For a single disorder sample, we define a lengthscale ξ, which measures the typical size of the identified local MI regions (equivalently, ξ measures the typical distance between the SF puddles). When $\xi \sim 0$, the system is globally SF, whereas for $\xi \sim L$ the system is globally MI. When $0 < \xi < L$, the system is a BG, and we expect ξ to vary continuously across the transition. By averaging over $N_{\mathrm{s}} = 15$ disorder samples, we compute the average value of ξ/L and its standard deviation and

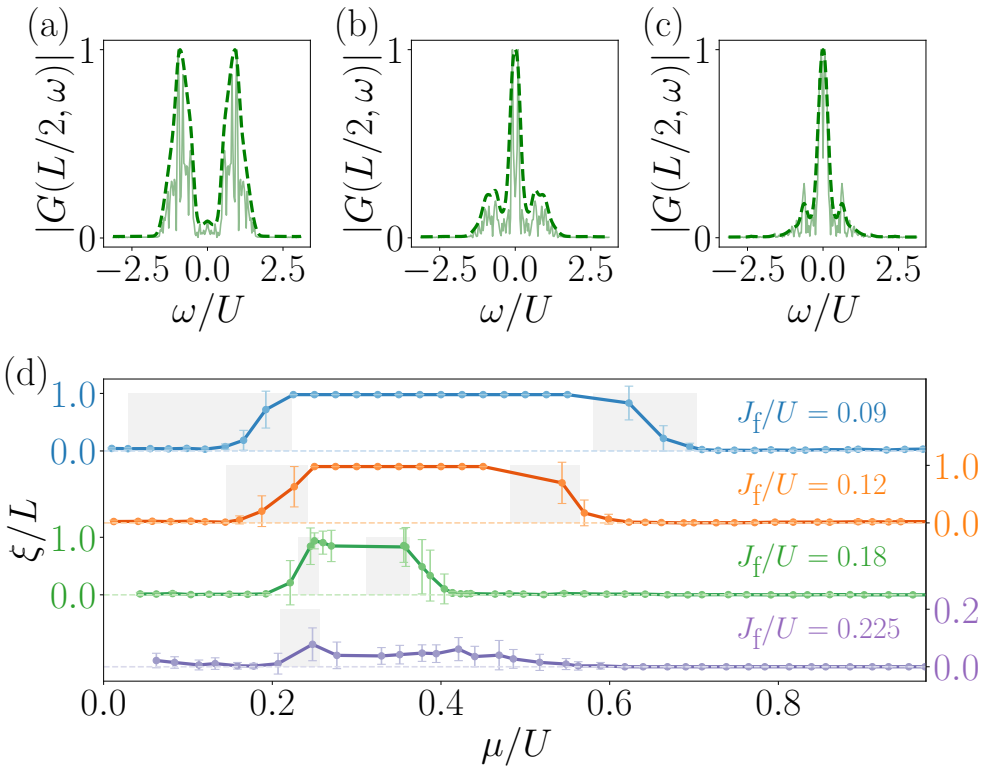

Fig. 4.18 (a-c) LSF of the density for a single disorder realisation representative of each phase at $U = 10J_i$ with (a) $\mu/U = 0.525$ corresponding to the MI with a gapped spectral feature, (b) $\mu/U = 0.625$ corresponding to the BG with the coexistence of a gapped and gapless features and (c) $\mu/U = 0.82$ corresponding to the SF with a gapless signal. (d) Evolution of the characteristic length ξ (rescaled by the length L) which tells apart the three phases and allows reconstruction of the phase diagram. It measures the typical size of the MI regions so that $\xi/L = 0$ in the SF, $0 < \xi/L < 1$ in the BG and $\xi/L = 1$ in the MI. Results are averaged over $N_s = 15$ samples for $J_f/U = 0.09$ and 0.12 and $N_s = 25$ samples for $J_f/U = 0.18$ and 0.225. The errorbars indicate the standard deviation of ξ/L across the samples (large in the BG, close to zero in the SF and MI). The gray area represents the BG region expected from Fig. 4.9. From [Villa et al., 2021b].

we represent its evolution for 4 different vertical cuts through the phase diagram in Fig. 4.18(d). Because the BG is a Griffiths phase, the standard deviation of ξ is large, which means that among the disorder samples the average number of MI regions varies substantially. This can also be used to distinguish the BG from the other two phases. Due to the finite size, we need at least one site locally SF-like or MI-like such that $1/L \leq \xi/L \leq 1 - 1/L$ corresponds to the BG. Together with the computed values of ξ/L, we represent in Fig. 4.18(d) the BG regions as identified from the phase diagram of Fig. 4.9 (gray areas). For all but the smallest interactions close to the tip of the lobe, the agreement between the predicted boundaries is excellent. Close to the tip of the lobe, a larger system size is ultimately necessary to distinguish the two gapless phases for which the values of ξ/L remain very small (note the vertical axis to 0.1 instead of 1 in the violet curve at $J_f/U = 0.225$). Numerically, working in the grand canonical ensemble is very costly, and reconstructing the full phase diagram from this method is computationally prohibitive. In the following, we move back to the canonical ensemble where $\bar{n} = 1$ to demonstrate that the full phase diagram can be reconstructed from the LSF.

We follow the same procedure, performing a weak quench over the ground state for a given set of parameters, compute the LSF of the density for a given disorder realisation on each site, smooth the signal using a Gaussian convolution to extract the energy of the peak and repeat for all lattice sites to evaluate ξ/L. We then average over all disorder samples to obtain the average value of

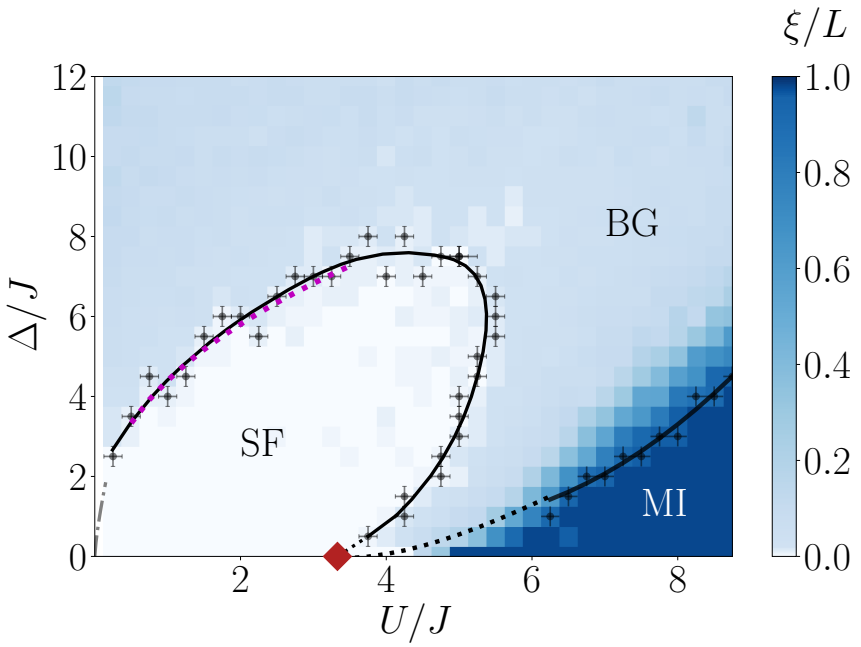

Fig. 4.19 Phase diagram of the Bose-Hubbard chain at $\bar{n} = 1$ reconstructed from the spacing between SF-like regions ξ/L obtained from the analysis of the LSF of the density ($L = 47$, $N_s = 10$). The SF corresponds to $\xi/L \simeq 0$, the MI to $\xi/L \simeq 1$ and the BG to $0 < \xi/L < 1$. The full lines are parametric fits to the data points as guides to the eye. The estimated boundary for the SF-BG transition is in excellent agreement with the results presented in Fig. 4.6(a) (the result from [Gerster et al., 2016] is indicated by the dotted magenta line). The MI-BG boundary is obtained from the first points for which $\xi/L < 1 - 1/L$. We also represent the expected scaling $U^{3/4}$ at vanishingly small interactions (dashed gray), the result obtained using $E_{\mathrm{gap}}(\Delta = 0) = \Delta$ from the QSF of the one-body correlator in Fig. 4.17 (dotted black). From [Villa et al., 2021a].

ξ/L and the associated standard deviation. Finally, we repeat this for all points in the phase diagram $(\Delta/J, U/J)$ using a 32×32 grid. We display our final result in Fig. 4.19, averaged over 10 disorder realisations. The SF phase is identified as the white region where $\xi/L \simeq 0$, the MI phase corresponds to the dark blue region where $\xi/L \simeq 1$, the BG corresponds to the intermediate case. The SF-BG boundary is reconstructed by scanning horizontally (vertical boundary, right side of the lobe) and vertically (top of the lobe) and extracting the first value for which $\xi/L \neq 0$ within the errorbars. The black line represents a parametric fit through the points. For reference, we also indicate the boundaries obtained from the analysis of the QSF (Fig. 4.17). The boundaries are dotted when our numerical frequency resolution (including the additional broadening due to the Gaussian convolution) is not sufficient and therefore we no longer clearly resolve the transition. The obtained phase diagram is in quantitative agreement with the one computed from standard numerical methods [Fig. 4.6(a)], and offers a more reliable and substantially less involved method compared to the one based on the QSF where the phases were distinguished from their spectral features in quasimomentum space. The agreement with the phase diagram obtained on much larger system sizes is even surprising given the fact that we generally expect to underestimate the size of the BG region, as a phase appears delocalised if its correlation length is larger than the system size.

We also emphasise that in principle, for a large enough system, a single disorder realisation would suffice to reconstruct the phase diagram. The most interesting feature of this method is its immediate implementation in experiments: it only requires the ability to perform controlled global quantum quenches and the use of quantum microscopes with on-site resolution to measure the density operator from a series of snapshots of the experiment.

5 Conclusions and perspectives

In this thesis, we have investigated the spreading of correlations in interacting quantum lattice models. We showed that the space-time spreading of quantum correlations is generally twofold, and the two characteristic velocities can be related to fundamental properties of the elementary excitations and depend on the underlying model. When the dispersion relation of the quasiparticles is non-linear, the two velocities have to be distinguished. Only the velocity of the correlation edge is linked to the fastest group velocity of the excitations and relates to the speed at which physical information propagates.

We then proposed a novel spectroscopic method called quench spectroscopy which uses the out-of-equilibrium space-time correlation pattern of equal-time observables (one-point functions or two-point correlators) obtained after a quantum quench (either local or global) in order to unveil spectral properties of the excitations with momentum resolution. We discussed the quench protocol in different phases and regimes for various models (Bose-Hubbard chain, Heisenberg chain, transverse-field Ising chain for short and long-range interactions in the quasi-local regime). We also detailed the role played by the observable on the probed spectral properties. Importantly, quench spectroscopy can be used to reconstruct the dispersion relation of the elementary excitations. Additionally, we warned that the observation of a well-defined excitation branch is not necessarily a signature of the excitation spectrum, and we provided various specific examples as well as a general analytical argument based on a cosine-like excitation spectrum to illustrate this. We also discussed the experimental implementation and advantages of the method compared to standard pump-probe spectroscopies.

Finally we extended our study to disordered systems and in particular we showed that quench spectroscopy can unambiguously detect the Bose glass phase of the Bose-Hubbard model in various regimes. Specific spectral features highlight the different types of excitations present within each phase of the model. We showed how a single probe, the QSF of the one-body correlator, can be used to locate both the MI-BG boundary from the existence of gapless excitations and the SF-BG boundary from the existence of a well-defined soundlike mode. Additionally, a local probe (the on-site density) can identify the real-space distribution of the isolated superfluid puddles constituting the Bose glass. Such a local spectral function was used to quantitatively reconstruct the full phase diagram of the disordered model.

To conclude let us mention a few outlooks. From the point of view of correlation spreading, a connection between the quasiparticle picture and hydrodynamic theory is desirable. The quasiparticle picture is semi-classical, and the role played by entanglement remains to be included in the description. It would also be interesting to pursue the analogy regarding classical hydrodynamical theory, in particular as the Kelvin wake-pattern bears some similarities with the quantum result which sparked interest recently (Appendix 2.A). The focus towards the propagation of entanglement, especially in long-range systems, is also of interest. Recent observations revealed a generic ballistic spreading of entanglement in the quasi-local regime of long-range models [Schneider et al., 2021].

From the quench spectroscopy perspective, a first experimental implementation of the technique would be suitable. Today, quantum gas microscopes allow the measurements of local on-site observables, and we also discussed the one-body correlator which is accessible through time-of-flight measurements. As the frequency resolution of quench spectroscopy is set by the inverse of the maximum time available for the dynamics, it would allow to experimentally obtain spectral

properties with an unmatched accuracy.

In disordered systems, we showed results for one type of disorder drawn from a random-box distribution, usually implemented experimentally from speckle patterns or spatial light modulators. Another type of disorder is quasi-random disorder, which is experimentally highly relevant and can be created by superimposing an additional lattice with incommensurate lattice spacing r (the wavelengths of the two lasers used to create the lattices are incommensurate). A few dramatic changes are expected, in particular, the shape of the phase diagram is strongly modified as we showed in the main text (for vanishing interactions there exists a threshold value in the disorder strength to localise the particles; the theorem of inclusions no longer holds such that a direct SF-MI transition is allowed). More importantly, there exists specific values of the quasi-momentum such as $k^\star = 2\pi(1-r)$ which are known to display strong satellite peaks in the behaviour of specific observables [Roscilde, 2008; Roux et al., 2008]. Such additional resonances may slightly complicate the numerical analysis, work to investigate such question is currently in progress.

Recently, [Gautier et al., 2021; H. Yao et al., 2020] proposed quasi-periodic potentials with low amplitude in order to alleviate the finite temperature constraint that has up to now limited the observation of the Bose glass and its associated physical behaviour. Despite the fact that we benchmarked quench spectroscopy on lattice models where numerically exact solutions are available, it also applies to continuum models and it would be interesting to see what can be learned from these models.

We have also focused on weak quenches around the ground state (zero temperature), however quench spectroscopy may also be adapted to investigate higher excited states (high temperature). Recently, this topic emerged in the context of many-body localisation in order to investigate the mobility edge (lowest energy value in the spectrum above which all states are delocalised) [Naldesi et al., 2016; R. Yao and Zakrzewski, 2020]. Besides, it would be interesting to extend disordered quench spectroscopy so as to study the existence and properties of many-body localised phases. A prime example is the quantum transverse field Ising chain, whose Hamiltonian reads as $\hat{H} = -\sum_{i<j} J_{ij}\hat{\sigma}_i^x\hat{\sigma}_{i+1}^x - h_i\hat{\sigma}_i^z$, where the on-site magnetic fields h_i are randomly drawn from a bounded probability distribution, with disorder strength h. This model has been studied experimentally by [Smith et al., 2016] on a trapped ions platform for a long-range chain ($J_{ij} = 1/|i-j|^\alpha$) of 10 spins. They found evidence of a MBL phase by measuring in particular the longitudinal magnetisation $\langle\hat{\sigma}_i^z\rangle$ starting from the staggered Néel state $|\uparrow\downarrow\uparrow\cdots\rangle_z$, and observing whether the magnetisation relaxes towards a thermal state. A MBL state emerged when the disorder strength was ramped up. It would be interesting to investigate the consequence of MBL on the observed spectral properties, as they depend upon the nature of the excitations generated by the system. Quench spectroscopy could also be a tool to investigate the existence of MBL in higher dimensions, in particular in light of recent experiments indicating evidence of MBL states in the two-dimensional Bose-Hubbard model [Choi et al., 2016]. In the latter experiment, times up to $t_{\max}J/\hbar = 190$ were used, well beyond the maximum time we used in our numerical simulations and would allow for an excellent resolution of spectral properties. So far evidence for MBL has been provided from thermodynamic properties, in particular as regards thermalisation of the long-time steady state. An extension of quench spectroscopy to higher energies in order to characterise MBL directly from the localisation of its excitations is desirable.

Bibliography

Abanin, D. A., Altman, E., Bloch, I., & Serbyn, M. (2019). *Colloquium*: Many-body localization, thermalization, and entanglement. *Reviews of Modern Physics*, *91*(2), 021001. https://doi.org/10.1103/RevModPhys.91.021001

Alet, F., & Laflorencie, N. (2018). Many-body localization: An introduction and selected topics. *Comptes Rendus Physique*, *19*(6), 498–525. https://doi.org/10.1016/j.crhy.2018.03.003

Altman, E., Demler, E., & Lukin, M. D. (2004). Probing many-body states of ultracold atoms via noise correlations. *Physical Review A*, *70*(1), 013603. https://doi.org/10.1103/PhysRevA.70.013603

Altman, E., Hofstetter, W., Demler, E., & Lukin, M. D. (2003). Phase diagram of two-component bosons on an optical lattice. *New Journal of Physics*, *5*(113). https://doi.org/10.1088/1367-2630/5/1/113

Anderson, P. W. (1958). Absence of diffusion in certain random lattices. *Physical Review*, *109*(5), 1492–1505. https://doi.org/10.1103/PhysRev.109.1492

Aspect, A., & Inguscio, M. (2009). Anderson localization of ultracold atoms. *Physics Today*, *62*(8), 30–35. https://doi.org/10.1063/1.3206092

Auerbach, A. (1994). *Interacting electrons and quantum magnetism*. Springer-Verlag.

Bakr, W. S., Gillen, J. I., Peng, A., Fölling, S., & Greiner, M. (2009). A quantum gas microscope for detecting single atoms in a Hubbard-regime optical lattice. *Nature*, *462*(7269), 74–77. https://doi.org/10.1038/nature08482

Barmettler, P., Poletti, D., Cheneau, M., & Kollath, C. (2012). Propagation front of correlations in an interacting Bose gas. *Physical Review A*, *85*(5), 053625. https://doi.org/10.1103/PhysRevA.85.053625

Barnes, T. (2003). Boundaries, cusps, and discontinuities in the multimagnon continua of one-dimensional quantum spin systems. *Physical Review B*, *67*(2), 024412. https://doi.org/10.1103/PhysRevB.67.024412

Barredo, D., Lienhard, V., de Léséleuc, S., Lahaye, T., & Browaeys, A. (2018). Synthetic three-dimensional atomic structures assembled atom by atom. *Nature*, *561*(7721), 79–82. https://doi.org/10.1038/s41586-018-0450-2

Bartenstein, M., Altmeyer, A., Riedl, S., Jochim, S., Chin, C., Denschlag, J. H., & Grimm, R. (2004). Collective excitations of a degenerate gas at the BEC-BCS crossover. *Physical Review Letters*, *92*(20), 203201. https://doi.org/10.1103/PhysRevLett.92.203201

Bergeman, T., Moore, M. G., & Olshanii, M. (2003). Atom-atom scattering under cylindrical harmonic confinement: Numerical and analytic studies of the confinement induced resonance. *Physical Review Letters*, *91*(16), 4. https://doi.org/10.1103/PhysRevLett.91.163201

Bernien, H., Schwartz, S., Keesling, A., Levine, H., Omran, A., Pichler, H., Choi, S., Zibrov, A. S., Endres, M., Greiner, M., Vuletić, V., & Lukin, M. D. (2017). Probing many-body dynamics on a 51-atom quantum simulator. *Nature*, *551*(7682), 579–584. https://doi.org/10.1038/nature24622

Bertini, B., Collura, M., De Nardis, J., & Fagotti, M. (2016). Transport in out-of-equilibrium XXZ chains: Exact profiles of charges and currents. *Physical Review Letters*, *117*(20), 207201. https://doi.org/10.1103/PhysRevLett.117.207201

Bethe, H. (1931). Zur theorie der metalle. *Zeitschrift für Physik*, *71*(3-4), 205–226.

Billy, J., Josse, V., Zuo, Z., Bernard, A., Hambrecht, B., Lugan, P., Clément, D., Sanchez-Palencia, L., Bouyer, P., & Aspect, A. (2008). Direct observation of Anderson localization of matter waves in a controlled disorder. *Nature*, *453*(7197), 891–894. https://doi.org/10.1038/nature07000

Blatt, R., & Roos, C. F. (2012). Quantum simulations with trapped ions. *Nature Physics*, *8*(4), 277–284. https://doi.org/10.1038/nphys2252

Bloch, I. (2005). Ultracold quantum gases in optical lattices. *Nature Physics*, *1*(1), 23–30. https://doi.org/10.1038/nphys138

Bloch, I., Dalibard, J., & Nascimbène, S. (2012). Quantum simulations with ultracold quantum gases. *Nature Physics*, *8*(4), 267–276. https://doi.org/10.1038/nphys2259

Bloch, I., Dalibard, J., & Zwerger, W. (2008). Many-body physics with ultracold gases. *Reviews of Modern Physics*, *80*(3), 885–964. https://doi.org/10.1103/RevModPhys.80.885

Bloch, I., & Greiner, M. (2005). Exploring quantum matter with ultracold atoms in optical lattices. *Advances In Atomic, Molecular, and Optical Physics* (pp. 1–47). Elsevier. https://doi.org/10.1016/S1049-250X(05)52001-9

Boéris, G., Gori, L., Hoogerland, M. D., Kumar, A., Lucioni, E., Tanzi, L., Inguscio, M., Giamarchi, T., D'Errico, C., Carleo, G., Modugno, G., & Sanchez-Palencia, L. (2016). Mott transition for strongly-interacting 1D bosons in a shallow periodic potential. *Physical Review A*, *93*(1), 011601. https://doi.org/10.1103/PhysRevA.93.011601

Bravyi, S., Hastings, M. B., & Verstraete, F. (2006). Lieb-Robinson bounds and the generation of correlations and topological quantum order. *Physical Review Letters*, *97*(5), 050401. https://doi.org/10.1103/PhysRevLett.97.050401

Browaeys, A., & Lahaye, T. (2020). Many-body physics with individually controlled Rydberg atoms. *Nature Physics*, *16*(2), 132–142. https://doi.org/10.1038/s41567-019-0733-z

Bucciantini, L. (2016). Stationary state after a quench to the Lieb–Liniger from rotating BECs. *Journal of Statistical Physics*, *164*(3), 621–644. https://doi.org/10.1007/s10955-016-1535-7

Buluta, I., & Nori, F. (2009). Quantum Simulators. *Science*, *326*(5949), 108–111. https://doi.org/10.1126/science.1177838

Buyskikh, A. S., Fagotti, M., Schachenmayer, J., Essler, F., & Daley, A. J. (2016). Entanglement growth and correlation spreading with variable-range interactions in spin and fermionic tunneling models. *Physical Review A*, *93*(5), 053620. https://doi.org/10.1103/PhysRevA.93.053620

Calabrese, P., & Cardy, J. (2006). Time dependence of correlation functions following a quantum quench. *Physical Review Letters*, *96*(13), 136801. https://doi.org/10.1103/PhysRevLett.96.136801

Carcy, C., Cayla, H., Tenart, A., Aspect, A., Mancini, M., & Clément, D. (2019). Momentum-space atom correlations in a Mott insulator. *Physical Review X*, *9*(4), 041028. https://doi.org/10.1103/PhysRevX.9.041028

Carleo, G., Becca, F., Sanchez-Palencia, L., Sorella, S., & Fabrizio, M. (2014). Light-cone effect and supersonic correlations in one- and two-dimensional bosonic superfluids. *Physical Review A*, *89*(3), 031602. https://doi.org/10.1103/PhysRevA.89.031602

Castro-Alvaredo, O. A., Doyon, B., & Yoshimura, T. (2016). Emergent hydrodynamics in integrable quantum systems out of equilibrium. *Physical Review X*, *6*(4), 041065. https://doi.org/10.1103/PhysRevX.6.041065

Caux, J.-S. (2009). Correlation functions of integrable models: A description of the ABACUS algorithm. *Journal of Mathematical Physics*, *50*(9), 095214. https://doi.org/10.1063/1.3216474

Caux, J.-S. (2016). The quench action. *Journal of Statistical Mechanics: Theory and Experiment*, *2016*(6), 064006. https://doi.org/10.1088/1742-5468/2016/06/064006

Caux, J.-S., & Calabrese, P. (2006). Dynamical density-density correlations in the one-dimensional Bose gas. *Physical Review A*, *74*(3), 031605. https://doi.org/10.1103/PhysRevA.74.031605

Caux, J.-S., & Essler, F. H. L. (2013). Time evolution of local observables after quenching to an integrable model. *Physical Review Letters*, *110*(25), 257203. https://doi.org/10.1103/PhysRevLett.110.257203

Caux, J.-S., & Mossel, J. (2011). Remarks on the notion of quantum integrability. *Journal of Statistical Mechanics: Theory and Experiment*, *2011*(02), P02023. https://doi.org/10.1088/1742-5468/2011/02/P02023

Cayla, H., Carcy, C., Bouton, Q., Chang, R., Carleo, G., Mancini, M., & Clément, D. (2018). Single-atom-resolved probing of lattice gases in momentum space. *Physical Review A*, *97*(6), 061609. https://doi.org/10.1103/PhysRevA.97.061609

Cazalilla, M. A. (2003). One-dimensional optical lattices and impenetrable bosons. *Physical Review A*, *67*(5), 053606. https://doi.org/10.1103/PhysRevA.67.053606

Cazalilla, M. A. (2004). Differences between the Tonks regimes in the continuum and on the lattice. *Physical Review A*, *70*(4), 041604. https://doi.org/10.1103/PhysRevA.70.041604

Cazalilla, M. A. (2006). Effect of suddenly turning on interactions in the Luttinger model. *Physical Review Letters*, *97*(15), 156403. https://doi.org/10.1103/PhysRevLett.97.156403

Cazalilla, M. A., Citro, R., Giamarchi, T., Orignac, E., & Rigol, M. (2011). One dimensional bosons: From condensed matter systems to ultracold gases. *Reviews of Modern Physics*, *83*(4), 1405–1466. https://doi.org/10.1103/RevModPhys.83.1405

Cevolani, L., Carleo, G., & Sanchez-Palencia, L. (2015). Protected quasilocality in quantum systems with long-range interactions. *Physical Review A*, *92*(4), 041603. https://doi.org/10.1103/PhysRevA.92.041603

Cevolani, L., Carleo, G., & Sanchez-Palencia, L. (2016). Spreading of correlations in exactly solvable quantum models with long-range interactions in arbitrary dimensions. *New Journal of Physics*, *18*(9), 093002. https://doi.org/10.1088/1367-2630/18/9/093002

Cevolani, L., Despres, J., Carleo, G., Tagliacozzo, L., & Sanchez-Palencia, L. (2018). Universal scaling laws for correlation spreading in quantum systems with short- and long-range interactions. *Physical Review B*, *98*(2), 024302. https://doi.org/10.1103/PhysRevB.98.024302

Cheneau, M., Barmettler, P., Poletti, D., Endres, M., Schauß, P., Fukuhara, T., Gross, C., Bloch, I., Kollath, C., & Kuhr, S. (2012). Light-cone-like spreading of correlations in a quantum many-body system. *Nature*, *481*(7382), 484–487. https://doi.org/10.1038/nature10748

Chin, C., Grimm, R., Julienne, P., & Tiesinga, E. (2010). Feshbach resonances in ultracold gases. *Reviews of Modern Physics*, *82*(2), 1225–1286. https://doi.org/10.1103/RevModPhys.82.1225

Choi, J.-y., Hild, S., Zeiher, J., Schauß, P., Rubio-Abadal, A., Yefsah, T., Khemani, V., Huse, D. A., Bloch, I., & Gross, C. (2016). Exploring the many-body localization transition in two dimensions. *Science*, *352*(6293), 1547–1552. https://doi.org/10.1126/science.aaf8834

Chomaz, L., Petter, D., Ilzhöfer, P., Natale, G., Trautmann, A., Politi, C., Durastante, G., van Bijnen, R. M. W., Patscheider, A., Sohmen, M., Mark, M. J., & Ferlaino, F. (2019). Long-lived and transient supersolid behaviors in dipolar quantum gases. *Physical Review X*, *9*(2), 021012. https://doi.org/10.1103/PhysRevX.9.021012

Choy, T., & Haldane, F. (1982). Failure of Bethe-ansatz solutions of generalisations of the Hubbard chain to arbitrary permutation symmetry. *Physics Letters A*, *90*(1-2), 83–84. https://doi.org/10.1016/0375-9601(82)90057-3

Cirac, J. I., & Zoller, P. (1995). Quantum computations with cold trapped ions. *Physical Review Letters*, *74*(20), 4091–4094. https://doi.org/10.1103/PhysRevLett.74.4091

Cirac, J. I., & Zoller, P. (2012). Goals and opportunities in quantum simulation. *Nature Physics*, *8*(4), 264–266. https://doi.org/10.1038/nphys2275

Clément, D., Fabbri, N., Fallani, L., Fort, C., & Inguscio, M. (2009). Multi-band spectroscopy of inhomogeneous Mott-insulator states of ultracold bosons. *New Journal of Physics*, *11*(10), 103030. https://doi.org/10.1088/1367-2630/11/10/103030

Clément, D., Fabbri, N., Fallani, L., Fort, C., & Inguscio, M. (2010). Bragg spectroscopy of strongly correlated bosons in optical lattices. *Journal of Low Temperature Physics*, *158*(1-2), 5–15. https://doi.org/10.1007/s10909-009-0040-7

Clément, D., Varón, A. F., Hugbart, M., Retter, J. A., Bouyer, P., Sanchez-Palencia, L., Gangardt, D. M., Shlyapnikov, G. V., & Aspect, A. (2005). Suppression of transport of an interacting elongated Bose-Einstein condensate in a random potential. *Physical Review Letters*, *95*(17), 170409. https://doi.org/10.1103/PhysRevLett.95.170409

Clément, D., Varón, A. F., Retter, J. A., Sanchez-Palencia, L., Aspect, A., & Bouyer, P. (2006). Experimental study of the transport of coherent interacting matter-waves in a 1D random potential induced by laser speckle. *New Journal of Physics*, *8*(8), 165–165. https://doi.org/10.1088/1367-2630/8/8/165

Crawford, F. S. (1984). Elementary derivation of the wake pattern of a boat. *American Journal of Physics*, *52*(9), 782–785. https://doi.org/10.1119/1.13550

D'Alessio, L., Kafri, Y., Polkovnikov, A., & Rigol, M. (2016). From quantum chaos and eigenstate thermalization to statistical mechanics and thermodynamics. *Advances in Physics*, *65*(3), 239–362. https://doi.org/10.1080/00018732.2016.1198134

Dalibard, J. (2012). *Des cages de lumière pour les atomes : la physique des pièges et des réseaux optiques*. Cours du Collège de France. https://www.college-de-france.fr/site/jean-dalibard/_course.htm

Dalibard, J. (2015). *Cohérence et superfluidité dans les gaz atomiques*. Cours du Collège de France. https://www.college-de-france.fr/site/jean-dalibard/_course.htm

Damascelli, A. (2004). Probing the electronic structure of complex systems by ARPES. *Physica Scripta*, *T109*, 61. https://doi.org/10.1238/Physica.Topical.109a00061

Dao, T.-L., Carusotto, I., & Georges, A. (2009). Probing quasiparticle states in strongly interacting atomic gases by momentum-resolved Raman photoemission spectroscopy. *Physical Review A*, *80*(2), 023627. https://doi.org/10.1103/PhysRevA.80.023627

De Nardis, J., Wouters, B., Brockmann, M., & Caux, J.-S. (2014). Solution for an interaction quench in the Lieb-Liniger Bose gas. *Physical Review A*, *89*(3), 033601. https://doi.org/10.1103/PhysRevA.89.033601

des Cloizeaux, J., & Pearson, J. J. (1962). Spin-wave spectrum of the antiferromagnetic linear chain. *Physical Review*, *128*(5), 2131–2135. https://doi.org/10.1103/PhysRev.128.2131

Despres, J., Villa, L., & Sanchez-Palencia, L. (2019). Twofold correlation spreading in a strongly correlated lattice Bose gas. *Scientific Reports*, *9*(1), 4135. https://doi.org/10.1038/s41598-019-40679-3

Despres, J. (2019). *Correlation spreading in quantum lattice models with variable-range interactions* (PhD thesis). Université Paris-Saclay.

Deutsch, J. M. (1991). Quantum statistical mechanics in a closed system. *Physical Review A*, *43*(4), 2046–2049. https://doi.org/10.1103/PhysRevA.43.2046

Dorlas, T. C. (1993). Orthogonality and completeness of the Bethe ansatz eigenstates of the nonlinear Schrödinger model. *Communications in Mathematical Physics*, *154*(2), 347–376. https://doi.org/10.1007/BF02097001

Duan, L.-M. (2006). Detecting correlation functions of ultracold atoms through Fourier sampling of time-of-flight images. *Physical Review Letters*, *96*(10), 103201. https://doi.org/10.1103/PhysRevLett.96.103201

Duan, L.-M., Demler, E., & Lukin, M. D. (2003). Controlling spin exchange interactions of ultracold atoms in optical lattices. *Physical Review Letters*, *91*(9), 090402. https://doi.org/10.1103/PhysRevLett.91.090402

Ejima, S., Fehske, H., & Gebhard, F. (2011). Dynamic properties of the one-dimensional Bose-Hubbard model. *Europhysics Letters*, *93*(3), 30002. https://doi.org/10.1209/0295-5075/93/30002

Ejima, S., Fehske, H., Gebhard, F., zu Münster, K., Knap, M., Arrigoni, E., & von der Linden, W. (2012). Characterization of Mott-insulating and superfluid phases in the one-

dimensional Bose-Hubbard model. *Physical Review A*, *85*(5), 053644. https://doi.org/10.1103/PhysRevA.85.053644

Endres, M., Cheneau, M., Fukuhara, T., Weitenberg, C., Schauss, P., Gross, C., Mazza, L., Banuls, M. C., Pollet, L., Bloch, I., & Kuhr, S. (2011). Observation of correlated particle-hole pairs and string order in low-dimensional Mott insulators. *Science*, *334*(6053), 200–203. https://doi.org/10.1126/science.1209284

Ernst, P. T., Götze, S., Krauser, J. S., Pyka, K., Lühmann, D.-S., Pfannkuche, D., & Sengstock, K. (2010). Probing superfluids in optical lattices by momentum-resolved Bragg spectroscopy. *Nature Physics*, *6*(1), 56–61. https://doi.org/10.1038/nphys1476

Essler, F. H. L., & Fagotti, M. (2016). Quench dynamics and relaxation in isolated integrable quantum spin chains. *Journal of Statistical Mechanics: Theory and Experiment*, *2016*(6), 064002. https://doi.org/10.1088/1742-5468/2016/06/064002

Fabbri, N., Huber, S. D., Clément, D., Fallani, L., Fort, C., Inguscio, M., & Altman, E. (2012). Quasiparticle dynamics in a Bose insulator probed by interband Bragg spectroscopy. *Physical Review Letters*, *109*(5), 055301. https://doi.org/10.1103/PhysRevLett.109.055301

Faddeev, L., & Takhtajan, L. A. (1981). What is the spin of a spin-wave? *Physics Letters*, *85*(6-7), 375–377. https://doi.org/10.1016/0375-9601(81)90335-2

Fallani, L., Lye, J. E., Guarrera, V., Fort, C., & Inguscio, M. (2007). Ultracold atoms in a disordered crystal of light: Towards a Bose glass. *Physical Review Letters*, *98*(13), 130404. https://doi.org/10.1103/PhysRevLett.98.130404

Fisher, M. P. A., Weichman, P. B., Grinstein, G., & Fisher, D. S. (1989). Boson localization and the superfluid-insulator transition. *Physical Review B*, *40*(1), 546–570. https://doi.org/10.1103/PhysRevB.40.546

Franchini, F. (2017). *An introduction to integrable techniques for one-dimensional quantum systems* (Vol. 940). Springer. https://doi.org/10.1007/978-3-319-48487-7

Frérot, I., Naldesi, P., & Roscilde, T. (2017). Entanglement and fluctuations in the XXZ model with power-law interactions. *Physical Review B*, *95*(24), 245111. https://doi.org/10.1103/PhysRevB.95.245111

Frérot, I., Naldesi, P., & Roscilde, T. (2018). Multispeed prethermalization in quantum spin models with power-law decaying interactions. *Physical Review Letters*, *120*(5), 050401. https://doi.org/10.1103/PhysRevLett.120.050401

Friedenauer, A., Schmitz, H., Glueckert, J. T., Porras, D., & Schaetz, T. (2008). Simulating a quantum magnet with trapped ions. *Nature Physics*, *4*(10), 757–761. https://doi.org/10.1038/nphys1032

Fukuhara, T., Kantian, A., Endres, M., Cheneau, M., Schauß, P., Hild, S., Bellem, D., Schollwöck, U., Giamarchi, T., Gross, C., Bloch, I., & Kuhr, S. (2013). Quantum dynamics of a mobile spin impurity. *Nature Physics*, *9*(4), 235–241. https://doi.org/10.1038/nphys2561

Fukuhara, T., Schauß, P., Endres, M., Hild, S., Cheneau, M., Bloch, I., & Gross, C. (2013). Microscopic observation of magnon bound states and their dynamics. *Nature*, *502*(7469), 76–79. https://doi.org/10.1038/nature12541

Garcia-Ripoll, J. J., & Cirac, J. I. (2003). Spin dynamics for bosons in an optical lattice. *New Journal of Physics*, *5*(76), 1–13. https://doi.org/10.1088/1367-2630/5/1/376

Gaul, C., Renner, N., & Müller, C. A. (2009). Speed of sound in disordered Bose-Einstein condensates. *Physical Review A*, *80*(5), 053620. https://doi.org/10.1103/PhysRevA.80.053620

Gautier, R., Yao, H., & Sanchez-Palencia, L. (2021). Strongly Interacting Bosons in a Two-Dimensional Quasicrystal Lattice. *Physical Review Letters*, *126*(11), 110401. https://doi.org/10.1103/PhysRevLett.126.110401

Ge, Y., & Eisert, J. (2016). Area laws and efficient descriptions of quantum many-body states. *New Journal of Physics*, *18*(8), 083026. https://doi.org/10.1088/1367-2630/18/8/083026

Georgescu, I. M., Ashhab, S., & Nori, F. (2014). Quantum simulation. *Reviews of Modern Physics*, *86*(1), 153–185. https://doi.org/10.1103/RevModPhys.86.153

Gerster, M., Rizzi, M., Tschirsich, F., Silvi, P., Fazio, R., & Montangero, S. (2016). Superfluid density and quasi-long-range order in the one-dimensional disordered Bose–Hubbard model. *New Journal of Physics*, *18*(1), 015015. https://doi.org/10.1088/1367-2630/18/1/015015

Giamarchi, T., & Schulz, H. J. (1987). Localization and interaction in one-dimensional quantum fluids. *Europhysics Letters*, *3*(12), 1287–1293. https://doi.org/10.1209/0295-5075/3/12/007

Giamarchi, T. (2004). *Quantum physics in one dimension*. Oxford University Press.

Gogolin, C., & Eisert, J. (2016). Equilibration, thermalisation, and the emergence of statistical mechanics in closed quantum systems. *Reports on Progress in Physics*, *79*(5), 056001. https://doi.org/10.1088/0034-4885/79/5/056001

Gogolin, C., Müller, M. P., & Eisert, J. (2011). Absence of thermalization in nonintegrable systems. *Physical Review Letters*, *106*(4), 040401. https://doi.org/10.1103/PhysRevLett.106.040401

Goldstein, S., Lebowitz, J. L., Tumulka, R., & Zanghì, N. (2010). Long-time behavior of macroscopic quantum systems. *The European Physical Journal H*, *35*(2), 173–200. https://doi.org/10.1140/epjh/e2010-00007-7

Greiner, M., Mandel, O., Esslinger, T., Hänsch, T. W., & Bloch, I. (2002). Quantum phase transition from a superfluid to a Mott insulator in a gas of ultracold atoms. *Nature*, *415*(6867), 39–44. https://doi.org/10.1038/415039a

Griffiths, R. B. (1969). Nonanalytic behavior above the critical point in a random Ising ferromagnet. *Physical Review Letters*, *23*(1), 17–19. https://doi.org/10.1103/PhysRevLett.23.17

Grimm, R., Weidemüller, M., & Ovchinnikov, Y. B. (1999). Optical dipole traps for neutral atoms. *Advances In Atomic, Molecular, and Optical Physics* (pp. 95–170). Elsevier. https://doi.org/10.1016/S1049-250X(08)60186-X

Gritsev, V., Demler, E., Lukin, M., & Polkovnikov, A. (2007). Spectroscopy of collective excitations in interacting low-dimensional many-body systems using quench dynamics. *Physical Review Letters*, *99*(20), 200404. https://doi.org/10.1103/PhysRevLett.99.200404

Guarrera, V., Fallani, L., Lye, J. E., Fort, C., & Inguscio, M. (2007). Inhomogeneous broadening of a Mott insulator spectrum. *New Journal of Physics*, *9*(4). https://doi.org/10.1088/1367-2630/9/4/107

Haegeman, J., Cirac, J. I., Osborne, T. J., Pižorn, I., Verschelde, H., & Verstraete, F. (2011). Time-dependent variational principle for quantum lattices. *Physical Review Letters*, *107*(7), 070601. https://doi.org/10.1103/PhysRevLett.107.070601

Haegeman, J., Lubich, C., Oseledets, I., Vandereycken, B., & Verstraete, F. (2016). Unifying time evolution and optimization with matrix product states. *Physical Review B*, *94*(16), 165116. https://doi.org/10.1103/PhysRevB.94.165116

Haldane, F. D. M. (1981a). 'Luttinger liquid theory' of one-dimensional quantum fluids. I. Properties of the Luttinger model and their extension to the general 1D interacting spinless Fermi gas. *Journal of Physics C: Solid State Physics*, *14*(19), 2585–2609. https://doi.org/10.1088/0022-3719/14/19/010

Haldane, F. D. M. (1981b). Effective harmonic-fluid approach to low-energy properties of one-dimensional quantum fluids. *Physical Review Letters*, *47*(25), 1840–1843. https://doi.org/10.1103/PhysRevLett.47.1840

Haldane, F. (1980). Solidification in a soluble model of bosons on a one-dimensional lattice: The Boson-Hubbard chain. *Physics Letters A*, *80*(4), 281–283. https://doi.org/10.1016/0375-9601(80)90022-5

Haller, E., Gustavsson, M., Mark, M. J., Danzl, J. G., Hart, R., Pupillo, G., & Nagerl, H.-C. (2009). Realization of an excited, strongly correlated quantum gas phase. *Science*, *325*(5945), 1224–1227. https://doi.org/10.1126/science.1175850

Haller, E., Hudson, J., Kelly, A., Cotta, D. A., Peaudecerf, B., Bruce, G. D., & Kuhr, S. (2015). Single-atom imaging of fermions in a quantum-gas microscope. *Nature Physics*, *11*(9), 738–742. https://doi.org/10.1038/nphys3403

Hauke, P., & Tagliacozzo, L. (2013). Spread of correlations in long-range interacting quantum systems. *Physical Review Letters*, *111*(20), 207202. https://doi.org/10.1103/PhysRevLett.111.207202

Hauschild, J., & Pollmann, F. (2018). Efficient numerical simulations with tensor networks: Tensor Network Python (TeNPy). *SciPost Physics Lecture Notes*, 5. https://doi.org/10.21468/SciPostPhysLectNotes.5

Havelock, T. H. (1908). The propagation of groups of waves in dispersive media, with application to waves on water produced by a travelling disturbance. *Proceedings of the Royal Society of London. Series A, Containing Papers of a Mathematical and Physical Character*, *81*(549), 398–430.

Hild, S., Fukuhara, T., Schauß, P., Zeiher, J., Knap, M., Demler, E., Bloch, I., & Gross, C. (2014). Far-from-equilibrium spin transport in Heisenberg quantum magnets. *Physical Review Letters*, *113*(14), 147205. https://doi.org/10.1103/PhysRevLett.113.147205

Hodgman, S. S., Khakimov, R. I., Lewis-Swan, R. J., Truscott, A. G., & Kheruntsyan, K. V. (2017). Solving the quantum many-body problem via correlations measured with a momentum microscope. *Physical Review Letters*, *118*(24), 240402. https://doi.org/10.1103/PhysRevLett.118.240402

Holstein, T., & Primakoff, H. (1940). Field dependence of the intrinsic domain magnetization of a ferromagnet. *Physical Review*, *58*(12), 1098–1113. https://doi.org/10.1103/PhysRev.58.1098

Huber, S. D., Altman, E., Büchler, H. P., & Blatter, G. (2007). Dynamical properties of ultracold bosons in an optical lattice. *Physical Review B*, *75*(8), 085106. https://doi.org/10.1103/PhysRevB.75.085106

Inglis, S., & Pollet, L. (2016). Accessing many-body localized states through the generalized Gibbs ensemble. *Physical Review Letters*, *117*(12), 120402. https://doi.org/10.1103/PhysRevLett.117.120402

Iucci, A., & Cazalilla, M. A. (2009). Quantum quench dynamics of the Luttinger model. *Physical Review A*, *80*(6), 063619. https://doi.org/10.1103/PhysRevA.80.063619

Jaksch, D., Bruder, C., Cirac, J. I., Gardiner, C. W., & Zoller, P. (1998). Cold bosonic atoms in optical lattices. *Physical Review Letters*, *81*(15), 3108–3111. https://doi.org/10.1103/PhysRevLett.81.3108

Jaynes, E. T. (1957). Information theory and statistical mechanics. *Physical Review*, *106*(4), 620–630. https://doi.org/10.1103/PhysRev.106.620

Jendrzejewski, F., Bernard, A., Müller, K., Cheinet, P., Josse, V., Piraud, M., Pezzé, L., Sanchez-Palencia, L., Aspect, A., & Bouyer, P. (2012). Three-dimensional localization of ultracold atoms in an optical disordered potential. *Nature Physics*, *8*(5), 398–403. https://doi.org/10.1038/nphys2256

Jensen, R. V., & Shankar, R. (1985). Statistical behavior in deterministic quantum systems with few degrees of freedom. *Physical Review Letters*, *54*(17), 1879–1882. https://doi.org/10.1103/PhysRevLett.54.1879

Jordan, P., & Wigner, E. P. (1928). About the Pauli exclusion principle. *Zeitschrift für Physik*, *47*(631), 14–75.

Julienne, P. S., Mies, F. H., Tiesinga, E., & Williams, C. J. (1997). Collisional stability of double Bose condensates. *Physical Review Letters*, *78*(10), 1880–1883. https://doi.org/10.1103/PhysRevLett.78.1880

Jurcevic, P., Hauke, P., Maier, C., Hempel, C., Lanyon, B. P., Blatt, R., & Roos, C. F. (2015). Spectroscopy of interacting quasiparticles in trapped ions. *Physical Review Letters*, *115*(10), 100501. https://doi.org/10.1103/PhysRevLett.115.100501

Karbach, M., Hu, K., & Müller, G. (1998). Introduction to the Bethe ansatz ii. *Computers in Physics*, *12*(6), 565. https://doi.org/10.1063/1.168740

Karbach, M., & Müller, G. (1997). Introduction to the Bethe ansatz i. *Computers in Physics*, *11*(1), 36. https://doi.org/10.1063/1.4822511

Kashurnikov, V. A., & Svistunov, B. V. (1996). Exact diagonalization plus renormalization-group theory: Accurate method for a one-dimensional superfluid-insulator-transition study. *Physical Review B*, *53*(17), 11776–11778. https://doi.org/10.1103/PhysRevB.53.11776

Kashurnikov, V. A., Krasavin, A. V., & Svistunov, B. V. (1998). Zero-point phase transitions in the one-dimensional truncated bosonic Hubbard model and its spin-1 analog. *Physical Review B*, *58*(4), 1826–1831. https://doi.org/10.1103/PhysRevB.58.1826

Kelvin, L. (1887). On ship waves. *Proceedings of the Institution of Mechanical Engineers*, *3*, 409–434.

Ketterle, W., Durfee, D. S., & Stamper-Kurn, D. M. (1999). Making, probing and understanding Bose-Einstein condensates. https://arxiv.org/pdf/cond-mat/9904034.pdf

Kinoshita, T., Wenger, T., & Weiss, D. S. (2004). Observation of a one-dimensional Tonks-Girardeau gas. *Science*, *305*(5687), 1125–1128. https://doi.org/10.1126/science.1100700

Kinoshita, T., Wenger, T., & Weiss, D. S. (2006). A quantum Newton's cradle. *Nature*, *440*(7086), 900–903. https://doi.org/10.1038/nature04693

Knap, M., Arrigoni, E., & von der Linden, W. (2010). Excitations in disordered bosonic optical lattices. *Physical Review A*, *82*(5), 053628. https://doi.org/10.1103/PhysRevA.82.053628

Koffel, T., Lewenstein, M., & Tagliacozzo, L. (2012). Entanglement entropy for the long-range Ising chain in a transverse field. *Physical Review Letters*, *109*(26), 267203. https://doi.org/10.1103/PhysRevLett.109.267203

Kogut, J. B. (1979). An introduction to lattice gauge theory and spin systems. *Reviews of Modern Physics*, *51*(4), 659–713. https://doi.org/10.1103/RevModPhys.51.659

Kohlert, T., Scherg, S., Li, X., Lüschen, H. P., Das Sarma, S., Bloch, I., & Aidelsburger, M. (2019). Observation of many-body localization in a one-dimensional system with a single-particle mobility edge. *Physical Review Letters*, *122*(17), 170403. https://doi.org/10.1103/PhysRevLett.122.170403

Kollath, C., Iucci, A., Giamarchi, T., Hofstetter, W., & Schollwöck, U. (2006). Spectroscopy of ultracold atoms by periodic lattice modulations. *Physical Review Letters*, *97*(5), 050402. https://doi.org/10.1103/PhysRevLett.97.050402

Kolomeisky, E. B., & Straley, J. P. (2018). Kelvin-Mach wake in a two-dimensional Fermi sea. *Physical Review Letters*, *120*(22), 226801. https://doi.org/10.1103/PhysRevLett.120.226801

Korepin, V. E., Bogoliubov, N. M., & Izergin, A. G. (1997). *Quantum inverse scattering method and correlation functions* (Vol. 3). Cambridge University Press.

Krauth, W. (1991). Bethe ansatz for the one-dimensional boson Hubbard model. *Physical Review B*, *44*(17), 9772–9775. https://doi.org/10.1103/PhysRevB.44.9772

Kühner, T. D., White, S. R., & Monien, H. (2000). The one-dimensional Bose-Hubbard model with nearest-neighbor interaction. *Physical Review B*, *61*(18), 12474–12489. https://doi.org/10.1103/PhysRevB.61.12474

Labuhn, H., Barredo, D., Ravets, S., de Léséleuc, S., Macrì, T., Lahaye, T., & Browaeys, A. (2016). Tunable two-dimensional arrays of single Rydberg atoms for realizing quantum Ising models. *Nature*, *534*(7609), 667–670. https://doi.org/10.1038/nature18274

Lake, B., Tennant, D. A., Caux, J.-S., Barthel, T., Schollwöck, U., Nagler, S. E., & Frost, C. D. (2013). Multispinon continua at zero and finite temperature in a near-ideal Heisenberg

chain. *Physical Review Letters*, *111*(13), 137205. https://doi.org/10.1103/PhysRevLett.111.137205

Langen, T., Gasenzer, T., & Schmiedmayer, J. (2016). Prethermalization and universal dynamics in near-integrable quantum systems. *Journal of Statistical Mechanics: Theory and Experiment*, *2016*(6), 064009. https://doi.org/10.1088/1742-5468/2016/06/064009

Lanyon, B. P., Hempel, C., Nigg, D., Muller, M., Gerritsma, R., Zahringer, F., Schindler, P., Barreiro, J. T., Rambach, M., Kirchmair, G., Hennrich, M., Zoller, P., Blatt, R., & Roos, C. F. (2011). Universal digital quantum simulation with trapped ions. *Science*, *334*(6052), 57–61. https://doi.org/10.1126/science.1208001

Läuchli, A. M., & Kollath, C. (2008). Spreading of correlations and entanglement after a quench in the one-dimensional Bose–Hubbard model. *Journal of Statistical Mechanics: Theory and Experiment*, *2008*(05), P05018. https://doi.org/10.1088/1742-5468/2008/05/P05018

Lebowitz, J. L., & Penrose, O. (1973). Modern ergodic theory. *Physics Today*, *26*(2), 23–29. https://doi.org/10.1063/1.3127948

Lewenstein, M., Sanpera, A., & Ahufinger, V. (2012). *Ultracold atoms in optical lattices: Simulating quantum many-body systems*. Oxford University Press.

Li, X., Li, X., & Das Sarma, S. (2017). Mobility edges in one-dimensional bichromatic incommensurate potentials. *Physical Review B*, *96*(8), 085119. https://doi.org/10.1103/PhysRevB.96.085119

Lieb, E., & Robinson, D. (1972). The finite group velocity of quantum spin systems. *Communications in Mathematical Physics*, *28*(3), 251–257. https://doi.org/10.1007/BF01645779

Lieb, E. (1963). Exact analysis of an interacting Bose gas. II. The excitation spectrum. *Physical Review*, *130*(4), 1616–1624. https://doi.org/10.1103/PhysRev.130.1616

Lieb, E., & Liniger, W. (1963). Exact analysis of an interacting Bose gas. I. The general solution and the ground state. *Physical Review*, *130*(4), 1605–1616. https://doi.org/10.1103/PhysRev.130.1605

Lieb, E., Schultz, T., & Mattis, D. (1961). Two soluble models of an antiferromagnetic chain. *Annals of Physics*, *16*(3), 407–466. https://doi.org/10.1016/0003-4916(61)90115-4

Lieb, E., & Wu, F. Y. (1968). Absence of Mott transition in an exact solution of the short-range, one-band model in one dimension. *Physical Review Letters*, *20*(25), 1445–1448. https://doi.org/10.1103/PhysRevLett.20.1445

Linden, N., Popescu, S., Short, A. J., & Winter, A. (2009). Quantum mechanical evolution towards thermal equilibrium. *Physical Review E*, *79*(6), 061103. https://doi.org/10.1103/PhysRevE.79.061103

Lugan, P., Aspect, A., Sanchez-Palencia, L., Delande, D., Grémaud, B., Müller, C. A., & Miniatura, C. (2009). One-dimensional Anderson localization in certain correlated random potentials. *Physical Review A*, *80*(2), 023605. https://doi.org/10.1103/PhysRevA.80.023605

Lugan, P., Clément, D., Bouyer, P., Aspect, A., & Sanchez-Palencia, L. (2007). Anderson localization of Bogolyubov quasiparticles in interacting Bose-Einstein condensates. *Physical Review Letters*, *99*(18), 180402. https://doi.org/10.1103/PhysRevLett.99.180402

Lugan, P., & Sanchez-Palencia, L. (2011). Localization of Bogoliubov quasiparticles in interacting Bose gases with correlated disorder. *Physical Review A*, *84*(1), 013612. https://doi.org/10.1103/PhysRevA.84.013612

Lüschen, H. P., Scherg, S., Kohlert, T., Schreiber, M., Bordia, P., Li, X., Das Sarma, S., & Bloch, I. (2018). Single-particle mobility edge in a one-dimensional quasiperiodic optical lattice. *Physical Review Letters*, *120*(16), 160404. https://doi.org/10.1103/PhysRevLett.120.160404

Lüscher, A., & Läuchli, A. M. (2009). Exact diagonalization study of the antiferromagnetic spin-1 2 Heisenberg model on the square lattice in a magnetic field. *Physical Review B*, *79*(19), 195102. https://doi.org/10.1103/PhysRevB.79.195102

Mandel, O., Greiner, M., Widera, A., Rom, T., Hänsch, T. W., & Bloch, I. (2003). Controlled collisions for multi-particle entanglement of optically trapped atoms. *Nature*, *425*(6961), 937–940. https://doi.org/10.1038/nature02008

Manmana, S. R., Wessel, S., Noack, R. M., & Muramatsu, A. (2009). Time evolution of correlations in strongly interacting fermions after a quantum quench. *Physical Review B*, *79*(15), 155104. https://doi.org/10.1103/PhysRevB.79.155104

McCoy, B. M. (1969). Incompleteness of the critical exponent description for ferromagnetic systems containing random impurities. *Physical Review Letters*, *23*(7), 383–386. https://doi.org/10.1103/PhysRevLett.23.383

Meinert, F., Panfil, M., Mark, M. J., Lauber, K., Caux, J.-S., & Nägerl, H.-C. (2015). Probing the excitations of a Lieb-Liniger gas from weak to strong coupling. *Physical Review Letters*, *115*(8), 085301. https://doi.org/10.1103/PhysRevLett.115.085301

Meldgin, C., Ray, U., Russ, P., Chen, D., Ceperley, D. M., & DeMarco, B. (2016). Probing the Bose glass–superfluid transition using quantum quenches of disorder. *Nature Physics*, *12*(7), 646–649. https://doi.org/10.1038/nphys3695

Menu, R., & Roscilde, T. (2018). Quench dynamics of quantum spin models with flat bands of excitations. *Physical Review B*, *98*(20), 205145. https://doi.org/10.1103/PhysRevB.98.205145

Mora, C., & Castin, Y. (2003). Extension of Bogoliubov theory to quasicondensates. *Physical Review A*, *67*(5), 053615. https://doi.org/10.1103/PhysRevA.67.053615

Mourigal, M., Enderle, M., Klöpperpieper, A., Caux, J.-S., Stunault, A., & Rønnow, H. M. (2013). Fractional spinon excitations in the quantum Heisenberg antiferromagnetic chain. *Nature Physics*, *9*(7), 435–441. https://doi.org/10.1038/nphys2652

Myerson, A. H., Szwer, D. J., Webster, S. C., Allcock, D. T. C., Curtis, M. J., Imreh, G., Sherman, J. A., Stacey, D. N., Steane, A. M., & Lucas, D. M. (2008). High-fidelity readout of trapped-ion qubits. *Physical Review Letters*, *100*(20), 200502. https://doi.org/10.1103/PhysRevLett.100.200502

Naldesi, P., Ercolessi, E., & Roscilde, T. (2016). Detecting a many-body mobility edge with quantum quenches. *SciPost Physics*, *1*(1), 010. https://doi.org/10.21468/SciPostPhys.1.1.010

Nandkishore, R., & Huse, D. A. (2015). Many-body localization and thermalization in quantum statistical mechanics. *Annual Review of Condensed Matter Physics*, *6*(1), 15–38. https://doi.org/10.1146/annurev-conmatphys-031214-014726

Natu, S. S., & Mueller, E. J. (2013a). Dynamics of correlations in a dilute Bose gas following an interaction quench. *Physical Review A*, *87*(5), 053607. https://doi.org/10.1103/PhysRevA.87.053607

Natu, S. S., & Mueller, E. J. (2013b). Dynamics of correlations in shallow optical lattices. *Physical Review A*, *87*(6), 063616. https://doi.org/10.1103/PhysRevA.87.063616

Neill, C., Roushan, P., Fang, M., Chen, Y., Kolodrubetz, M., Chen, Z., Megrant, A., Barends, R., Campbell, B., Chiaro, B., Dunsworth, A., Jeffrey, E., Kelly, J., Mutus, J., O'Malley, P. J. J., Quintana, C., Sank, D., Vainsencher, A., Wenner, J., … Martinis, J. M. (2016). Ergodic dynamics and thermalization in an isolated quantum system. *Nature Physics*, *12*(11), 1037–1041. https://doi.org/10.1038/nphys3830

Nelson, K. D., Li, X., & Weiss, D. S. (2007). Imaging single atoms in a three-dimensional array. *Nature Physics*, *3*(8), 556–560. https://doi.org/10.1038/nphys645

Olshanii, M. (1998). Atomic scattering in the presence of an external confinement and a gas of impenetrable bosons. *Physical Review Letters*, *81*(5), 938–941. https://doi.org/10.1103/PhysRevLett.81.938

Olshanii, M., & Dunjko, V. (2003). Short-distance correlation properties of the Lieb-Liniger system and momentum distributions of trapped one-dimensional atomic gases. *Physical Review Letters*, *91*(9), 090401. https://doi.org/10.1103/PhysRevLett.91.090401

Orús, R. (2014). A practical introduction to tensor networks: Matrix product states and projected entangled pair states. *Annals of Physics*, *349*, 117–158. https://doi.org/10.1016/j.aop.2014.06.013

Pai, R. V., Pandit, R., Krishnamurthy, H. R., & Ramasesha, S. (1996). One-dimensional disordered bosonic Hubbard model: A density-matrix renormalization group study. *Physical Review Letters*, *76*(16), 4. https://doi.org/10.1103/PhysRevLett.76.2937

Paredes, B., Widera, A., Murg, V., Mandel, O., Fölling, S., Cirac, I., Shlyapnikov, G. V., Hänsch, T. W., & Bloch, I. (2004). Tonks–Girardeau gas of ultracold atoms in an optical lattice. *Nature*, *429*(6989), 277–281. https://doi.org/10.1038/nature02530

Penrose, O. (1979). Foundations of statistical mechanics. *Reports on Progress in Physics*, *42*(12), 1937. https://doi.org/10.1088/0034-4885/42/12/002

Piraud, M., Lugan, P., Bouyer, P., Aspect, A., & Sanchez-Palencia, L. (2011). Localization of a matter wave packet in a disordered potential. *Physical Review A*, *83*(3), 031603. https://doi.org/10.1103/PhysRevA.83.031603

Pitaevskii, L. P., & Stringari, S. (2016). *Bose-Einstein condensation and superfluidity*. Oxford University Press.

Pokrovsky, V. L., & Talapov, A. L. (1979). Ground state, spectrum, and phase diagram of two-dimensional incommensurate crystals. *Physical Review Letters*, *42*(1), 65–67. https://doi.org/10.1103/PhysRevLett.42.65

Polkovnikov, A., Sengupta, K., Silva, A., & Vengalattore, M. (2011). Colloquium : Nonequilibrium dynamics of closed interacting quantum systems. *Reviews of Modern Physics*, *83*(3), 863–883. https://doi.org/10.1103/RevModPhys.83.863

Pollet, L., Prokof'ev, N. V., Svistunov, B. V., & Troyer, M. (2009). Absence of a direct superfluid to Mott insulator transition in disordered Bose systems. *Physical Review Letters*, *103*(14), 140402. https://doi.org/10.1103/PhysRevLett.103.140402

Popov, V. N. (2001). *Functional integrals in quantum field theory and statistical physics*. Springer.

Porras, D., & Cirac, J. I. (2004). Effective quantum spin systems with trapped ions. *Physical Review Letters*, *92*(20), 207901. https://doi.org/10.1103/PhysRevLett.92.207901

Pottier, N. (2012). *Physique statistique hors d'équilibre-processus irréversibles linéaires*. EDP Sciences.

Prokof'ev, N. V., & Svistunov, B. V. (1998). Comment on "One-dimensional disordered bosonic Hubbard model: A density-matrix renormalization group study". *Physical Review Letters*, *80*(19), 4355–4355. https://doi.org/10.1103/PhysRevLett.80.4355

Rapsch, S., Schollwöck, U., & Zwerger, W. (1999). Density matrix renormalization group for disordered bosons in one dimension. *Europhysics Letters*, *46*(5), 559–564. https://doi.org/10.1209/epl/i1999-00302-7

Richerme, P., Gong, Z.-X., Lee, A., Senko, C., Smith, J., Foss-Feig, M., Michalakis, S., Gorshkov, A. V., & Monroe, C. (2014). Non-local propagation of correlations in quantum systems with long-range interactions. *Nature*, *511*(7508), 198–201. https://doi.org/10.1038/nature13450

Rigol, M., Dunjko, V., & Olshanii, M. (2008). Thermalization and its mechanism for generic isolated quantum systems. *Nature*, *452*(7189), 854–858. https://doi.org/10.1038/nature06838

Rigol, M., Dunjko, V., Yurovsky, V., & Olshanii, M. (2007). Relaxation in a completely integrable many-body quantum system: An *ab initio* study of the dynamics of the highly excited states of 1D lattice hard-core bosons. *Physical Review Letters*, *98*(5), 050405. https://doi.org/10.1103/PhysRevLett.98.050405

Rispoli, M., Lukin, A., Schittko, R., Kim, S., Tai, M. E., Léonard, J., & Greiner, M. (2019). Quantum critical behaviour at the many-body localization transition. *Nature*, *573*(7774), 385–389. https://doi.org/10.1038/s41586-019-1527-2

Ristivojevic, Z. (2014). Excitation spectrum of the Lieb-Liniger model. *Physical Review Letters*, *113*(1), 015301. https://doi.org/10.1103/PhysRevLett.113.015301

Ristivojevic, Z., & Matveev, K. A. (2016). Decay of Bogoliubov excitations in one-dimensional Bose gases. *Physical Review B*, *94*(2), 024506. https://doi.org/10.1103/PhysRevB.94.024506

Roati, G., D'Errico, C., Fallani, L., Fattori, M., Fort, C., Zaccanti, M., Modugno, G., Modugno, M., & Inguscio, M. (2008). Anderson localization of a non-interacting Bose–Einstein condensate. *Nature*, *453*(7197), 895–898. https://doi.org/10.1038/nature07071

Roscilde, T. (2008). Bosons in one-dimensional incommensurate superlattices. *Physical Review A*, *77*(6), 063605. https://doi.org/10.1103/PhysRevA.77.063605

Roscilde, T. (2009). Probing correlated phases of bosons in optical lattices via trap squeezing. *New Journal of Physics*, *11*(2), 023019. https://doi.org/10.1088/1367-2630/11/2/023019

Roth, R., & Burnett, K. (2004). Dynamic structure factor of ultracold Bose and Fermi gases in optical lattices. *Journal of Physics B: Atomic, Molecular and Optical Physics*, *37*(19), 3893–3907. https://doi.org/10.1088/0953-4075/37/19/009

Roux, G., Barthel, T., McCulloch, I. P., Kollath, C., Schollwöck, U., & Giamarchi, T. (2008). Quasiperiodic Bose-Hubbard model and localization in one-dimensional cold atomic gases. *Physical Review A*, *78*(2), 023628. https://doi.org/10.1103/PhysRevA.78.023628

Roux, G., Minguzzi, A., & Roscilde, T. (2013). Dynamic structure factor of one-dimensional lattice bosons in a disordered potential: A spectral fingerprint of the Bose-glass phase. *New Journal of Physics*, *15*(5), 055003. https://doi.org/10.1088/1367-2630/15/5/055003

Sachdev, S. (2011). *Quantum phase transitions* (Second edition). Cambridge University Press.

Sanchez-Palencia, L., Clément, D., Lugan, P., Bouyer, P., Shlyapnikov, G. V., & Aspect, A. (2007). Anderson localization of expanding Bose-Einstein condensates in random potentials. *Physical Review Letters*, *98*(21), 210401. https://doi.org/10.1103/PhysRevLett.98.210401

Sanchez-Palencia, L., & Lewenstein, M. (2010). Disordered quantum gases under control. *Nature Physics*, *6*(2), 87–95. https://doi.org/10.1038/nphys1507

Sbroscia, M., Viebahn, K., Carter, E., Yu, J.-C., Gaunt, A., & Schneider, U. (2020). Observing localization in a 2D quasicrystalline optical lattice. *Physical Review Letters*, *125*(20), 200604. https://doi.org/10.1103/PhysRevLett.125.200604

Scalettar, R. T., Batrouni, G. G., & Zimanyi, G. T. (1991). Localization in interacting, disordered, Bose systems. *Physical Review Letters*, *66*(24), 3144–3147. https://doi.org/10.1103/PhysRevLett.66.3144

Schäfer, F., Fukuhara, T., Sugawa, S., Takasu, Y., & Takahashi, Y. (2020). Tools for quantum simulation with ultracold atoms in optical lattices. *Nature Reviews Physics*, *2*, 411–425. https://doi.org/10.1038/s42254-020-0195-3

Schemmer, M., Johnson, A., & Bouchoule, I. (2018). Monitoring squeezed collective modes of a one-dimensional Bose gas after an interaction quench using density-ripple analysis. *Physical Review A*, *98*(4), 043604. https://doi.org/10.1103/PhysRevA.98.043604

Schneider, J. T., Despres, J., Thomson, S. J., Tagliacozzo, L., & Sanchez-Palencia, L. (2021). Spreading of correlations and entanglement in the long-range transverse Ising chain. *Physical Review Research*, *3*(1), L012022. https://doi.org/10.1103/PhysRevResearch.3.L012022

Schollwöck, U. (2005). The density-matrix renormalization group. *Review of Modern Physics*, *77*(1), 57.

Schollwöck, U. (2011). The density-matrix renormalization group in the age of matrix product states. *Annals of Physics*, *326*(1), 96–192. https://doi.org/10.1016/j.aop.2010.09.012

Schulz, H. J. (1995). Fermi liquids and non–Fermi liquids. https://arxiv.org/pdf/cond-mat/9503150.pdf

Schwabl, F. (2002). *Quantum mechanics*. Springer. https://doi.org/10.1007/978-3-662-04840-5

Semeghini, G., Landini, M., Castilho, P., Roy, S., Spagnolli, G., Trenkwalder, A., Fattori, M., Inguscio, M., & Modugno, G. (2015). Measurement of the mobility edge for 3D Anderson localization. *Nature Physics*, *11*(7), 554–559. https://doi.org/10.1038/nphys3339

Sherson, J. F., Weitenberg, C., Endres, M., Cheneau, M., Bloch, I., & Kuhr, S. (2010). Single-atom-resolved fluorescence imaging of an atomic Mott insulator. *Nature*, *467*(7311), 68–72. https://doi.org/10.1038/nature09378

Smith, J., Lee, A., Richerme, P., Neyenhuis, B., Hess, P. W., Hauke, P., Heyl, M., Huse, D. A., & Monroe, C. (2016). Many-body localization in a quantum simulator with programmable random disorder. *Nature Physics*, *12*(10), 907–911. https://doi.org/10.1038/nphys3783

Srednicki, M. (1994). Chaos and quantum thermalization. *Physical Review E*, *50*(2), 888–901. https://doi.org/10.1103/PhysRevE.50.888

Stamper-Kurn, D. M., Chikkatur, A. P., Görlitz, A., Inouye, S., Gupta, S., Pritchard, D. E., & Ketterle, W. (1999). Excitation of phonons in a Bose-Einstein condensate by light scattering. *Physical Review Letters*, *83*(15), 2876–2879. https://doi.org/10.1103/PhysRevLett.83.2876

Steinhauer, J., Katz, N., Ozeri, R., Davidson, N., Tozzo, C., & Dalfovo, F. (2003). Bragg spectroscopy of the multibranch Bogoliubov spectrum of elongated Bose-Einstein condensates. *Physical Review Letters*, *90*(6), 060404. https://doi.org/10.1103/PhysRevLett.90.060404

Steinhauer, J., Ozeri, R., Katz, N., & Davidson, N. (2002). Excitation spectrum of a Bose-Einstein condensate. *Physical Review Letters*, *88*(12), 120407. https://doi.org/10.1103/PhysRevLett.88.120407

Stenger, J., Inouye, S., Chikkatur, A. P., Stamper-Kurn, D. M., Pritchard, D. E., & Ketterle, W. (1999). Bragg spectroscopy of a Bose-Einstein condensate. *Physical Review Letters*, *82*(23), 4569–4573. https://doi.org/10.1103/PhysRevLett.82.4569

Stöferle, T., Moritz, H., Schori, C., Köhl, M., & Esslinger, T. (2004). Transition from a strongly interacting 1D superfluid to a Mott insulator. *Physical Review Letters*, *92*(13), 130403. https://doi.org/10.1103/PhysRevLett.92.130403

Sutherland, B. (1985). An introduction to the Bethe ansatz. In B. S. Shastry, S. S. Jha, & V. Singh (Eds.), *Exactly Solvable Problems in Condensed Matter and Relativistic Field Theory* (pp. 1–95). Springer. https://doi.org/10.1007/3-540-16075-2_7

Sutherland, B. (2004). *Beautiful models: 70 years of exactly solved quantum many-body problems*. World Scientific.

Szabó, A., & Schneider, U. (2020). Mixed spectra and partially extended states in a two-dimensional quasiperiodic model. *Physical Review B*, *101*(1), 014205. https://doi.org/10.1103/PhysRevB.101.014205

Tan, S. (2008a). Energetics of a strongly correlated Fermi gas. *Annals of Physics*, *323*(12), 2952–2970. https://doi.org/10.1016/j.aop.2008.03.004

Tan, S. (2008b). Generalized virial theorem and pressure relation for a strongly correlated Fermi gas. *Annals of Physics*, *323*(12), 2987–2990. https://doi.org/10.1016/j.aop.2008.03.003

Tan, S. (2008c). Large momentum part of a strongly correlated Fermi gas. *Annals of Physics*, *323*(12), 2971–2986. https://doi.org/10.1016/j.aop.2008.03.005

Tong, D. (2012). *Lecture notes on kinetic theory*. http://www.damtp.cam.ac.uk/user/tong/kinetic.html

Trotzky, S., Cheinet, P., Folling, S., Feld, M., Schnorrberger, U., Rey, A. M., Polkovnikov, A., Demler, E. A., Lukin, M. D., & Bloch, I. (2008). Time-resolved observation and control of superexchange interactions with ultracold atoms in optical lattices. *Science*, *319*(5861), 295–299. https://doi.org/10.1126/science.1150841

Trotzky, S., Chen, Y.-A., Flesch, A., McCulloch, I. P., Schollwöck, U., Eisert, J., & Bloch, I. (2012). Probing the relaxation towards equilibrium in an isolated strongly correlated one-dimensional Bose gas. *Nature Physics*, *8*(4), 325–330. https://doi.org/10.1038/nphys2232

Trotzky, S., Chen, Y.-A., Schnorrberger, U., Cheinet, P., & Bloch, I. (2010). Controlling and detecting spin correlations of ultracold atoms in optical lattices. *Physical Review Letters*, *105*(26), 265303. https://doi.org/10.1103/PhysRevLett.105.265303

Vidmar, L., & Rigol, M. (2016). Generalized Gibbs ensemble in integrable lattice models. *Journal of Statistical Mechanics: Theory and Experiment*, *2016*(6), 064007. https://doi.org/10.1088/1742-5468/2016/06/064007

Villa, L., Despres, J., & Sanchez-Palencia, L. (2019). Unraveling the excitation spectrum of many-body systems from quantum quenches. *Physical Review A*, *100*(6), 063632. https://doi.org/10.1103/PhysRevA.100.063632

Villa, L., Despres, J., Thomson, S. J., & Sanchez-Palencia, L. (2020). Local quench spectroscopy of many-body quantum systems. *Physical Review A*, *102*(3), 033337. https://doi.org/10.1103/PhysRevA.102.033337

Villa, L., Thomson, S. J., & Sanchez-Palencia, L. (2021a). Finding the phase diagram of strongly-correlated disordered bosons using quantum quenches. https://arxiv.org/pdf/2105.06396.pdf

Villa, L., Thomson, S. J., & Sanchez-Palencia, L. (2021b). Quench spectroscopy of a disordered quantum system. https://arxiv.org/pdf/2105.05774.pdf

Wampler, M., Schauss, P., Kolomeisky, E. B., & Klich, I. (2020). Quantum wakes in lattice fermions. https://arxiv.org/pdf/2006.09469.pdf

Weinberg, P., & Bukov, M. (2017). QuSpin: A Python package for dynamics and exact diagonalisation of quantum many body systems part I: Spin chains. *SciPost Physics*, *2*(1), 003. https://doi.org/10.21468/SciPostPhys.2.1.003

Weinberg, P., & Bukov, M. (2019). QuSpin: A Python package for dynamics and exact diagonalisation of quantum many body systems. Part II: Bosons, fermions and higher spins. *SciPost Physics*, *7*(2), 020. https://doi.org/10.21468/SciPostPhys.7.2.020

Weitenberg, C., Endres, M., Sherson, J. F., Cheneau, M., Schauß, P., Fukuhara, T., Bloch, I., & Kuhr, S. (2011). Single-spin addressing in an atomic Mott insulator. *Nature*, *471*(7338), 319–324. https://doi.org/10.1038/nature09827

White, S. R. (1992). Density matrix formulation for quantum renormalization groups. *Physical Review Letters*, *69*(19), 2863–2866. https://doi.org/10.1103/PhysRevLett.69.2863

White, S. R. (1993). Density-matrix algorithms for quantum renormalization groups. *Physical Review B*, *48*(14), 10345–10356. https://doi.org/10.1103/PhysRevB.48.10345

Wölfle, P. (2018). Quasiparticles in condensed matter systems. *Reports on Progress in Physics*, *81*(3), 032501. https://doi.org/10.1088/1361-6633/aa9bc4

Yang, C. N., & Yang, C. P. (1969). Thermodynamics of a one-dimensional system of bosons with repulsive delta-function interaction. *Journal of Mathematical Physics*, *10*(7), 1115–1122. https://doi.org/10.1063/1.1664947

Yao, H., Clément, D., Minguzzi, A., Vignolo, P., & Sanchez-Palencia, L. (2018). Tan's contact for trapped Lieb-Liniger bosons at finite temperature. *Physical Review Letters*, *121*(22), 220402. https://doi.org/10.1103/PhysRevLett.121.220402

Yao, H., Giamarchi, T., & Sanchez-Palencia, L. (2020). Lieb-Liniger bosons in a shallow quasiperiodic potential: Bose glass phase and fractal Mott lobes. *Physical Review Letters*, *125*(6), 060401. https://doi.org/10.1103/PhysRevLett.125.060401

Yao, H., Khoudli, H., Bresque, L., & Sanchez-Palencia, L. (2019). Critical behavior and fractality in shallow one-dimensional quasiperiodic potentials. *Physical Review Letters*, *123*(7), 070405. https://doi.org/10.1103/PhysRevLett.123.070405

Yao, R., & Zakrzewski, J. (2020). Many-body localization in the Bose-Hubbard model: Evidence for mobility edge. *Physical Review B*, *102*(1), 014310. https://doi.org/10.1103/PhysRevB.102.014310

Yao, Z., Pollet, L., Prokof'ev, N., & Svistunov, B. (2016). Superfluid–insulator transition in strongly disordered one-dimensional systems. *New Journal of Physics*, *18*(4), 045018. https://doi.org/10.1088/1367-2630/18/4/045018

Zurek, W. H. (2003). Decoherence, einselection, and the quantum origins of the classical. *Reviews of Modern Physics*, *75*(3), 715–775. https://doi.org/10.1103/RevModPhys.75.715

Zwerger, W. (2003). Mott Hubbard transition of cold atoms in optical lattices. *Journal of Optics B: Quantum and Semiclassical Optics*, *5*(2), S9–S16. https://doi.org/10.1088/1464-4266/5/2/352

ECOLE DOCTORALE

Titre : Dynamique hors de l'équilibre et spectroscopie par quench de modèles quantiques ultrafroids à N-corps

Mots clés : quench quantique, cône de lumière, propagation des corrélations, systèmes désordonnés, verre de Bose, spectre d'excitation

Résumé : Les atomes ultrafroids sont devenus une plateforme polyvalente pour réaliser et contrôler des systèmes quantiques fortement corrélés. Les méthodes spectroscopiques sont les outils courants pour sonder les propriétés des excitations qui contrôlent les phénomènes dynamiques de transport. Dans cette thèse, nous développons une nouvelle méthode de spectroscopie par quench qui utilise la dynamique hors équilibre générée par un quench quantique pour fournir des informations sur les excitations résolues en vecteur d'onde. Nous testons la méthode sur des modèles unidimensionnels où des simulations numériques performantes et exactes par le groupe de renormalisation de la matrice densité sont disponibles. Premièrement, nous analysons la structure spatio-temporelle des corrélations quantiques hors équilibre dans les modèles sur réseau. Celle-ci présente une forme de cône de lumière avec une structure double. Deux vitesses caractéristiques peuvent être extraites des corrélations proches du bord du cône, dont une donne la vitesse de propagation des corrélations quantiques. Ces deux vitesses dépendent des propriétés dynamiques du spectre d'excitation du modèle sous-jacent. Deuxièmement, nous discutons comment la spectroscopie par quench peut être utilisée pour reconstruire les propriétés spectrales à partir des corrélations spatio-temporelles de simples observables ou corrélateurs à temps égaux. Ceci offre la possibilité de reconstruire la relation de dispersion des excitations à partir d'instantanés de l'expérience obtenus à l'aide de microscopes quantiques, en évitant les fastidieux balayage et étalonnage en vecteur d'onde nécessaires dans les méthodes pompe-sonde standard. Nous étudions des quenchs globaux et locaux sur des systèmes non-désordonnés, et discutons du rôle joué par l'observable sur les caractéristiques spectrales. La méthode générale est illustrée sur divers exemples incluant le modèle de Bose-Hubbard et des modèles de chaînes de spin, dans diverses phases, régimes et pour différentes observables. Troisièmement, nous étendons la spectroscopie par quench aux systèmes désordonnés. En prenant comme exemple la chaîne de Bose-Hubbard désordonnée, nous montrons à l'aide d'une seule sonde comment la méthode peut distinguer sans ambiguïté le verre de Bose de l'isolant de Mott et du superfluide. En utilisant une sonde spectrale à résolution spatiale, nous reconstruisons également le diagramme de phase complet du modèle.

Title : Out-of-equilibrium dynamics and quench spectroscopy of ultracold many-body quantum systems

Keywords : quantum quench, light-cone dynamics, correlation spreading, disordered systems, Bose glass, excitation spectrum

Abstract : Ultracold atoms have emerged as a versatile platform to realise and control strongly-correlated quantum systems. Spectroscopic methods are the common tools to probe the properties of the excitations which control dynamical transport phenomena. In this thesis, we develop a novel spectroscopic method named quench spectroscopy that uses the out-of-equilibrium dynamics generated by a quantum quench to grant momentum-resolved information about the excitations. We benchmark the method on one-dimensional models where efficient density matrix renormalisation group numerical simulations are available. First, we analyse the out-of-equilibrium space-time pattern of quantum correlations in lattice models following a quantum quench. It displays a generic light-cone like pattern with a twofold structure. Two characteristic velocities can be extracted from the correlations close to the cone edge, one of which gives the velocity for the propagation of quantum correlations throughout the system. Both of these velocities can be related to dynamical properties of the excitation spectrum of the underlying model. Second, we discuss how quench spectroscopy reconstructs spectral properties from space-time patterns using simple equal-time observables or correlators. It allows to reconstruct the full dispersion relation from a series of snapshots of the experiment using quantum gas microscopes, and avoids the tedious scan and calibration in momentum necessary in standard pump-probe methods. We investigate both global and local quenches on clean systems, and discuss the role played by the observable on the spectral features. We discuss the implementation on various examples including the Bose-Hubbard model and spin chain models in various phases, regimes and for different observables. Third, we extend quench spectroscopy to disordered systems. Using as an example the disordered Bose-Hubbard chain, we show using a single probe how the method can unambiguously tell apart the Bose glass from the Mott insulator and the superfluid. Using a spatially-resolved spectral probe, we also reconstruct the full phase diagram of the model.

Institut Polytechnique de Paris
91120 Palaiseau, France